

**Experimental and Theoretical Study of High
Frequency Magnetic Fields around a Railway Track**

by

MAURIZIO ANGELO MORESCO

DISSERTATION

**Submitted in partial fulfilment
of the requirements for the degree**

MASTERS IN ENGINEERING

in

ELECTRICAL AND ELECTRONIC ENGINEERING

at the

UNIVERSITY OF JOHANNESBURG

SUPERVISOR: PROF. W.A. CRONJÉ

CO-SUPERVISOR: I.W. HOFSAJER

DECEMBER 2006

Abstract

The South African railway company makes use of a train wheel detection system to monitor the trains present on a particular track, noting their lengths, positions and speeds. Interference due to distorted traction currents cause havoc with this system rendering the information gathered unreliable. To combat this interference two paths are available to reduce the detection systems susceptibility. These paths include the addition of shielding between the railway track and the wheel detectors, which form the functional entities of the train wheel detection system, and the installation of a cable running parallel to the railway track with connections to it some distance before and after the position of the wheel detector. To verify these paths, high frequency experiments were performed in the lab as well as FEM simulations. To perform the high frequency experiments a source capable of producing the high frequency current needed was designed and constructed, along with a well shielded measurement system to enable the mapping of the flux density within the region occupied by and surrounding the wheel detector. The results of both the experimental measurements and simulations yielded that the interfering magnetic field could indeed be reduced through the use of the two available paths, when they are both applied separately and in combination. To obtain the greater reduction in the interfering field within the area occupied by and surrounding the wheel detector the paths should be used in combination. Therefore through the use of a shield that is constructed from a magnetic material and the installation of a parallel cable the train wheel detection system can be made more robust.

Acknowledgement

I would like to thank my parents for their encouragement, support and patience throughout my studies.

I would like to thank my girlfriend for her support, help and understanding through the completion of this dissertation.

I thank my supervisors, Prof. W.A Cronjé and Prof. I.W. Hofsajer, for their guidance and intellectual input.

Additional special thanks to Spoornet for sponsorship towards the completion of my masters.

Table of Contents

1	INTRODUCTION.....	1
1.1	BACKGROUND.....	1
1.2	PROXIMITY SENSOR.....	1
1.2.1	<i>Background on Inductive Proximity Sensor</i>	1
1.2.2	<i>Problems with the Inductive Proximity Sensor</i>	4
1.3	GOALS OF THIS INVESTIGATION.....	5
1.3.1	<i>Ultimate Goal</i>	5
1.3.2	<i>Restrictions for achieving Goals</i>	5
1.3.3	<i>Available paths to achieving the Goals</i>	5
1.3.4	<i>Assumptions Made</i>	8
1.4	PROBLEM DEFINITION.....	8
1.5	APPROACH USED TO MEET PROBLEM DEFINITIONS.....	9
1.5.1	<i>Tests to be performed</i>	9
1.5.1.1	Low Frequency Tests at 650A 50Hz.....	9
1.5.1.2	High Frequency tests at 2A 300 kHz.....	10
1.5.2	<i>Apparatus needed to perform the tests for both the low and high frequency cases</i>	11
1.5.3	<i>Mapping techniques used</i>	13
1.5.3.1	Grid layout used for mapping the Test Area.....	13
1.5.3.2	Measurement Technique.....	14
1.5.4	<i>Technique used for the comparison of the different Test Cases</i>	14
2	LOW FREQUENCY TEST AT 650A 50HZ.....	16
2.1	INTRODUCTION.....	16
2.2	APPARATUS: TEST SETUP.....	17
2.2.1	<i>Railway Track System</i>	17
2.2.2	<i>Measurement System</i>	18
2.2.2.1	The Magnetic Flux Density Sensor.....	18
2.2.2.1.1	Design of Magnetic Flux Density Sensor.....	18
2.2.2.1.2	Construction of Magnetic Flux Density Sensor Coil.....	20
2.2.2.2	Constructed Test Rig.....	21
2.3	EXPERIMENTAL RESULTS.....	22
3	PREPARATION OF THE RAILWAY TRACK SYSTEM FOR THE HIGH FREQUENCY TEST AT 2A 300KHZ.....	25
3.1	INTRODUCTION.....	25
3.2	HIGH FREQUENCY CURRENT SOURCE: 300 KHZ RESONATOR.....	26
3.2.1	<i>Introduction</i>	26
3.2.2	<i>Theory</i>	28
3.2.3	<i>Operation of the Half Bridge Resonant Converter</i>	32

3.2.4	<i>Design of Resonant Converter</i>	35
3.2.4.1	Determining Railway Track Inductance.....	36
3.2.4.2	Choosing Values of Inductance and capacitance for the resonant circuit.....	37
3.2.4.3	The Driving Circuit for the Resonator	39
3.2.4.4	300 kHz Resonator Board: Resonant Converter.....	44
3.2.4.5	Final Assembly of the 300 kHz Resonator.....	47
3.2.4.6	New Proposed Higher Frequency Driving Circuit (300 kHz to 1 MHz).....	49
4	PREPARATION OF THE MEASUREMENT SYSTEM FOR THE HIGH FREQUENCY TEST AT 2A 300KHZ	53
4.1	INTRODUCTION.....	53
4.2	INTERFERENCE PROBLEMS WITH MEASUREMENT SYSTEM.....	54
4.2.1	<i>Capacitive Coupling</i>	54
4.2.2	<i>Magnetic Coupling</i>	55
4.2.3	<i>Imbalance</i>	55
4.2.4	<i>Methods to increase the Measurement Systems Resistance to Interference</i>	56
4.2.4.1	Shielding or Screening.....	56
4.2.4.2	Conductor Path Layout	58
4.2.4.3	Grounding system and reducing common mode currents	58
4.3	REDUCING THE MEASUREMENTS SYSTEMS SUSCEPTIBILITY TO EMI.....	59
4.3.1	<i>Steps to Combat EMI on the Measurement System</i>	59
4.3.2	<i>Improvements to the Magnetic Flux Density Sensor</i>	61
4.3.2.1	Adapting the Winding layout.....	61
4.3.2.2	Addition of Copper Shield	62
4.3.3	<i>Improving the Cabling System for the Measurement System</i>	63
4.3.3.1	Composite Cable.....	63
4.3.3.2	Flux Density Sensor.....	64
4.3.3.3	Connectors	66
4.3.4	<i>Trance Conduction Amplifier</i>	69
4.3.4.1	Amplification.....	69
4.3.4.2	Connection and Buffering.....	72
4.3.5	<i>Common Mode Chokes</i>	72
4.3.5.1	Impedance Matching.....	73
4.3.6	<i>Improved Grounding System</i>	74
4.4	NEW FLUX DENSITY SENSOR COIL	76
4.5	CALIBRATION.....	77
4.5.1	<i>Apparatus</i>	77
4.5.2	<i>Calibration Setup</i>	78
4.5.3	<i>Model of the Calibration System</i>	80
5	EXPERIMENTAL RESULTS FOR 2A 300 KHZ HIGH FREQUENCY TESTS	86
5.1	INTRODUCTION.....	86
5.2	PREPARATION	87

5.2.1	<i>Test Rig</i>	87
5.2.2	<i>Railway Track System</i>	87
5.2.3	<i>Measurement System</i>	88
5.3	EXPERIMENTAL RESULTS	91
5.3.1	<i>Tests to be performed</i>	91
5.3.2	<i>Measurement Technique and Results Presentation</i>	92
5.3.3	<i>First Test: Base Measurement</i>	93
5.3.4	<i>Second test: Shield Measurement with No Cable or Isolation</i>	95
5.3.5	<i>Third Test: Shield Measurement with Isolation and No Cable</i>	96
5.3.6	<i>Fourth Test: First Cable Test set (sub-base), with no shield or isolation</i>	97
5.3.7	<i>Fifth Test: First Cable Test set with the inclusion of the shield but no isolation</i>	98
5.3.8	<i>Sixth Test: First Cable Test set with the inclusion of the shield and isolation</i>	99
5.3.9	<i>Subsequent Tests</i>	100
5.4	DIRECT COMPARISON.....	101
5.4.1	<i>Direct comparison for the first test set with no parallel cable</i>	102
5.4.2	<i>Direct comparison for the second test set with the first cable connected in parallel</i> ...	104
5.4.3	<i>Direct comparison for the third test set with the second cable connected in parallel</i> ..	106
5.4.4	<i>Direct comparison for the fourth test set with the third cable connected in parallel</i> ...	108
5.4.5	<i>Direct comparison, comparing the effect of the three different cables directly</i>	110
5.4.6	<i>Direct comparison, comparing the effect of the shielded cases for the three different cables directly</i>	111
5.4.7	<i>Direct comparison, comparing the effect of the shielded and isolated cases for the three different cables directly</i>	112
6	SIMULATIONS	113
6.1	INTRODUCTION.....	113
6.2	PREPARING THE SIMULATION PACKAGE.....	113
6.2.1	<i>Solver Type chosen</i>	113
6.2.2	<i>Drawing Plane used</i>	113
6.2.3	<i>Defining the Model to be simulated</i>	114
6.2.4	<i>Defining the materials used</i>	115
6.2.5	<i>Setting up Boundaries and Sources</i>	115
6.2.6	<i>Setting up the Solutions</i>	116
6.3	DIFFICULTIES EXPERIENCED WITH THE SIMULATIONS	117
6.4	SIMULATION RESULTS	119
6.4.1	<i>Base Simulation (Simulated Base Measurement)</i>	119
6.4.2	<i>Base Simulation with the addition of a shield</i>	120
6.4.3	<i>Sub-base Simulation including the First Parallel Cable</i>	121
6.4.4	<i>First Cable Simulation including a shield</i>	122
6.4.5	<i>Sub-Base Simulation including the Second Parallel Cable</i>	123
6.4.6	<i>Second Cable Simulation including a shield</i>	124

6.4.7	<i>Sub-Base Simulation including the Third Parallel Cable</i>	125
6.4.8	<i>Third Cable Simulation including a shield</i>	126
6.5	DIRECT COMPARISON OF SIMULATION RESULTS.....	127
6.5.1	<i>Direct comparison for all the unshielded Simulation</i>	128
6.5.2	<i>Direct comparison for all the shielded Simulation</i>	129
6.6	OTHER SIMULATIONS PERFORMED.....	130
6.6.1	<i>Simulation Illustrating the Deflection Principle</i>	131
6.6.2	<i>Simulation Illustrating the Absorption Principle</i>	132
6.6.3	<i>Direct comparison of the flux densities for the simulations of the deflection and absorption principles</i>	133
6.7	DIFFERENCES BETWEEN THE SIMULATED AND MEASURED RESULTS.....	135
7	CONCLUSION	136
8	RECOMMENDATIONS	139
9	REFERENCES	140
10	APPENDICES	141
10.1	APPENDIX 1: RESULTS FOR THE LOW FREQUENCY TEST.....	141
10.2	APPENDIX 2: HIGH FREQUENCY CURRENT SOURCE, RESONATOR.....	143
10.2.1	<i>Appendix 2.1: Determination of the laboratory railway track inductance by use of a buck converter</i>	143
10.2.1.1	Measurement Technique for determining Inductance with the use of a Buck Converter ..	143
10.2.1.2	Design procedure for a Buck converter.....	145
10.2.2	<i>Appendix 2.2: Design of an Inductor using a Ferrite E-Core</i>	147
10.2.2.1	Introduction.....	147
10.2.2.2	Design Procedure.....	148
10.2.3	<i>Appendix 2.3: PCB Design of Driving Circuit and 300 kHz Resonator Board</i>	151
10.2.3.1	Driving Circuit of the Resonator (PWM Half Bridge Mosfet Driver).....	151
10.2.3.2	300 kHz Resonator Board.....	152
10.2.4	<i>Appendix 2.4: P-Spice Simulations of the Resonant Converter (Resonator)</i>	153
10.2.5	<i>Appendix 2.5: Testing of the 300 kHz Resonator</i>	156
10.2.5.1	Differences between the simulated and constructed resonator.....	158
10.2.6	<i>Appendix 2.6: New PCB Layouts for the New Higher Frequency Driving Circuit and Resonator Board</i>	160
10.2.6.1	PCB Layout of the New 300 kHz to 1 MHz Driving Circuit	160
10.2.6.2	PCB of the New Modified Resonator Board for higher frequency operation.....	161
10.3	APPENDIX 3: INITIAL IMPROVEMENT TO THE MEASUREMENT SYSTEM TO REDUCE ITS SUSCEPTIBILITY TO ELECTRO-MAGNETIC INTERFERENCE.....	163
10.3.1	<i>Shielded Cable</i>	164
10.3.2	<i>Connection Shielding</i>	165
10.4	APPENDIX 4: EXPERIMENTAL RESULTS.....	167

10.4.1	<i>Appendix 4.1: Y-Component Contour Plots for Experimental Results showing the measured magnetic flux densities</i>	167
10.4.1.1	Seventh Test: Second Cable Test set (Sub-Base) with No shield or Isolation.....	167
10.4.1.2	Eighth Test: Second Cable Test set with the inclusion of a shield but no Isolation	168
10.4.1.3	Ninth Test: Second Cable Test set with the inclusion of a shield and Isolation	169
10.4.1.4	Tenth Test: Third Cable Test set (Sub-Base) with No shield or Isolation.....	170
10.4.1.5	Eleventh Test: Third Cable Test set with the inclusion of a shield but no Isolation.....	171
10.4.1.6	Twelfth Test: Third Cable Test set with the inclusion of a shield and Isolation.....	172
10.4.2	<i>Appendix 4.2: X-Components and Combined contour plots showing the measured flux densities for the Experimental Results</i>	173
10.4.2.1	First Test: Base Measurements of X-Component and Combined Results.....	173
10.4.2.2	Second Test: Shield Measurement with No Cable or Isolation.....	175
10.4.2.3	Third Test: Inclusion of isolation between shield and proximity sensor platform.....	176
10.4.2.4	Fourth Test: First Cable Test (Sub-Base), with no shield or isolation.....	178
10.4.2.5	Fifth Test: First Cable Test set with the inclusion of the shield but no isolation.....	179
10.4.2.6	Sixth Test: First Cable Test set with the inclusion of the shield and isolation	180
10.4.2.7	Seventh Test: Second Cable Test set (Sub-Base) with No shield or Isolation.....	181
10.4.2.8	Eighth Test: Second Cable Test set with the inclusion of a shield but no Isolation	182
10.4.2.9	Ninth Test: Second Cable Test set with the inclusion of a shield and Isolation	183
10.4.2.10	Tenth Test: Third Cable Test set (Sub-Base) with No shield or Isolation.....	184
10.4.2.11	Eleventh Test: Third Cable Test set with the inclusion of a shield but no Isolation.....	185
10.4.2.12	Twelfth Test: Third Cable Test set with the inclusion of a shield and Isolation.....	186
10.4.3	<i>Appendix 4.3: Direct Comparison, Results in Micro Tesla</i>	187
10.4.3.1	Direct comparison, comparing the effect of the three different cables directly	187
10.4.3.2	Direct comparison Bar Graph, comparing the effect of the shielded cases for the three different parallel cables directly	188
10.4.3.3	Direct comparison, comparing the effect of the shielded and isolated cases for the three different cables directly.....	189
10.5	APPENDIX 5: SIMULATION RESULTS.....	190
10.5.1	<i>Appendix 5.1: Simulation Results showing the Flux Lines Present in the Test Area next to the Railway Track</i>	190
10.5.1.1	Base Simulation (Simulated Base Measurement)	190
10.5.1.2	Base Simulation with the addition of a shield	190
10.5.1.3	Sub Base Simulation including the First Parallel Cable	191
10.5.1.4	First Cable Simulation including a shield	191
10.5.1.5	Sub Base Simulation including the Second Parallel Cable.....	192
10.5.1.6	Second Cable Simulation including a shield	192
10.5.1.7	Sub Base Simulation including the Third Parallel Cable	193
10.5.1.8	Third Cable Simulation including a shield.....	193
10.5.2	<i>Appendix 5.2: Comparison Bar graphs for each of the Simulated Results</i>	194
10.5.2.1	Direct comparison for the shielded and un-shielded Base Simulations with no cable installed running parallel to the Railway Track.....	194
10.5.2.2	Direct comparison with the first parallel cable connected between the shielded and un-shielded simulations.....	195

10.5.2.3	Direct comparison with the Second parallel cable connected between the shielded and unshielded simulations.....	196
10.5.2.4	Direct comparison with the Third parallel cable connected between the shielded and unshielded simulations.....	197
10.5.3	<i>Appendix 5.3: Flux lines within the test area for the other simulations Performed.</i>	198
10.5.3.1	Inclusion of an Aluminium Shield.....	198
10.5.3.2	Inclusion of a Ferrite Shield.....	198
10.6	APPENDIX 6: MATLAB CODE.....	199
10.6.1	<i>Appendix 6.1: Matlab Code for Finding the Calibration Coefficients for the Measurement System.....</i>	199
10.6.2	<i>Appendix 6.2: Matlab Program For converting the Measured Results to Tesla and displaying the flux density distribution within the test area in the form of contour plots.</i>	200
10.6.3	<i>Appendix 6.3: Matlab program for generating the bar graphs used for the direct comparison of the measured results.....</i>	205
10.6.4	<i>Appendix 6.4: Matlab program for generating the Normalized bar graphs used for the direct comparison of the measured results.....</i>	208
10.6.5	<i>Appendix 6.5: Matlab Program for determining the total percentage reduction of the flux density within the sensing region</i>	211
10.6.6	<i>Appendix 6.6: Matlab Program written to produce the direct comparison of the simulated results</i>	212
10.6.7	<i>Appendix 6.7: Matlab Program used to determine the total percentage reduction of the flux density within the sensing region for each of the simulation cases.....</i>	215
10.7	APPENDIX 7: DATA SHEETS.....	216
10.7.1	<i>Appendix 7.1: SG3525 – Pulse Width Modulator Control Circuit</i>	216
10.7.2	<i>Appendix 7.2: IR2113 – High and Low Side Driver</i>	219
10.7.3	<i>Appendix 7.3: IRFZ44 – 60V 50A Mosfet</i>	224
10.7.4	<i>Appendix 7.4: UC3825 – High Speed Pulse Width Modulator (PWM) Controller .</i>	227
10.7.5	<i>Appendix 7.5: MAX436 – Wideband Transconductance Amplifier.....</i>	230
11	LIST OF FIGURES.....	235
12	LIST OF TABLES.....	243

1 Introduction

1.1 Background

The South African Railway Company (Spoornet) makes use of a train wheel detection system to achieve the overarching goal of counting the number of wheels present on any train that passes a particular detection point. The data here generated is further extrapolated to determine the number of carts the train is pulling, the speed of the train and its position along the railway track. The wheel detectors that perform the necessary train wheel counting form an integral part of this detection system.

The wheel detectors, or more specifically, the proximity sensors, form the functional entities of the train wheel detection system. These proximity sensors are purported to detect any metallic material (such as that of the iron comprising a train wheel) brought into their sensing regions as the underlying basis for their operation. A deficiency however exists as some of these proximity sensors (wheel detectors) are miscounting the train wheels passing detection points situated along the railway track.

The errors incurred by some of the train wheel detection systems are caused by magnetic fields generated around the railway track by distorted traction currents. These magnetic fields interfere with the proximity sensors and subsequently deter their performance. This is a significant problem since the information determined from this data will be incorrect and consequently the decisions made may have undesirable results. To this end, stemming from the impending reduction of proximity sensor effectiveness coupled with the geometric growth of errors, the principle aim of this study is to circumvent this problem in a pragmatic manner.

1.2 Proximity Sensor

1.2.1 Background on Inductive Proximity Sensor

The proximity sensors used are of the inductive type and consist of a resonant circuit with an exposed magnetic field which is used to detect the presence of any metallic material, as is the case for the train wheel. This exposed magnetic field is generated by the inductor core of the resonant circuit, which serves as the sensing head of the

proximity sensor. The particular sensor being employed has an operating resonant frequency of 300 kHz.

When a metallic material such as a train wheel is brought into the exposed magnetic field, or sensing field, eddy currents are induced in the material and flow in a direction opposite to that of the current in the sensing head of the proximity sensor. These eddy currents produce a magnetic field which opposes the field generated by the sensor. This occurrence may have one of two effects on the proximity sensor, either of which being dependant on the type of sensor used.

The first of such effects would assume a shift in the resonant point of the proximity sensor and the in second effect an increase in the energy loss in the magnetic field due to the introduction of the metallic material may ensue. For both cases the amplitude of the 300 kHz oscillation in the proximity sensor decreases. This decrease in amplitude is detected by an electronic circuit within the proximity sensor and a digital signal is sent out to an external system where the information is analyzed.

An elevation in digital output indicates the presence of a metallic material (the train wheel) and when the output declines, the opposite is true. In this manner each pulse on the digital output can be counted thereby yielding the number of train wheels that have passed the detection point within a designated time frame. The speed of the train is determined by applying the time between each pulse and the known distance between each wheel set to appropriate kinetic formulae.

The proximity sensor used in the field is based on a Turck Uprox Inductive proximity sensor and has an operating voltage of 10 to 30 VDC input and one digital output.

Figure 1-1 below depicts the test setup as used in the laboratory to emulate the field situation.

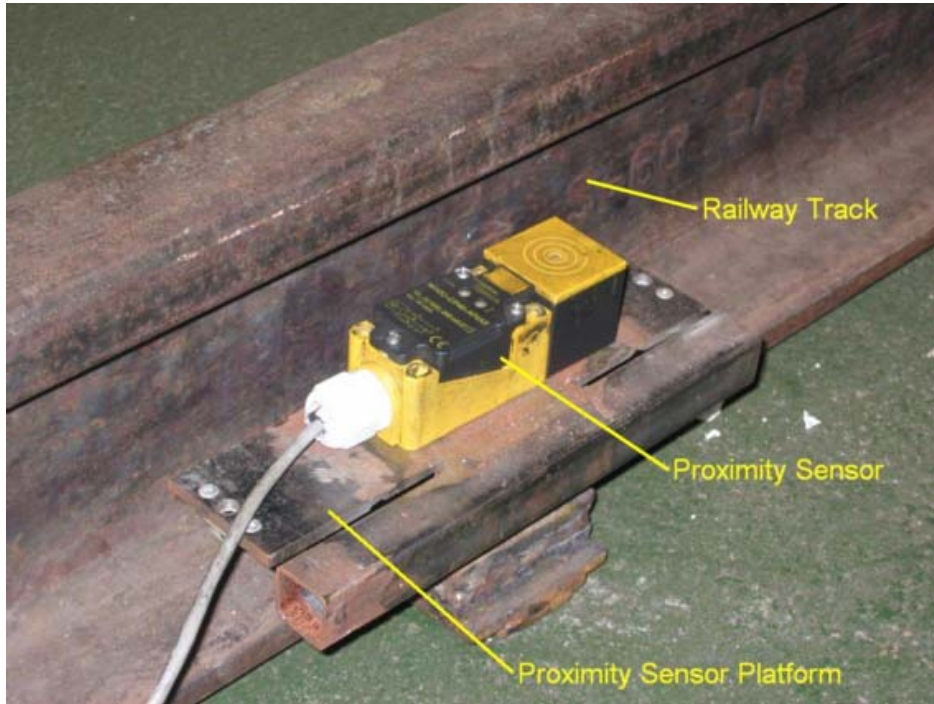


Figure 1-1: Inductive proximity sensor on proximity sensor platform next to a railway track in laboratory.

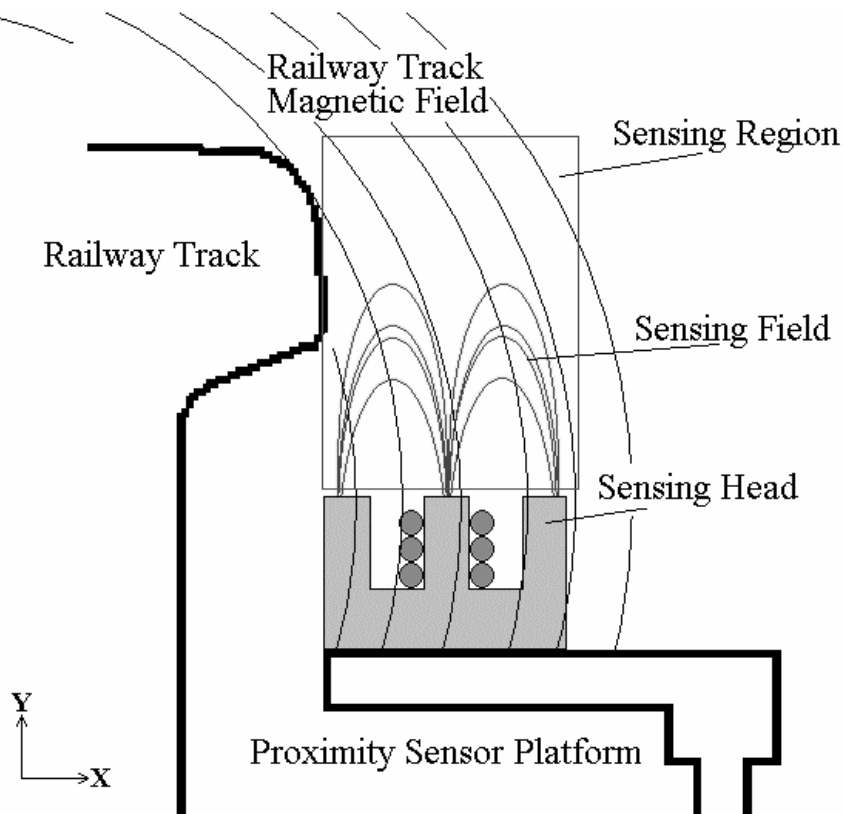


Figure 1-2: A diagrammatic representation of the sensing head of the inductive proximity sensor and its position relative to proximity sensor platform adjacent to the railway track.

Figure 1-2 delineates the construction of the sensing head of the proximity sensor. This diagram serves to illustrate the emission of the sensing field from the upper limit of the sensing head. It is by virtue of a train wheel passing through this produced field

that its detection by the proximity sensor can be made. It can also be seen from Figure 1-2 that the sensing head of the proximity sensor generates a magnetic field primarily in the Y direction so as to detect the train wheels as they pass by.

Since the sensor uses a field primarily in the Y direction, the X component of the interfering magnetic field generated by the distorted traction currents should not greatly effect the proximity sensors operation. It can thus be confidently assumed that the greatest proportion of interference picked up by the proximity sensor will be due to the Y component of the magnetic field.

1.2.2 Problems with the Inductive Proximity Sensor

The problems engendered within the current system are due to the profuse amounts of magnetic fields present in and around the area of the proximity sensor as shown in Figure 1-2. The prevalence of these magnetic fields is explained in terms of the incidence of traction currents flowing in the railway track.

The presence of the current in the railway track is made accountable owing to its key role of forming part of the electrical circuit connecting the locomotive to a substation. The power being delivered to the locomotive is supplied by a Utility substation. The AC voltage supplied to the locomotive is converted to a DC voltage that is in turn implemented to drive the DC motors which propel the train. A return path is mandatory to complete the circuit between the substation and the locomotive and so the railway track was chosen as the most superlative and cost effective solution, this being the system of universal usage.

The traction current consists of the main driving current supplied by the Utility substation and a wide variety of much higher frequency currents. The higher frequency currents are injected into the railway track by many different sources. These higher frequency currents generate magnetic fields of the same frequency, which interfere with the proximity sensor.

These higher frequency magnetic fields, especially the 300 kHz component, have a detrimental effect on the proximity sensor's success with regards to its sensing distance, thereby causing the sensor to miscount the train wheels that pass it.

1.3 Goals of this Investigation

1.3.1 Ultimate Goal

The penultimate vision for this research endeavour was to develop a means by which the train wheel detection system's susceptibility to magnetic interference could be reduced. This would result in a reduction in the occurrence of errors in the counting of the train wheels, this in turn ensuring more accurate information being generated by this system, thus making the system itself more robust.

1.3.2 Restrictions for achieving Goals

The current proximity sensors being used for the detection process cannot be replaced by a different mechanism as there are too many already installed in the field and the replacement costs would be too great. Furthermore a new measurement device would be accompanied by different problems. An optical measurement system, for example, would be susceptible to dust and sunlight as a source of interference and would need to be cleaned on a regular basis, a problem not relevant to the current system.

The distorted traction currents which generate the interfering magnetic field are injected into the railway track by a variety of different sources. Two known examples of the origins of the distorted traction currents are found in the switching circuitry in the locomotive and the junction on a railway track line when it switches from one line to another.

The goal of this investigation is to make the wheel detection system more robust, hence decreasing the effect the interference has on it. Finding the source of the distorted traction currents and reducing them at the source are not covered within the scope of this study.

1.3.3 Available paths to achieving the Goals

To reduce the interference experienced by the proximity sensor, the magnetic field in the region around the proximity sensor must be reduced, as this would lower the effect the interfering magnetic field has on the sensing field of the proximity sensor.

Two paths are available to reduce the interfering magnetic field. One such path requires implementation of shielding to move or deflect the magnetic field away from the proximity sensor. The other involves using a cable connected to some position a distance before and after the proximity sensor platform to redirect a percentage of the current flowing in the railway track.

The shielding path consists of placing a shield between the railway track and the proximity sensor to either absorb the magnetic field or deflect it back towards the railway track. For a shield constructed from conductive material the magnetic field from the railway track will be deflected away from the shield and towards the railway track as in accordance to Lenz's law.

Lenz's law states that when a conductive material is brought into the vicinity of a changing magnetic field, a current is induced in the conductor that will flow in the opposite direction to that of the active conductor current flow. The magnetic field that is emitted from the passive conductor tends to cancel the magnetic field from the active conductor. The more conductive the passive material, the greater the cancelling effect. The higher the frequency of the magnetic field, the more the mirror effect is heightened and so too more of the electromagnetic field is deflected away from the shield [1], [2].

However, on utilising magnetic material for the shield construction, the magnetic field from the railway track will be absorbed by the shield, proportional to its relative permeability, and flow through it, only to exit the shield opposite its initial entry point.

A materials relative permeability is a measure of how it influences magnetic fields in its vicinity. For a material with a relative permeability of unity, which is the same for free space, the magnetic field remains unaffected by its presence. For a relative permeability of less than unity less of the magnetic field travels through it with the greater percentage moving around the material as the resistance experienced by the magnetic field within the material is greater than that experienced in the free space surrounding it with most of the field moving around it since the lesser the relative permeability the lower the resultant field intensity within the material. When a material has a relative permeability greater than units the resistance it presents to the

magnetic field is lower than that presented by the free space surrounding it. This lower resistance caused by the relative permeability results in more of the magnetic field flowing through the material and less in the free space surrounding it. As materials with increasing relative permeability's are placed within the magnetic field an increasing quantity of the magnetic field will flow through it with a diminishing amount flowing in the surrounding free space.

The magnitude of the magnetic field around the railway track is a function of the proportion of current flowing in the track. The path involving the addition of a cable to redirect a percentage of the traction current exploits this relation. By virtue of this, the magnetic field around the railway track will be reduced owing to the attenuated current flow in the track.

In addition, if the cable is placed running parallel to the track, orientated in such a manner that the proximity sensor platform intervenes between the newly installed cable and the railway track, the magnetic field generated around the cable will oppose some of the magnetic field around the railway track in the region surrounding the proximity sensor platform. This in turn acts to further decrease the magnetic field in that region (See example in Figure 1-3).

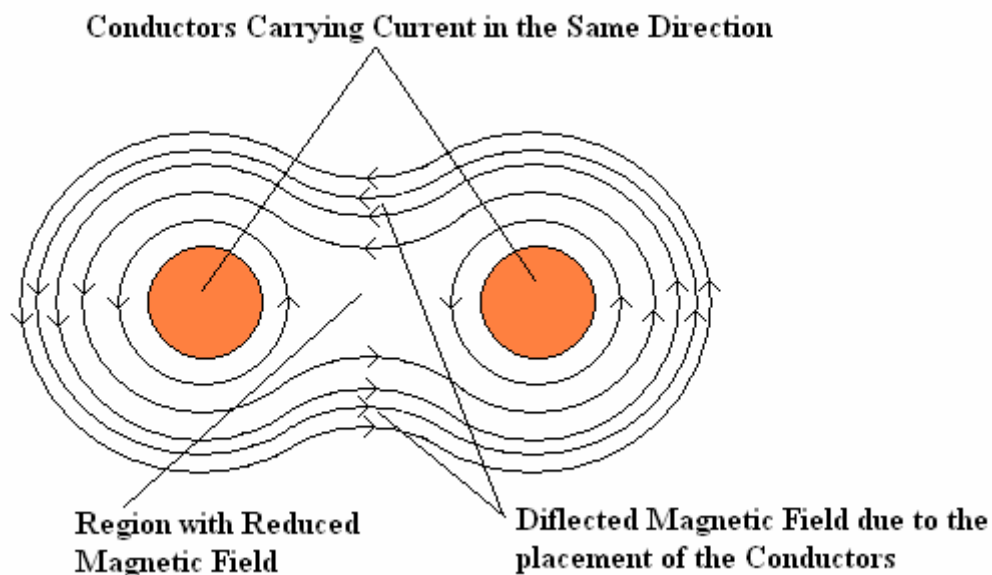


Figure 1-3: Example of magnetic field distortion when two conductors carrying current are placed in parallel.

1.3.4 Assumptions Made

It was assumed that the relationship between the magnetic flux around the railway track and the traction current was linear. Similarly it was assumed that the interaction between the magnetic flux and the shield proposed was also linear. This permitted the traction current to be broken down into its main components, the driving current of 650 A at 50 Hz and a number of higher frequency distortion currents of which the 2 A 300 kHz current was envisioned as the more influentially prominent.

1.4 Problem Definition

The principle aim of the study was to determine whether the interfering magnetic field particularly in the sensing region of the proximity sensor could be reduced, and by what means this reduction could be achieved.

As a means to realise this aim the problem was partitioned along two main dimensions the first of which comprised a brief low frequency test so as to determine whether it was plausible for the magnetic field to be reduced and furthermore stipulated the mode of measurement. Within this established framework the more extensive high frequency tests, constituting the second dimension of study, could be developed

For the low frequency portion, the measurement of the magnetic field above the proximity sensor platform situated next to the railway track, carrying the 650A 50 Hz traction current, was seen as essential. To accomplish this, a sensor designed and constructed to perform the necessary flux density measurements as well as a test rig to provide the crucial method of easily moving the Flux Density Sensor proved to be prerequisites. These items would allow the distribution and magnitude of the magnetic flux density above the proximity sensor platform to be mapped.

The higher frequency tests involved generating a 2A 300 kHz current in the railway track and measuring the magnetic flux density produced in the region above the proximity sensor platform. Firstly a method of generating the 2A 300 kHz current in the railway track had to be instituted, designed and constructed. Secondly an improved flux density measurement system was necessary as additional factors that

had exerted a minimal impact at the level of the lower frequency tests would become more pronounced with regard to the higher frequency tests.

1.5 Approach used to meet problem definitions

1.5.1 Tests to be performed

1.5.1.1 Low Frequency Tests at 650A 50Hz

For the low frequency case the first test was performed to map the magnetic flux density in the region above the proximity sensor platform in an unshielded state. This was carried out to obtain a base measurement representing the magnetic flux density normally present in this region, thus giving a comparative base measurement that can be used to determine the effect on the magnetic flux density when any change occurs in this region.

The second test performed involved placing a shield between the railway track and the proximity sensor platform and mapping the magnetic flux density in the region of interest. This data is then compared to the base measurement for the low frequency case and any differences found will show that the introduction of the shield has an effect on the magnetic field in this region. Further, if in interpreting this effect it is found that the data for the shielded case indicates comparatively lower results to the unshielded base data, the shield has then succeeded in reducing the interfering magnetic field above the proximity sensor platform at this low frequency of 50Hz.

Figure 1-4 below expresses the results of a rough simulation depicting the magnetic flux lines around the railway track with the proximity sensor platform, situated next to it on the right, when a 650A 50Hz current is flowing through it. The approximate placement of the shield required for the shielded test can also be seen on the proximity sensor platform in this figure. It can also be seen how the magnetic flux lines are deflected by the introduction of the shield.

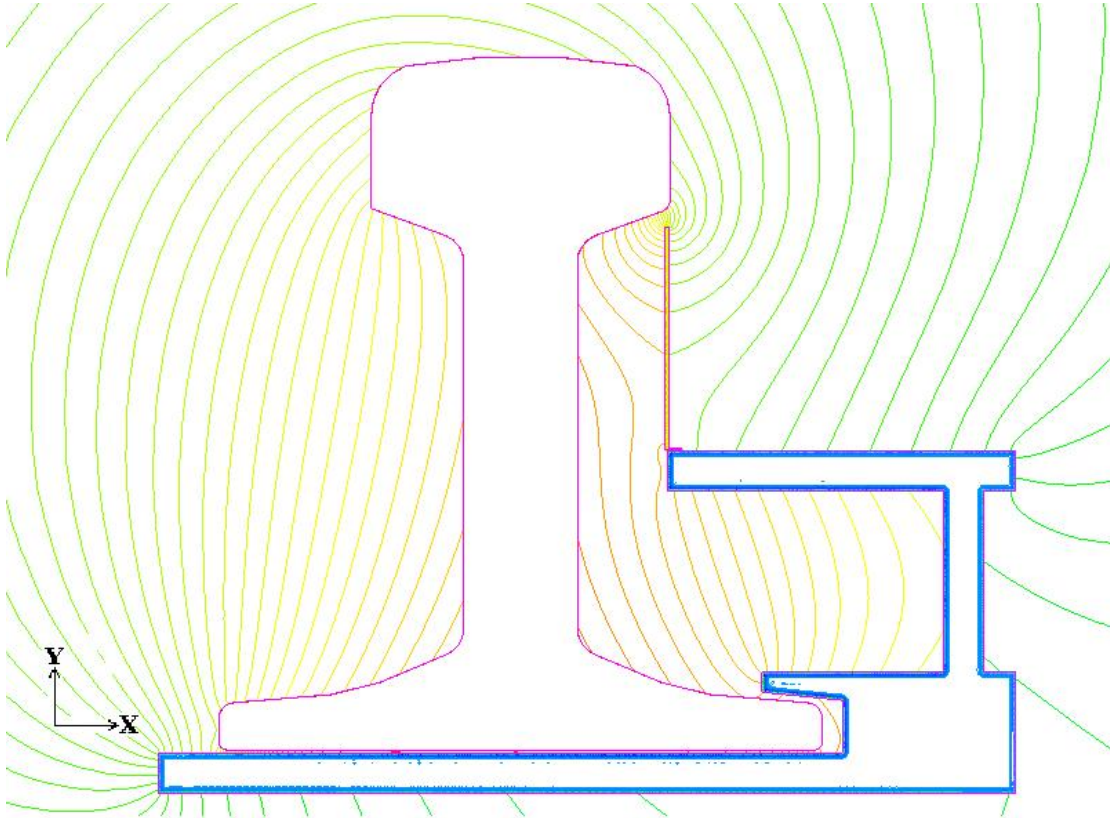


Figure 1-4: Proposed shielding solution geometry, showing the influence of the shield on the magnetic flux lines.

According to the rough simulation depicted in Figure 1-4, the introduction of the shield will indeed have an effect on the magnetic field in the region above the proximity sensor platform.

1.5.1.2 High Frequency tests at 2A 300 kHz

Similarly, for the high frequency case, the first test to be performed involves the mapping of the magnetic flux density above the proximity sensor platform in its unaltered state, once more giving a base measurement at 300 kHz that can be used to determine the change in the magnetic flux density in this region when the different tests are performed.

The next test would involve, as for the low frequency tests, the placement of a shield between the railway track and the proximity sensor platform and thereafter mapping the region above the platform. The third test involves placing a sheet of insulation material between the shield and the proximity sensor platform. Doing this would prevent direct conduction of electricity from the proximity sensor platform to the

shield. Furthermore this would also increase the capacitive impedance between the two, again lowering the current flowing through the shield.

The results from the second and third tests would then be compared to the base data obtained in the first test. The rationale supporting this comparative investigation aims to discern how great an effect is had following the addition of a shield and insulation material respectively.

Common to the subsequent tests to be performed is the incorporation of parallel cabling running next to the proximity sensor platform on the opposite side to the railway track. Three cables of different thicknesses are to be tested. Each cable permits a different percentage of the total current to flow through it, thereby lowering the current flowing in the railway track by that amount and simultaneously permitting the formation of opposing magnetic fields of varying intensities by virtue of the current magnitudes. Both consequences of introducing the cables serves to lower the magnetic field above the proximity sensor platform by different amounts depending on the cable used.

For each of the different cables that were employed it was essential to repeat the first, second and third high frequency tests as previously outlined so as to obtain the necessary flux density measurements. These tests are typified as follows: firstly individual connection of the different cables alone to obtain the sub-base measurements, secondly with the shield in place and thirdly with the insertion of the insulation material between the shield and the proximity sensor platform.

The cumulative results from all the independent tests are to be compared to the base 300 kHz results as a means to ascertain which tests yields the best reduction of the magnetic flux density in the region above the proximity sensor platform, or more specifically in the sensing region situated above the proximity sensor platform as shown in Figure 1-2 on page 3.

1.5.2 Apparatus needed to perform the tests for both the low and high frequency cases

For the low frequency case a current source capable of producing the 650A 50Hz current, which is that used as the driving current for locomotives in the field, had to be

reproduced under controlled conditions in the laboratory. This was necessary to perform the magnetic flux density mapping in the region above the proximity sensor platform.

The subsequent requirement was a test rig with a dual purpose of not only holding the sensor in place but in addition being permissive to easy movement of the sensor around the proximity sensor region thereby making the mapping process possible. Ultimately a flux density measurement system was necessitated in order to capture the magnetic flux density at the different points in the proximity sensor region.

The high frequency case involved the design and subsequent construction of a 2A 300 kHz current generator to emulate, in the laboratory, the high frequency distortion current found on the railway track line out in the field. The test rig of identical specifications and functions was common to both low and high frequency cases.

However, a new flux density measurement system needed to be designed. This requirement stems from observation that, at this higher frequency and lower current when compared to the low frequency case, the magnetic field being measured would have a much lower magnitude, this coupled with interference from the electric field generated by the changing voltage across the railway track and external sources would have a greater influence on the measurements taken.

1.5.3 Mapping techniques used

1.5.3.1 Grid layout used for mapping the Test Area

To perform the flux density measurements the proximity sensor region had to be broken down into a grid with the variable X representing the horizontal position along the top of the proximity sensor platform and the variable Y representing the vertical position above the proximity sensor platform as revealed in Figure 1-5 below.

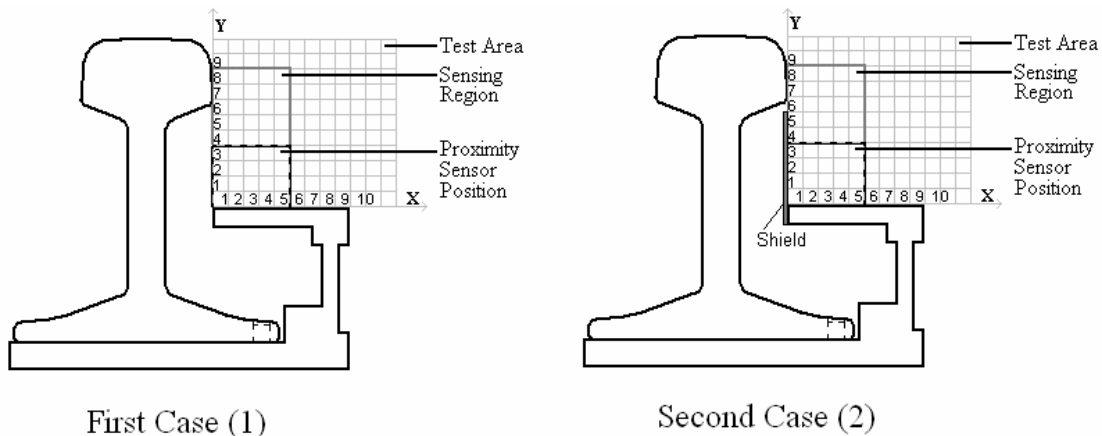


Figure 1-5: Measurement grid used for the mapping process, for both the unshielded and shielded cases.

The region above the proximity sensor platform covered by this grid was to be known as the Test Area, and all measurements performed were taken in this area.

Each block on the grid represents an area of 10mm horizontally by 10mm vertically or 1cm by 1cm, there for at a point on the grid with an X value of 4 would be 40mm (4cm) away from the edge of the proximity sensor platform closest to the railway track. Similarly a point with a Y value of 5 would be 50mm above the proximity sensor platform.

For the first grid case, shown on the left of Figure 1-5, no shield is present and this would be the setup used to obtain the base measurements for both the low and high frequency tests, including the sub-base tests when the different cables are tested. The grid case shown on the right represents the layout used for all the shielded measurement. The second grid layout is identical to the first case except the position and height of the shield to be tested is indicated in the figure.

From Figure 1-4 the position of the proximity sensor on top of the proximity sensor platform is shown, as well the sensing region of the proximity sensor. From this it can be seen where Figure 1-2 fits in, and that the sensing field of the proximity sensor is situated within the sensing region shown.

1.5.3.2 Measurement Technique

From the flux lines shown in Figure 1-4 it can be seen that the magnetic field is a vector and consists of horizontal (X) and vertical (Y) components, similarly the magnitude of the magnetic flux density also consists of X and Y components. As a consequence of this fact the magnitude of the magnetic flux density in the Test Area can not be measured in one go but must be split into its X and Y components where each component is measured separately.

To measure the Y component of the magnetic flux density the Flux Density Sensor must be placed oriented to measure the flux density in the vertical direction. The Flux Density Sensor is placed at the beginning of the grid at the position where X and Y both equal one. Measurements are then taken at each position along the X axis keeping the Y position constant, then incrementing the Y position when all the X positions have been completed, and sweeping through the X positions again. This procedure is continued until the flux density at all the desired positions in the Test Area has been measured.

To measure the X component the same method mentioned above is used except that the Flux Density Sensor is orientated in a direction conducive to measuring the horizontal component of the magnetic flux density.

1.5.4 Technique used for the comparison of the different Test Cases

The interference picked up by the proximity sensor is due to the interfering magnetic field presents in the sensing region as can be seen from Figure 1-2, which is situated within the Test Area as shown in Figure 1-5.

To determine the change in the interfering magnetic field within the sensing region caused when the environment is modified due to the introduction of a shield and or a

cable, a direct comparison between the unaltered or base measurement and the other different cases is carried out.

Figure 1-6 shows how the direct comparison is performed by dividing the sensing region in to horizontal paths at different levels with constant values of Y, above the proximity sensor platform. The measured magnitudes of the interfering magnetic flux density for the different cases at each point along these paths are compared to the base measurement to determine the change experienced at those points. This is repeated at different levels above the proximity sensor platform until all measured results with in the sensing region have been compared.

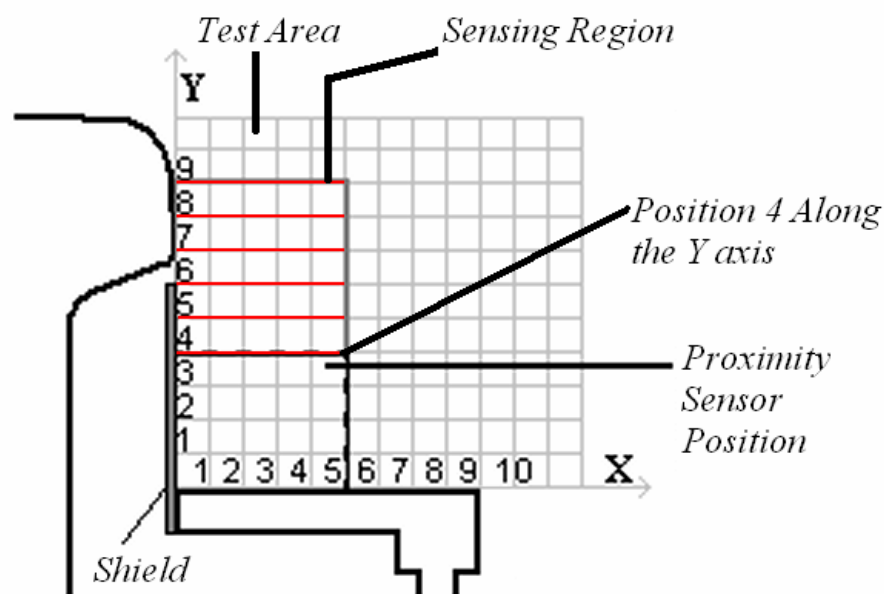


Figure 1-6: Break down of the sensing region for the direct comparison between all different Test cases.

Once the comparison is complete the differences are recorded in a bar graph format thereby making it easier to determine if the modification introduced had a positive influence in reducing the magnitude of the interfering magnetic field in the sensing region.

From these comparison bar graphs the configuration of the shield and or cable, which yielded the optimal reduction in the magnitude of the interfering magnetic field, can be determined. This is the technique to be implemented for all the measured results obtained and will ultimately lead to the discovery of the best solution out of those tested.

2 Low Frequency Test at 650A 50Hz

2.1 Introduction

This current section is that devoted to the abbreviated low frequency tests and forms a foreground for the more substantial high frequency tests to follow. The priority purpose of this section serves to determine whether the introduction of a shield next to the railway track on top of the proximity sensor platform (as shown in Figure 1-4) will have any effect and, if so, how much of an effect is had on the magnetic field in the Test Area (the area previously denoted to reside above the proximity sensor platform).

So as to accomplish this, a high current source was employed to generate the 650A 50Hz current required. This current was then passed through a railway track section to emulate the current flowing through commercially used railway tracks in the field that act as return paths for the electricity used by the locomotives.

The magnetic field mapping was achieved by designing and then constructing a Flux Density Sensor capable of detecting the magnetic field in the Test Area when the desired traction current was present. In addition a test rig was constructed to allow the Flux Density Sensor to be easily moved around the Teat Area, allowing the flux density to be measured at all points in this area.

The measured results were then depicted in the form of contour plots which express the distribution of the flux density in the Test Area, allowing comparison of the different test cases. To this end, a comparison between the unshielded or base measurement case and the shielded case was performed in order to ascertain whether the introduction of the shield had a positive influence in reducing the magnetic field present within the designated Test Area.

2.2 Apparatus: Test Setup

2.2.1 Railway Track System

In the laboratory, the railway track system is composed of two principal structures; a high current transformer and the railway track section where both are used to emulate the situation in the field.

The high current source available in the lab consists of a three phase 3000A transformer along with a control bench which enables the adjustment and monitoring of the current flowing through it. This transformer was elicited to generate the 650A 50Hz traction current as deemed necessary in the low frequency test protocol. Figure 2-1 shows the high current transformer to the left and its control bench on the right.



Figure 2-1: High Current Transformer (Left) and its Control Bench (Right).

The railway track section was connected between two of the phases of the current transformer so as to permit the traction current to flow through it (Figure 2-2), while the third phase remained unconnected.

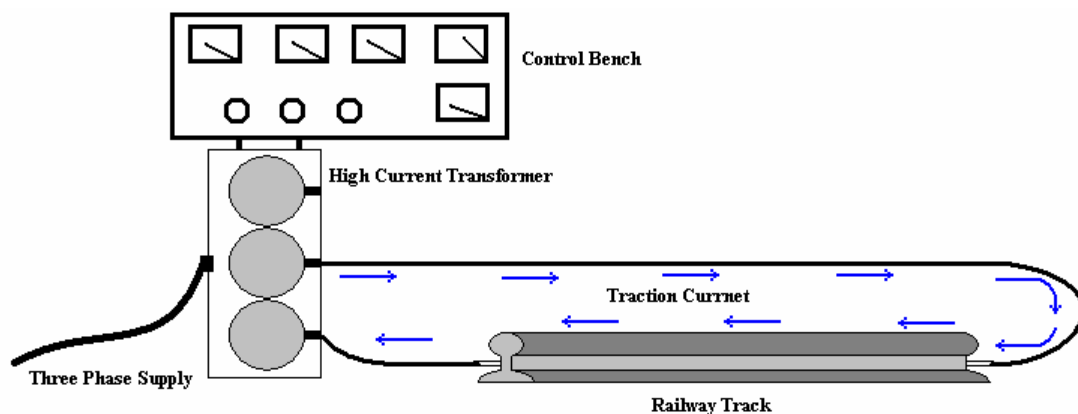


Figure 2-2: Connection diagram showing the railway track system for the low frequency tests.

2.2.2 Measurement System

The measurement system entails all the apparatus needed to perform the measurements, these include the Flux Density Sensor, the test rig, the oscilloscope and essentially the cabling used to connect these together into a functional unison.

2.2.2.1 The Magnetic Flux Density Sensor

2.2.2.1.1 Design of Magnetic Flux Density Sensor

The characteristic equation for the magnetic Flux Density Sensor was derived applying Faraday's law [1]-[3], beginning with the following equation:

$$e = -N \frac{d\phi}{dt} \quad (2-1)$$

Where

$$\phi = \int \bar{B} \cdot d\bar{A} \quad (2-2)$$

And where:

B	-	<i>Flux density</i>
N	-	<i>Number of turns</i>
ϕ	-	<i>Flux</i>
A	-	<i>Area inside the coil.</i>

The assumptions made are as follows:

1. As the geometry of the constructed magnetic Flux Density Sensor is fixed, the area in-between the sensor's coil will invariably also be fixed. Therefore the value of A does not alter.
2. The frequency of the railway track current will be constant for each measurement set. It can thus be stipulated that the magnitude of the flux density will not be time dependant and so the integral in equation (2-2) will disappear and equation (2-3) is obtained.
3. Since the inner diameter of the coil is small the flux density is assumed to be uniform inside the coil area of the magnetic Flux Density Sensor.

Using the above Assumptions equation (2-2) becomes:

$$\phi = B \cdot A \quad (2-3)$$

By substituting this into equation (2-1) the following is obtained:

$$e = \frac{-N\pi d^2}{4} \cdot \frac{d}{dt} B \quad (2-4)$$

By using phasors, B becomes:

$$B = B_0 \cdot e^{j\omega t}$$

Where $B_0 = |B|$ and so equation (2-4) becomes

$$e = \frac{-N\pi d^2}{4} \cdot B_0 j\omega \cdot e^{j\omega t} \quad (2-5)$$

By taking the magnitude of both sides of equation (2-5) the following equation is obtained:

$$e_0 = \frac{N\pi d^2}{4} \omega \cdot B_0$$

Where $e_0 = |e|$ and $\omega = 2\pi f$

By substituting in for ω the following is obtained:

$$e_0 = \frac{N\pi^2 d^2 f}{2} B_0 \quad (2-6)$$

This equation expresses incrementing sensor sensitivity is attainable as the number of turns used in the construction of the magnetic Flux Density Sensor is increased, thereby indicating a positive relation between the two.

By rearranging equation (2-6) the final version has been derived:

$$B_0 = \frac{2}{N\pi^2 d^2 f} e_0 \quad (2-7)$$

Where:

- B_0 - Magnitude of magnetic flux density.
- e_0 - Magnitude of voltage across the sensor coil.
- d - Diameter of wood rod (gap in the centre of the coil).
- f - Frequency of magnetic field being measured.

By using equation (2-7) the measured voltage (V) output from the magnetic Flux Density Sensor is converted to a relative (un-calibrated) value in tesla (T)

When magnetic flux passes through the coil of the magnetic Flux Density Sensor a voltage is induced across the outlet terminals of the coil and the magnitude of this voltage, in mV, is measured with the use of an oscilloscope.

2.2.2.1.2 Construction of Magnetic Flux Density Sensor Coil

The magnetic Flux Density Sensor was constructed using a 4mm diameter wooden rod. The rationale supporting the use of this non-conductive and non-magnetic material is that it would not affect the magnetic field. Insulation material was used to build two circular flanges that were glued onto the rod to form a bobbin for holding the wire coil for the sensor in place (as shown in Figure 2-3).

The magnetic Flux Density Sensor used to obtain the measured results for the low frequency tests was wound with 1000 turns of 0.2 mm diameter wire. This yielded a high enough sensitivity to perform the measurements (See equation (2-7))

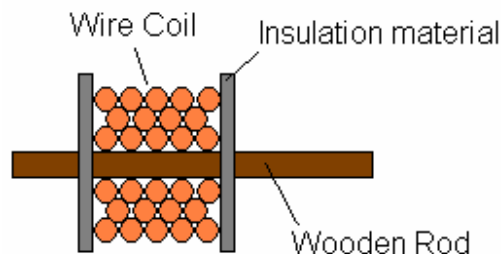


Figure 2-3: Construction of Magnetic Flux Density Sensor Coil.

2.2.2.2 Constructed Test Rig

A test rig was constructed from a non-magnetic wooden sheet made to fit around the track and over the proximity sensor platform. As can be seen in Figure 2-4 the test area (see also Figure 1-5 and Figure 1-6) is the rectangular region above the sensor platform, this region was divided into a XY grid with a 10 mm spacing between each division. The test area is 90 mm high and 100 mm across.



Figure 2-4: Test rig placed around railway track, showing metal shield and magnetic Flux Density Sensor and mounting.

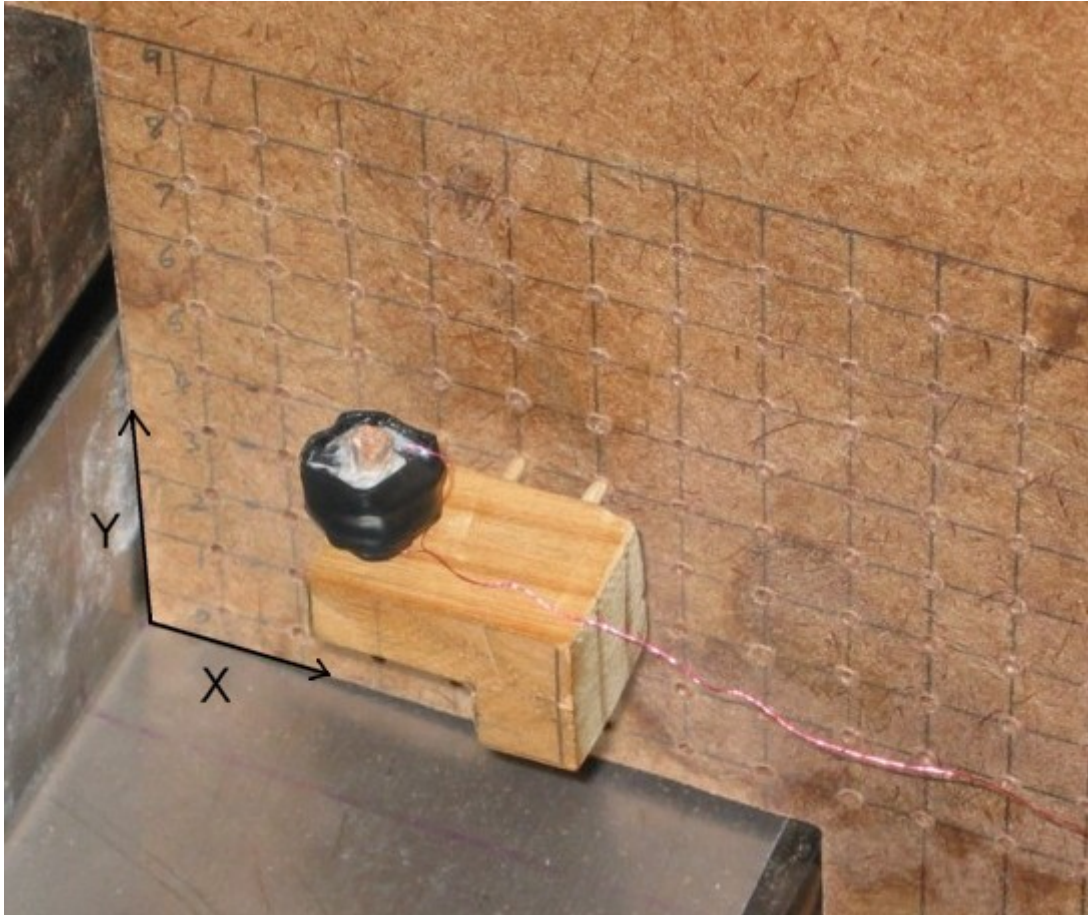


Figure 2-5: Magnetic Flux Density Sensor mounted onto the test rig in the XY grid.

Figure 2-5 zoomed in on the test area more clearly illustrates the spatial domain of the XY grid and how the magnetic Flux Density Sensor is mounted onto the test rig. The sensor mounting was constructed using a small wooden block and was cut to the shape shown, the important dimensions being a length of 30 mm and a height of 10 mm. The mounting pins are 10 mm apart and slot easily into the holes drilled into the XY grid. The magnetic Flux Density Sensor is shown as the black circular object in the figure and is mounted onto the sensor mounting (as shown above). Using this setup the sensor can be moved easily and accurately around the grid.

2.3 Experimental Results

To perform the measurements needed for these test cases, the constructed test rig and Flux Density Sensor were used in accordance to the measurement technique described in section 1.5.3.2 on page 14. Once the measurements were taken they were entered in to a computer and processed using Matlab. This was a necessary step as the measured data obtained from the Measurement System was in Volts and had to be

converted to relative values in Tesla. From this data Contour plots were constructed which enabled an undemanding comparison between the two test cases.

It must be noted that the axis numbering on all the contour plots shown match the numbering shown in Figure 1-5 and as described in section 1.5.3.1.

Firstly the base measurement was performed to obtain the data for the unshielded case, once obtained the contour plot of this data was derived to indicate the distribution of the magnetic flux density in the test area. The contour plot showing the combined X & Y components and the X component alone can be seen in Appendix 1, however the Y component is present below in Figure 2-6 as it is the contour plot of relevant significance for purposes of this study.

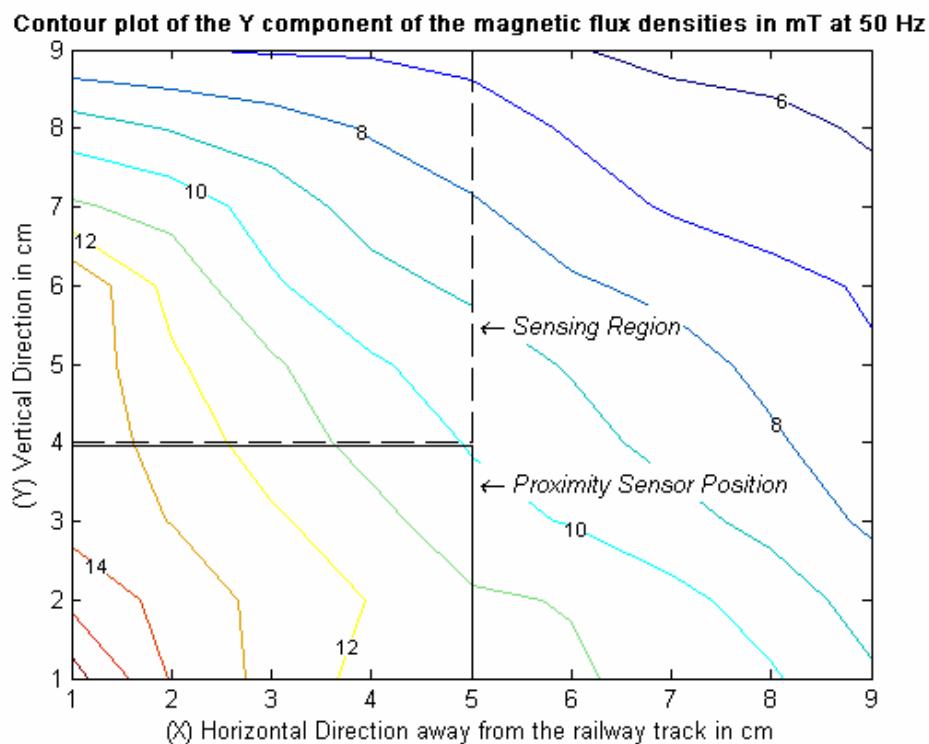


Figure 2-6: Contour plot of the magnitude of the Y component of the magnetic flux density for the unshielded base measurement at 50 Hz.

The contour plot for the shielded case was also obtained using the same procedure and the contour plot for the Y component of the magnetic flux density can be seen in Figure 2-7 (again the additional contour plots as previously stipulated of the unshielded scenario can be viewed in Appendix 1). Using these two contour plots the two test cases can be compared to determine whether the objectives of the low frequency test have been met.

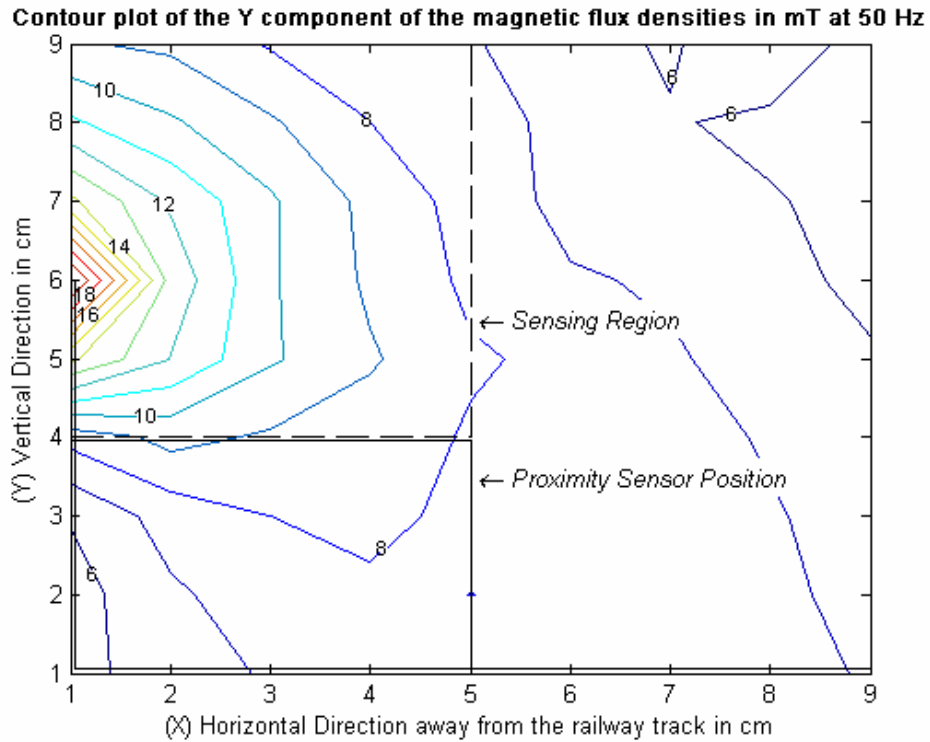


Figure 2-7: Contour plot of the magnitude of the Y component of the magnetic flux density for the shielded measurement at 50 Hz.

By comparing Figure 2-6 and Figure 2-7 it can be seen that the introduction of the shield does indeed have a noticeable effect on the magnetic flux density present in the test area. Moreover it can be deduced from this simple comparison that the overall magnetic flux density in the test area has been reduced.

3 Preparation of the Railway Track System for the High Frequency Test at 2A 300kHz

3.1 Introduction

The purpose of the high frequency test is to determine which of the techniques mentioned for the high frequency case (section 0 on page 10), would result in the greatest reduction in the interfering magnetic field present within the sensing region.

However, prior to commencing the high frequency measurements, the Railway Track System and the Measurement System had to be adapted to achieve the additional tasks required for these new tests conditions.

For the Railway Track System the high current low frequency source had to be replaced with a low current high frequency source in order to generate the high frequency traction current needed.

It was found by Spoornet that the 300 kHz traction current had the most detrimental effect on the proximity sensor. This was due to the fact that the interfering magnetic field generated by this current oscillates at the operating frequency of the proximity sensor, causing the sensing field of the proximity sensor to either be amplified or cancelled perpetuating the miscounting of the train wheels that pass it.

Therefore the new low current high frequency source needed for the high frequency test had to generate a traction current at a frequency of 300 kHz to produce the desired interfering magnetic field and thus enable the subsequent testing to ensue.

3.2 High Frequency Current Source: 300 kHz Resonator

3.2.1 Introduction

To perform the duty of producing the high frequency 300 kHz current needed for the generation of the interfering magnetic field, which emulates the high frequency interference experience in the field, it was elected to use a resonant converter.

A resonant converter topology was selected as it serves to connect a DC system to an AC system with the dual ability to control the power transfer between them, as well as the output voltage and current. [7]

These converters are used in such applications as the very high frequency DC to DC power supplies, sonar transmitters and ultrasonic generators, among many others. The three applications listed reveal that these types of converters work exemplarily in high frequency applications, and would perform well in the design of the high frequency current source intended. [7]

There exist two basic shortcomings of DC-DC and DC-AC converters, the first occurring during the turn-on and turn-off times. As high currents and voltages appear simultaneously across the switches at these times, a high power loss and high switching stresses result. This power loss increases linearly as the switching frequency increases, and, so as to maintain a reasonable efficiency, the switching frequency may not increase above a certain maximum value. [7]

The second shortcoming is due to the large dv/dt and di/dt values in the circuit, and owing to these, the generation of Electromagnetic Interference (EMI) becomes problematic. These limitations are emphasized by the trend to reduce the converter size and weight by pushing the switching frequencies to incrementally higher levels. [7]

Resonant converters have the advantage that when the switching frequency of the converter is close to its resonant frequency the current flowing through it, as well as the voltage, are almost perfectly sinusoidal in shape, resulting in a lower dv/dt and di/dt in the circuit thereby reducing the EMI generated. This is achieved due to the

Resonant L-C circuit within the resonant converter, which behaves analogous to a filter, removing any unwanted harmonics within the circuit. [7]

A second advantage manifests during the turn-off process as a zero current crossing is provided to the switches, reducing the total power loss in the circuit and reducing the switching stress experienced. [7]

The characteristics of the resonant converter bode well in accomplishing the requirements for a source to generate the high frequency current needed to emulate the distortion current responsible for the interfering magnetic field, as the resonant converter has the ability to produce an almost perfect sinusoidal current at the high frequency required. In addition it has a lower implementation cost than other alternatives such as building a high power amplifier system.

To achieve this, the resonant half bridge topology was chosen for the resonant converter, and its circuit diagram can be seen in Figure 3-1 below.

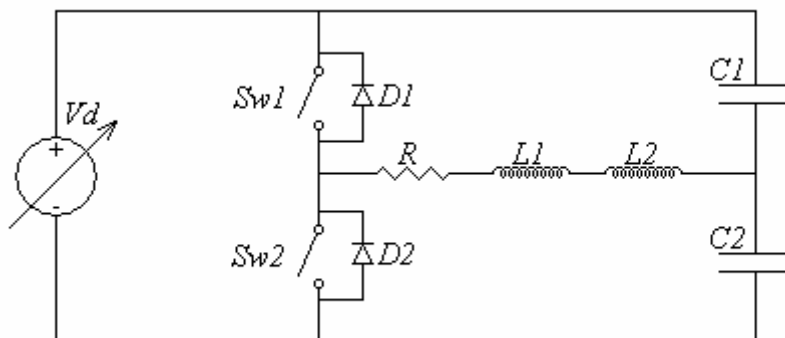


Figure 3-1: Circuit diagram for a Half Bridge Phase arm Resonator.

The variables present in Figure 3-1 represent the following components:

- | | | |
|------------------|---|---|
| R | - | <i>Resistance in the circuit</i> |
| $L1$ | - | <i>Internal inductor</i> |
| $L2$ | - | <i>Inductance of the railway track</i> |
| $C1 \ \& \ C2$ | - | <i>Capacitance of each capacitor bank in the circuit, which are both equal in value ($C1=C2=C$).</i> |
| $Sw1 \ \& \ Sw2$ | - | <i>Switches (Mosfets)</i> |
| Vd | - | <i>Variable Voltage Source</i> |
| $D1 \ \& \ D2$ | - | <i>Internal protection diodes within switches 1 & 2</i> |

The L-C circuit for the resonator shown in Figure 3-1 is realised by the combination of inductors $L1$, $L2$ and the two equal capacitor banks $C1$ & $C2$. This means that the

railway track forms part of the resonant circuit and its inductance will affect the resonant frequency of the converter.

3.2.2 Theory

In order to find the transfer function of the resonator circuit in Figure 3-1, it must first be simplified by short circuiting the variable supply V_d and closing each switch individually, and thereafter simplifying each resultant circuit. It was found that the two simplifications resulted in identical circuits.

This simplified circuit is shown below in Figure 3-2.

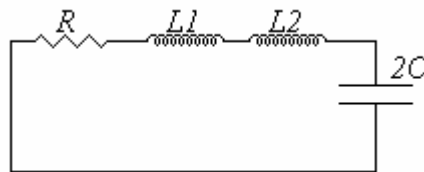


Figure 3-2: Simplified circuit diagram showing a series resonant circuit.

Where C represents the value of each of the capacitor banks in Figure 3-1, and is equivalent to $C1$ and $C2$ ($C1=C2=C$).

The circuit shown in Figure 3-2 represents a series-resonant circuit. The derivation of the following equation is due to the use of Kirchhoff's voltage law for a series resonant circuit.

$$v_i = v_L + v_R + v_C = i_i \left(sL + R + \frac{1}{s2C} \right) \quad (3-1)$$

In this equation L represents the combination of the internal inductor ($L1$) of the resonator and the inductance of the railway track ($L2$).

The input current for the series circuit is given by the following representation of Ohms law:

$$i_i = Y_s(s)v_i = \frac{1}{Z_s(s)}v_i \quad (3-2)$$

By comparing equation (3-2) to equation (3-1) the admittance of the circuit can be represented by the following equation:

$$Y_s(s) = \frac{1}{sL + R + \frac{1}{2sC}} \quad (3-3)$$

By rearranging and simplifying equation (3-3) the final admittance equation was obtained.

$$Y_s(s) = \frac{1}{R} \cdot \frac{2CRs}{2CLs^2 + 2CRs + 1} \quad (3-4)$$

A comparison was performed between equation (3-4) above and the transfer function for second order series resonant circuits shown here below in equation (3-5). [7]

$$Y_s(s) = \frac{1}{R} \cdot \frac{2\xi_s T_s}{T^2 s^2 + 2\xi_s T_s + 1} \quad (3-5)$$

Where:

$$\begin{array}{ll} \xi_s & - \quad \text{Dampening Factor of the Circuit} \\ T & - \quad \text{Time Constant} \end{array}$$

The results of this comparison yielded the key equations needed to design the particular resonant converter chosen.

These equations comprised the derivation of the time constant, which results in the attainment of expressions for the resonant frequency and the dampening factor of the circuit.

The analogue circuit components relate to the time constant in the following manner:

$$T = \sqrt{2 \cdot C \cdot L} \quad (3-6)$$

The resonant frequency (f_0) and the dampening factor are expressed by equations (3-7) and (3-8) below.

$$f_0 = \frac{1}{2\pi \cdot \sqrt{2 \cdot C \cdot L}} \quad (3-7)$$

$$\xi_s = R\sqrt{\frac{C}{2 \cdot L}} = 2 \cdot \pi \cdot f_0 \cdot C \cdot R \quad (3-8)$$

For the resonator to have an oscillatory response, its dampening factor must be less than unity, as this will result in complex roots in the denominator of the transfer function.

The closer the dampening factor is to unity the greater its effect will be on the resonant frequency of the system. The result of this dampening factor is such that a new damped resonant frequency is established, and this new frequency would be the resonant frequency for the system. This damped resonant frequency is given by equations 3-9 (radians) and 3-10 (Hz) below.

$$w_d = w_0 \cdot \sqrt{1 - \xi_s^2} \quad (3-9)$$

Therefore,

$$f_d = f_0 \cdot \sqrt{1 - \xi_s^2} \quad (3-10)$$

At resonance the impedances of the capacitive and inductive components will have an identical magnitude ensuring the cancellation of these reactive components, leaving only the real resistive portion of the impedance functioning in the circuit.

Since at resonance, only the resistive impedance has any effect on the current and voltage in the circuit, the total impedance at this frequency will be at a minimum, thus ensuring that the current flowing through the circuit will be at a maximum. Moreover, due to the fact that there is no reactive influence, the current and switching voltage wave forms will be in phase (Figure 3-3).

To determine how effective the resonant converter will be, its quality factor can be determined by use of equation 3-11 below [7].

$$Q_s = \frac{1}{2 \cdot \xi_s} \quad (3-11)$$

The quality factor given in equation 3-11 indicates that the higher the resonant current and voltage, on comparison to the input supply voltage, the higher the quality factor

will be. It stands to reason that a good resonant converter will indisputably have a high quality factor.

The significance of the quality factor also resides in the fact that the higher it is the better the filtration, hence the harmonics are attenuated to a greater extent and therefore fewer harmonics with significantly reduced magnitudes will be allowed to propagate through the converter. This also has the advantage of making the control of the output voltage and power easier with a small change in switching frequency.

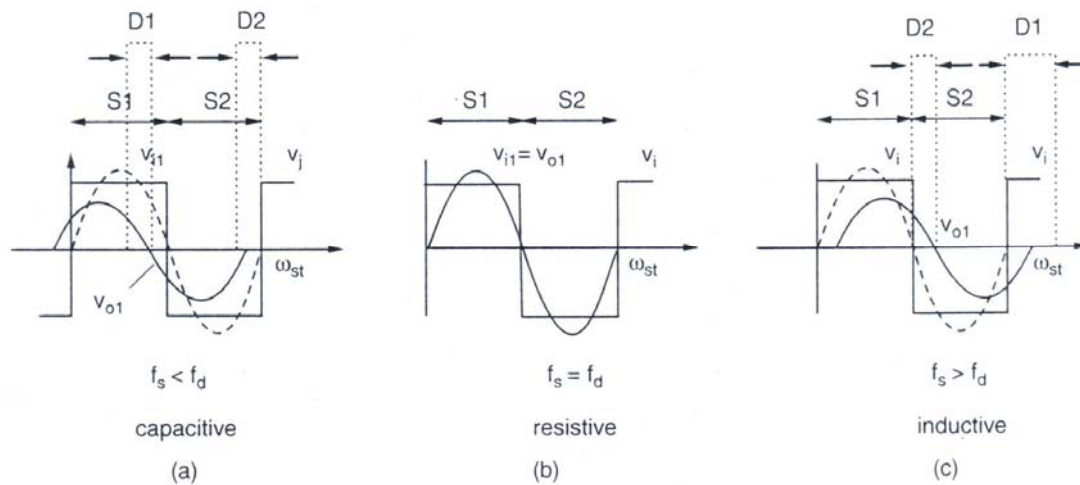


Figure 3-3: Output voltage wave forms compared to input voltage at frequencies below, equal to and above resonance, for a series resonant circuit [7].

By considering Figure 3-3 and Figure 3-1, the output voltage (V_{O1}) of the circuit relates to the voltage across the railway track ($L2$), and the input voltage (V_{i1}) is the square wave formed by the switches as they turn on and off in sequence.

Figure 3-3 demonstrates the phase shift between the output and input voltages at switching frequencies below, equal to and above the resonant point. When the switching frequency is below resonance the L-C network behaves as a capacitor causing the output voltage to lead the input, when it is above resonance it behaves as an inductor causing the output voltage to lag, and intervening at resonance it acts as a short circuit.

When the switching frequency equals the resonant frequency no switching losses are developed since the current through them will be zero, in exact step with the state change of the switches (Figure 3-3).

However when the switching frequency is either below or above the resonant point, the current will flow through the switch, at the beginning of each half-cycle and then divert through the diode (internal to the switch/Mosfet packages in Figure 3-1) when the current reverses polarity, resulting in a lossless transition.

Conversely when the switch turns on, it is subjected to an immediate step change in voltage and current, resulting in a lossy transition.

At these operating frequencies about the resonant point, the resonant converter still offers the advantage of only enduring switching losses at turn on, thus reducing the switching losses by half.

Furthermore, owing to the current possessing a sinusoidal waveform when the switch turns on, the instantaneous current flowing is lower the closer to the resonant frequency the converter is operating.

3.2.3 Operation of the Half Bridge Resonant Converter

The half bridge resonant converter (Figure 3-1) comprises of four operational stages:

1. The first stage begins as switch 1 turns on and encompasses its entire cycle, terminating when it turns off.
2. The second stage occurs when both switches $Sw1$ and $Sw2$ are open (turned off).
3. The third stage begins as switch 2 closes (turns on), and ends when it opens.
4. The fourth stage in the cycle involves reverting to a state in which both switches are open.

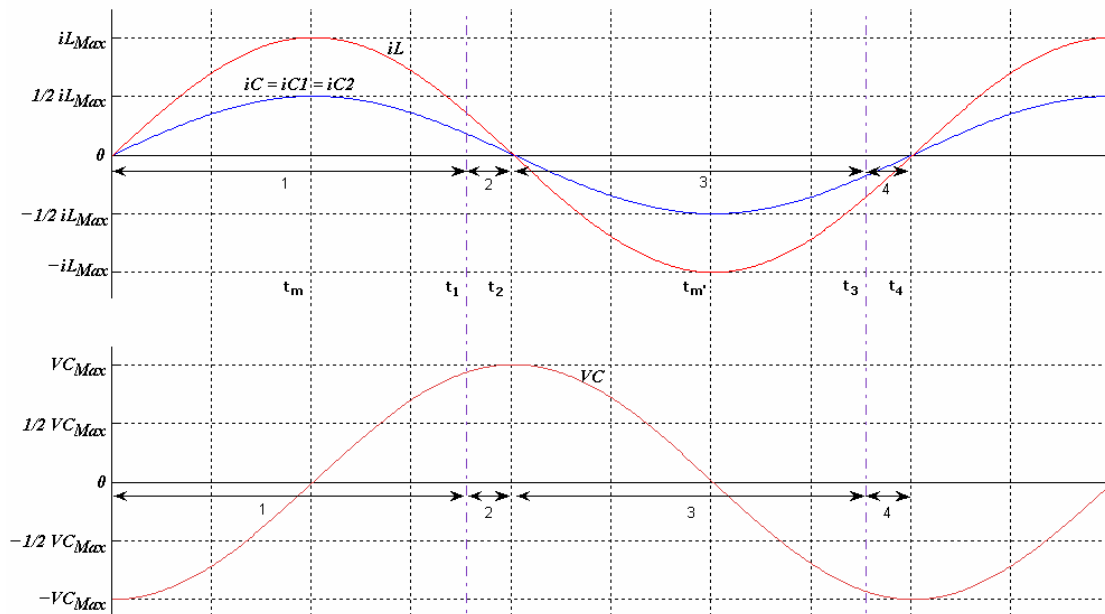
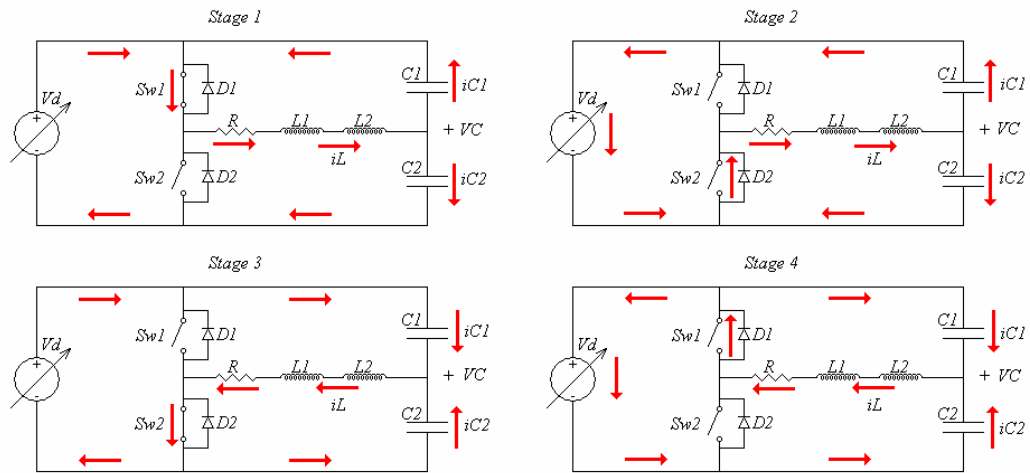


Figure 3-4: Operation of the Half Bridge Resonant Converter (Resonator) at switching at its resonant frequency.

The descriptions of each of the operational stages of the half bridge resonant converter are given in Figure 3-4 above. The operational time being considered entails a lag period after the initial turn on of the converter, this being the instant when it has reached its stable operating point.

For stage 1 ($0 \leq t \leq t_1$), the current flowing through the inductor (railway track) and the capacitor banks are both zero, and the voltage across the capacitor banks is at a negative maximum. Between the times 0 and t_m the current flowing through the inductors (i_L) and into the capacitor banks (i_C) is increasing, due to the negative voltage VC situated between the capacitor banks and the inductors (L_2).

While current is flowing into the capacitor banks $C1$ and $C2$ the voltage VC decreases as the current charges the capacitors in the opposite direction.

The current i_C indicates the current of i_{C1} or i_{C2} since they are both equal, from this it can be seen that the current i_L splits evenly into the two capacitor banks $C1$ and $C2$, in such a manner that every i_L action is accompanied by an i_C reaction following suite. At the point when VC reaches zero (at time t_m) the currents i_L and i_C both reach a maximum value.

Between times t_m and t_1 the voltage VC becomes positive and starts increasing. As a consequence of this, the current i_L begins to decrease since the voltage difference across the inductors is decreasing, and current flowing through an inductor cannot come to an immediate stop but must slowly begin to reverse direction. Also the greater the voltage difference across the inductor the quicker the current will come to a stop. This phenomenon can be appreciated from Figure 3-4, as at first the current i_L decreases slowly but then begins to accelerate as the voltage VC becomes greater.

At time equals t_1 , switch 1 closes and the current flowing through the circuit diverges to the freewheeling diode $D2$ (top of Figure 3-4 labelled *Stage 2*). This results in the switch being devoid of current flowing through it after it has opened (turns off), resulting in no switching losses. For stage 2 the current i_L continues to decrease until it reaches zero (at $t = t_2$), when VC reaches a positive maximum.

For stage 3 at time t_2 switch 2 turns on and begins to conduct, due to the fact that there is no current flowing through the circuit the switching loss at turn on is also zero. The current i_L now begins to flow in the opposite direction to the previous stages, discharging the capacitor banks causing the voltage VC to start falling. As VC approaches zero volts, i_L increases at a slower and slower rate until it reaches a maximum when VC achieves zero volts at time t_m' . The draining of the capacitor begin to slow as VC become negative, and continues until VC attains a negative maximum value.

At time t_3 , switch 2 turns off, causing the current i_L to diverge through the freewheeling diode $D1$. Stage 4 then continues until the current i_L again reaches zero and VC reaches a negative maximum at time t_4 .

The only time that energy is injected into the system by the DC voltage source V_d occurs during stages 1 and 3. Stages 2 and 4 simply transfer power to and from the capacitor banks and the inductors. If the duty cycle is decreased (Stages 1 and 3), power transferred to the system will decrease resulting in a lower maximum resonant current and voltage.

If the operating frequency of the converter is below or above resonance the switch turn-off phases will still result in zero current switching and a lossless situation. Unfortunately at the turn-on phases an instantaneous current will appear through the switch resulting in switching losses. However, the closer to resonance the converter is operating, the lower the current will be that is coursing through the switch at turn-on relative to the resonant current.

3.2.4 Design of Resonant Converter

The purpose of the resonant converter was to perform the task of the high frequency current source needed to emulate the interfering magnetic field present around the railway track out in the field.

Equation 3-7 provides the key to designing the resonant converter, as the required relationship between the total inductance, the value of each capacitor bank and the resonant frequency is provided.

By substituting in a resonant frequency value of 300 kHz the relationship between the inductance and capacitance was found to be:

$$C \cdot L = 140 \times 10^{-15} \quad (3-12)$$

The inductance (L) of the resonant converter consists of the internal inductor, which must be designed, and the railway track, so as to enable selection of capacitance and inductance values for equation 3-12, the minimum possible inductance must be determined. This minimum inductance is the inductance of the railway track present in the laboratory, and it has an unknown value.

3.2.4.1 Determining Railway Track Inductance

To determine the inductance of the railway track a buck converter was chosen as the ideal apparatus as it produces a square voltage wave form across its inductor with no dead time between the positive and negative pulses. Due to the properties of the inductor (L), the current through it (i_L) will increase linearly from a minimum to a maximum value.

This linear escalation occurs during the positive phase at a gradient dictated by the magnitude of the voltage (V_L) wave form, only to decline to its original minimum value during the negative phase at a gradient once more dictated by the voltage wave form. This property allows the use of the following equation that represents the voltage across an inductor relative to its inductance and the change in current raging through it with respect to time (di_L/dt).

$$V_L = L \frac{di_L}{dt} \quad (3-13)$$

Equation (3-13) describes how to use the voltage and current wave forms to determine the inductance of the railway track. This technique is described in more detail in the first section of Appendix 2.1.

For this technique the inductor of the Buck converter consists of a main (safety) inductor and the railway track. The purpose of the safety inductor is to limit the current flowing through the Buck converter, allowing it to be designed using this limited current as its maximum.

The detailed design procedure of the Buck converter is covered in the second section of Appendix 2.1 along with an inductor design procedure, for the safety inductor, covered in Appendix 2.2.

Once the Buck converter was constructed and the railway track connected in series with the safety inductor, the converter was turned on. Through several tests the railway track inductance was found to be approximately 10 μH .

3.2.4.2 Choosing Values of Inductance and capacitance for the resonant circuit

With the aid of simulations and experimental testing it was found that the higher the inductance, the higher the resonant voltage and the lower the resonant current, with the inverse also being true.

The principle function of the resonant converter is to generate a high frequency (300 kHz) current with a sizeable amplitude of around 2 A peak. This current would be sufficient in producing a measurable interfering magnetic field, which would allow the determination of the effect of the different techniques employed to reduce this interference.

Due to the principle function of the converter the resonant magnitude voltage does not need to be high, and must be kept below the rated maximum voltage of the capacitors used in the two capacitor banks.

Another consideration in choosing a value for the internal inductor pivoted on the notion that the larger its value the smaller the influence of any inaccuracy that may have occurred during the inductance measurement of the railway track.

These inaccuracies can be attributed to measurement error occurring when significant values from the voltage and current wave forms were read off the oscilloscope, including the measurement of the duty cycle of the Buck converter. Augmenting this, all the components used in the construction of the Buck converter were considered ideal therefore any losses over them were neglected.

Consequently as a requirement, a balance had to be reached between reducing the significance of the inaccuracy embodied by the railway track inductance and keeping the resonant voltage low enough for the capacitor banks to endure. Therefore through simulations (Appendix 2.4) and experimentation it was chosen to assign the internal inductor a value of 25 μH , as this would conform to its requirements.

The E-Core used for the construction of the internal inductor of the resonant converter was an E42-3C90 Core and it has the following specifications, which were obtained from its data sheet:

B	=	0.2 mT	-	<i>Magnetic Flux Density</i>
H	=	37 A/m	-	<i>Magnetic Field Intensity</i>
A_C	=	$1.77\text{E-}4 \text{ m}^2$	-	<i>Core cross sectional area</i>
l_C	=	0.108 m	-	<i>Magnetic path length of the core</i>
μ_C	=	0.0054054	-	<i>Permeability of ferrite 3C90 core</i>
μ_0	=	$1.257\text{e-}6$	-	<i>Permeability of free space</i>
A_W	=	$2.77\text{e-}4 \text{ m}^2$	-	<i>Window area of the core</i>

Using these specifications and the procedure described in Appendix 2,2, the internal inductor was designed and constructed, using 8.5 turns of copper wire and a total air gap length of 0.608 mm, which is much smaller than the width of the E-Core, and giving an inductance of 25.2 μH .

By adding the value of the internal inductor (25.2 μH) to the inductance of the railway track (10 μH) a total inductance value of 35.2 μH was obtained. By substituting the total inductance into equation (3-12), the value for each capacitor bank was found to be almost 4 nF.

The value of each capacitor bank was chosen to be 4 nF as its value can be achieved by using standard sizes available. By going back and substituting the value of 4 nF into equation (3-12) a value of 35.18 μH was found for the inductor, this value being close to the value of the inductor designed.

3.2.4.3 The Driving Circuit for the Resonator

The control of the resonant converter was accomplished with the use of a Driving Circuit, which consisted of a pulse width modulator (PWM) in conjunction with a half-bridge Mosfet driver. The layout of the Driving Circuit is described in the circuit diagram shown in Figure 3-5 below.

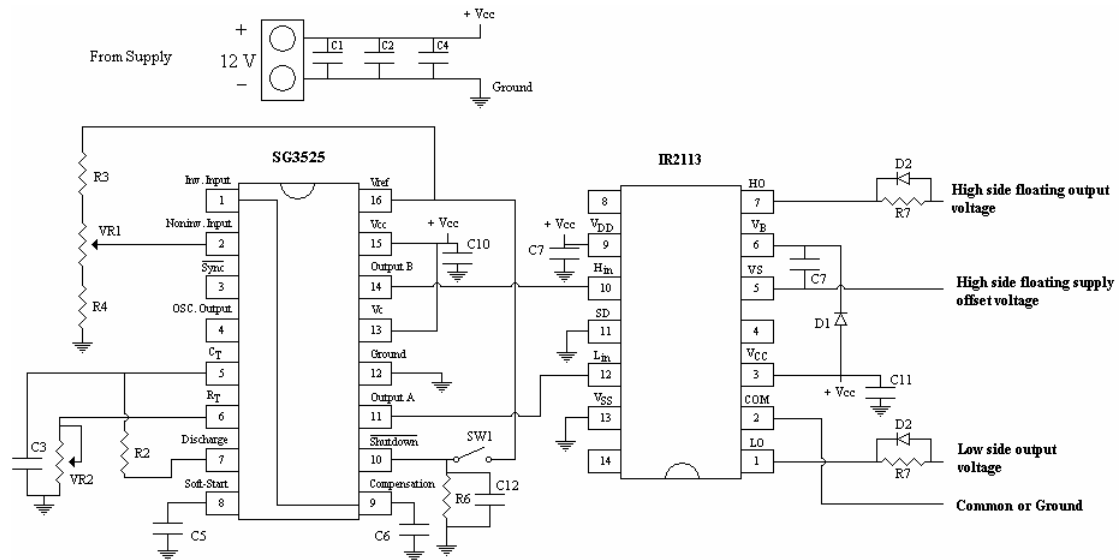


Figure 3-5: Circuit diagram of the Pulse Width Modulator (PWM) Controller.

Where each variable in the circuit diagram represents the following components along with their respective magnitudes:

- R2 - Discharge resistance = 1.2 Ω
 - R3 - 1.5 KΩ R4 - 820 Ω
 - R6 - 10 KΩ R7 - 10 Ω
 - VR1 - 2 KΩ Multi turn variable resistor
 - VR2 - 1 KΩ Multi turn variable resistor
 - C1 & 2 - 1μF Electrolytic
 - C3 - 2.7nF Ceramic
 - C4, 5 & 6 - 10μF Electrolytic
 - C7 & 8 - 0.43μF Polyethylene
 - C10 & 11 - 1μF Polyethylene
 - C12 - 103J63 Polyethylene
 - D1, 2 & 3 - 1N4148 or BAW 76R Diodes
 - SG3525 - Pulse Width Modulator (PWM) Chip (IC)
 - IR2113 - Half Bridge Mosfet Driver IC
- Note: C – Capacitors & R – Resistors

This driving circuit alternatively activates the two switches of the resonator with a period of dead time between each signal (see Figure 3-6). The dead time is important to ensure that both switches are never turned on at the same time as this would result in a short circuit, culminating in both switches becoming damaged.

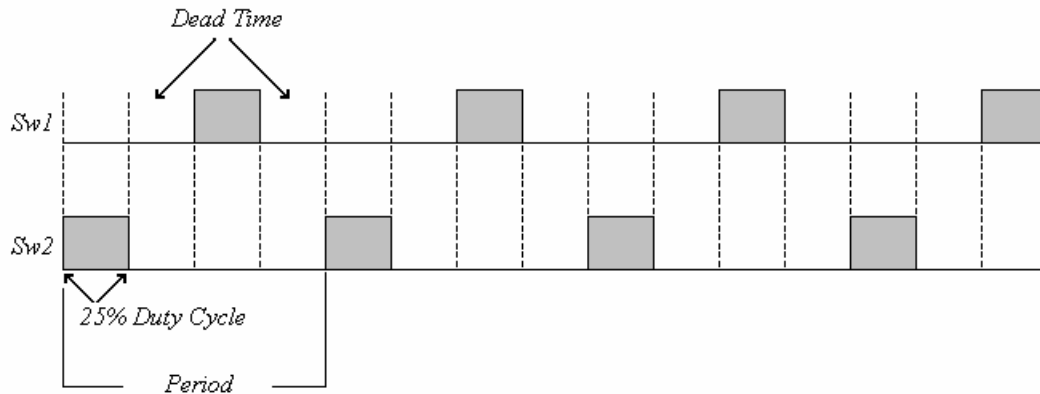


Figure 3-6: Driving Signals for the two switches $Sw1$ and $Sw2$.

A pulse width modulator was used in the driving circuit to allow the duty cycle of the driving signal to be set above 25%, resulting in the dead time between the high side switch ($Sw1$ in Figure 3-1) and the low side switch ($Sw2$ in Figure 3-1) to be reduced but nonetheless maintaining a safe value to buffer for a short circuit.

This increase in duty cycle permits the maximum amount of current to flow through the railway track during the on-times of each switch, which results in a decrease in the supply voltage needed to obtain the desired 2 A peak current.

A variable frequency control was also incorporated into the design, allowing the adjustment of its output frequency. This gives some fine tuning ability to the driving circuit allowing the finally constructed resonator to be tuned to the desired frequency of operation, correcting for any neglected factors.

The input capacitors C1, C2 and C4 regulate the 12V input ensuring that a steady DC supply is available for the Driving Circuit. Capacitors C10, C11 and C7 are placed as close to the power pins of their respective IC's to ensure that the power being drawn by these pins are kept steady and that no high frequency interference was picked up.

SW1 in Figure 3-5 controls the shutdown of the Driving Circuit, for when the Shutdown pin (pin 10) on the SG3525 PWM integrated circuit (IC) elevates, the IC turns off. The capacitor C12, which lies across the shutdown resistor R6, filters any

high frequency fluctuations at the shutdown pin to ground, which prevents erratic turning off of the PWM chip while the system is in operation.

The diodes labelled D2 allow swift discharging of the Mosfets used in the Resonator Circuit, this ability to quickly discharge the Mosfets decreases the turn-off time required, resulting in a reduction in the turn-off losses. This, however, is not fully applicable for the resonant converter as no switching losses occur. This reduction in turn-off time also allows higher frequency operations to be achieved.

For the half bridge Mosfet driver the common pin (pin 2) connects to the common ground of the resonator converter and Driving Circuit, with the Low side output (pin 1) connecting to the low side Mosfet ($Sw2$ Figure 3-1) supplying it with a driving signal.

Pin 5 (VS) connects between the high and low side Mosfets on the resonator, and monitors the voltage level between them, the importance of this lies in the fact that the high side Mosfet requires a higher voltage to turn on than does the low side Mosfet since its ground connection is floating from zero (when the low side Mosfet is on) to the supply voltage (when the low side Mosfet is off). This allows the Mosfet driver to self-regulate the magnitude of the signal sent to the high side Mosfet (via pin 7) with this signal serving to turn it on when the low side Mosfet is off.

Finally the soft start capacitor (C5) was imperative as it limits the rate of change in the duty cycle as the PWM turns on. This was paramount to control the transient response of the resonator circuit and decrease its in-rush current.

Using the circuit diagram given in Figure 3-5 the Driving Circuit was constructed on a PCB as shown in Figure 3-7 below. The layout of the PCB for the Driving Circuit can be found in the first section of Appendix 2.3.

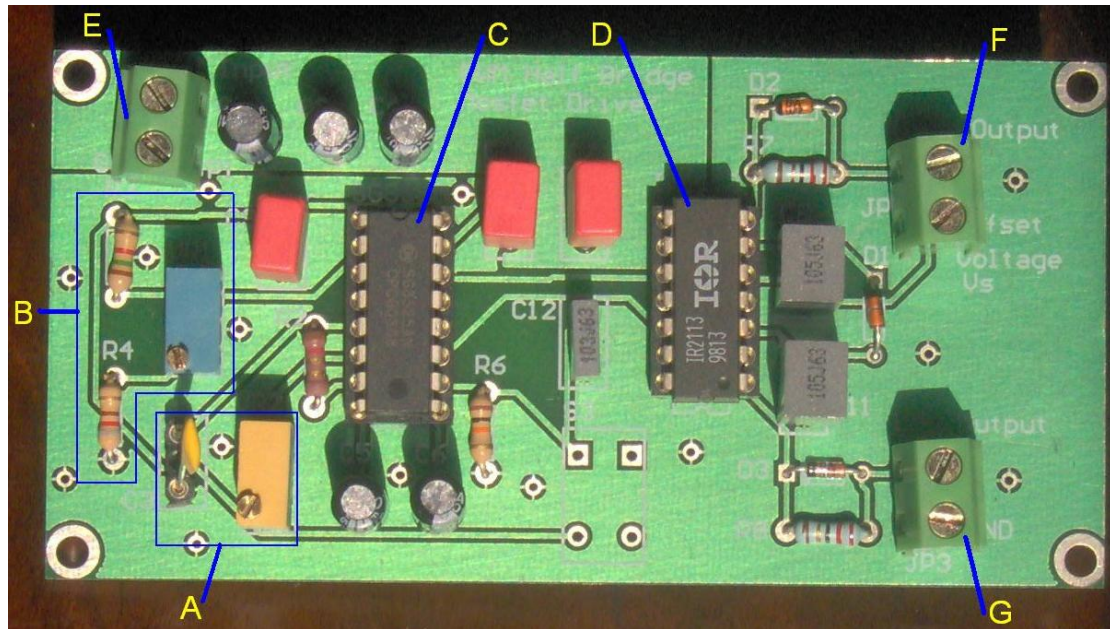


Figure 3-7: Constructed Pulse Width Modulator (PWM) Controller.

From Figure 3-7 the important component areas have been label A to G.

The quadrant labelled A demarcates the frequency control section of the PWM circuit and has the following configuration:

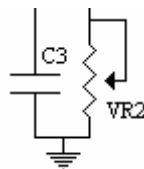


Figure 3-8: Frequency control circuit (Label A Figure 3-7).

By changing the capacitor C3 the frequency range is set, within that specified range a suitable frequency is obtained by adjusting the variable resistance VR2. VR2 can be varied by turning the gold adjustment screw on top of the yellow potentiometer shown. The Capacitor C3 is placed in a socket so as to facilitate effortless substitution if a different frequency is required. The capacitor is currently a 2.7nF ceramic and gives the correct frequency range to obtain 300 KHz by adjusting VR2.

The section Labelled B allows alteration in duty cycle to occur by adjusting the blue potentiometer, this section can be seen in figure 3-1 in the top left hand side and consists of the components marked R3, R4 and VR1

Label C is the SG3525 Pulse Width Modulator IC which controls the pulse width and the frequency of its two output channels which operate alternatively to control the two Mosfets on the resonator board. This IC has a maximum operating frequency of 400 KHz and must not be run at a frequency greater than. (See Data Sheet in Appendix 7.1).

The IC labelled D is the IR2113 and it is a high and low side Mosfet driver and has a maximum Mosfet voltage rating of 600V DC, and its supply voltage may not exceed 25V DC. It has an operating frequency well beyond that of the SG3525 and is not envisioned to pose a problem (See Data Sheet in Appendix 7.2).

Labels E, F and G represent input and output connectors. E is the input for the supply voltage needed to power the PWM circuit, where the top connector provides a link for the input voltage supply, which must lie between 10 to 15 Volts DC, and the bottom connector is the ground connection and the supply's ground must be connected here.

Connector F provides a connection for the high side Mosfet, where the top port supplies the driving signal and the bottom port monitors the necessary offset voltage. Finally terminal G connects to the low side Mosfet where the top port supplies the driving signal, and the bottom port links the ground or common connection to the ground on the resonator board.

3.2.4.4 300 kHz Resonator Board: Resonant Converter

The final circuit diagram of the Resonator or resonant converter, which was derived from Figure 3-1, appears in Figure 3-9 below.

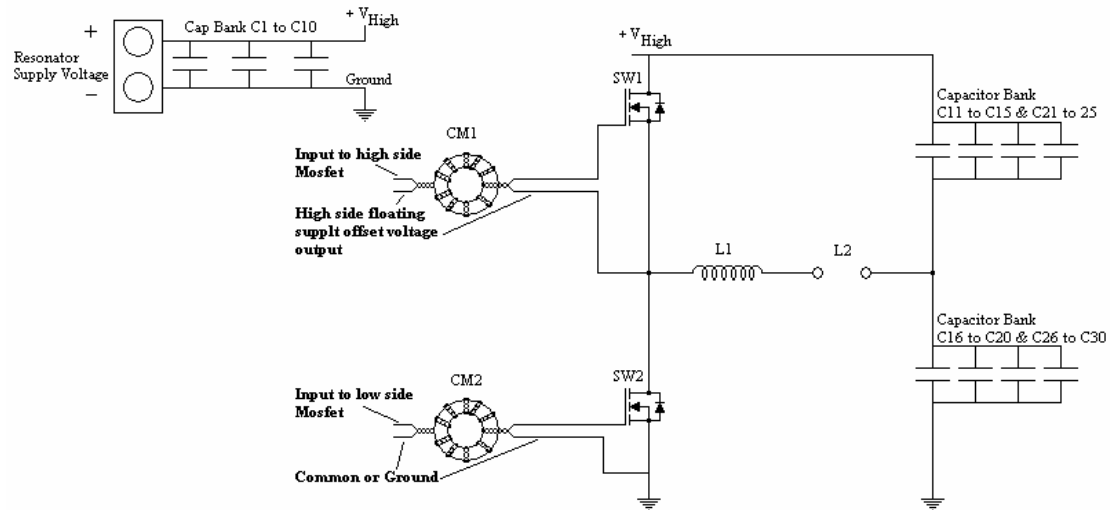


Figure 3-9: Final Circuit Diagram of the 300 kHz Resonator.

- C1 to C10* - *Supply voltage Capacitor Bank (1 μ Polyethylene MKP)*
- C11 to C30* - *Resonant Capacitor Bank (Polyethylene, 150V to 300V)*
- L1* - *Resonant Inductor – Wound E42Core*
- L2* - *External Conductor (Railway Track)*
- SW1* - *High side Mosfet – IRFZ44N, 60V 50A Maximum*
- SW2* - *Low side Mosfet – IRFZ44N, 60V 50A Maximum*
- CM1 & CM 2* - *Common Mode Chokes*

The High side (top in Figure 3-9 Figure 3-10) and Low side (bottom in Figure 3-9 Figure 3-10) Mosfets with their attached heat sinks are shown in Figure 3-10 (Label A). Heat sinks were installed to ensure good heat flow would be established, keeping the Mosfets cool.

The Mosfet chosen for this task was the IRFZ44N as it has a maximum constant current rating of 50A at 25°C and 36A at 100°C, which is well beyond the maximum current required from the converter, thereby providing a good safety factor. The maximum voltage it can withstand lies at 60V which conferred a proficient window for adjusting the supply until the desired current had been achieved (See Appendix 7.3 for Data Sheet).

The constructed Resonator Board is pictured in Figure 3-10 below, with the PCB layout given in the second section of Appendix 2.3.

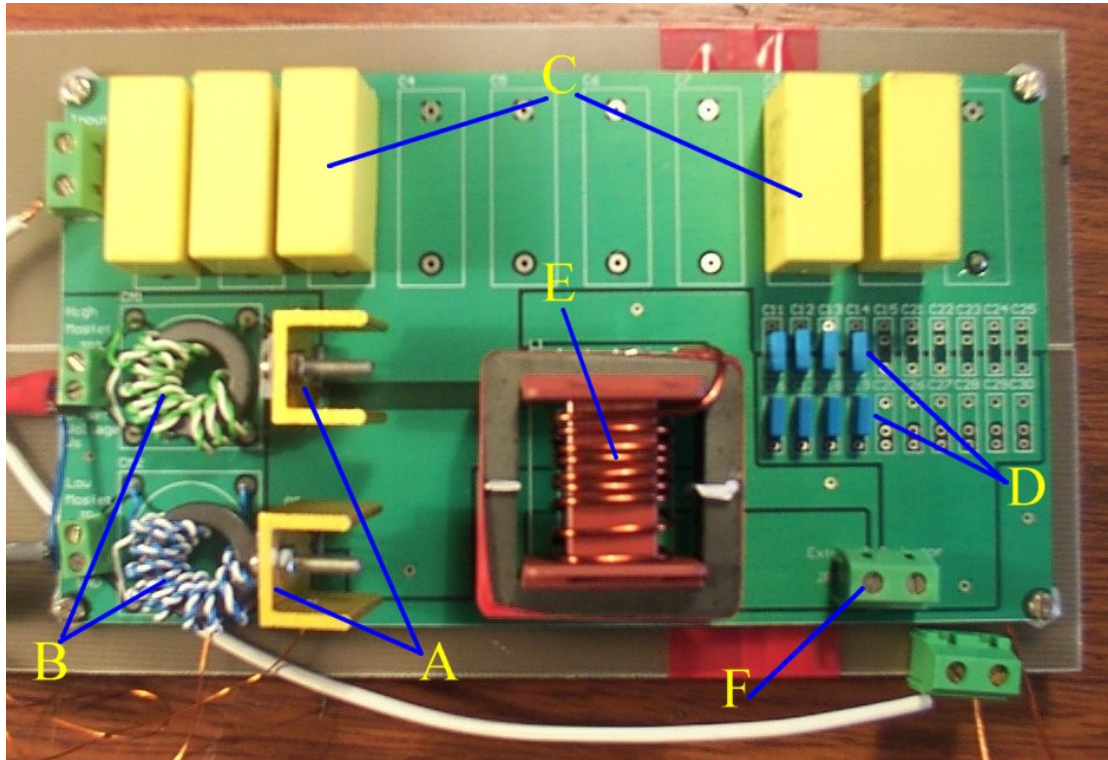


Figure 3-10: Constructed 300 kHz Resonator, where A indicates the switches (Mosfets), B the common mode chokes, C the input power capacitor bank, D the resonant capacitor banks, E the internal inductor and F the output terminal for the railway track.

The common mode chokes (Label B) were installed to prevent any common mode currents from flowing through the signal cables connecting the Mosfets of the resonator to the output of the driving circuit.

The input power capacitor (Label C) bank was put in place to keep the power levels in the resonator circuit constant and impede any fluctuations that may occur due to the changing power requirements of the resonating components.

For the resonant capacitor banks (Label D) four smaller capacitors were used (in each bank) instead of one larger capacitor to obtain the chosen 4 nF capacitance. This was done to reduce the value of the series total inductance and resistance of each capacitor bank.

Polypropylene Film capacitors were employed as they possess superior high frequency characteristics. These include a voltage rise time of around $1000\text{V}/\mu\text{S}$, a

resonant frequency of 50 MHz (for 1000 pF capacitor) and a constant capacitance value of up to 2 MHz.

The internal inductor (Label E) works in conjunction with the resonant capacitor banks to produce the resonant current that flows through the railway track, which is connected across the output terminal, indicated by label F in Figure 3-10, as shown in Figure 3-11 below.

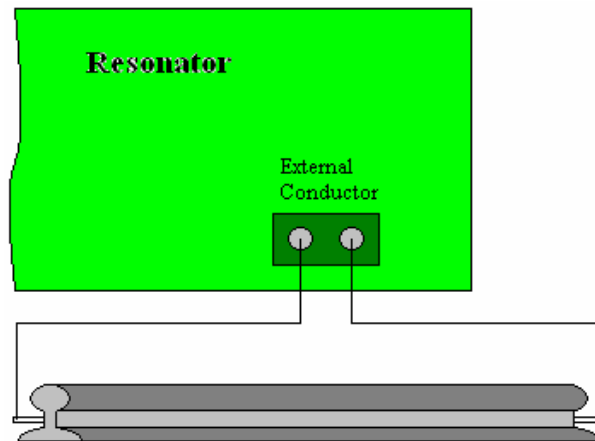


Figure 3-11: Railway Connected across output terminal (Label F) of Resonator.

For future construction it is recommended to distribute the total inductance needed for the internal inductor between itself and a tuneable inductor, and to subsequently connect this tuneable inductor in series with the railway track across the output terminals (Label F in Figure 3-10 and shown above in Figure 3-11).

The advantage of such a construction would allow for the inductance of the system to be rendered adjustable. This in turn permits the resonator to be tuned, bringing its resonant frequency closer to the operating frequency, thus improving the resonant current allowing less power to be consumed by the system, ultimately making it more efficient.

The higher efficiency is the result of lower to no turn-on losses in the Mosfets and fewer losses within the resonator. This would also result in an improved quality factor, hence a lower supply voltage.

3.2.4.5 Final Assembly of the 300 kHz Resonator

The Driving Circuit and Resonator Board were connected together with the use of microphone cable as show in Figure 3-12 below.

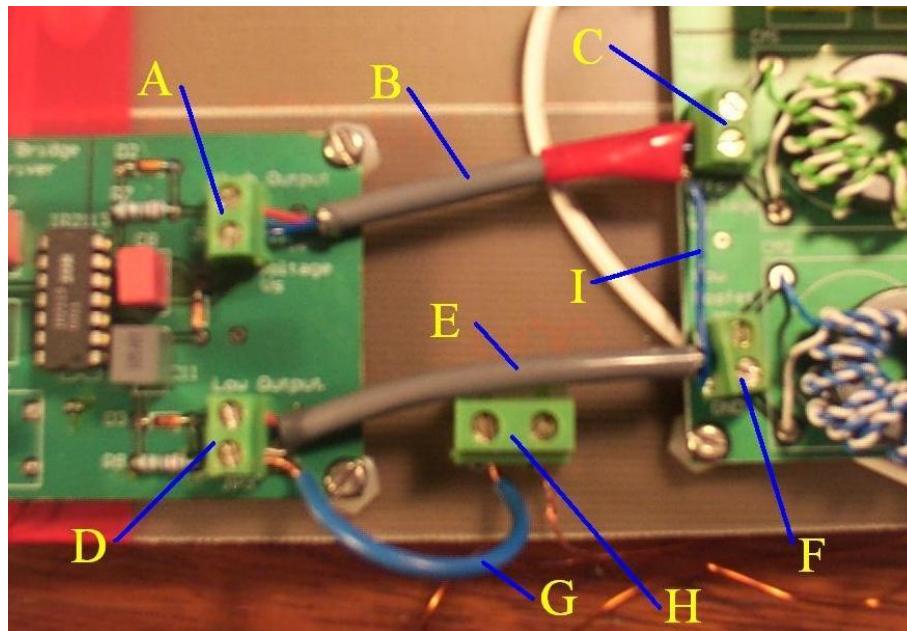


Figure 3-12: Connection between the Driving Circuit (PWM) and the Resonator Board.

From Figure 3-12 it can be seen that the Driving Circuit and the Resonator boards are connected using microphone cable (Labelled B & E). The microphone cable consists of two conducting wires with an un-isolated ground wire which is in contact with the aluminium foil shield that encloses the conductors.

Microphone cable was used to provide a grounded shield that protects the driving signals from any interference that may occur due to the electric field. Another advantage of microphone cable lies in the fact that its conductor wires form a twisted pair reducing any interference picked up due to the magnetic field.

The high side Mosfet driver output (Label A) is connected to the high side driver input on the Resonator board (Label C). The top port is the driving signal for the high side Mosfet and is connected to the top port of Connector B. The bottom port is the high side floating supply offset voltage and is connected to the bottom port of connector C.

The low side Mosfet driver output connector (Label D) is connected to the low side input on the Resonator board (Label F). The top port on D is the Mosfet gate driving

signal output and is connected to the top port of F. The bottom port of F is the ground or common connection and is connected to the bottom port of connector F, which is a ground connection on the Resonator board.

The wire connection labelled I exists to connect the shield of the microphone cable carrying the high side Mosfet signal (Label I) to ground, with the shield for the cable carrying the low side Mosfet signal (Label E) also terminating to ground at the same point (Connector Labelled F).

H is a connector on the ground plain (Label E in Figure 3-13 on pg 48) and is used to join some of the grounds from the two boards to the ground plain, for example the wire labelled G is connected to the ground of the Driving circuit and to connector H on the ground plain. The Resonator board is also connected to the ground plain through connector H.

The Driving Circuit and the Resonator Board were both mounted onto a large ground plane as shown in Figure 3-13 below.

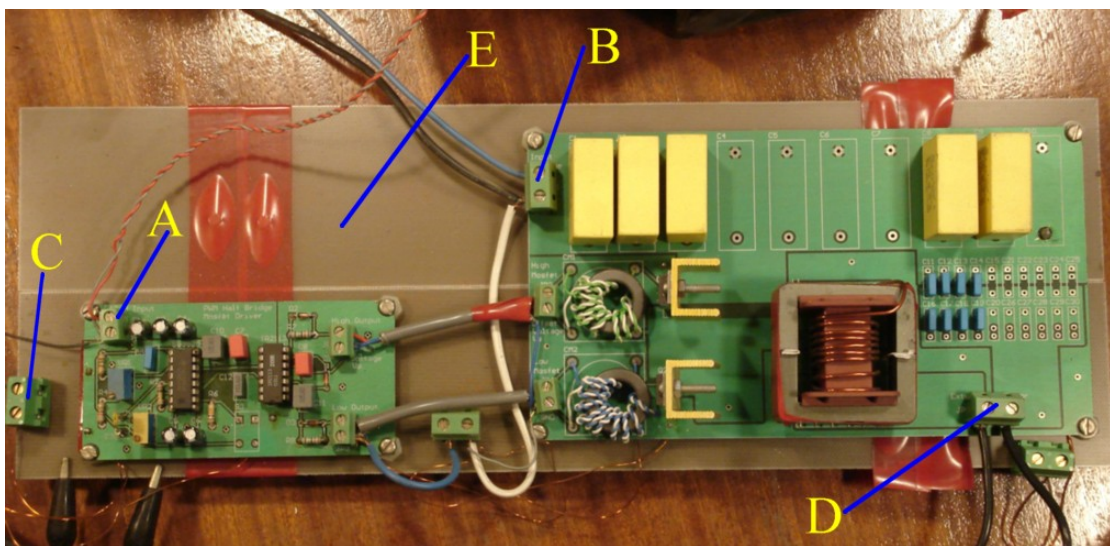


Figure 3-13: The Finally Assembled 300 kHz Resonator, with all the Ports Marked.

In Figure 3-13, connectors C and D form two additional ground connectors used to link the driving circuit and the resonator board to the common ground plane. Many connections are used to ensure that the grounds of the driving circuit and the resonator board are at the same level.

Connectors A and B are the power supply ports for the Driving Circuit and Resonator Boards respectively. The top port of connector A is the +12V supply input and the bottom port is the ground connection. It can be noticed that the ground port is also connected to ground plain through connector C.

A variable supply was connected to the top port of connector B, thus powering the resonator board, with the ground connected to the bottom port. It was important to have both the grounds from the power supplies connected together through the ground plain, as this would ensure that both ground levels were equal.

The large ground plane (label E) consists of a large copper plate, which forms a capacitor between itself and ground. The ground plane forms a curtail component in the resonator system as it acts as a resilient ground for any high frequency signals that may persist within the system.

The Resonator was tested with the railway track connected across the output terminals and the results are given in Appendix 2.5.

3.2.4.6 New Proposed Higher Frequency Driving Circuit (300 kHz to 1 MHz)

To allow any future higher frequency test to be performed, a new driving circuit was designed to incorporate a higher range of operating frequencies. The main requirement of the new driving circuit was to unwaveringly retain operation at the current 300 kHz, with an increased operational range of up to 1 MHz.

To achieve this requirement a new pulse width modulator IC was selected to replace the currently used SG3525, with its specified operational limit of 400 kHz. The New PWM IC selected was the UC3825, which has a potential operating frequency of up to 1.5 MHz (See Data sheet in Appendix 7.4). The UC3825 has a similar pin layout to the SG3525 therefore requiring minimal alterations to the current driving circuit.

The circuit diagram for the new driving circuit with the UC3825 fully integrated, with the half-bridge Mosfet driver, appears in Figure 3-14 below.

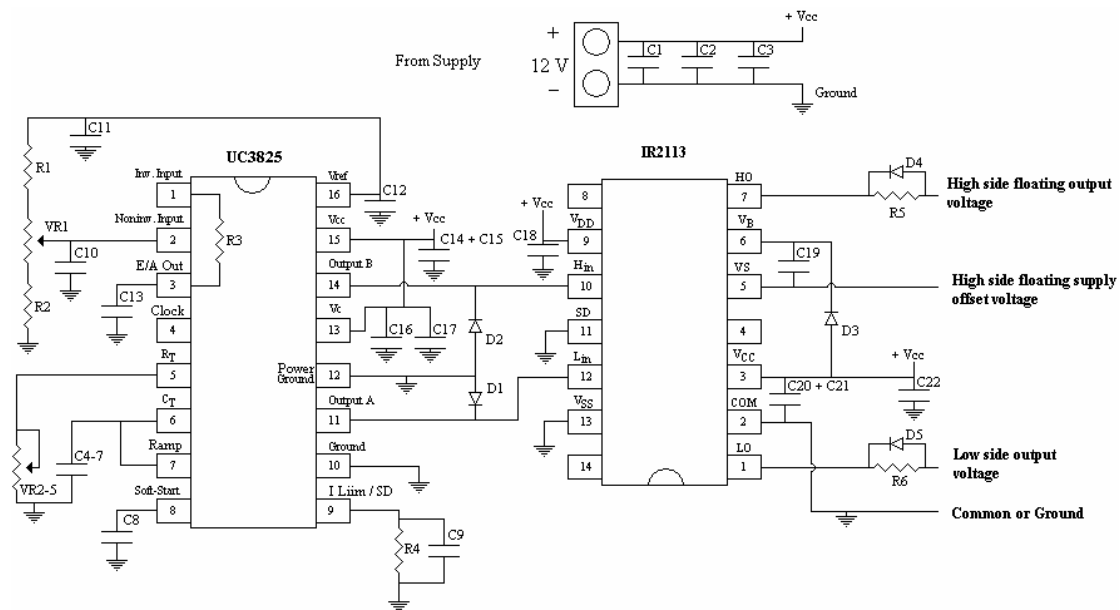


Figure 3-14: Circuit diagram for the new 300 kHz to 1 MHz Driving Circuit incorporating the UC3825 IC.

Where each component has the following application and typical values:

- C1, 2 & 3* - *Input supply regulation capacitors typically 1 μ F and 10 μ F Electrolytic.*
- C4-C7* - *Ceramic capacitors used for setting the frequency range of the PWM, starts at 2.7 nF for 300 kHz and will decrease to around 470 pF for 1MHz.*
- VR2-VR5* - *Variable resistors used in conjunction with C4-7 to set the operating frequency of the driving circuit, used 2 to 5K Ω multi turn potentiometers.*
- R1 & R2* - *Limiting resistors for the pulse width control, chosen to be 27K Ω .*
- VR1* - *Variable resistor for adjusting the pulse width of the driving circuit, used 100K Ω multi turn potentiometer.*
- R3* - *Forms the feed back resistor for the build in error Amp, and was assigned a value of 68K Ω .*
- C10, 11 & 12* - *Are filter capacitors for the pulse width controller, typically 100 nF (C10 & 11) Ceramic and 1 nF (C12) Polyethylene.*
- C13* - *100nF Ceramic capacitor used to filter any high frequency signal that may occur at the output of the error Amp.*

- C14 – C17* - *Regulation capacitors for the UC3825 PWM IC, put in place to ensure constant voltage supply to the IC allowing it to perform better at all frequencies.*
- C8* - *Soft Start Capacitor, same purpose as for the previous driving circuit using the SG3525 PWM IC, typically chosen to be 10 μ F.*
- R4* - *Shutdown resistor, chosen to be 3.3K Ω , used to keep the shutdown pin (9) low ensuring the device stays on.*
- C9* - *Filter capacitor placed across the shutdown resistor to ensure that any high frequency noise picked up at the shut sown pin finds a quick route to ground (10 nF 103J63).*
- D1 – D5* - *1N4148 or BAW 76R Diodes.*
- C19* - *1 μ F (105J63)*
- C18* - *One of the supply regulation capacitors for the IR2113 half-bridge Mosfet, typically 1 μ F to 0.47 μ F.*
- C20 – C22* - *The other supply regulation capacitors.*
- R5 & R6* - *Performs the task of slowing down the turn on time of the Mosfet, with the purpose of reducing any negative voltage and current spikes that occur when the Mosfet turns on.*

C4–C7 and VR2-VR5 are used in conjunction with dip switches to allow preset operating frequencies to be set, giving the driving circuit a rapid means of shifting from one frequency to another.

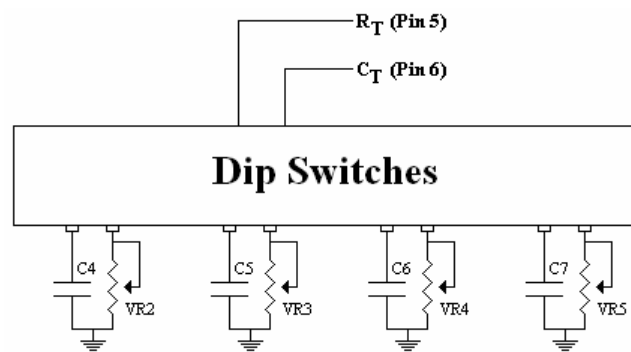


Figure 3-15: Preset operating frequency switcher.

Figure 3-15 signifies the manner by which presetting an operating frequency is achieved. The capacitors are connected in combinations with the variable resistors to set a frequency, each unique for each combination. Following this initial step the different combinations are switched into the circuit, thereby setting the operating frequency of the driving circuit.

For example C4 and VR2 are set in combination to produce an operating frequency of 300 kHz, where C5 and VR3 produce an operating frequency of 600 kHz, C6 and VR4 produce an operating frequency of 800 kHz, until the final set C7 and VR5 produces an operating frequency of 1 MHz.

The PCB of the new driving circuit is shown in Appendix 2.6, along with the PCB of a modified resonator board.

The filter capacitors are in place to remove any high frequency noise from areas in the driving circuit that must be purely DC. For example if any fluctuations occur at the shutdown (SD) pin, the PWM IC will begin to turn off and on erratically. Also if any noise exists on the pulse width controlling circuit (R1, R2 and VR1), fluctuations in the pulse width will occur causing the on times of the switches on the resonator board to fluctuate resulting in the current through the converter, including the railway track, to fluctuate as well.

4 Preparation of the Measurement System for the High Frequency Test at 2A 300kHz

4.1 Introduction

Following on from the modifications made to the railway track system rendering it conducive to produce a high frequency magnetic field around the railway track, the high frequency tests are primed to commence, barring one dilemma. The only problem preventing progress into the testing phase finds its source in the very interference that was essential for performing the high frequency tests to begin with.

The identical interference that creates detrimental effects in the field with regard to the proximity sensors, the functional entities used to perform the train wheel counting in the train wheel detection system, now forms the basis of the incorrect measurements being taken in the vicinity above the proximity sensor platform.

The manifesting measurement inaccuracies occur owing to the generated interference, consisting of both electric and magnetic fields, which spread out from the railway track coupling to most of the Measurement System.

These field couplings result in the measurements containing not only the flux density in the test area but also the electric and magnetic field picked up along the cable connecting the flux density (FD) sensor to the oscilloscope. Furthermore an imbalance problem was discovered, which caused the measurement observed on the oscilloscope to vary dramatically when the Flux Density Sensor was rotated by 180°.

To combat these debilitating issues the Measurement System had to be made more robust, diminishing the amount of interference it picked up, restricting its magnetic susceptibility to where it was intended, at the Flux Density Sensor.

This was achieved through the use of shielded cable with an improved conductor layout, addition of shielding, in some form, to any sections in the system not already shielded, along with an improved grounding system including the use of common mode chokes.

4.2 Interference Problems with Measurement System

4.2.1 Capacitive Coupling

A changing voltage across a conductor will generate an electric field that may couple to a nearby conductor and induce a voltage across it. This form of coupling is known as capacitive coupling. The greater the change in voltage over time (dv/dt), the greater the capacitive coupling effect will become since the coupling impedance will decrease [6].

The ratio of the change in voltage over time (dv/dt) can be increased in two ways. The first is to increase the gradient of the change in voltage i.e. increase the maximum voltage across the conductor. The second is to decrease the time per cycle i.e. increase the frequency at which the voltage changes. Therefore, as the operating frequency increases, the greater an influence the capacitive coupling will have on the Measurement System.

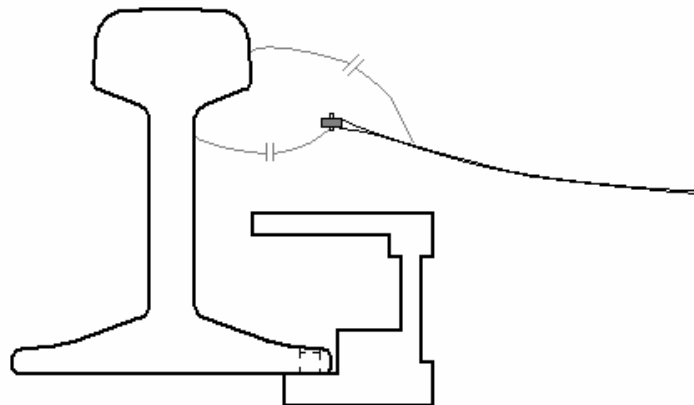


Figure 4-1: Diagrammatic representation of the capacitive coupling between the railway track and the Flux Density Sensor.

Figure 4-1 depicts the capacitive coupling between the railway track (source) and the Measurement System (victim). Due to this capacitive coupling adding to the field being measured, the results obtained are overwhelmed by it and therefore cannot be used to map the magnetic flux density in the test area.

It therefore became a matter of importance to incorporate shielding in the Measurement System so as to reduce the effect of the electric field emanating from the railway track.

4.2.2 Magnetic Coupling

Alternating current flowing in a conductor creates a magnetic field which will couple to a nearby conductor and induce a voltage across it. The voltage induced across the victim conductor is given by the following equation,

$$V = -M \frac{di_L}{dt} \quad (4-1)$$

Where:

- V - *Induced voltage across nearby conductor*
- M - *Mutual inductance between the two conductors (in henries)*
- di_L/dt - *Change in current through the conductor over the time period dt*

The mutual inductance M depends on the areas of the source and victim current loops, their orientation and separation distance, and the presence of any magnetic screening [6].

The area of the current loop of the Measurement System must be kept small to reduce the effect of magnetic coupling with the railway track. In addition magnetic shielding should be included to increase the Measurement System's resistance to magnetic coupling, and thus providing more reliable measurements.

From equation 4-1 it can be seen that if the frequency increases, the time period decreases, and then the voltage ultimately induced in the victim conductor increases, thereby making the steps to reduce magnetic coupling even more crucial.

4.2.3 Imbalance

The causes of the imbalance problem are due to the unbalanced capacitances between the terminals of the oscilloscope and ground. As for the first attempt to improve the Measurement System (Section 4.3.1 to follow) where the cable screen was connected directly to the ground on the oscilloscope, common mode currents flowed into the oscilloscope, combining with the screen current flowing to the ground port.

The problem embodied by this, results in different charge levels occurring at the measurement and ground ports, and since the oscilloscope measures the difference between these points, the displayed measurements will be inaccurate. Further compounding these inaccuracies is when the Flux Density Sensor is rotated by 180°, the charge characteristic in the cable screen changes and, detrimentally, the displayed measurement changes.

4.2.4 Methods to increase the Measurement Systems Resistance to Interference

Fortunately avenues are available to improve the electro-magnetic interference (EMI) indaba and these can be enlisted in successful combination to achieve improved protection; these include shielding or screening, conductor path layout, grounding system and reducing common mode currents.

4.2.4.1 Shielding or Screening

Shielding provides a barrier to EMI preventing it from coupling to any conductors (circuits) that lie beyond the shield. If grounding is incorporated with the shield it affects are exponentially improved.

The method of shielding entails the use of shielded cables, which consist of a screen enclosing the internal conductors of the cable and shielded enclosures that surround sensitive circuits protecting them from EMI.

The most significant source for EMI to couple into a system are its external cables. Due to their lengths they are more efficient in interacting with EM fields than enclosures and PCB's. Cables and connectors form the interface to the equipment and must be selected with caution and due consideration to ensure that common mode currents are not introduced onto the cables, and that external fields are not coupled into the signal circuit via these cables [6].

The method used to terminate the cable screen at the connector interface is crucial in maintaining the screening properties of the cable, for, if performed incorrectly, can result in an increased impedance in series with the cable screen reducing the screens

effectiveness at high frequencies. This is so as it inhibits the swift flow of screen currents to the ground plane.

Two types of screening are available for the cabling, firstly aluminium foil with a drain wire, which fully encloses the signal carrying conductors it contains, and secondly braided wire screen that consists of braided conductors enclosing the signal carrying conductors within the cable.

The aluminium foil screen has a high effectiveness against electric field coupling but little effect on the magnetic coupling, as the aluminium foil possesses a high resistance, forcing screen currents to flow through the drain wire. Also to make a proper termination of this type of cable is difficult since connecting the drain wire to ground causes a loop between the drain wire and the signal carrying conductors, known as a pigtail connection (see Figure 4-2). The loop formed by the drain wire can result in an inductance of up to tens of nano henries in series with the screen connection. This impedance increases rapidly with an increase in frequency until it dominates the impedance of the screen negating the advantage of a good high frequency screened cable.

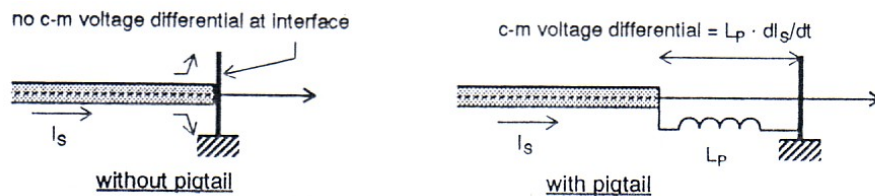


Figure 4-2: Inductance caused by the Pigtail connection of the drain wire linking the cable screen to the ground of an instrument.

The braided screen cable offers better magnetic field screening but a lower effectiveness against electric field coupling depending on the optical coverage of the braiding. The braided screen cable has the advantage that a better termination between the cable's screen and the ground of the connector can be accomplished.

By using a connector that allows the braiding to be terminated in a solid 360° connection to the ground plane or chassis, a much reduced impedance is accomplished allowing the interference currents on the screen to be routed to ground without passing through or being coupled to the signal conductors.

To achieve the advantages of both screen types, a composite cable can be used. The composite cable consists of an aluminium foil and braided screens wound over it. This type of cable provides the advantages of having very good electric field screening with magnetic field screening and the ability to form a good 360° connection to the ground plane, allowing it to operate well at high frequencies.

All sensitive circuits should be enclosed in a grounded all metal container to give good protection from high to low frequency electromagnetic fields.

4.2.4.2 Conductor Path Layout

The conductor path layout consists of decreasing the current loop area of any current paths in the system, as this will reduce the inductance of the current path and reduce the area to which any magnetic coupling can occur.

All wires connections used in the system must be formed in to twisted wire pairs as it decreases both the magnetic and capacitive interference they pick up. Twisting the wires tends to ensure a uniform distribution of capacitance, and that both the capacitance to ground and other sources are balanced, which means that common mode capacitance is also balanced. Resulting in a high common mode rejection providing the rest of the system is also balanced [6].

The use of a composite screened cable consisting of twisted pairs of conductors would give all the advantages of each and providing the better protection against EMI along the cable and the connections between equipment.

4.2.4.3 Grounding system and reducing common mode currents

The inclusion of common mode chokes in the signal path of the measurement system prevents common mode currents to flow. This takes place since common mode currents recognise the choke as a source of high impedance owing to the direction of current flow and magnetic field orientation being common to both the wires passing through the choke.

The magnetic fields produced by these common mode currents travel within the ferrite material of the common mode choke thereby creating the high impedance they experience. Differential mode currents, on the other hand, have opposing magnetic

field that do not flow in the ferrite material resulting in a reduced impedance being observed by these currents.

An improved grounding system with the inclusion of a large copper ground plane with a low impedance link to the screening of the Measurement System will ensure that the screen currents will flow into the ground plane. Also by keeping the screening separated from the ground conductor of the Measurement System and the ground port of the oscilloscope prevents the screen currents from flowing into the oscilloscope.

4.3 Reducing the Measurements Systems Susceptibility to EMI

4.3.1 Steps to Combat EMI on the Measurement System

Two iterations were performed to obtain a better Measurement System with the second iteration being an improvement on the first. The first iteration on the Measurement System consisted of the Flux Density Sensor connected to an aluminium foil screened cable that carried the measured signal directly to the oscilloscope where it terminated through a BNC connector with the cable screen grounded through the drain wire connected to a ground port on the oscilloscope, with the details of the construction being provided in Appendix 3.

One advantage of this system was its provision of good electric field screening through the aluminium foil screened cable and conductive tape applied to all sections unscreened by other means such as those connections between the Flux Density Sensor, oscilloscope and screened cable.

Another advantage was the reduced magnetic field coupling that occurred due to the use of a twisted wire pair, which was incorporated in the screened cable and applied to the connection wires from the Flux Density Sensor to the cable.

The disadvantages of this system include:

1. Little magnetic field screening due to the screen current flowing in the drain wire on the screened cable.

2. Low resonance point, at approximately 300 kHz, which matches the frequency of the magnetic field to be measured. This was due to the high capacitance of the screened cable and the inductance of the Flux Density Sensor.
3. Pigtail connection where the shield terminates to ground, and the chassis of the oscilloscope, resulting in a high series inductance in the screen current path.

Due to the disadvantages of the system produced from the first iteration a second improved system was developed, incorporating composite cable with braided and aluminium foil screening, which allowed better termination to ground.

The addition of an amplification buffering system was also included to offer amplification to the measured signal increasing the resolution of the measurements and to incorporate a buffering mechanism serving to separate the Flux Density Sensor from the main cable, thereby increasing the resonant point of the system and so increasing its measurement bandwidth.

The Steps taken to improve the Measurement System are listed below and were implemented in the following sections:

1. Improvements to the Flux Density Sensor.
 - 1.1. Adapting the winding layout of the sensor and where to connect the terminals of the oscilloscope.
 - 1.2. Wrapping a grounded copper shield around the sides of the Flux Density Sensor (FD sensor).
2. Improving the cabling system for the Measurement System.
 - 2.1. The use of composite cable for improved electric and magnetic field screening, and better terminations.
 - 2.2. Improved connectors and terminations to the shielded enclosures, Flux Density Sensor and oscilloscope.
 - 2.3. Ensuring that all conductor wires, not enclosed within the cabling, form twisted pairs and are enclosed by screens.

3. Inclusion of a Transimpedance Amplifier (TC Amp).
 - 3.1. For amplification of measured signal to increase the resolution.
 - 3.2. And buffering between the Flux Density Sensor and cable to increase the bandwidth for potential measurement frequencies.
4. Addition of common mode chokes to prevent the flow of common mode currents through the Measurement System.
 - 4.1. Add common mode choke before the oscilloscope.
 - 4.2. Add common mode choke before Transimpedance Amplifier.
 - 4.3. Implement impedance matching between the TC Amp and the oscilloscope.
5. Improve the grounding system for the Measurement System.
 - 5.1. Make use of a large copper plate to form a ground plane for high frequency grounding with the inclusion of a DC and low frequency connection to Earth.
 - 5.2. Ensure good connections between the Measurement System and the ground plane, and the oscilloscope and the ground plane.

The use of these steps resulted in a much improved Measurement System ready to tackle the high frequency tests.

The subsequent sections contain details on each of the steps taken to improve the final iteration of the Measurement System.

4.3.2 Improvements to the Magnetic Flux Density Sensor

4.3.2.1 Adapting the Winding layout

To reduce the effects of capacitive coupling consideration was given to the winding layout of the Flux Density Sensor (Figure 2-5). Each winding on the FD sensor was kept as close as possible to the previous winding to ensure less magnetic coupling

between the windings, the layout can be seen in Figure 4-3 below. The connection to the inner winding was designated to carry the measured signal to the measurement point on the oscilloscope where the outer winding connects to its ground point.

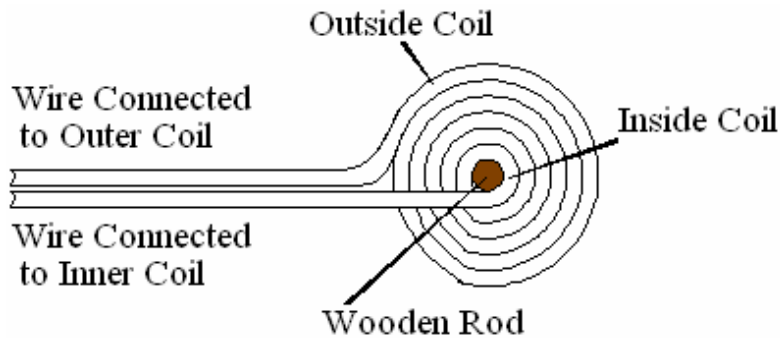


Figure 4-3: Winding layout for the Flux Density Sensor

This layout effectively creates a shield at the outer winding as the electric field becomes coupled to ground. This results in a reduced effect from the electric field on the measurements taken.

4.3.2.2 Addition of Copper Shield

A copper sheet was utilized to form a primary shield around the outside of the Flux Density Sensor. A link between this shield and the screen of the cabling system was formed to ensure that any interference coupling to it would be connected to ground.

Due to the positioning of the shield and the winding layout incorporated, the measured flux density should not be greatly effected since the inner winding of the FD sensor feeds the measurements to the oscilloscope, and the flux density would be measured close to the centre of the FD sensor.

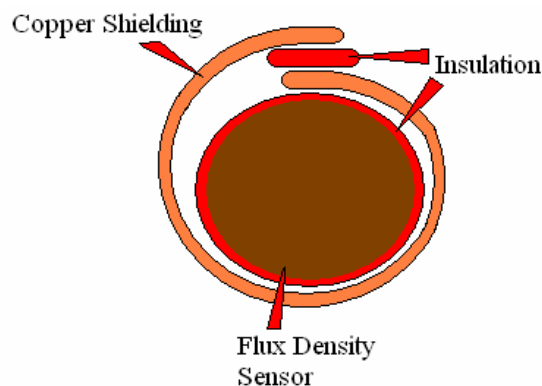


Figure 4-4: Placement of copper shield around the Flux Density Sensor

The placement of the copper shield can be seen in Figure 4-4 above. The layout of this shield was important since a closed ring must not be allowed as this would cause induced currents to flow in it. The consequences of such induced currents is embodied by Lenz's Law stipulating that opposing magnetic field would be setup, repelling the railway track's magnetic field and preventing the Flux Density Sensor from performing its duty.

Figure 4-5 below shows the strip of copper used for the shielding of the flux density and, by following the example outlined in Figure 4-4, can be applied to the Flux Density Sensor.



Figure 4-5: Copper sheet used for the shield of the Flux Density Sensor

4.3.3 Improving the Cabling System for the Measurement System

4.3.3.1 Composite Cable

Composite cable was used to retain the steadfast screening against electric coupling and add better screening against magnetic coupling. The cable chosen also incorporated twisted wire pairs to further reduce the effect of magnetic coupling. An example of the cable used can be seen in Figure 4-6 below.

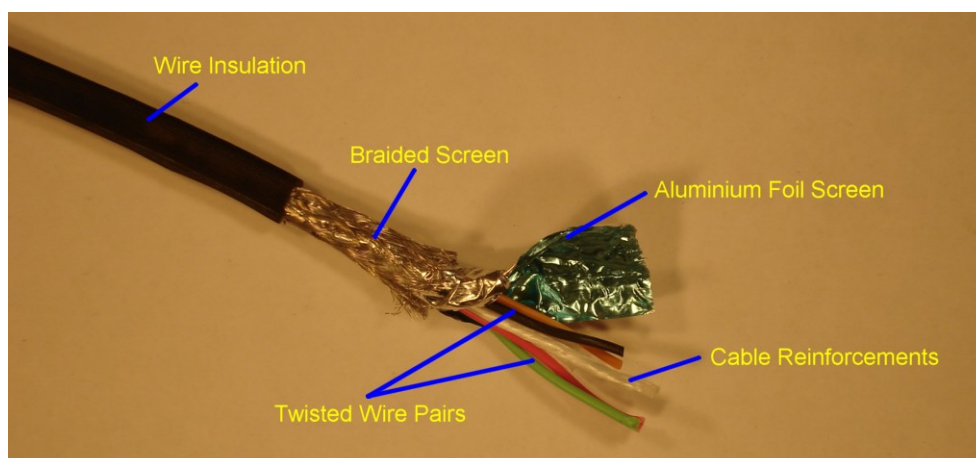


Figure 4-6: Composite Cable Used for Improved Measurement System.

From Figure 4-6 the braided screen can be seen covering the aluminium foil screen, and currents in this composite screen will flow through the braiding as its resistance is much lower than that of the aluminium foil. The braiding encircles the cable and allows a beneficial 360° termination to any connectors used contrary to the aluminium screened cable employed for the first iteration.

The cable reinforcements are in place to strengthen the cable and allow long sections of cabling to be used. There are two twisted pairs of conductive wires available for carrying the measured signal from the Flux Density Sensor, through the system to the oscilloscope. The green and red pair was used for the Measurement System, while the other pair was left unconnected. This cable was used as it was the only composite cable found to be available.

4.3.3.2 Flux Density Sensor

Once the shielding for the Flux Density Sensor was completed a connection between it and the cabling became necessary. For this to be achieved the wires of the Flux Density Sensor were twisted together, forming a twisted pair and covered in a double braiding before it was connected to a twisted pair from the cable.

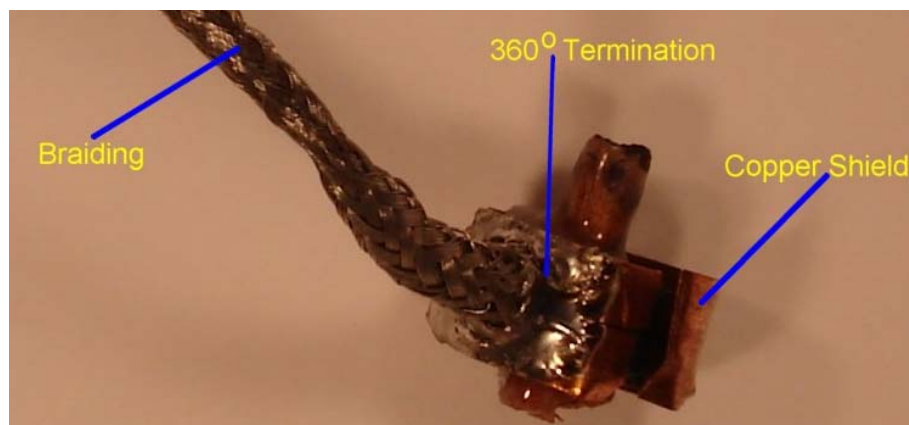


Figure 4-7: 360° Termination at copper shield of Flux Density Sensor.

Figure 4-7 shows the 360° termination constructed between the copper shield of the Flux Density Sensor and the braided screen. The signal wires from the Flux Density Sensor pass from the coil through a slot in the copper shield and then through the centre of the braided screen so as not to expose it to the EMI present.

A double braiding with good optical coverage was used to ensure good electric and magnetic screening after the Flux Density Sensor. Figure 4-8 shows the screened Flux Density Sensor with the double braiding in place.

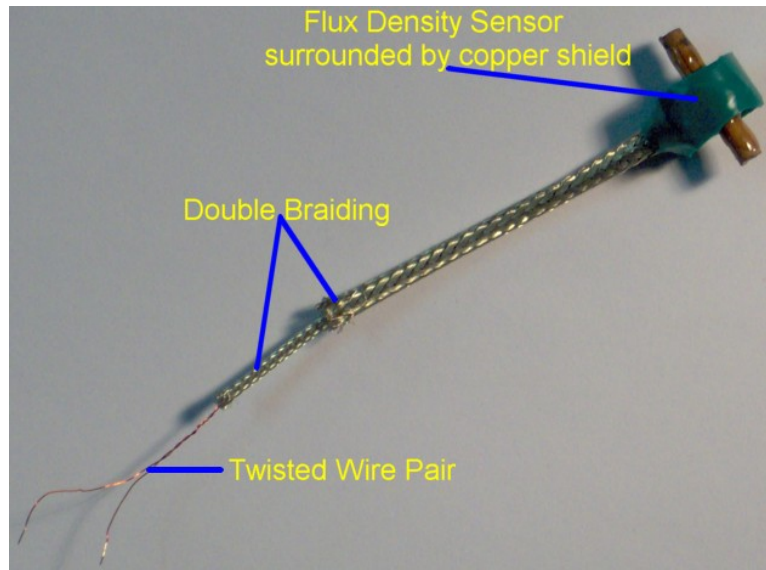


Figure 4-8: Flux Density Sensor with double braiding screen connected to copper shield with a 360° termination.

The prepared Flux Density Sensor (Figure 4-8) was connected to the cable, using another section of braiding to join the braiding of the Flux Density Sensor to the braiding screen of the cable.

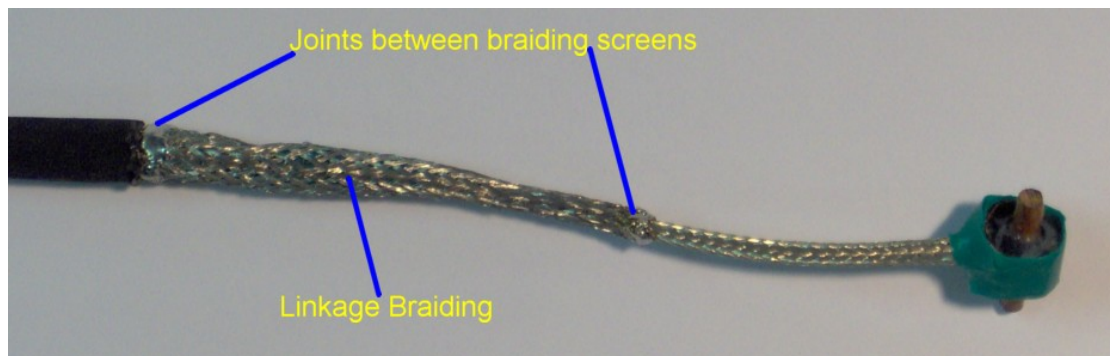


Figure 4-9: Braided link between the prepared Flux Density Sensor and the cabling.

Finally to ensure good electric field screening over the linkage, conductive silver tape; with conductive glue, was wrapped around the exposed area from the end of the cable isolation (left) to just after the second joint (right) for the link between the Flux Density Sensor braiding and the linkage braiding (Figure 4-9 and Figure 4-10).

The silver tape was not applied all the way to the Flux Density Sensor as it has a very high rigidity and it was found from the initial iteration that the Flux Density Sensor

would continuously break off, so a flexible braiding was used as this allowed movement of the Flux Density Sensor without continuous breakage.

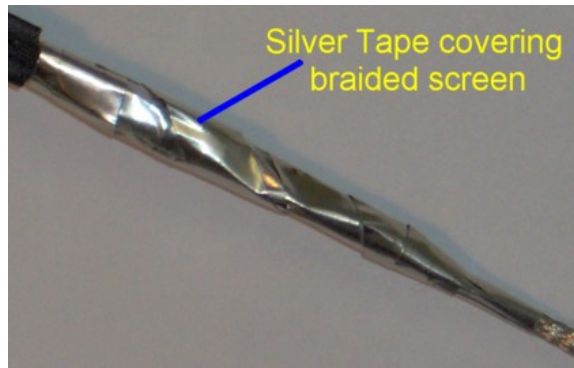


Figure 4-10: Silver tape for improved electric field screening over the constructed braided sections.

4.3.3.3 Connectors

IN-Line Microphone Connector

To provide good screening the signal wires enclosed within the composite cable were kept separate from its screen. Figure 4-11 below shows the signal wires connected to the tip of a 2 port In-Line Microphone connector with the red wire carrying the measured signal and the green wire attached to the ground of the oscilloscope.

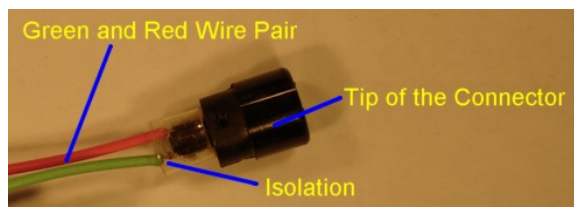


Figure 4-11: Green and red wire pair connected to tip of the IN-Line 2 Port Microphone connector.

The plastic isolation ring shown ensures that the two conductors do not make contact with the screen of the cable.

Once the connector has been fully assembled and the screen has been terminated to the shield of the Microphone connector, the assembly appears as follows:

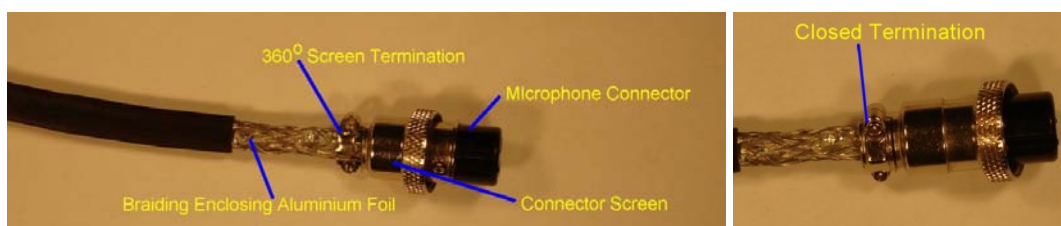


Figure 4-12: Screen of cable terminating with 360° of contact on the Microphone connector (Left), and with the contact point closed (Right).

The 360° termination shown in Figure 4-12 was formed by adding solder to the braiding, ensuring it is kept in place and that the Microphone connector makes full all-round contact with it when it is closed.

Chassis Microphone Plug Connector

The Microphone connector shown in Figure 4-12 connects to a two port Microphone plug connector, which for this case was mounted on to the chassis of the shielded enclosures used.



Figure 4-13: 2 Port Microphone Plug connector mounted to the chassis of one of the shielded enclosures, Top view on the Left with a front view on the Right.

Figure 4-13 illustrates how the microphone plug connector was joined to the shielded enclosures used. The insulation layer coating the metal of the shielded enclosure was scraped off before the microphone plug connector was installed to ensure a good conductive connection between the shield and the shielded enclosure. The two connectors shown in the middle of the microphone plug are the connectors for the signal carrying conductors, which are kept isolated from the cable screen and the shield of the enclosures.

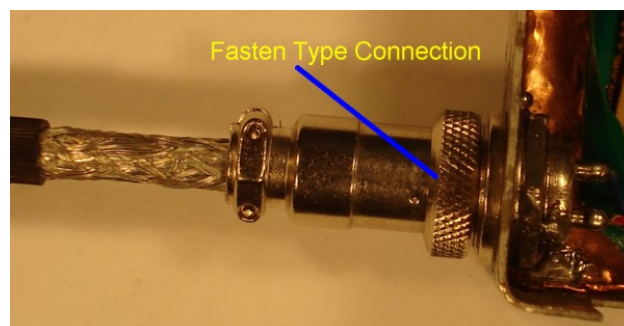


Figure 4-14: Screened Cable Connected to Shielded Enclosure Via Shielded Microphone Connectors.

From Figure 4-14, the continuous connection of the shielding from the screen of the cable through the shields of the two microphone connectors to the shielded enclosure can be seen with the signal carrying conductors, passing from the cable through to the circuit inside the shielded enclosure, remaining isolated from any of the shielding.

BNC Connection for Oscilloscope

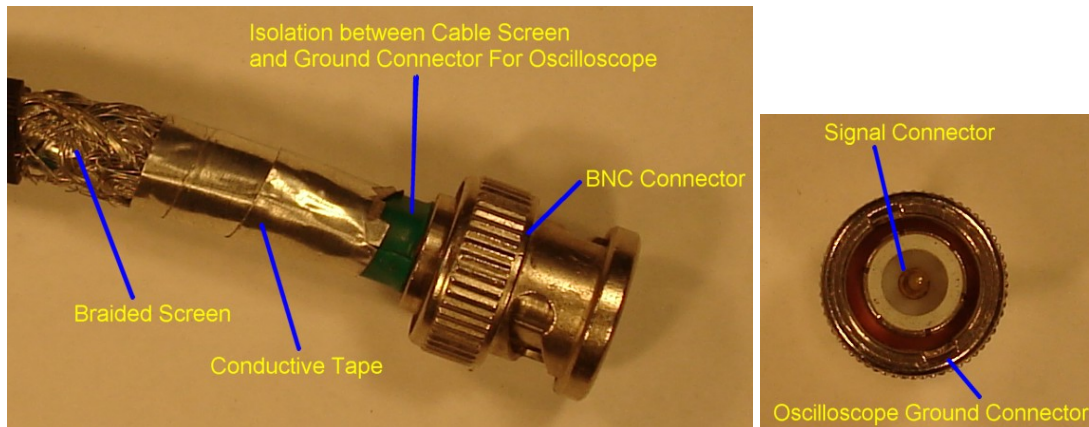


Figure 4-15: Screened Cable Connected to BNC Connector for the Oscilloscope (Left), and Connections from the signal conductors for the BCN Connector (Right).

The signal wires within the screened cable are connected directly to the BCN connector, with the measurement cable connected to the inside pin and the ground connection linked to the outer part of the BCN Connector (Shown to the right of Figure 4-15).

Isolation tape was placed between the ground connection of the BCN connector and the screen of the cable to prevent conduction between the two. Conductive tape was placed from the braided screen of the cable covering most of the isolation layer to increase the screen cover.

4.3.4 Trance Conduction Amplifier

4.3.4.1 Amplification

To increase the resolution of the Measurement System it was deliberated to progress from a passive system in the first iteration to an active system. This was accomplished through the introduction of an amplification system, which incorporated an amplifier and filter.

The demands from the amplification system include a bandwidth of about 10 MHz that will provide reasonable amplification up to 1 MHz, a filtration system and the ability to accept a differential input.

To meet these demands a Wideband Transconductance amplifier was chosen, which incorporated an easy to implement filtering system and a high bandwidth.

The specific Wideband Transconductance amplifier IC selected was the Maxim MAX436, which achieves a bandwidth of 200 MHz and a slew rate of 850 V/ μ s (See the Data Sheet in Appendix 7.5 for all the specifications).

The high input impedance of the MAX436 also proved advantageous as this would ensure a very low current was flowing through the Flux Density Sensor, minimising any negative effects.

Using the MAX436, the amplification system was constructed and fitted inside a shielded enclosure where the only conductors entering are the signal wires from the Flux Density Sensor, and the only conductors leaving the system carry the amplified and filtered signals to the oscilloscope.

External power could not be applied to the amplification system as this would provide a route for interference to enter the system, and so it was decided to use batteries to supply the required power.

The Wideband Transconductance amplifier requires positive and negative voltages of +/- 5V to operate, to realize this power requirement the batteries were connected in series with the centre connection linked to the ground of the amplification system (See Figure 4-16).

The required supply was achieved with the use of positive (7805) and negative (7905) 5V voltage regulators as shown in Figure 4-16 below.

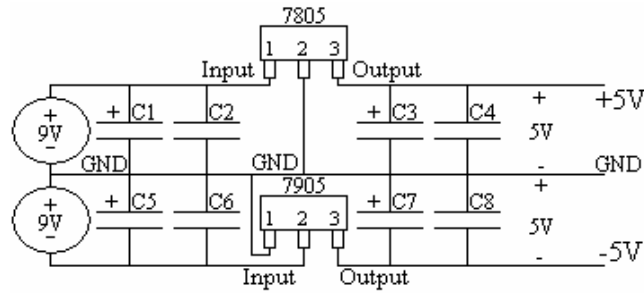


Figure 4-16 : Circuit diagram of +/- 9V to +/- 5V Voltage Regulator.

Where:

- $C1, 3, 5 \text{ \& } C7$ - $10\mu\text{F}$ Electrolytic Capacitors used for regulation to ensure a constant DC supply voltage.
- $C2, 4, 6 \text{ \& } C8$ - 220nF Polyethylene Capacitors also for regulation, and filtering for high frequency noise occurring on the DC supply.

The Wideband Transconductance amplifier was connected according to the circuit diagram shown in Figure 4-17 below and was powered using the Regulator shown in Figure 4-16 above.

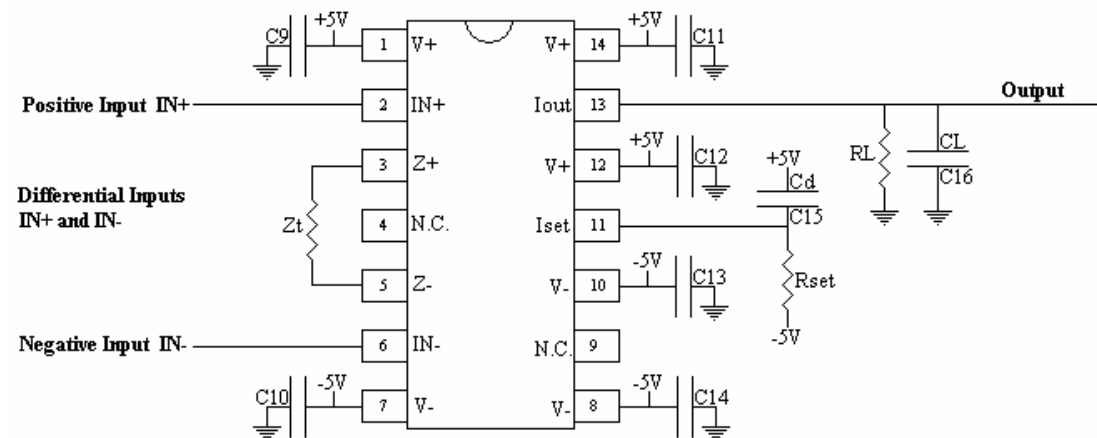


Figure 4-17: Circuit Diagram of the Wideband Transconductance amplifier.

The components shown in Figure 4-17 serve the following purpose:

- $C9 \text{ to } C14$ - Represent regulation capacitors, used to ensure a steady DC voltage at each of the IC's supply terminals, typically 220nF Polyethylene capacitors.
- $C15 \text{ \& } Rset$ - These form the current limiting circuit for the amplifier, used $5.6 \text{ K}\Omega$ and 200nF .
- Z_t - Transconductance element connected between $Z+$ and $Z-$ to set part of the gain factor and control the high

pass filter characteristics of the amplifier, chosen to be 51 Ω.

RL - The resistance at the output of the amplifier that forms another part of the gain factor.

CL - Capacitance at the output of the amplifier controlling the filtering.

The Gain equation of the Wideband Transconductance amplifier was extracted from the data sheet supplied:

$$V_{OUT} = K \left(\frac{Z_L}{Z_i} \right) \cdot V_{IN} \quad (4-2)$$

The variables in equation 4-2 represent the following:

K - The Gain factor of the Wideband Transconductance amplifier, typically 8 for the MAX436 as obtained from the data sheet.

Z_L - Load impedance at the output of the amplifier.

V_{OUT} - Output voltage of the amplifier.

V_{IN} - Input voltage of the amplifier.

RL and CL from Figure 4-17 form part of the load impedance (Z_L), which consists of the resistance introduced at the output, the input resistance of the receiving circuit at the other side of the cable, the filter capacitance introduced at the output of the amplifier and the capacitance of the cable.

For details on amplification, filtering and current limiting for the amplification system reference must be made to the MAX436 data sheet in Appendix 7.5.

The output of the amplifier was connected to the signal conductor, which leads to the measurement port of the oscilloscope, and the ground of the amplifier system was connected to the ground conductor that connects to the ground terminal on the oscilloscope.

4.3.4.2 Connection and Buffering

The Wideband Transconductance amplifier was connected along the cable between the Flux Density Sensor and oscilloscope to buffer the inductance of the Flux Density Sensor from the capacitance of the cable to increase the resonant point of the Measurement System and thus increase its frequency bandwidth.

The Wideband Transconductance amplifier was installed in a shielded enclosure with shielded chassis mounted microphone plug connectors for its input and output terminals, as shown in Figure 4-18 below.

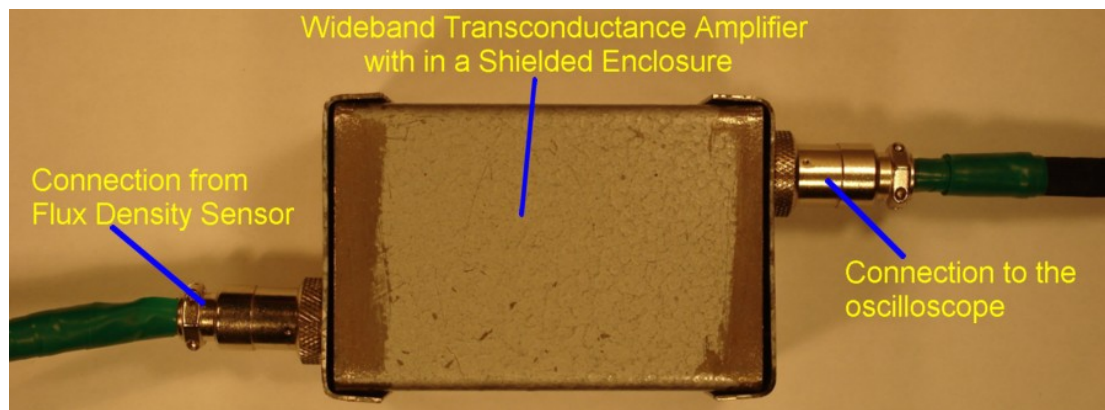


Figure 4-18: Wideband Transconductance amplifier with in a shielded enclosure, with the Flux Density Sensor connected to the input and the output connected to the remainder of the Measurement System.

4.3.5 Common Mode Chokes

Common mode chokes were introduced before the input to the oscilloscope and before the input to the amplification system to ensure only differential signals were allowed through.

The common mode choke before the oscilloscope was placed in a shielded enclosure, which was secured on to the ground plane (Section 4.3.6) with good conduction between the two.

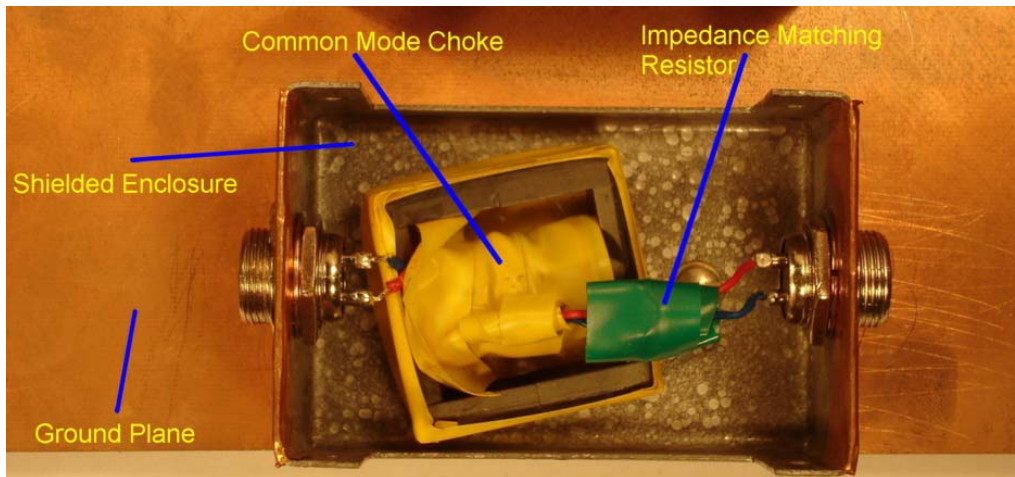


Figure 4-19: Common mode choke before the Oscilloscope with in a shielded enclosure and secured with conductive contact to the ground plane.

The common mode choke used at the input to the amplification system was encased within the shielded enclosure to protect it from external interference of the electric and magnetic fields present.

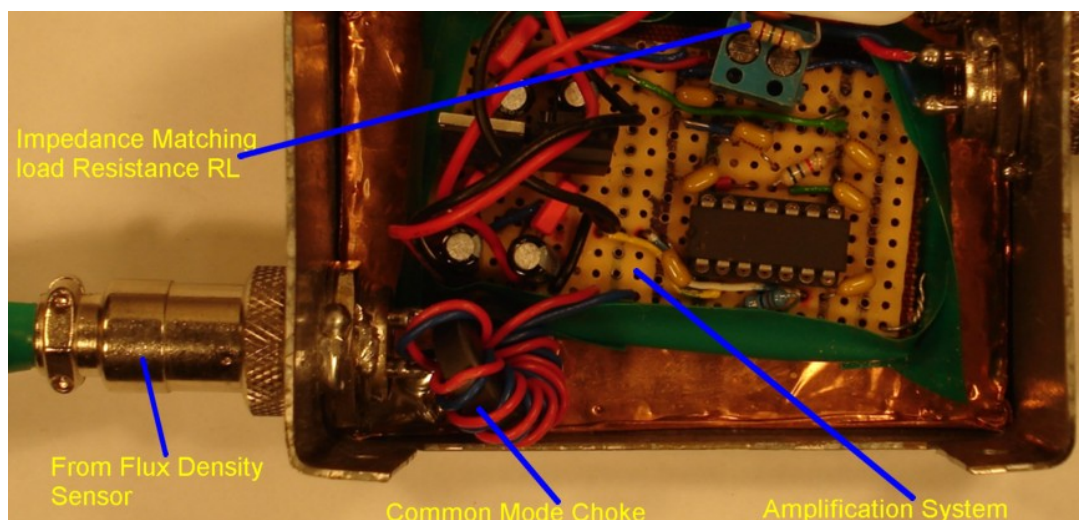


Figure 4-20: Common mode choke at input to Wideband Transconductance amplifier.

4.3.5.1 Impedance Matching

Impedance matching was performed on the cable connecting the amplifier system to the oscilloscope to obtain good signal transmission between the two. The characteristic impedance of the cable used was 150Ω so the output resistor of the amplification system (R_L in Figure 4-17 and shown installed in Figure 4-20) was set to this value. To match this impedance on the oscilloscope side a 150Ω resistor was connected across the signal and ground wires heading to the oscilloscope. This

resistance can be seen in Figure 4-19 between the common mode choke and the output microphone plug connector on the right.

4.3.6 Improved Grounding System

The grounding arrangement of the Measurement System was improved through the addition of a large copper ground plane, which provided a good ground point for the high frequency signals present on the shielding of the Measurement System, as shown in Figure 4-21 below.

This connection was made large with the oxide layer scraped off the copper plane and the copper sheet to ensure satisfactory low impedance conduction between the two, also much of the isolation layer around the outside of the shielded enclosed was removed to provide enhanced conduction to the copper sheet. The shields of the chassis mounted microphone plug connectors, at both ends of the enclosure, were tightly fastened to give it a secure press contact with the copper sheet. Solder was also added to guarantee conduction between the connector shields and the copper sheet. This was performed to ensure a low impedance passage linking the shielding of the Measurement System to the ground plane.

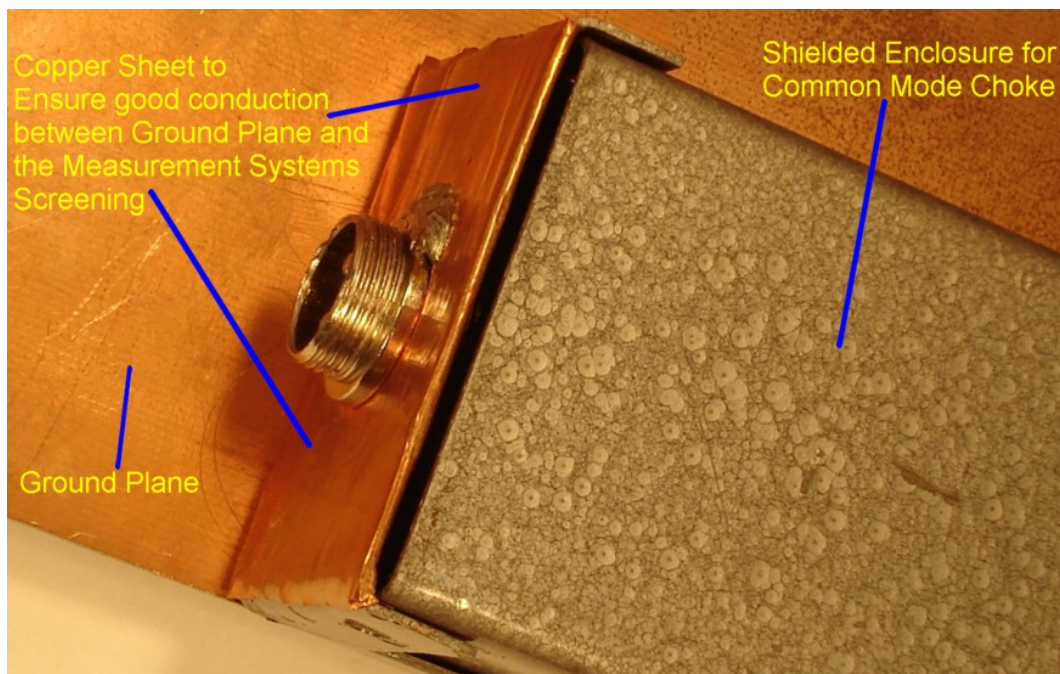


Figure 4-21: Grounding connection between the shielding system of the Measurement System to the ground plane.

To include DC and low frequency grounding on the ground plane a connection was introduced allowing it to be connected directly to the Earth connection of the mains, this connection can be seen in Figure 4-22 below.

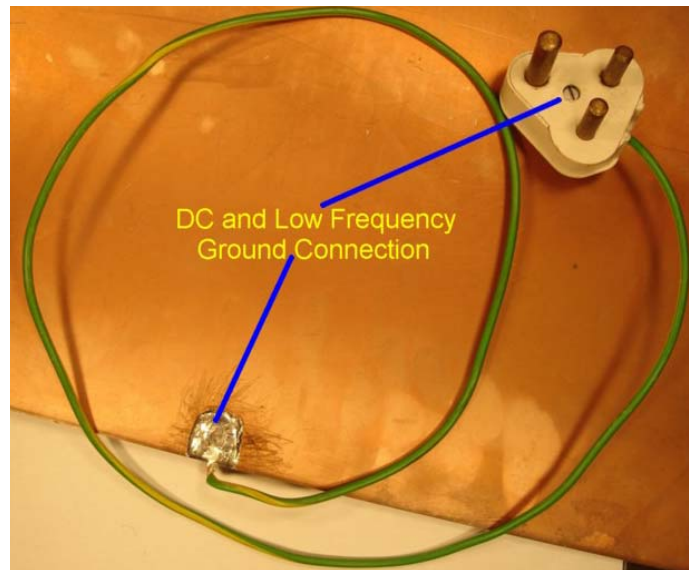


Figure 4-22: DC and low frequency ground connection.

To establish a common ground connection between the oscilloscope and the shielding of the Measurement System, braided links were constructed with a good 360° termination into a BNC connector on the one side and thick solder connection on the ground plane, as shown in Figure 4-23 below. A double braiding was used to better the conduction of this cable link.

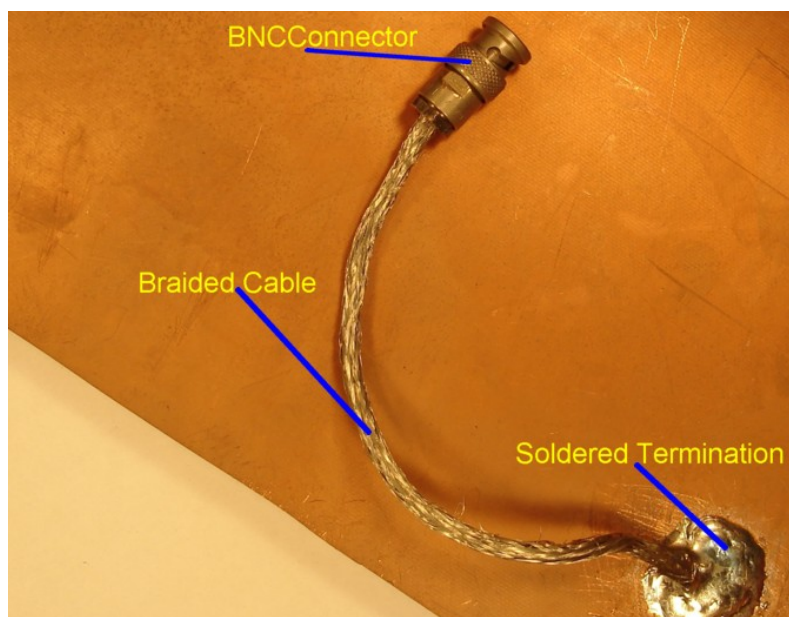


Figure 4-23: Braided connection on ground plane to link to the Oscilloscope's ground.

4.4 New Flux Density Sensor Coil

To further improve the Measurement System, a reconstruction of the Flux Density Sensor coil was necessary to reduce its self-capacitance, thus increasing its resonant point and effectively its potential bandwidth.

To achieve this goal the number of turns on the Flux Density Sensor coil were reduced in stages and tested to determine the frequency of the new resonant point. To perform the test for each coil the setup used for the calibration (Section 4.5) was employed as it allowed a frequency sweep of the first portion of the Measurement System, which included the Flux Density Sensor, the first section of composite cabling and the amplification/buffering system, known as the Calibration Measurement System.

From the results of this test it was determined that a 200turn coil using 0.4 mm diameter copper wire would achieve the desired bandwidth of 300 kHz to 1MHz. To perform this test a network analyser was utilized, which provided the signal used to generate the magnetic field, and then measured the output from the test setup. The result obtained can be seen in Figure 4-24 below.

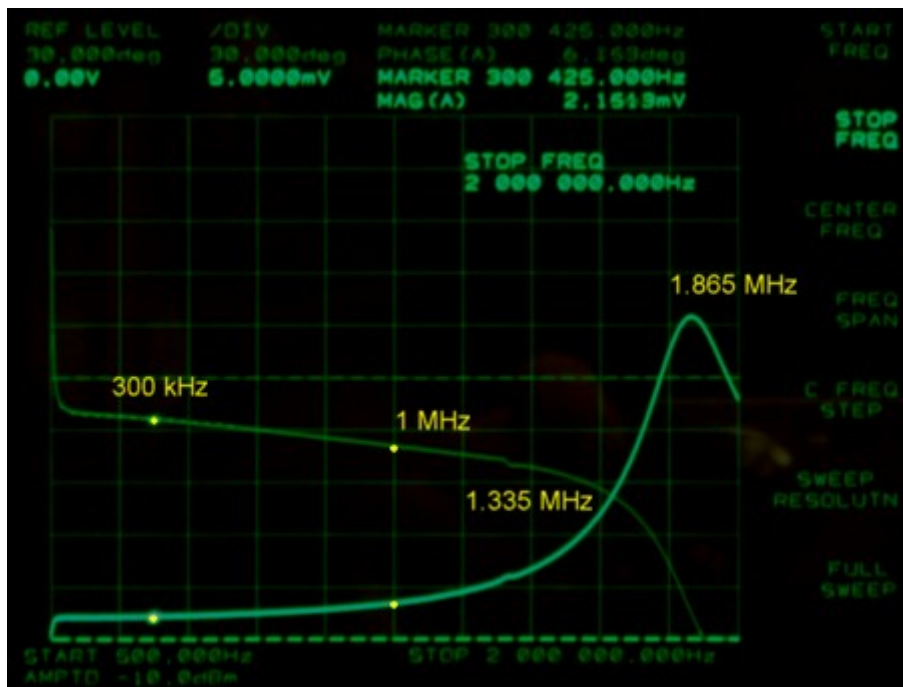


Figure 4-24: Display on the Network Analyser for the tests on the 200 turn Flux Density Sensor coil.

From Figure 4-24 it can be seen that the desired frequency range from 300 kHz to 1 MHz is reasonably linear with the first irregularity occurring at 1.335 MHz and the main resonant point occurring at 1.865 MHz, which meets the bandwidth required for the Measurement System.

The main motivation accompanying the choice in the thickness of the copper wire used for the coil was to strengthen the coil and prevent the wire from easily breaking when the Flux Density Sensor coil was moved during the experimental tests.

4.5 Calibration

4.5.1 Apparatus

The apparatus used to perform the calibration included the following:

- *Network Analyser*
- *Solenoid*
- *Calibration Measurement System*
 - *Amplification System, which includes the Wideband Transconductance amplifier*
 - *Cabling connecting to the Flux Density Sensor*
- *Finally the Flux Density Sensor to be Calibrated*

The Network Analyser used was the “Hewlett Packard 3577B 5 Hz to 200 MHz Network Analyser”, which consists of one output for inputting the driving signal to the solenoid of the calibration system and two input ports to measure the signal entering the solenoid and the signal leaving the Calibration Measurement System.

The Solenoid was constructed to generate a constant flux density within it allowing the Flux Density Sensor to be placed in this field inevitably determining the quantity of the field that it detects.

The solenoid was constructed using a cardboard tube with a length of 722mm and diameter of 45mm to ensure that its length is more than 10 times its diameter, this permitting a uniform flux density distribution within it. [2]

The Calibration Measurement System consists of the first portion of the final Measurement System, which includes the Flux Density Sensor, the amplification system and the cabling connecting the two.

4.5.2 Calibration Setup

The calibration setup used to determine the calibration constants for the Measurement System is shown in Figure 4-25 below.

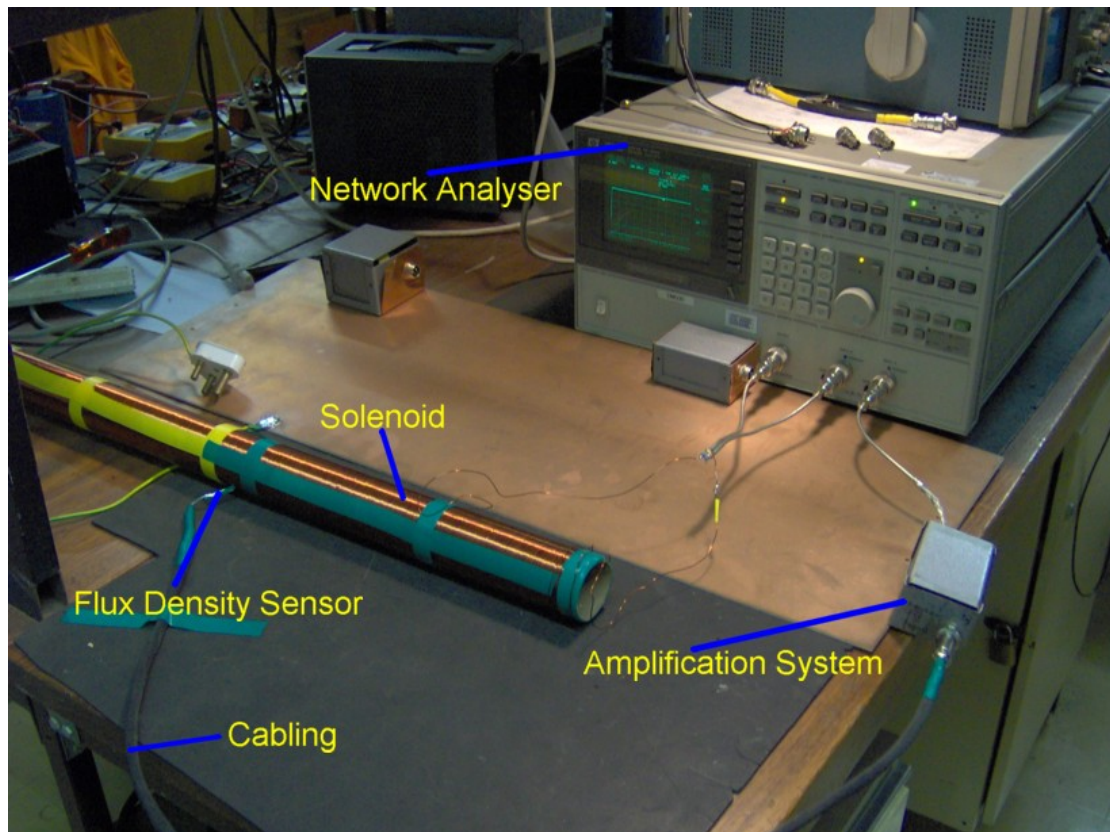


Figure 4-25: The Calibration Setup used to determine the calibration coefficients for the Measurement System.

From Figure 4-25 the Flux Density Sensor is enclosed within the centre of the solenoid, a position indicative of where the flux density is the most uniform. The length of the solenoid was chosen to be much longer (722mm) than its diameter (46mm), at least 10 times or more to give a uniform flux density distribution within the solenoid.

Its diameter was chosen, and deemed sufficient, to ensure that the Flux Density Sensor would not be situated anywhere near the sides of the solenoid, keeping it within the region of uniform flux density distribution.

The solenoid was driven by the output of the network analyser with a sweeping frequency from 50 Hz to 2 MHz to determine the bandwidth of the Measurement System and perform the calibration at the four principle frequencies of 300, 600, 800 kHz and 1 MHz.

This driving signal is measured by the first measurement port (Input R), with the output of the calibration system (output of the Amplification System) being recorded by the second measurement port (Input A), the positions of these ports are clarified in Figure 4-26.

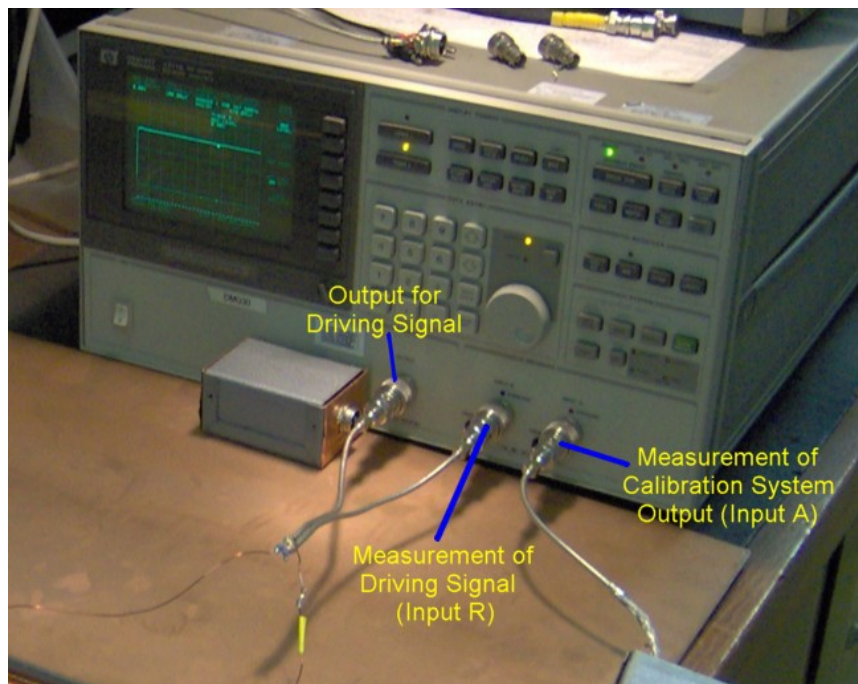


Figure 4-26: Ports on the Network Analyser for use with the Calibration System.

To ensure that the maximum amount of current flows through the solenoid, effectively generating the highest magnetic field strength within it, Input R used for the driving signal (Centre port in Figure 4-26) was connected to the Output driving port through a 10 K Ω resistor. The introduction of the resistor diminishes the voltage across the measurement port but nonetheless kept it high enough to be easily measured by the network analyser.

The output impedance of the amplification system was set to 50 Ω so as to correlate with the input impedance of the network analyser, with all the grounds of the Calibration System linked and connected to the copper ground plane. This ensured a good ground level and shielding of the Flux Density Sensor, the Amplification System and the cabling.

4.5.3 Model of the Calibration System

An electrical model for the Calibration System, shown in Figure 4-25, was constructed allowing the mathematical model for the system to be setup. From this mathematical model the calibration constant can be determined allowing any unknown parameters to be taken into account.

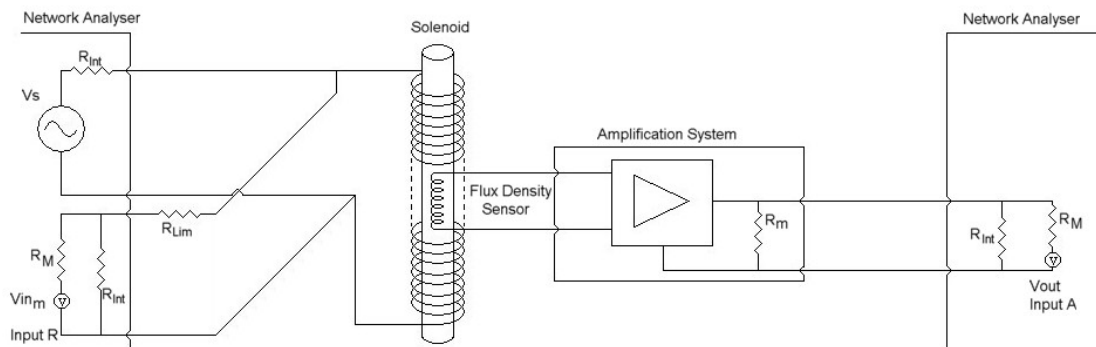


Figure 4-27: Circuit Diagram for the electrical model of the Calibration System.

Figure 4-27 depicts the circuit diagram for the Calibration System pronouncing the connections between the network analyser and the solenoid (on the left), and between the Flux Density Sensor, amplification system and the network analyser (on the right). The variables in Figure 4-27 have the following purpose and values:

- | | | |
|-----------|---|--|
| R_{Int} | - | 50Ω Internal Resistances of the Network Analyser. |
| R_M | - | Internal Resistance before the measurement point within the Network Analyser, with a value of $1M\Omega$. |
| R_{Lim} | - | Limiting resistor of value $10.4 K\Omega$ before Measurement Input, which limits the current flowing through the Input, maximising the current through the Solenoid increasing the magnetic field generated within it. |
| R_m | - | Load resistor output of the Amplification System chosen to match the Network Analyser's input impedance. |
| V_{inm} | - | Measured Source Voltage at Input R. |
| V_{out} | - | Measured output Voltage at Input A. |

Measurement Input R quantifies the signal being sent to the solenoid by the Network Analyser, where measurement Input A records the output from the Amplification System. The solenoid performs the task of generating the B-field to be picked up by the Flux Density Sensor. Once the measurements have been performed the only known voltages are the source measurement at Input R (V_{in_m}) and the measured output from the Amplification System (V_{out}) at Input A, consequently the actual

source voltage is unknown. In order to circumvent this enigma and subsequently determine the calibration constant, equations must be established which have no dependence on the unknown source.

A dichotomous approach was enlisted so as to find the calibration constant by stratifying the calibration system into two sections. The first division defines the B-field generating portion (left of Figure 4-27) consisting of the solenoid and its power source and measurement point (Input R), and the second comprises the B-field pick-up portion (right of Figure 4-27) consisting of the Flux Density Sensor, amplification system and the output measurement point (Input A).

For the first section the current through the solenoid was required to determine the B-field flowing through its centre. To find this current, the voltage across the solenoid has to be determined from the measured voltage at Input R.

To determine the voltage across the solenoid, the current flowing through measurement Input R (i_m) was preliminarily required and obtained from the following:

$$i_m = \frac{Vin_m}{R_{Int}} = \frac{Vin_m}{50\Omega} \quad (4-3)$$

Through the use of equation 4-3 and the limiting resistance, the voltage across the solenoid (V_L) was determined with the use of equation 4-4 below:

$$V_L = Vin_m \cdot \left(1 + \frac{R_{Lim}}{R_{Int}}\right) \quad (4-4)$$

The current flowing through the solenoid was determined using Ohms law, with the layout expressed in equation 4-5 below,

$$i_\phi = \frac{V_L}{Z_L} \quad (4-5)$$

Where:

- i_ϕ - *Current flowing through the Solenoid*
- Z_L - *Impedance of the Solenoid*

The equation governing the flux density through the solenoid that links to the current flowing through it follows in equation 4-6. [2]

$$B_S = \frac{\mu_0 \cdot N_S \cdot i_\phi}{L} \quad (4-6)$$

Where:

- B_S - Flux Density in Tesla (T), generated within the Solenoid.
- μ_0 - Permeability of free space, with a value of $4\pi \times 10^{-7}$ H/m.
- N_S - Number of wire turns around the Solenoid (871).
- L - Length of the Solenoid in meters (m).

From the use of equations 4-3 to 4-6 the final equation linking the measured voltage at Input R (V_{in_m}) to the flux density (B_S) generated within the solenoid culminates in equation 4-7 below:

$$B_S = \frac{\mu_0 \cdot N_S \cdot \left(1 + \frac{R_{Lim}}{R_{Int}}\right)}{L \cdot Z_L} \cdot V_{in_m} \quad (4-7)$$

For the second portion of the calibration system, a link between the flux density measured by the Flux Density Sensor and the voltage measured at Input A (V_{out}) is mandatory. To achieve this link the relationship for the Flux Density Sensor relating the measures flux density to the voltage across the coil was used. This relationship was derived in section 2.2.2.1.1 on page 18 and is reiterated below in equation 4-8.

$$B_0 = \frac{2}{N\pi^2 d^2 f} e_0 \quad (4-8)$$

Where:

- B_0 - Magnitude of magnetic flux density
- N - Number of turns chosen for the Flux Density Sensor (200)
- d - Diameter of wood rod, 4mm (gap in the centre of the coil)
- f - Frequency of magnetic field being measured
- e_0 - Magnitude of voltage across the sensor coil

Due to the high impedance at the input to the Amplification System, as a consequence of the Wideband Transconductance amplifier, the current flowing through the Flux Density Sensor will be in the range of a couple of micro amps. This minute current has little effect on the Flux Density Sensor and was neglected allowing the voltage across the coil to connect directly to the input of the Amplification System.

The input and output voltage of the amplification system relates to equation 4-9, which incorporates its output impedance and the input resistance of the network analyser.

$$V_{out} = K \cdot \frac{Z_{TCL}}{Z_i} \cdot e_0 = G \cdot e_0 \quad (4-9)$$

Where:

- V_{out} - Output voltage from the Amplification System being measured by Input A of the Network Analyser.
- K - Gain factor of 8 from the Wideband Transconductance Amplifier used in the Amplification System.
- Z_{TCL} - Output impedance of the Amplification System, including the output impedance of the Amplifier, the output impedance matching resistance, the input resistance of the Network Analyser and the filter capacitance of the Amplification System.
- Z_i - Transconductance impedance as defined in section 4.3.4, with a value of 50Ω .
- G - Total gain of the Amplification System.

To determine Z_{TCL} all impedances between the output of the Wideband Transconductance Amplifier and the network analyser input were linked in a parallel combination as shown in equation 4-10 below.

$$\frac{1}{Z_{TCL}} = \frac{1}{3.3K\Omega} + \frac{1}{R_m} + \frac{1}{Z_C} + \frac{1}{R_{int}} \quad (4-10)$$

Where:

- $3.3K\Omega$ - The output resistance of the Wideband Transconductance Amplifier.
- Z_C - Impedance of the filter capacitance used at the output of the Amplification System.

As common to all capacitors, the filter capacitors' impedance decreases with an increase in frequency which results in a decrease in Z_{TCL} and thus a decrease in the overall gain of the Amplification System.

When a higher frequency noise signal occurs with the measured signal, it will be subjected to a reduced gain compared to the measured signal and its significance will be reduced. The greater the frequency differences between the noise and measured signals the greater the difference in the gain experienced by each.

For the calibration process a value of 1nF was chosen for the filter capacitor at the output of the Amplification System, and the impedance and inductance of the solenoid at 300 kHz was determined to be 4.54K Ω and 2.409mH respectively.

The final equation for the second portion was obtained by linking equations 4-8 and 4-9, can be seen in equation 4-11 below.

$$B_0 = \frac{2}{N \cdot \pi^2 \cdot d^2 \cdot f} \cdot \frac{1}{k} \cdot \left(\frac{Z_t}{Z_{TCL}} \right) \cdot V_{out} = \frac{2}{G \cdot N \cdot \pi^2 \cdot d^2 \cdot f} \cdot V_{out} \quad (4-11)$$

Using equations 4-9 and 4-10 the impedance and the gain for the Amplification System for the principle frequencies were obtained and are displayed in Table 4-1 below.

Table 4-1: Load Impedance and Gain for the Amplification System for the Calibration Setup.

Frequency f	Load Impedance Z_{TCL}	Gain G	Gain in dB G (dB)
300 kHz	23.70 Ω	3.79	11.58
600 kHz	22.69 Ω	3.63	11.20
800 kHz	22.06 Ω	3.53	10.95
1 MHz	21.47 Ω	3.43	10.72

Finally to determine the calibration factor the flux density generated by the solenoid was compared to the flux density measured by the Flux Density Sensor with the use of equation 4-12 below.

$$\alpha = \frac{B_s}{B_0} \quad (4-12)$$

The impedance of the Solenoid at the principle frequencies was determined through the use of a “Hewlett Packard Precision LCR Meter”, and can be seen in Table 4-2.

Table 4-2: Impedance of the Solenoid at the Different Principle Frequencies.

Frequency f	Impedance Z_L	Phase	Resistance	Inductance
300 kHz	4.54 K Ω	89.63 $^\circ$	29 Ω	2.409 mH
600 kHz	9.62 K Ω	89.60 $^\circ$	67 Ω	2.551 mH
800 kHz	13.70 K Ω	89.54 $^\circ$	109 Ω	2.727 mH
1 MHz	18.76 K Ω	89.4 $^\circ$	176 Ω	2.986 mH

By use of the Calibration System the Measured voltages were obtained at the principle frequencies and are given below in Table 4-3.

Table 4-3: Measured Voltages from the Calibration System.

Frequency F	Source Measurement V_{in_m}	Output of the Amplification System V_{out}
300 kHz	686.91 μ V	2.1493 mV
600 kHz	691.00 μ V	2.4479 mV
800 kHz	693.44 μ V	2.8244 mV
1 MHz	690.80 μ V	3.4414 mV

Through the use of equations 4-12, 4-11 and 4-7 with Table 4-1 and Table 4-2 and with the aid of Matlab the calibration Coefficients for the principle frequency were found and are given in Table 4-4 below.

Table 4-4: Calibration Coefficients for the Principle Frequencies.

Frequency F	Calibration Coefficient A
300 kHz	0.3867
600 kHz	0.3087
800 kHz	0.2445
1 MHz	0.1773

See Matlab Code in Appendix 6.1 for the mathematical solution to the Calibration System.

5 Experimental Results for 2A 300 kHz High Frequency Tests

5.1 Introduction

Before the experimental results could be attained final adjustments were made to ensure reasonable repeatability.

These adjustments included securing the rest rig to the proximity sensor platform and railway track, preventing it from moving thus making sure that each repeated measurement would be in the same physical space as the previous, and that all consecutive measurement would occur in the same plane.

The railway track system now included the high frequency traction current source with connections across the railway track. To monitor this system, two oscilloscopes with voltage probes, as well as current amplifiers with their probes were used. The voltage probes were utilized to monitor the resonant voltage across the railway track and between the resonant capacitors. The current probes allowed the observation of the traction current generated within the railway track and the quantity of current diverted into the parallel connected cables during the cable tests.

Preparation of the Measurement System consisted of placing the Flux Density Sensor in the starting position on the test rig ready to follow the measurement procedure. The end of the Measurement System includes a signal conductor link to the Oscilloscope with a shield link to the high frequency ground plane removing interference to reduce its effect on the measurements.

Once the results were obtained a comparison was performed between them to determine the affects of the shield and cabling on the magnetic field in the sensing region of the proximity sensor with the overarching goal revolving about the determination of the optimal method of reducing the interference experienced by the proximity sensor.

5.2 Preparation

5.2.1 Test Rig

Ensuring that the test rig was perpendicular to the lengths of both the proximity sensor platform and the railway track guaranteed that the true X and Y components of the flux density were being measured by the Measurement System.

Securing the test rig was a paramount phase since any slight shift of the test rig would result in a measurement being performed at a different position and a different angle with the damaging outcome of the measurements not correlating with the measurement grid used for the experiment. To secure the test rig on the proximity sensor platform and railway track the used of double sided tape was employed as it would hold the test rig in place, preventing any movement.

5.2.2 Railway Track System

The designed and constructed high frequency traction current source was connected to the system allowing the execution of the high frequency test by producing the required high frequency current needed to generate the high frequency Electro Magnetic interference experienced by the proximity sensor in the field.

To monitor the operation of the high frequency traction current source, voltage and current probes were put in place. These connections are described in Figure 5-1.

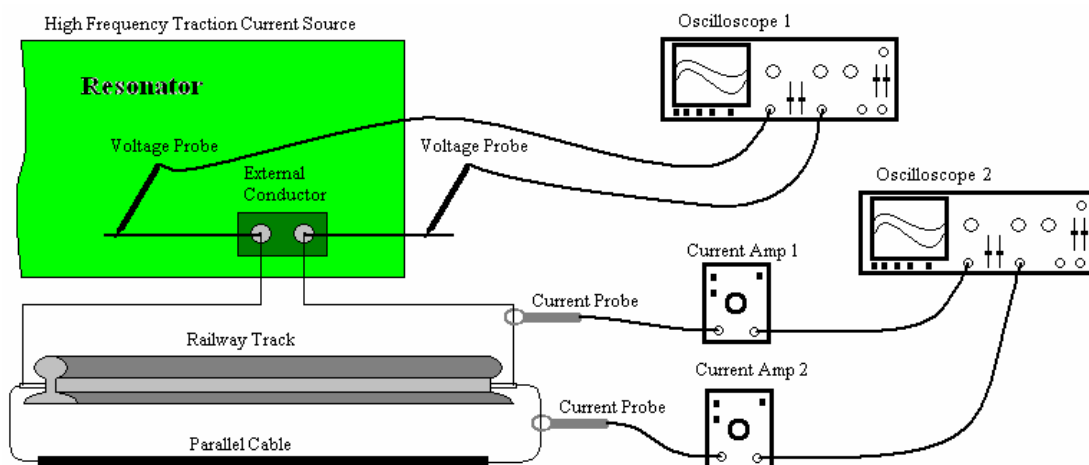


Figure 5-1: Railway Track System's Probe Connections to Monitor Resonant Voltages and Currents.

For the 300 kHz high frequency test considered in this investigation the resonant current must be maintained at 2 A peak, resulting in a resonant voltage between the capacitor banks of 135 V.

The second current amplifier (Current Amp 2 in Figure 5-1) along with its probe was only connected to the system after the initial three tests of the first test set were performed, as they did not involve the addition of a parallel cable. The initial test set included measurements for the unaltered state (base), introduction of a shield on the proximity sensor platform and finally the inclusion of an isolation layer between the shield and the platform. For the subsequent three test sets that involve the inclusion of the three different parallel cables the current amplifier and probe were connected as depicted in Figure 5-1.

5.2.3 Measurement System

An electrical model for the final Measurement System, see Figure 5-2 below, was constructed permitting the mathematical model of the system to be derived. From this mathematical model the voltages measured on the oscilloscope can be converted to equivalent values in Tesla, representing the flux density in the test area.

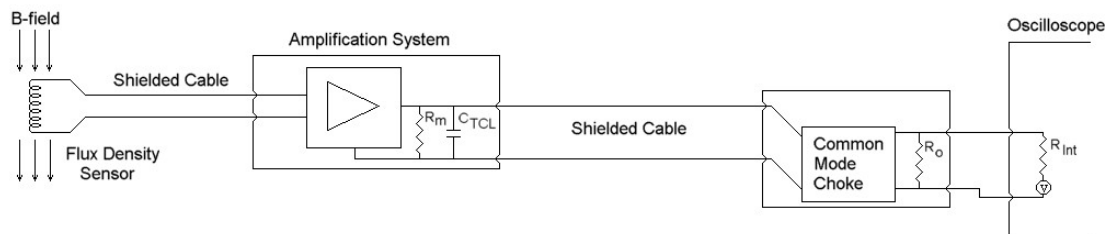


Figure 5-2: Circuit Diagram for the electrical model of the final Measurement System.

Figure 5-2 illustrates the circuit diagram for the final Measurement System used to attain the measured results for the high frequency tests, including the links between the Flux Density Sensor and the Amplification System, Common Mode Choke enclosure and finally the oscilloscope.

The variables in Figure 5-2 have the following purpose and values:

- R_m - Load Resistor output from the Amplification System, which was given a value of 150 Ω to match the characteristic impedance of the shielded cable connecting to the common mode choke enclosure.

- C_{TCL} - Filter Capacitor given a value of 5 nF to ensure good filtering of frequencies above 300 kHz.
- R_o - Impedance matching resistance at the opposite end of the Measurement System next to the oscilloscope to ensure good signal transmission across the three meter shielded cable connecting the Amplification System to the common mode choke enclosure.
- R_{Int} - Internal Impedance of the oscilloscope, which has a value of 1 M Ω .

By combining equation 4-8, which provides an association between the flux density measured by the Flux Density Sensor coil to the voltage produced across it, and equation 4-9, which relates the input and output of the Amplification System, equation 5-1 (below) was derived and forms the link between the voltage magnitude read off the oscilloscope to the flux density present in the test area.

$$B_0 = \frac{2}{G \cdot N \cdot \pi^2 \cdot d^2 \cdot f} \cdot V_{OSC} \quad (5-1)$$

Where

- V_{OSC} - Voltage Magnitude measured off the Oscilloscope.

A modification of equation 4-10 (equation 5-2) was sought as it provides a solution to the total output impedance seen by the Amplification System due to the load resistor, filter capacitor, impedance matching resistor, output resistance of Wideband Transconductance amplifier and the input impedance of the Oscilloscope.

$$\frac{1}{Z_{TCL}} = \frac{1}{3.3K\Omega} + \frac{1}{R_m} + \frac{1}{Z_C} + \frac{1}{R_{Int}} + \frac{1}{R_o} \quad (5-2)$$

Due to the high input impedance of the oscilloscope (R_{Int}) its internal impedance was neglected as it would have little effect on the impedance seen by the Amplification System.

The Table 5-1 below gives the gain of the Amplification System for the different principle frequencies, maintaining a constant filter capacitor, resulting in a reduction in gain for the higher frequency signals.

Table 5-1: Total output Impedance of the Amplification System and its accompanying Gain.

Frequency f	Output Impedance Z_{TCL}	Gain G	Gain in dB G (dB)
300 kHz	43.36	6.94	16.82
600 kHz	30.78	4.93	13.85
800 kHz	25.79	4.13	12.31
1 MHz	22.20	3.55	11.01

Note that when measurements are performed at frequencies above 300 kHz a lower valued filter capacitor should be made use of to increase the gain of that signal.

Through the use of equation 5-1 the measured voltages from the oscilloscope can be converted to equivalent quantities in Tesla revealing the flux density pattern occupying the test area for each different test setup to be performed.

Using equations 5-1, 5-2 and 4-9 Matlab Code (shown in Appendix 6.2) was created to convert the measured results to Tesla, apply the calibration coefficient and finally displaying the flux density distribution in the form of contour plots.

5.3 Experimental Results

5.3.1 Tests to be performed

Section 1.5.1.2 in chapter 1 describes the high frequency tests that were needed to determine the effect on the magnetic field within the test area due to their requirements.

The initial step for the first test set involves mapping the magnetic flux density in the test area for the unaltered state thereby obtaining the base measurement representative of the magnetic field present in this region for the real life situation. The subsequent step requires the placement of a mild steel shield on top of the proximity sensor platform between the test area and the railway track, as shown in Figure 5-3 below. The final step for the initial test entailed the insertion of isolation material between the shield and the proximity sensor platform to reduce conduction between them; this can once more be seen in Figure 5-3.

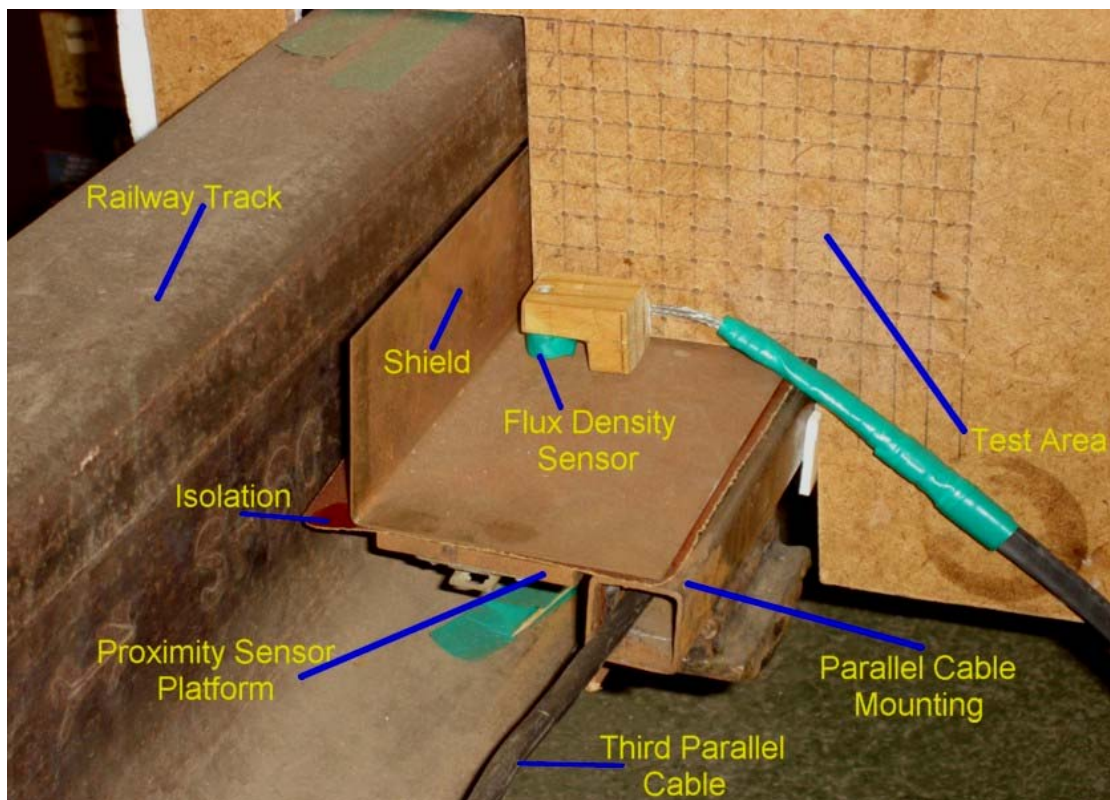


Figure 5-3: Final test setup used for the 2A 300 kHz high frequency tests, showing the shield position, isolation, parallel cable mounting and positioning all relative to the railway track and the proximity sensor platform.

The subsequent test sets involved the inclusion of one of three parallel cables for each set, where one of the cables was placed parallel to the railway track and proximity sensor platform within the cable mounting shown in Figure 5-3. Each test performed for the first test set was repeated for each of the three cables to obtain comparative contour maps of the flux density in the test area allowing the effects of differences between each test setup to be observed.

The three cables provided for use in the parallel cable test sets have the following given and determined properties.

- *The first cable tested permitted a peak current of 0.22 A to flow through it at the test frequency of 300 kHz, and a given approximate copper area of 75 mm² and diameter of 9.5mm.*
- *The Second cable tested allowed a peak current of 0.2 A through it at the test frequency and a given approximate copper area of 50 mm² and diameter of 8.25mm.*
- *The third and final cable tested allowed a peak current of 0.16 A to flow and it was given that it had the lowest copper area of 16 mm² and diameter of 5.5mm.*

Other properties of the cables were unknown such as the number of threads in each cable and the diameter of each tread.

5.3.2 Measurement Technique and Results Presentation

To perform the measurements the measurement technique portrayed in section 1.5.3.2 on page 14 was employed, which yielded in the attainment of all the results necessary for the analysis to be performed in the subsequent sections.

The results obtained from the tests were depicted in the form of contour plots so as to provide a clear description of the distribution of the magnetic field within the test area and to allow an easy comparison between the different test cases. The axes used for the contour plots coincide with the numbering used for the XY grid on the test rig (Figure 2-4 and Figure 2-5 on pages 21 and 22). A further description of the grid layout and axes numbering used can be found in section 1.5.3.1 with a depicted description given in Figure 1-5 on page 13.

5.3.3 First Test: Base Measurement

The first test was performed with no shield in place and no parallel cable attached, this giving a Base measurement of the flux density distribution showing the unaltered state of the magnetic interference present within the test area, so as to give a point of reference for observing the effects of the different modifications to be tested.

Only the vertical (Y) component of the measured magnetic flux density is reviewed in the subsequent sections as it was purported that this component posed a more significant threat to the operation of the proximity sensor. Furthermore it is a reduction in this vertical field that would ultimately have a more substantial impact on sensor efficacy. The horizontal and combined results are available in Appendix 4.2 for the full description of the flux density distribution present in the test area.

Contour plot of the magnetic flux densities of the Y component in μT at 300 kHz

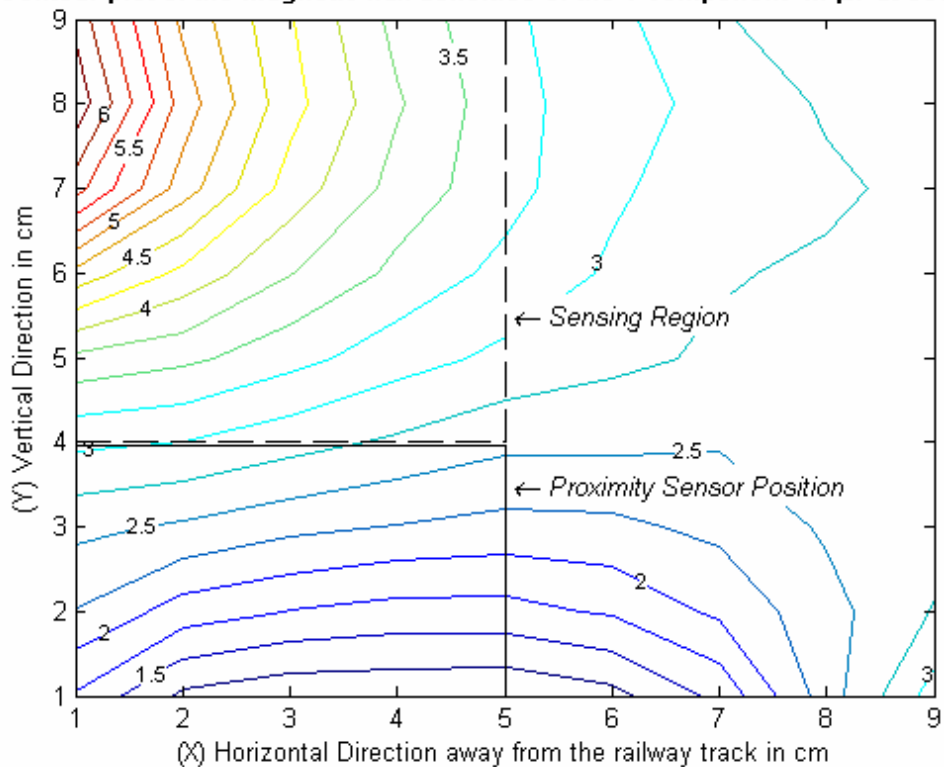


Figure 5-4: Contour Plot of the Y component of the magnetic flux density for the base measurement with no shield, cable and isolation.

The resultant vertical (Y component) flux density distribution obtained from this initial test is depicted in Figure 5-4 above, indicating all effects of the surrounding structures.

The highest vertical flux density in the test area occurs in the top left corner of the test area as the top of the railway track is situated just to the left of this region. The occurrence of this signifies that the flux density close to the railway track would be of a greater intensity than in any area further away from the railway track. This is true since the traction current responsible for the magnetic field present within the test area does flow through the railway track. An additional observation of the flux density distribution results in the determination that the further away from the railway track the flux density is observed, the lower its intensity will be.

The region of lowest magnetic field intensity was determined to be situated at the bottom of Figure 5-4, below 3 on the Y axis and between 1 and 8 on the x axis. This region of low magnetic field intensity occurs due to the fact that it lies just above the proximity sensor platform. Since the proximity sensor platform was constructed from iron, which is a magnetic material, it provided a lower impedance path for the magnetic field to flow through yielding the resultant lower intensity region above it.

5.3.4 Second test: Shield Measurement with No Cable or Isolation

This test was performed through the inclusion of a shield, maintaining the basic setup used to obtain the base measurement. The shield was placed on the proximity sensor platform, see Figure 5-3, with the aim of reducing the flux density within the test area.

From the test results presented in Figure 5-5 a defined transformation in the pattern shown for the base measurement can be seen. Due to the introduction of the shield, the flux density patterns have changed in the region closer to it, with an overall reduction in the magnetic field intensity.

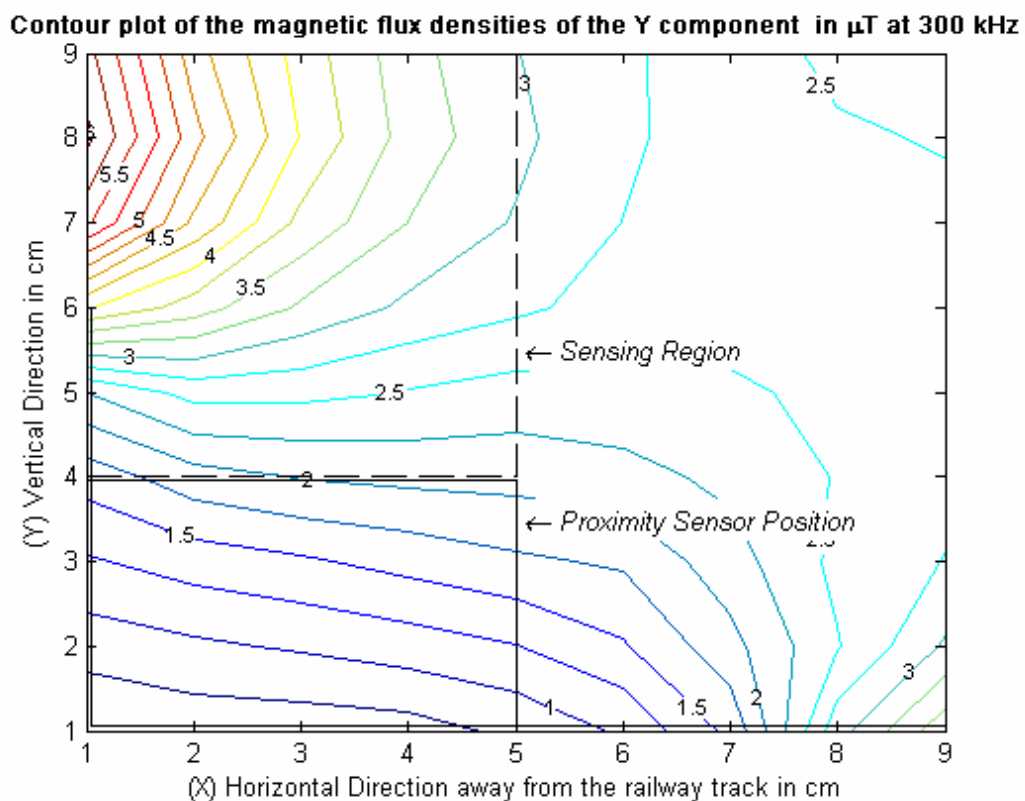


Figure 5-5: Contour Plot of the Y component of the magnetic flux density for shielded case no cable or isolation.

The shield shown to the left and bottom of the contour plot in Figure 5-5, and all subsequent plots where a shield was used, is not situated at the exact coordinates shown in the figure but in reality lies at position zero, where both the X and Y position values are zero, the actual placement of the shield can be seen in Figure 1-6, Figure 2-5 and Figure 5-3, with the vertical portion one centimetre to the left of the Y axis, and the horizontal section one centimetre below the X axis. The shield shown in the

contour plots was put in place to show the height of the shield along the Y axis (up to point 6) and its coverage along the X axis (from 0 to point 9) at the bottom.

5.3.5 Third Test: Shield Measurement with Isolation and No Cable

For the third test, isolation material was included between the shield and the proximity sensor platform. The results stemming from its introduction are shown in Figure 5-6, but little visual effect occurs when the two shielded cases (second and third test, Figure 5-5 and Figure 5-6) are compared, as the contour plots follow similar patterns. To determine the effect on the flux density due to the inclusion of the isolation layer, a direct comparison between the two data sets must be performed as to determine if the magnitudes of the flux density have changed. A comparison comprises the contrast of the magnitudes on the flux densities between the different tests along identical points within the sensing area, to determine differences in their magnitudes.

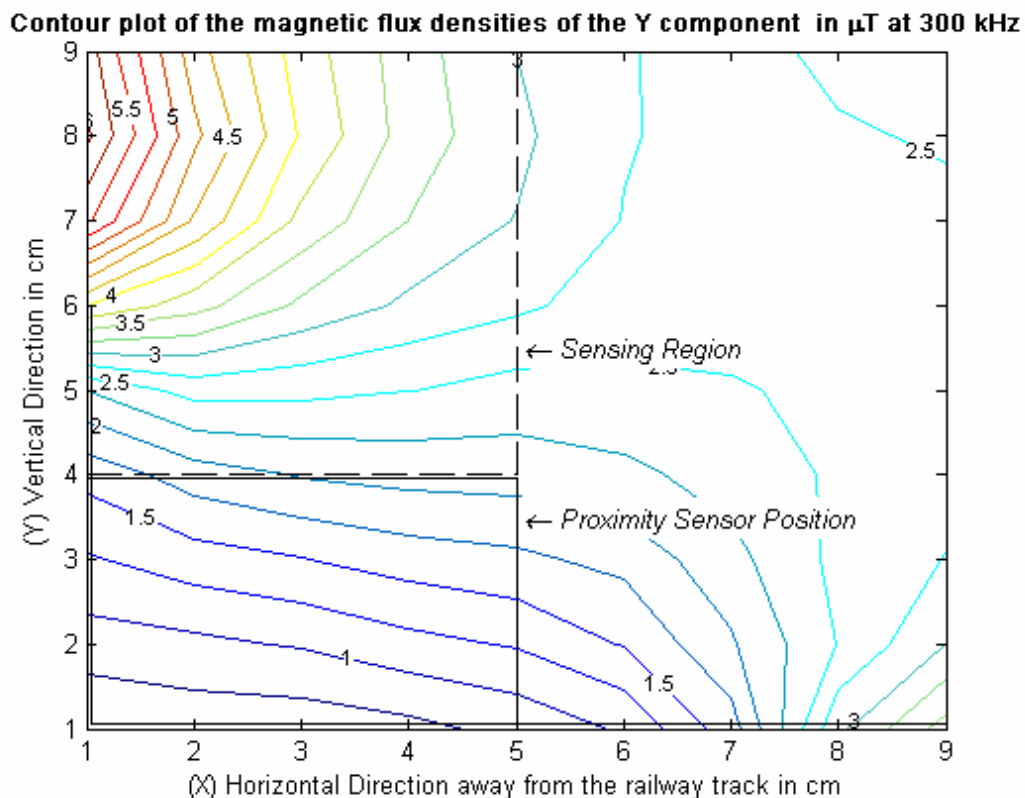


Figure 5-6: Contour Plot of the Y component of the magnetic flux density for shielded case with isolation but no cable.

5.3.6 Fourth Test: First Cable Test set (sub-base), with no shield or isolation

The fourth test included the first of the parallel cables to be tested, but does not include the shield or isolation.

The comparison between this test, Figure 5-7, and the Base Measurement shown in Figure 5-4 yields small differences between the patterns observed between the two. Firstly the magnitude of the high intensity region closer to the top of the railway track, top left in Figure 5-7, has decreased. Secondly, due to current flowing through the cable, the flux density in the region to the lower right of Figure 5-7 has increased. This region is affected as the cable is situated below points 8 and 9 on the X axis in Figure 5-7.

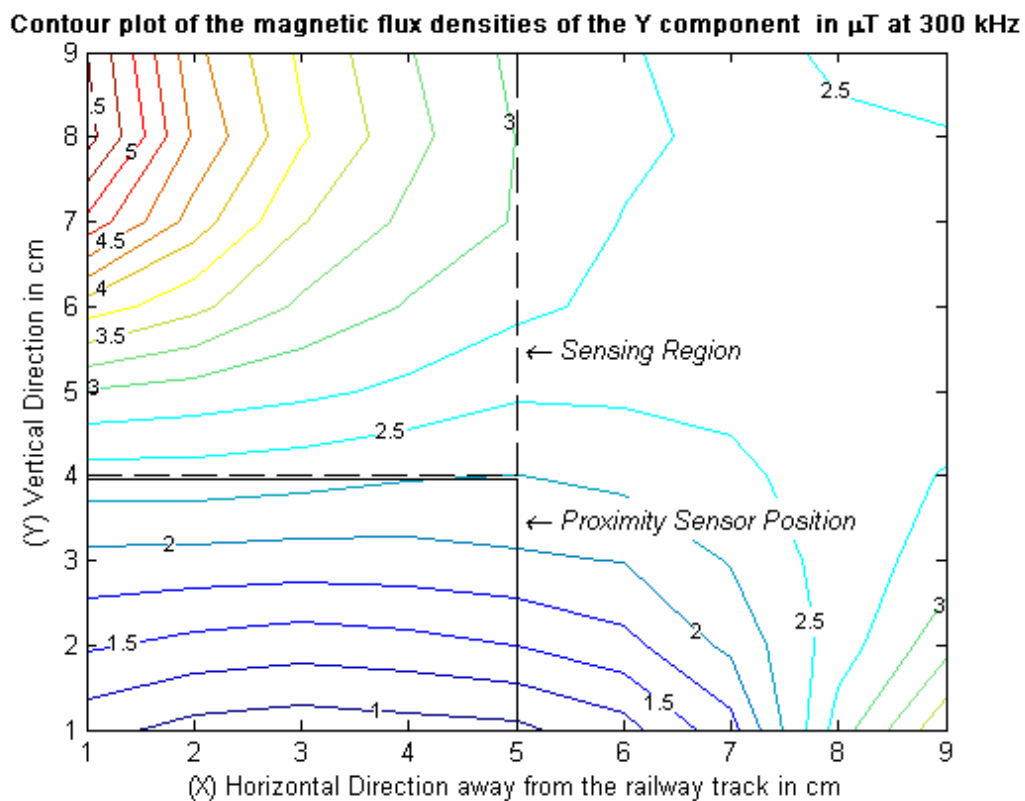


Figure 5-7: Contour Plot of the Y component of the magnetic flux density for the sub-base measurement with the first cable in place with no shield or isolation.

5.3.7 Fifth Test: First Cable Test set with the inclusion of the shield but no isolation

A shield has been included for the purpose of this test, resulting in a decrease in the flux density to the left on the test area as can be seen in Figure 5-8. This reduction occurs due to the inclusion of the shield, with coverage as shown in the figure, which deflects and absorbs a portion of the flux density usually present in the region. Compared to the Base measurement the magnitude of the flux density in the highest region, top left, has reduced due to the diversion of some current and the area to the lower right has suffered an increase in flux density.

The increase to the lower right does not have a significant effect on the proximity sensor since it is situated far away from the sensing region, but the decrease experienced in the highest region does have a significant effect in reducing the overall flux density in the sensing region and hence the interference experienced by the proximity sensor.

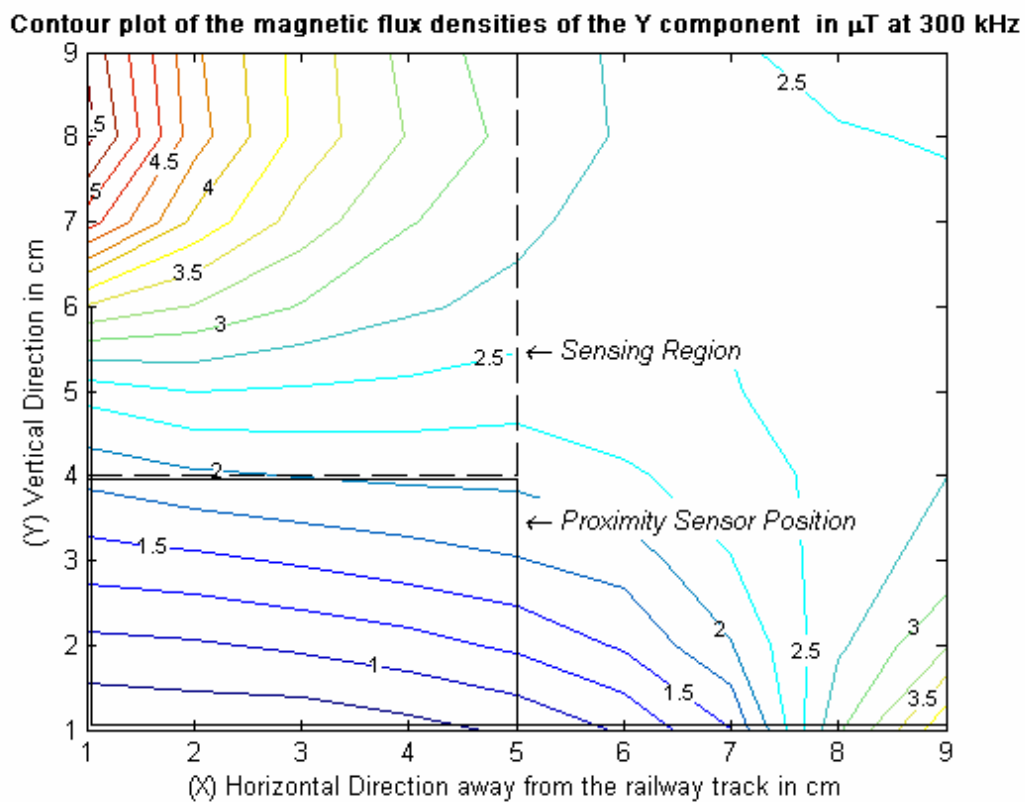


Figure 5-8: Contour Plot of the Y component of the magnetic flux density for the first cable in place with shield but no isolation.

5.3.8 Sixth Test: First Cable Test set with the inclusion of the shield and isolation

For this test, isolation material was included, sandwiched between the shield and the proximity sensor platform.

The patterns observed by comparing this test, Figure 5-9, to Figure 5-8 in test five, which lacked the isolation layer, are very similar with no distinctly noticeable changes in the pattern, except small reduction and increases in the flux density through out the test area. To determine if the effect within the sensing region was positive, a direct comparison must again be performed.

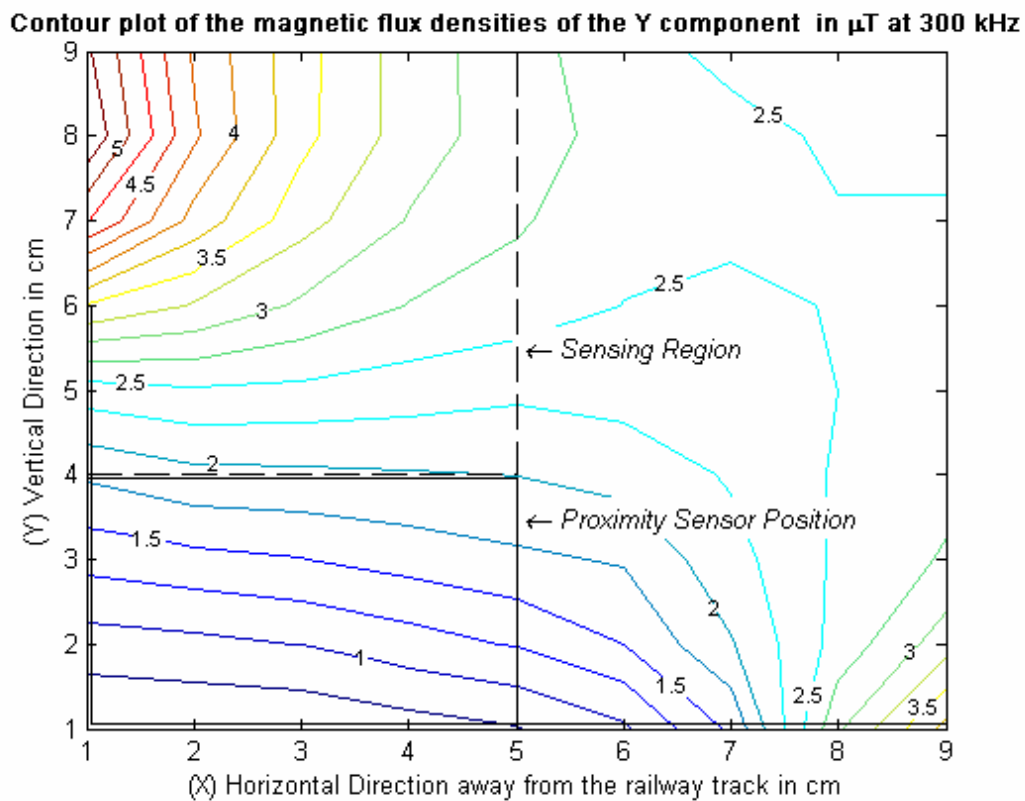


Figure 5-9: Contour Plot of the Y component of the magnetic flux density for the first cable in place with shield and isolation.

5.3.9 Subsequent Tests

The subsequent test for the second and third cables are included in Appendix 4.1, as the patterns observed are similar to those seen in the previous test. The main differences observed include changes in the flux density within the sensing region and around the test area.

In general by observing the contour plots for all the tests performed it can be deduced that, firstly, the introduction of the shield does have a positive effect in reducing the interference within the sensing region. Secondly optimistic results were obtained through the introduction of either of the three cables, since a reduction in flux density was observed within the sensing region, as compared to the Base measurement. And finally the introduction of the isolation layer provided a further reduction in the flux density within the sensing region. The greater reduction appears to occur when all three are combined, as the effect of each is additive.

To perform a more comprehensive comparison a direct comparison between the results from each dataset was performed so as to ascertain the extent of the reductions experienced within the sensing region.

5.4 Direct Comparison

To perform the direct comparison the technique detailed in section 1.5.4 on page 14 was employed, and then bar graphs were used to perform the comparison, refer to the results of the first comparison bar graph in Figure 5-10 on the next page.

A series of six bar graphs were utilized, allowing the flux density at each coordinate point within the sensing region to be displayed with its magnitude represented on the vertical (Y) axis of each graph. For each graph the X axis corresponds to the X axis displayed in all the contour plots shown and the grid layout used for the test rig. Details of how the sensing region was broken up to perform the direct comparison are shown in Figure 1-6.

Each bar graph includes points 1 to 5 on the X axis, as they fall within the sensing region, and represents a specific point on the Y axis. The first bar graph covers all the points within the sensing region (first five points along the X axis) along point four on the Y axis, as this is the first region enclosed within the sensing region. The next graph covers all the values along point five on the Y axis, and so on until finally the last set is covered comprising all the values within the sensing region along point nine on the Y axis.

Using these bar graphs the change in magnitude of the flux density at each point within the sensing region for each of the different tests can be determined. This allows the discovery of the optimum configuration that provides the greatest decrease in the Y component of the interfering magnetic field within the sensing region.

To generate the bar graphs employed for use in direct comparison, the written Matlab program outlined in Appendix 6.3 was used. The Normalized direct comparison plots generated were created by the written Matlab program described in Appendix 6.4.

5.4.1 Direct comparison for the first test set with no parallel cable

For this comparison the first, second and third tests were included, which comprise of the Base measurement, measurement including the addition of a shield on top of the proximity sensor platform and the measurement with the addition of an isolation layer between the shield and the proximity sensor platform.

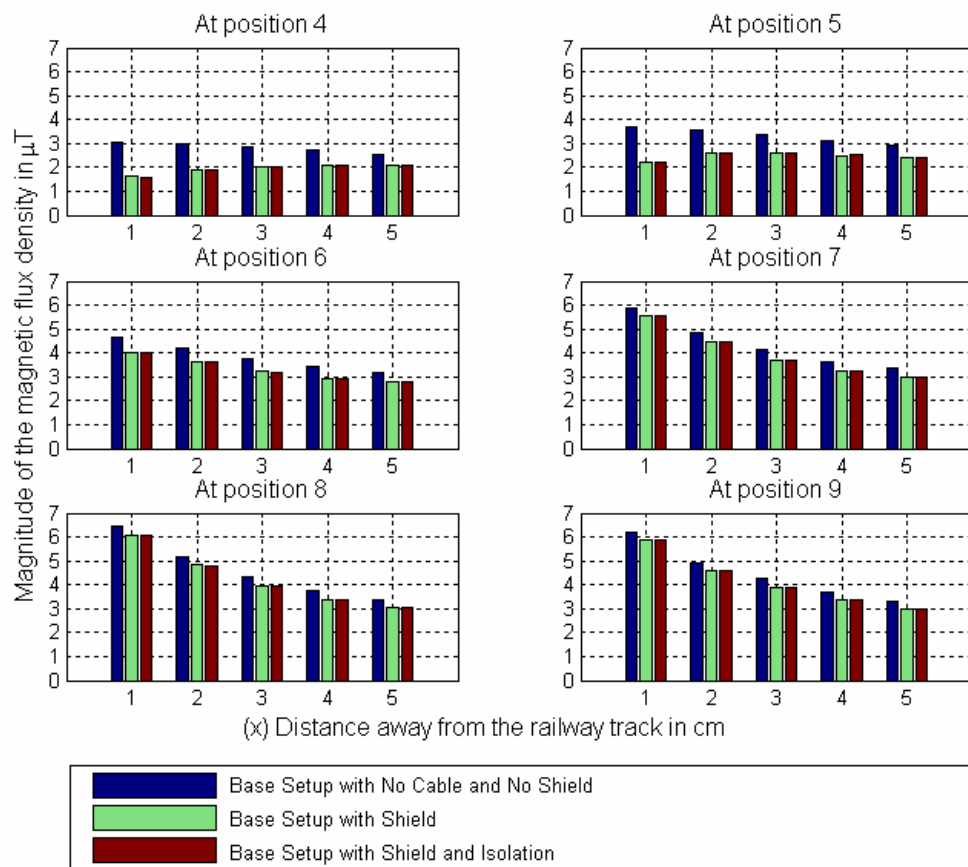


Figure 5-10: Direct Comparison for the first test set with no parallel cable installed comprising of the Base measurement, the inclusion of a shield and the inclusion of both the shield and isolation layer.

By examining Figure 5-10 it can be seen that the inclusion of the shield has a positive effect in reducing the flux density within the sensing region, to a greater effect at position 6 and below, and a lesser effect above it. The isolation layer has a very small effect when included with the shield and is barely noticeable in this graphical format.

Normalizing the data at each coordinate point in Figure 5-10 to the Base measurement at the corresponding coordinate point was then necessitated. Doing this, results in the Base data at each coordinate point attaining a value of 100% and the data values for each of the other tests at each corresponding coordinate point being represented as a percentage of the Base measurement at that point.

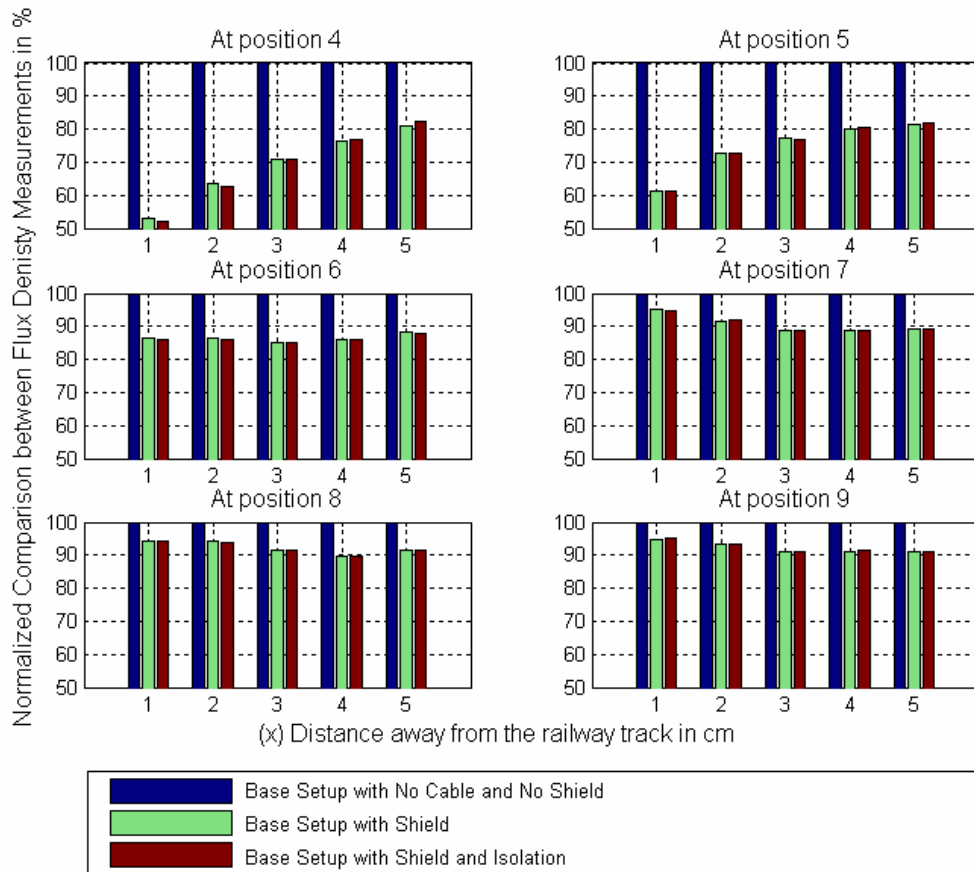


Figure 5-11: Normalized data for the direct comparison of the first test set with the inclusion of no parallel cable.

From the normalized bar graphs shown in Figure 5-11 it can clearly be seen that the shield has an effect in reducing the flux density within the sensing region. Again the effect is greater from position 6 and below than above it due to the coverage position of the shield. The advantageous effect of the isolation layer can more clearly be seen in this figure although its effects still remain small.

The total flux density reduction obtained within the sensing region by the inclusion of the shield was 14.28% and with the inclusion of the isolation layer the total reduction was 14.33%, these were obtained through the use of the Matlab program shown in Appendix 6.5.

5.4.2 Direct comparison for the second test set with the first cable connected in parallel

This comparison comprises the test set performed with the addition of the first cable, which includes the fourth, fifth and sixth tests. These tests include the sub-base measurement where only the cable was present, the shield measurement and finally the measurement including both the shield and isolation layer.

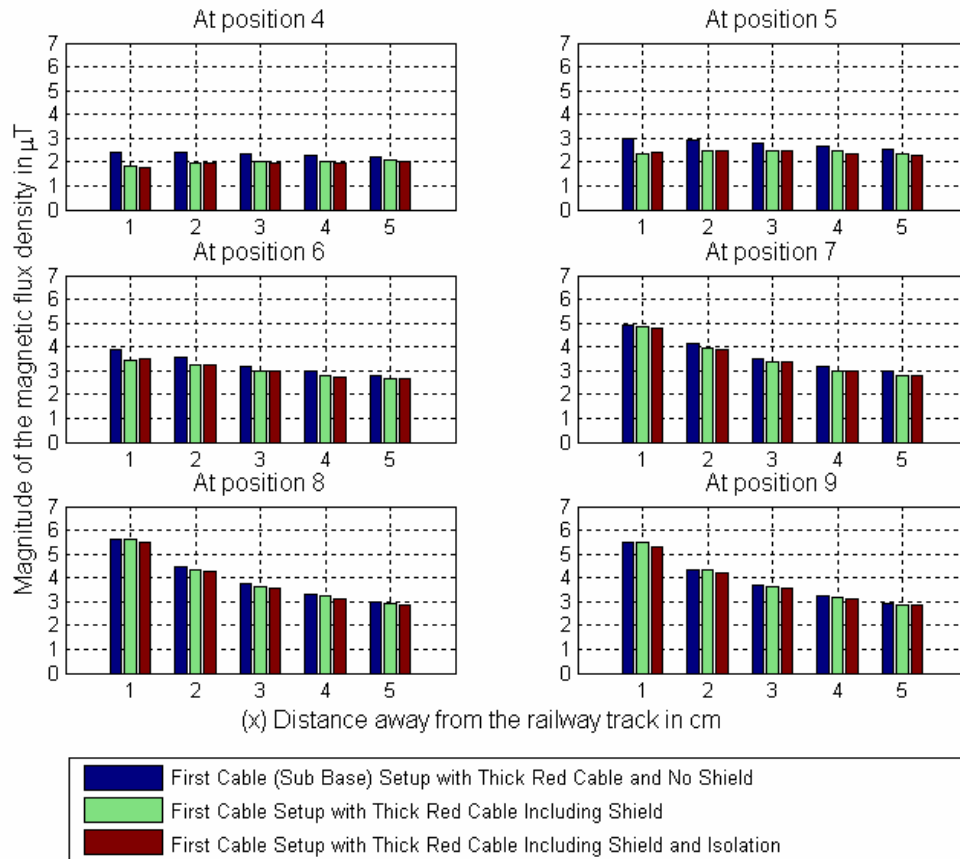


Figure 5-12: Direct Comparison for the second test set with the addition of the first parallel cable, comprising of the sub-base measurement, the inclusion of a shield and the inclusion of both the shield and isolation layer.

Through an examination of Figure 5-12 it can be established that the addition of a shield along with the parallel cable provides additional improvement as compared to the unshielded case. The inclusion of the isolation layer for this comparison yields a small but noticeable improvement compared to the solely shielded case.

For a more detailed comparison the normalized bar graph was generated and can be seen in Figure 5-13 on the next page.

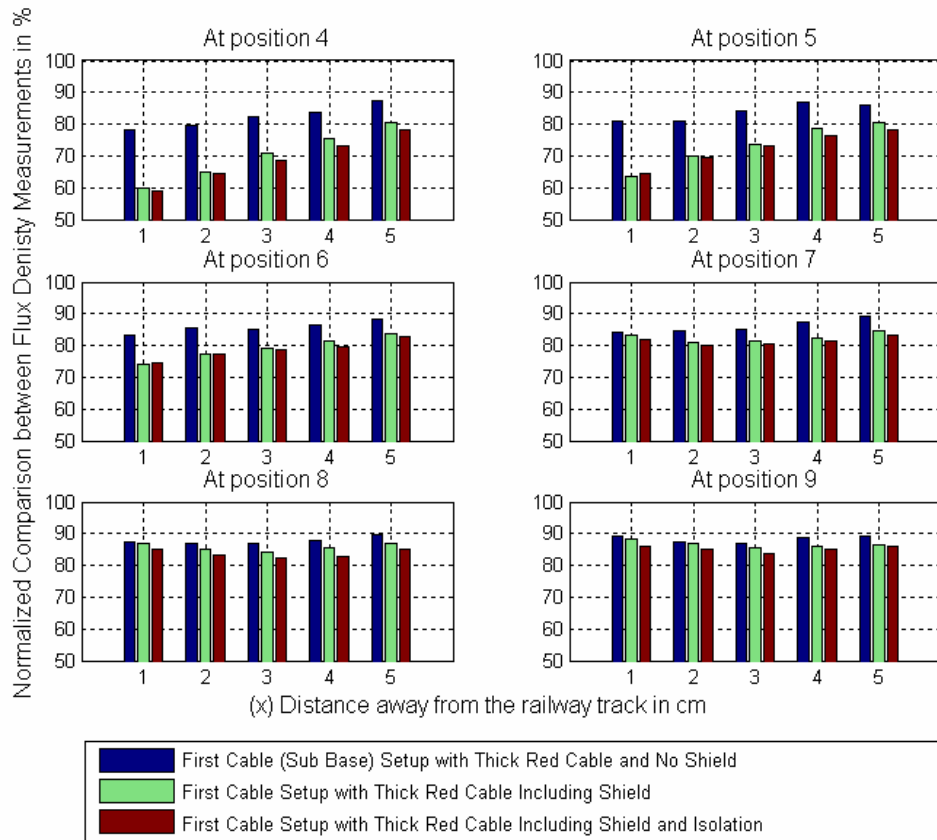


Figure 5-13: Normalized data for the direct comparison of the second test set that includes the addition of the first parallel cable.

An observation of the normalized results depicted in Figure 5-13 shows that for the sub-base measurement, where only the parallel cable was added, the flux density was reduced throughout the sensing region by a minimum of at least ten percent. The inclusion of a shield results in a further reduction in the flux density. This reduction was high from position 6 and below, and low above it. The addition of the isolation layer increases the reduction throughout the sensing region with no dramatic influence due to the shield coverage.

The total reduction in flux density within the sensing region due to the addition of the first parallel cable was found to be 14.16%, when the shield was included a further reduction was obtained and the total reduction increased to 19.55%. The addition of the isolation layer yielded a further reduction in the flux density increasing the total reduction to 20.83%.

5.4.3 Direct comparison for the third test set with the second cable connected in parallel

Tests seven, eight and nine were incorporated into this comparison. These tests were performed with the inclusion of the second parallel cable, and comprise measurements for the sub-base case where only the cable was present, the shielded measurement and thirdly the inclusion of both the shield and the isolation layer.

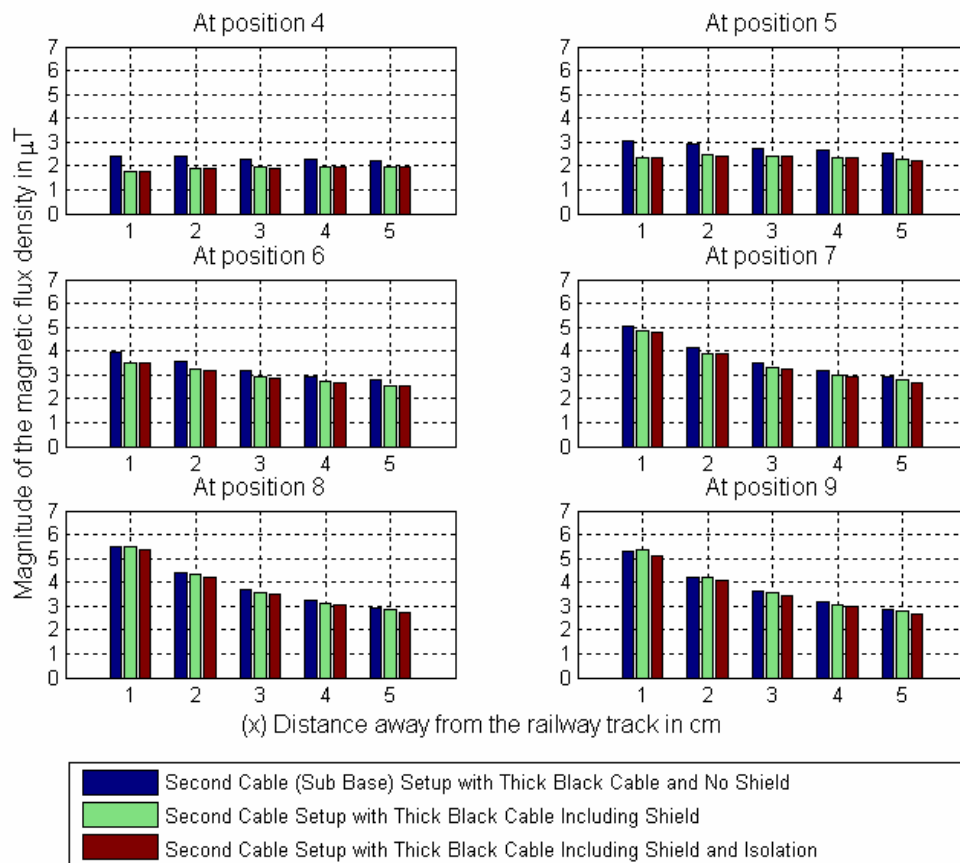


Figure 5-14: Direct Comparison for the third test set with the addition of the second parallel cable, comprising of the sub-base measurement, the inclusion of a shield and the inclusion of both the shield and isolation layer.

Figure 5-14 demonstrates that the inclusion of the shield still yields a decrease in the flux density at and below position 6 but a lesser effect above it. The inclusion of the isolation layer provides a small reduction in the flux density throughout the sensing region.

The normalized comparison, which yields a better comparison for the reduction in the flux density at each point within the sensing region, can be seen in Figure 5-15 below.

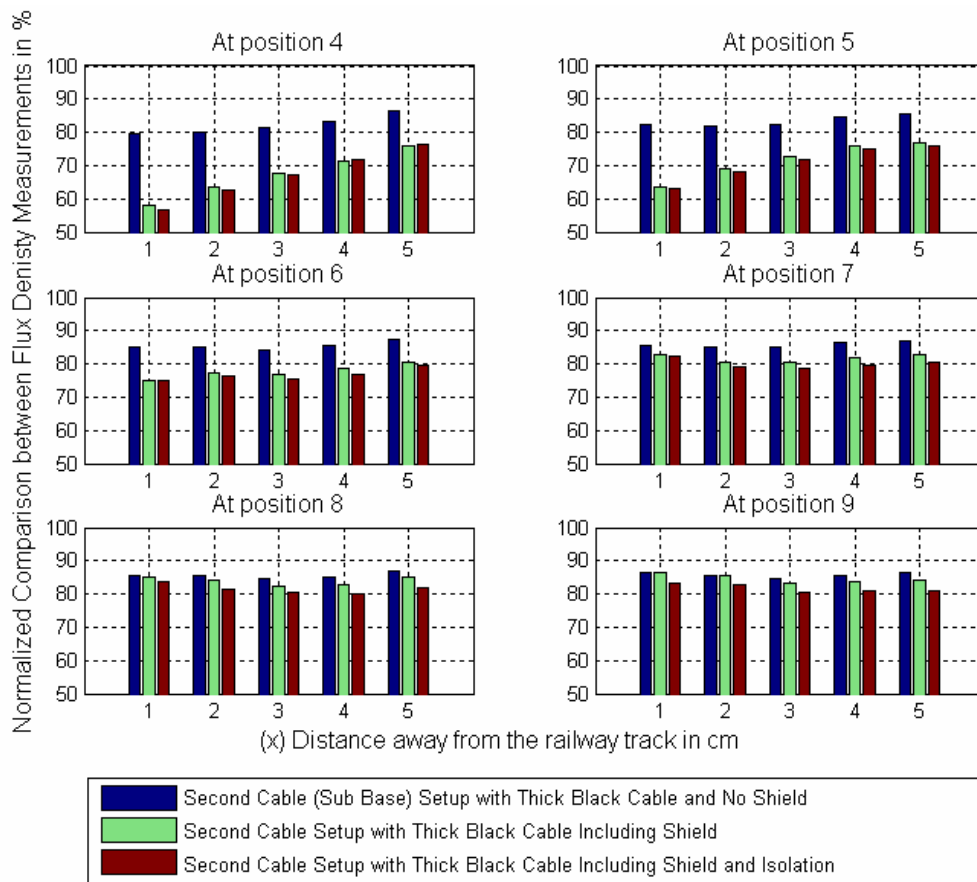


Figure 5-15: Normalized data for the direct comparison of the third test set that includes the addition of the second parallel cable.

The normalized comparison shown in Figure 5-15 again shows a reduction due to the introduction of the second parallel cable, with an improved reduction when the shield was added. The incorporation of the isolation layer provided a further improvement in the reduction of the flux density within the sensing region.

A total reduction in flux density experienced within the sensing region due to the inclusion of the second parallel cable was found to be 15.2%, which increased to 21.22% with the addition of the shield and finally the reduction increased to 22.8% when the isolation layer was installed.

5.4.4 Direct comparison for the fourth test set with the third cable connected in parallel

The comparison for the final three test (ten, eleven and twelve), are given below in Figure 5-16. These tests comprised the sub-base measurement for the third cable, the shield measurement and combination measurement including both the shield and isolation layer.

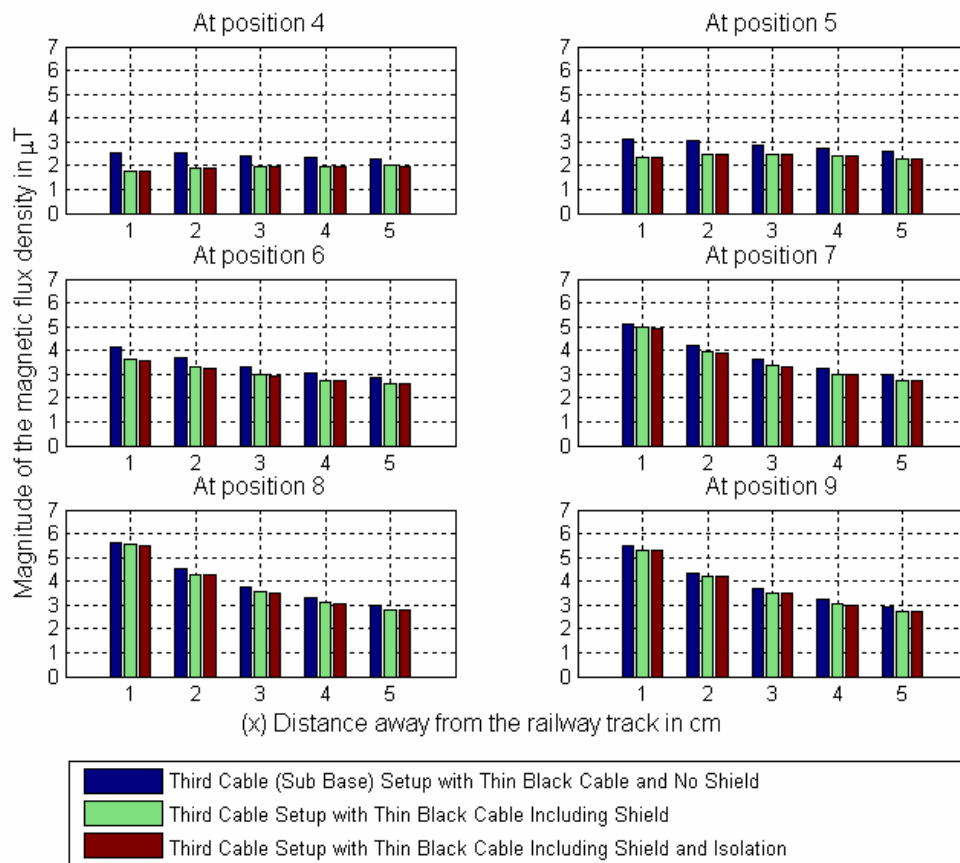


Figure 5-16: Direct Comparison for the fourth test set with the addition of the third parallel cable, comprising of the sub-base measurement, the inclusion of a shield and the inclusion of both the shield and isolation layer.

Figure 5-16 shows that the introduction of the shield again results in the reduction of the flux density within the sensing region, and again the isolation layer provides a further reduction.

To obtain a better comparison for the reduction of the flux density within the sensing region a normalized graph was generated and can be seen in Figure 5-17 on the next page.

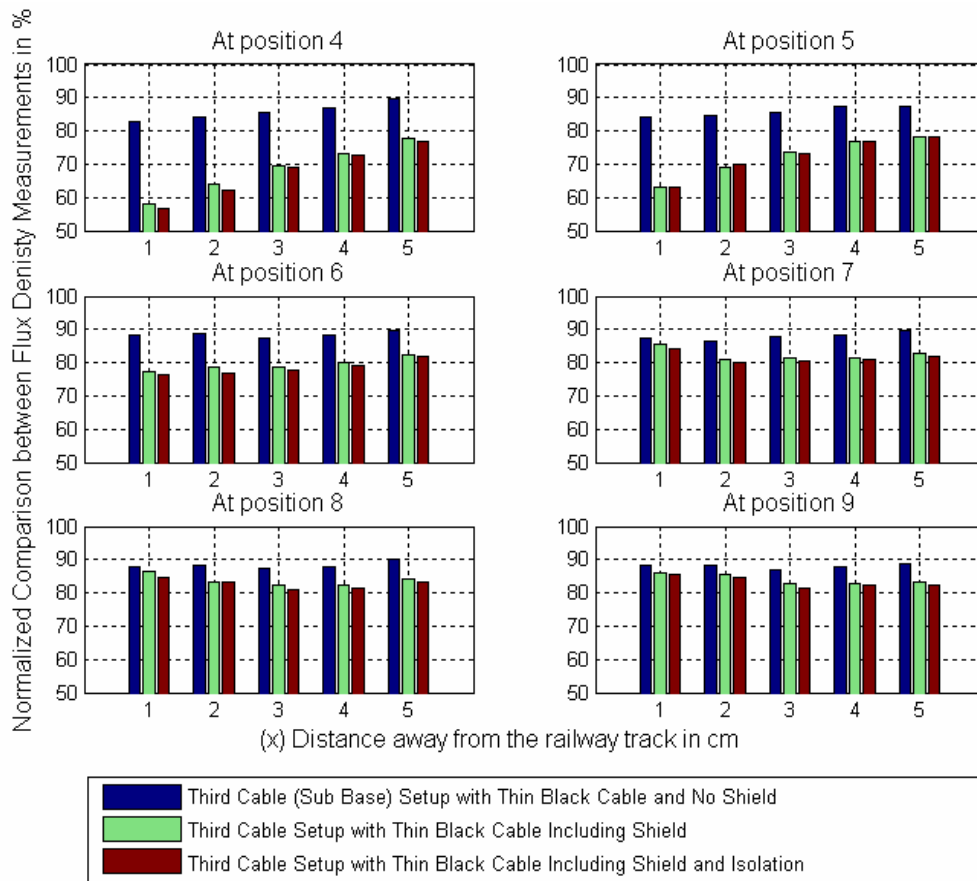


Figure 5-17: Normalized data for the direct comparison of the fourth test set that includes the addition of the third parallel cable.

Comparing Figure 5-17 to the base measurement, which yields a value of 100% at each point, it can be seen that a reduction in the flux density was obtained due to the introduction of the third cable, although the reduction is less than for the first and second cables. The introduction of the shield again has a positive effect in the reduction of the flux density, along with the inclusion of the isolation layer, which also provided an improvement. The total improvement for this test due to the sole inclusion of the cable was found to be lower than that obtained for either of the two previous cable tests, but better than the test performed without the inclusion of a parallel cable.

The total reduction within the sensing region due to the addition of the third cable was found to be 12.55%, and with the introduction of the shield increased to 20.6%, and finally when the isolation layer was included the reduction increased to 21.48%. These values indicate that this test in question yielded the second best improvements out of the four test sets performed.

5.4.5 Direct comparison, comparing the effect of the three different cables directly

For this comparison all the normalized base and sub-base measurements were compared, these included the base measurement, and the sub-base measurements for the first, second and third parallel cables. See Appendix 4.3 for the following three normalised comparison bar graphs represented in terms of flux density (μT).

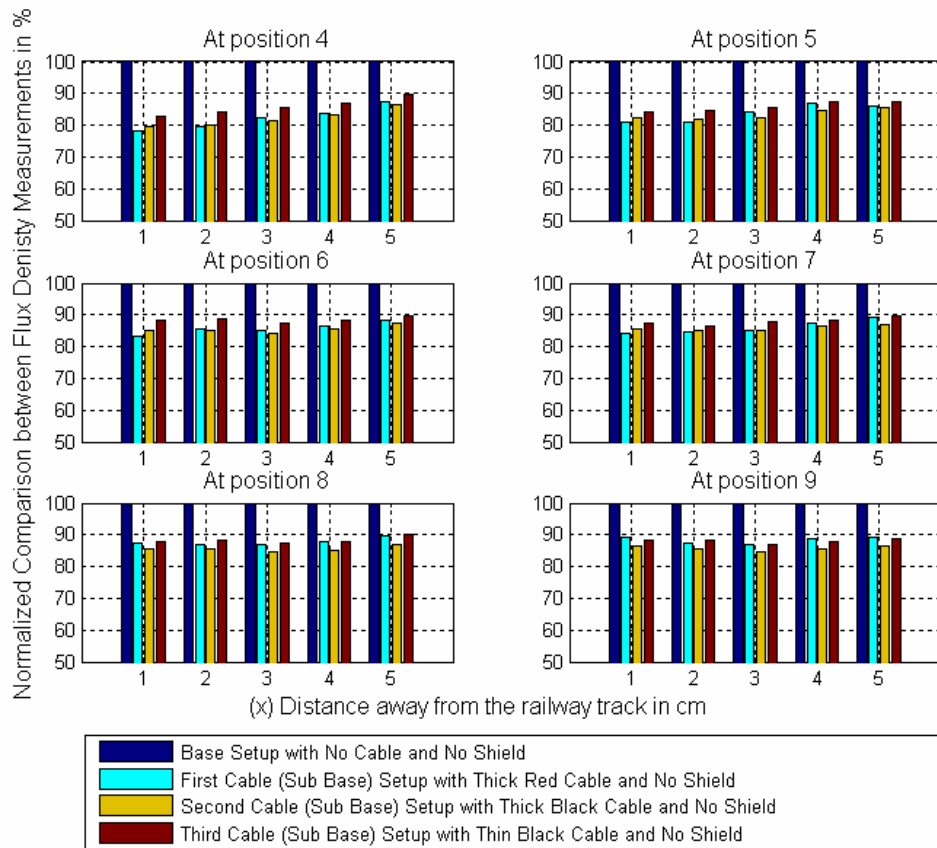


Figure 5-18: Normalised direct comparison to determine the effect of the addition of the three separate cables to the railway track system.

For Figure 5-18 it can be observed that the introduction of any of the cables has a positive effect on the reduction in the flux density within the sensing region. It would appear that the greater reduction occurs due to the inclusion of the second cable, with the degree of reduction being less using the first cable and even less so by the third cable.

5.4.6 Direct comparison, comparing the effect of the shielded cases for the three different cables directly

All the shielded measurements within the sensing region obtained during the measurements were normalised and compared to each other; these include the purely shielded measurement and the shielded measurements for each of the three different cables.

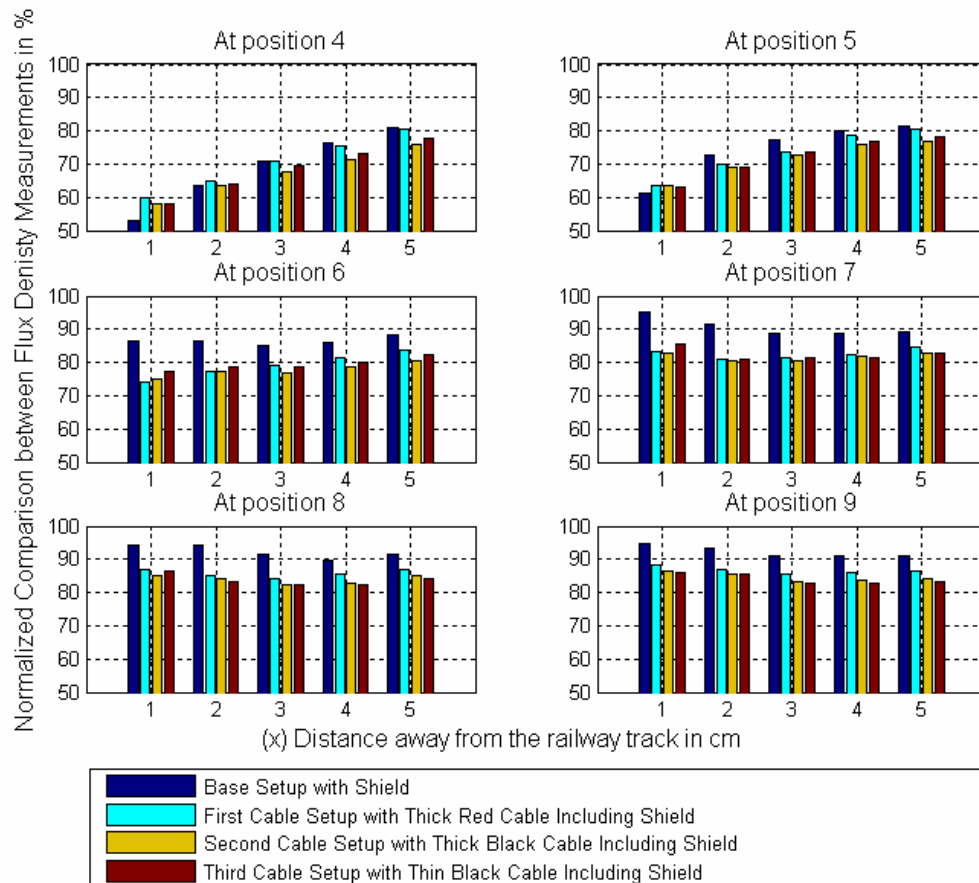


Figure 5-19: Normalised direct comparison to determine the effect of the inclusion of the shield for the three separate cables.

From position 5 and upwards, the combination of the shield and cable yield definitively positive results in reducing the flux density in the sensing region over the shielded case alone.

The test involving the second cable yields the better results for position 6 and below, and the third cable provides the better results for positions 8 and 9 with a mixture at position 7.

5.4.7 Direct comparison, comparing the effect of the shielded and isolated cases for the three different cables directly

This final normalised comparison includes the results for the shielded and isolated cases, which comprises all three cables as well as when no cable was installed.

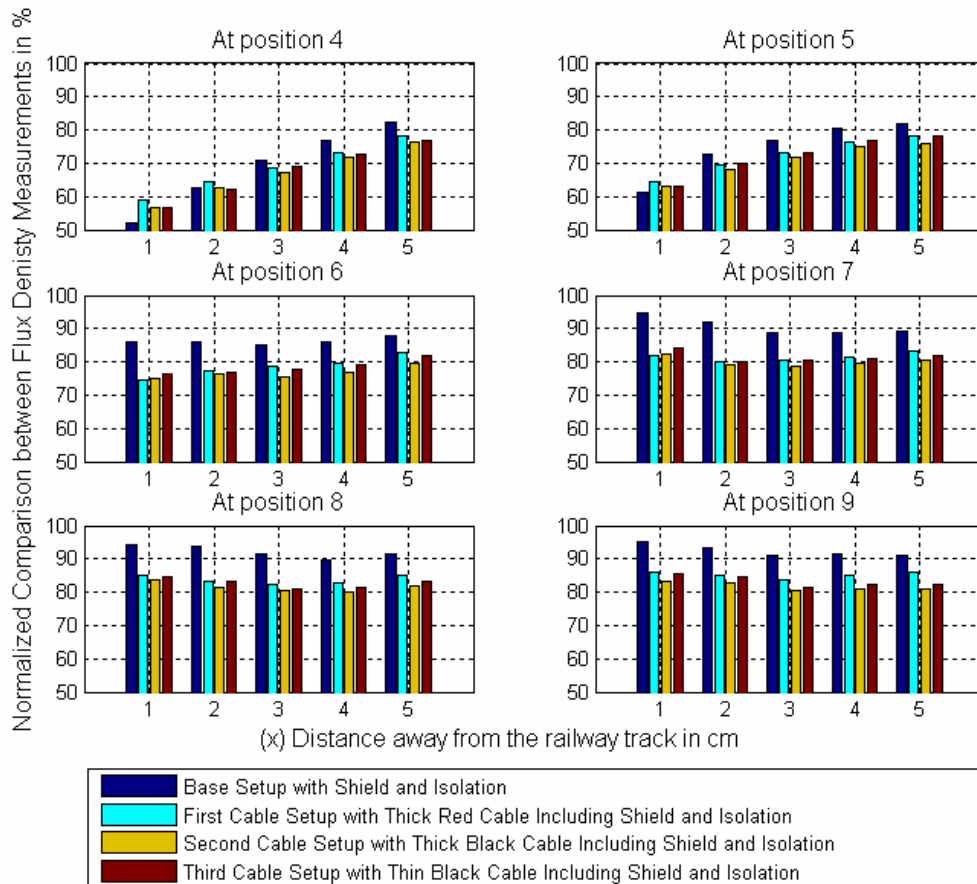


Figure 5-20: Normalised direct comparison to determine the effect of the inclusion of the shield and isolation layer for the three separate cables.

The inclusion of the shield combined with an isolation layer provides an increased reduction when combined with one of the three cables compared to the case with no cable combination (Base setup). The combination that includes the second cable provided the best reduction in flux density within the sensing region for this test case, with a lesser achieved with the third cable and the poorest using the first cable.

The culmination of results regarding the second cable's performance in all measurement tests indicates that its inclusion enables the greatest reduction of the flux density within the sensing region and hence is a superlative choice as a means of curbing the flux density within the sensing region, with a total reduction of 22.8%.

6 Simulations

6.1 Introduction

Simulations were utilized to provide a correlation between the experimental results and the magnetic field theory. The Maxwell 2D field simulator was employed to carry out the required simulations of the magnetic field present within the test area.

The Maxwell 2D field Simulator is an interactive software package that uses finite element analysis (FEM) to solve two-dimensional electromagnetic problems. To analyze a given problem, the geometry of the system along with the material properties and the excitation experienced are required. [9]

Once the required solver has been selected, the Maxwell software performs the following tasks:

- *Automatic creation of meshes for the defined problem geometry.*
- *Calculates the desired electric or magnetic field solutions and any other special quantities required.*
- *Allows analyzes, manipulation and displaying of the field solution obtained.*

6.2 Preparing the Simulation Package

6.2.1 Solver Type chosen

The eddy currents solver was chosen to simulate the magnetic field around the railway track. This was done because the solver allows the simulation of time varying currents to flow within the railway track, which produce magnetic fields in a direction perpendicular to the current flow. These magnetic fields in turn induce currents to flow in adjacent conductors, which will produce an opposing magnetic field. All currents present flow perpendicular to the cross sectional area of the model.

6.2.2 Drawing Plane used

Maxwell 2D allows the model to be drawn in either the Cartesian (X Y Plane) or axisymmetric (R Z Plane) systems. For the simulations of the railway track system it was chosen to use the Cartesian system as all current flows would be set to the Z

direction (in or out of the screen) and all flux flow would remain exclusively within the X Y plane, allowing the solved field patterns to easily be analysed.

6.2.3 Defining the Model to be simulated

The model to be used in the Maxwell 2D simulation can either be drawn within Maxwell using the tools available in the “draw model” option, or it can be drawn using other software packages such as CAD and subsequently imported into Maxwell.

To draw the model required, a cross section of the railway track was primarily drawn, followed by the addition of the proximity sensor platform. This model includes the constant structures always present for every simulation. The shield and parallel cable were added individually or together depending on the configuration required for the specific simulation being run.

The original model used for the simulations, which includes the railway track, the proximity sensor platform, the shield and the parallel cable can be seen in Figure 6-1 below.

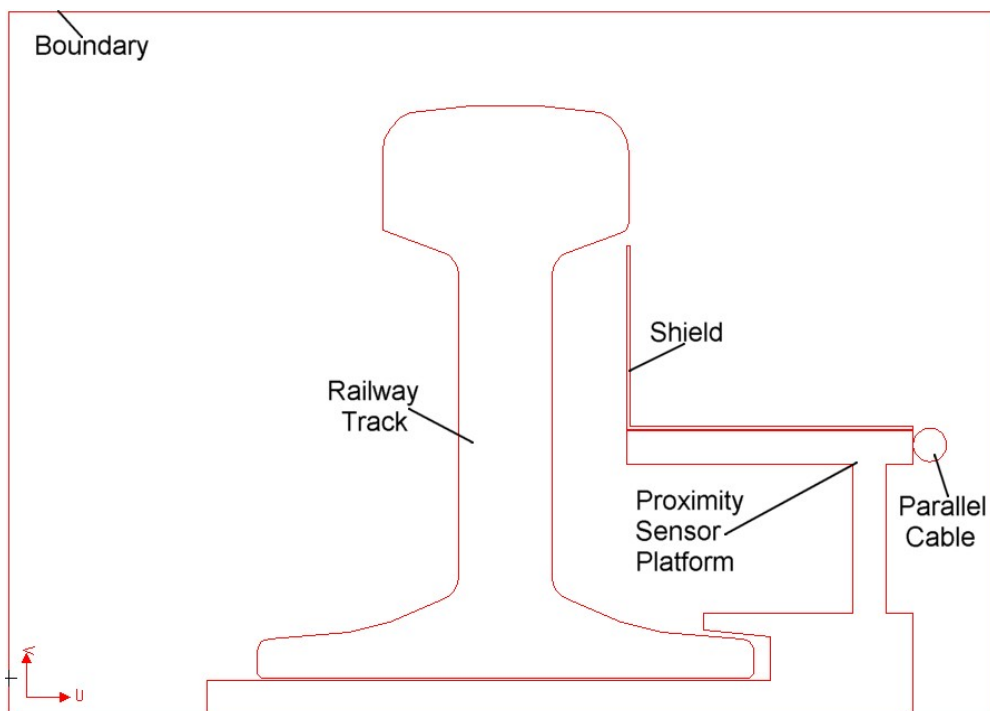


Figure 6-1: Simulation model used, showing the constant railway track and proximity sensor platform and the some times present shield and or parallel cable.

This model was later modified to decrease the simulation time required for a reasonable convergence. For the new model the proximity sensor platform was

reduced by removing the entire section that passes below the railway track. The new model, and the one used for the simulations, can be seen in Figure 6-2 below.

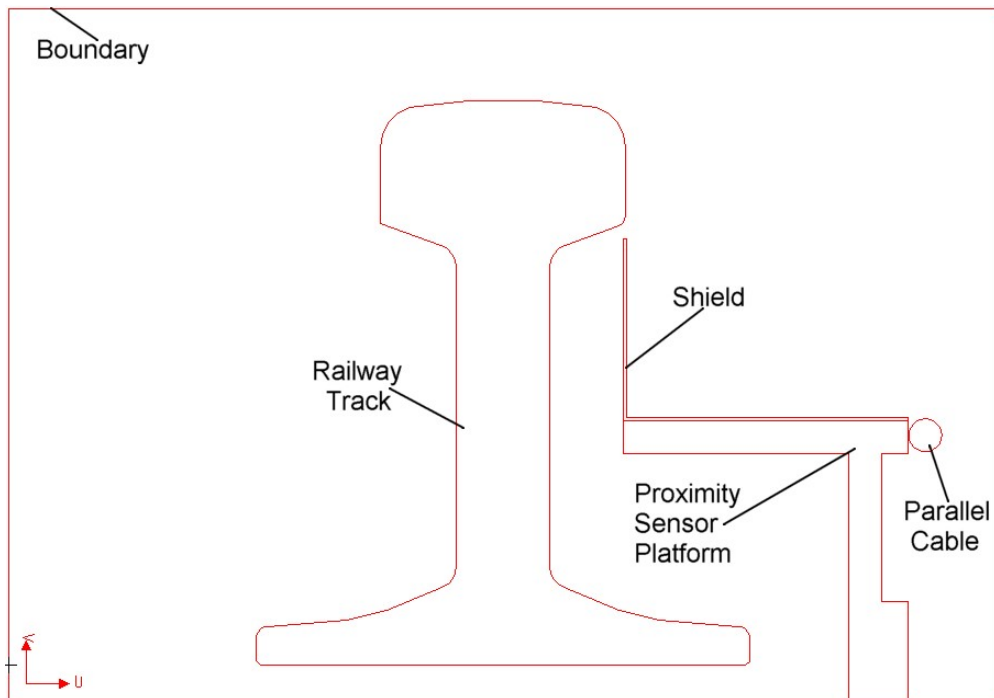


Figure 6-2: New and Final Simulation model used, showing the constant railway track and proximity sensor platform and the some times present shield and or parallel cable.

6.2.4 Defining the materials used

This step involves assigning materials to the structures present within the simulation model to ensure that they behave similarly to their counterpart structured in the lab setup of the railway track system.

The different structures present within the simulation model were assigned the following materials:

<i>Railway track</i>	-	<i>Iron</i>
<i>Proximity Sensor Platform</i>	-	<i>Iron</i>
<i>Parallel Cable</i>	-	<i>Copper</i>
<i>Shield</i>	-	<i>Steel_1008</i>

6.2.5 Setting up Boundaries and Sources

The importance of this step lies in the fact that the outer edges or boundaries of the simulation model can be defined with boundary properties and all current carrying conductors such as the railway track and the parallel cable can be defined as sources.

When a source is defined for the eddy current solver, a peak current is assigned to the source which coincides with the current flowing in that conductor for the lab setup.

For the case when only the railway track conducts and no parallel cable was present the current flowing through the railway track was set to 2 A. When the parallel cables are attached the total current remained 2 A but varying amounts will flow through the separate cables. For the first cable simulation the peak current flowing through the cable was set to 0.22 A and the current flowing through the railway track was set to 1.78 A to obtain a total of 2 A. For the second cable simulation the current in the cable was set to 0.2 A and the current through the railway track was set to 1.8 A. For the final simulation set involving the third cable the current through the cable was set to 0.16 A and the railway track was set to 1.84 A.

The boundary of the simulation model was set to balloon as this defines the drawing space as being nearly infinitely large, effectively isolating the model from other sources of current or magnetic fields. This can also be seen as the background of the model extending to infinity along the edges of the simulation model where it was defined as a balloon boundary.

6.2.6 Setting up the Solutions

To setup the solution before running the simulation some of the options need to be customised firstly the starting mesh was set to initial meaning that the simulation would start with larger and few triangles for the first pass. Secondly the frequency was set to 300 kHz as the simulation was carried out to obtain comparative results for the high frequency test performed.

Thirdly the percentage refinement per pass was set to 10%, which was below the default of 15%, as it was found that a smaller refinement allowed for better simulation results and a quicker convergence. Finally the energy error target was set to 10% meaning that the simulation would only stop once an energy error of less than 10% was reached.

The default of 1% for the percent error was not used as it would take a week to reach this level and the computers used kept crashing at around the third or fourth day of

simulation. Also the energy conversion lies below 1.4% when the energy error falls below 10%.

6.3 Difficulties Experienced with the Simulations

Due to the high frequency of the time varying current flowing through the railway track difficulties were experienced in attaining reasonable results. To determine whether a simulation result is reasonable Maxwell 2D provides two criteria the first being an energy error and the second being a delta energy rating.

The delta energy rating determines the difference between the total energy in the current simulation solution and that of the previous simulation. When the difference between the consecutive solutions becomes very low it is said that the simulation has converged. The meaning of the energy error rating refers to errors in some of the triangles used to form the mesh necessary for the FEM analysis of the simulation model. [9]

To obtain an ideal simulation results the delta energy and energy error must be low, but a proficient simulation result can be obtained when the delta energy is low but the energy error is high, as this means that the simulation result is good overall with some small erroneous regions. [9]

The difficulties arose when the endeavour sought was to aspire to a good simulation result as, to attain this, small delta energy and low energy error was required. To attain this at the high frequency necessary a very refined mesh with small triangle was required to ensure that all current flows induced within adjacent conductors are taken into account.

Due to the more substantial mesh size, the calculation time required for solving the simulation increased compared to a lower frequency simulation. To circumvent this dilemma, improvement of the simulation process was mandated. To this end a new model shown in Figure 6-2 was employed which yielded a reduction in the simulation time and allowed for a better convergence than was attainable using the original model.

However, even with the improved model in place, the simulations took between 27 to 51 hours to attain a solution within the stipulated error bounds required. The computers used to perform the simulations would crash, due to lack of memory (RAM) if the simulation was run for longer than 51 hours, and so the target energy was set to 10% to prevent this. The simulation performed usually converged to between six to seven percent, with a delta energy convergence of less than 1.4%, and these results were deemed ample.

6.4 Simulation Results

6.4.1 Base Simulation (Simulated Base Measurement)

The first simulation result obtained was for the Base simulation, where no shield and no cable were installed. The contour plot for the flux density can be seen in Figure 6-3, where the equivalent position test area used to obtain the measured results has been included for each of the contour plots attained. The sensing region shown in the simulation contour plots coincides with the position of the sensing region in the test setup used in the lab and hence coincides with the sensing region shown in the measurement results given in the experimental results in section 5.3.

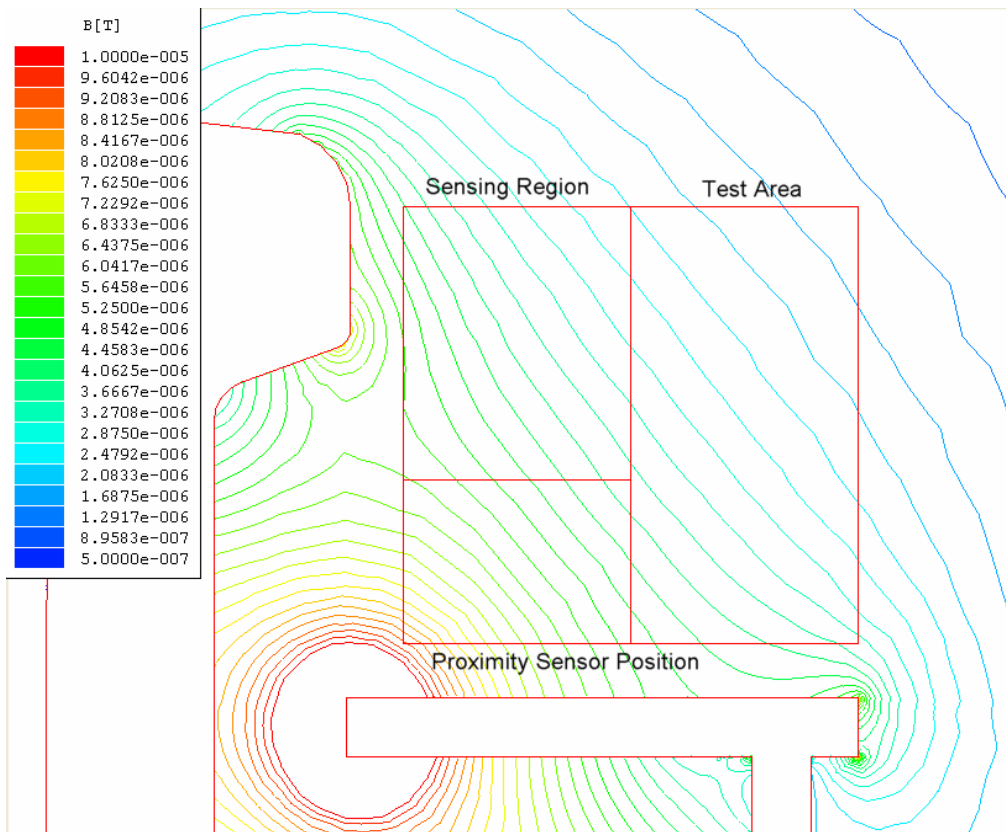


Figure 6-3: Simulated Results showing the Flux Density within the Test Area for the Base Simulation, with no shield or cable.

From Figure 6-3 it can be seen that the magnitude ranges of the flux densities present within the test area are in a similar range to those measured in the same area. The Meaning of this implies that the measured and simulated results yield similar magnitudes of flux density therefore showing that the measurements produced reasonably accurate results. The flux lines for all the simulated results shown can be found in Appendix 5.1.

6.4.2 Base Simulation with the addition of a shield

The addition of a shield clearly has a visible effect of the flux density distribution shown in Figure 6-4, more specifically within the test area. A visible change in the field pattern can be observed within the test area along with a general reduction in the flux density, except in the region closest to the top of the shield where an increase was experienced.

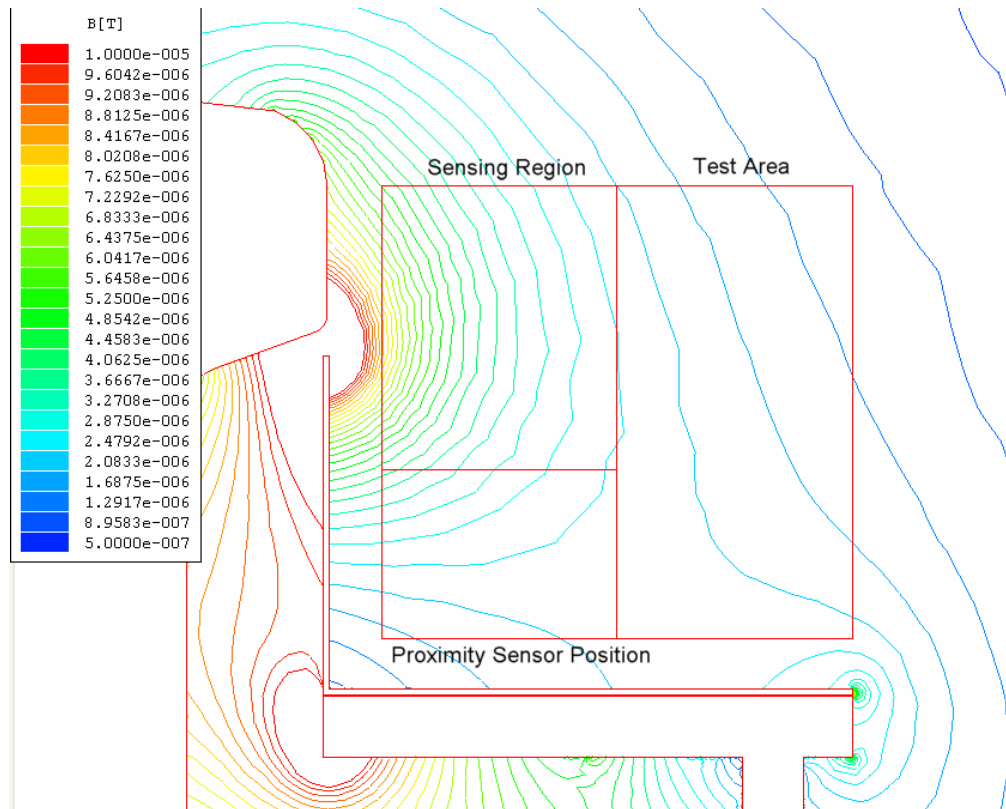


Figure 6-4: Simulated Results showing the Flux Density within the Test Area for the Base Simulation, with the inclusion of a shield but no cable.

It can be seen how the flux density increases between the top of the shield and the railway track due to the flux lines compressing to pass through.

6.4.3 Sub-base Simulation including the First Parallel Cable

The introduction of the parallel cable also has a clear effect on the flux density patterns when a comparison between Figure 6-5 and Figure 6-3 is performed.

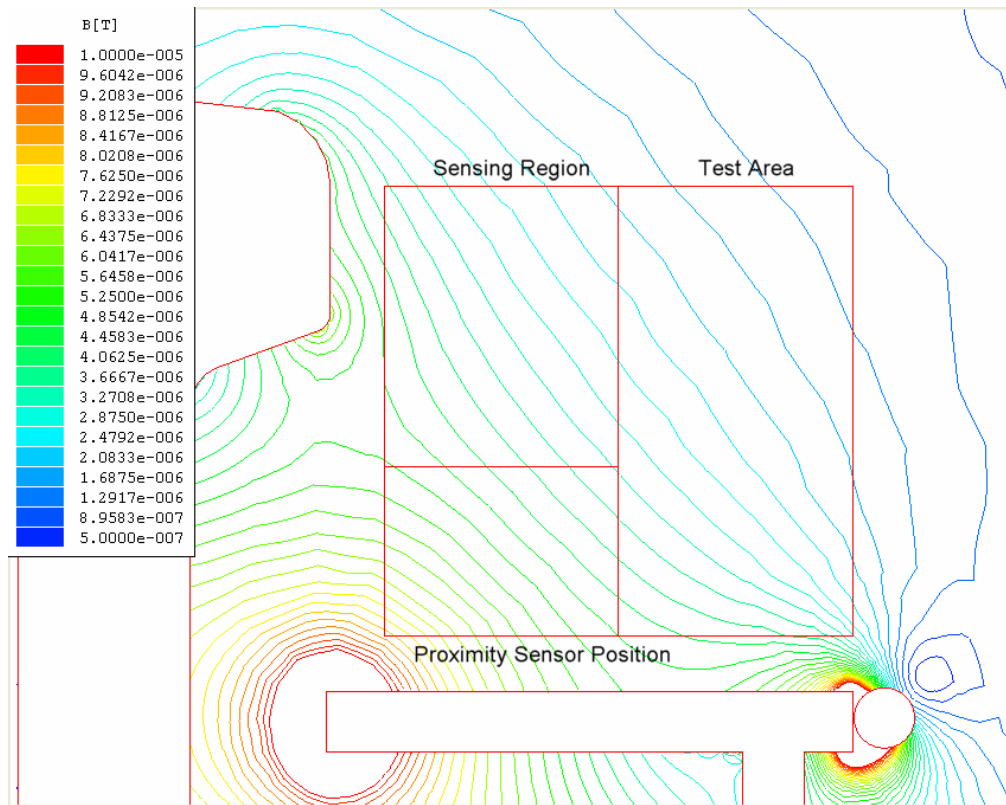


Figure 6-5: Simulated Results showing the Flux Density within the Test Area for the sub-base Simulation involving the First parallel Cable carrying a 0.22 A current, with no shield.

It can be seen that the flux density in the lower left region of the test area has decreased and to the upper left has also decreased, with a slight increase to the lower right of the test area. The increase to the lower right does not have a large effect on the proximity sensor since it lies far away from the sensing region. Within the sensing region there is a drop in the flux density signifying that the introduction of the parallel cable has a positive effect.

6.4.4 First Cable Simulation including a shield

The addition of the shield to the setup already including a parallel cable can be seen in Figure 6-6, where again the introduction of the shield has a visible effect on the flux density distribution within the test area.

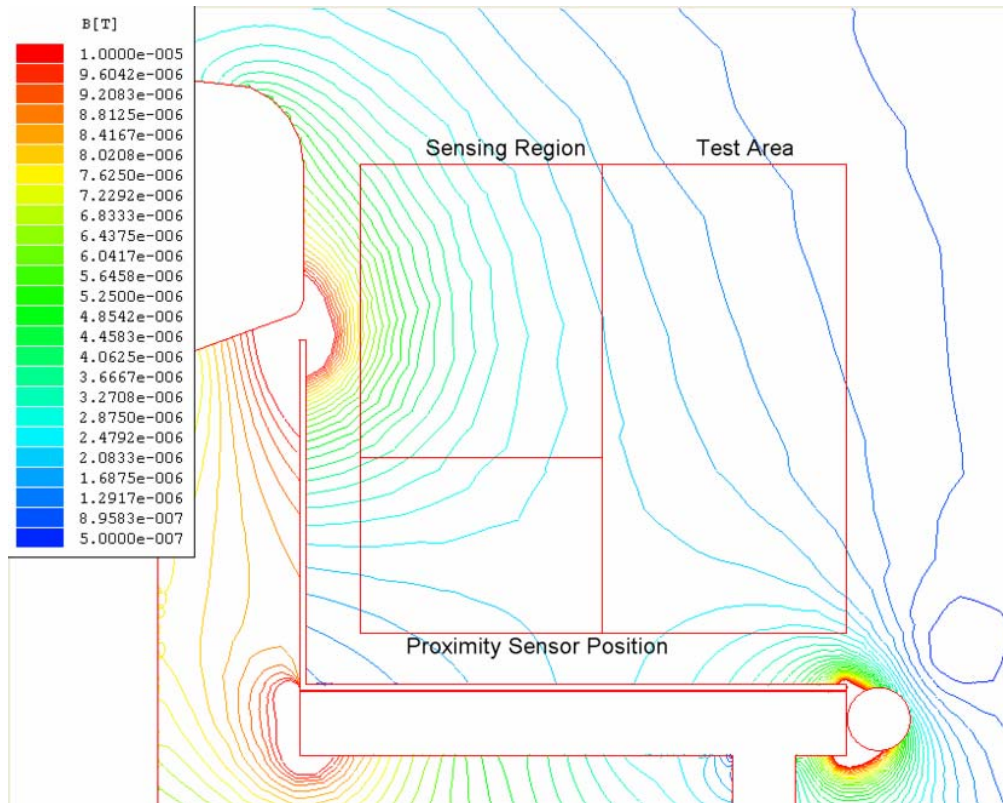


Figure 6-6: Simulated Results showing the Flux Density within the Test Area for the sub-base Simulation involving the First parallel Cable carrying a 0.22 A current, with the inclusion of the shield.

Comparing this case (Figure 6-6) to the base shielded case (Figure 6-4), which does not include a parallel cable, it can be seen that the effect of combining the shield and cable results in a lower total flux density within the test area and sensing regions therefore the inclusion of the cable with the shield has an improved effect over the solely shielded case. Also by comparing this case (Figure 6-6) to the base measurement case (Figure 6-3), proves that a reduction in the flux density within the test area and sensing region has been achieved due to the combined introduction of a shield and parallel cable.

6.4.5 Sub-Base Simulation including the Second Parallel Cable

To perform this simulation, the current passing through the parallel cable was changed to the same value as that connected in the lab setup, which was 0.2A, this being slightly lower than the previous cable tested. This was done to emulate a different cable connected to the system with a different current flowing through it.

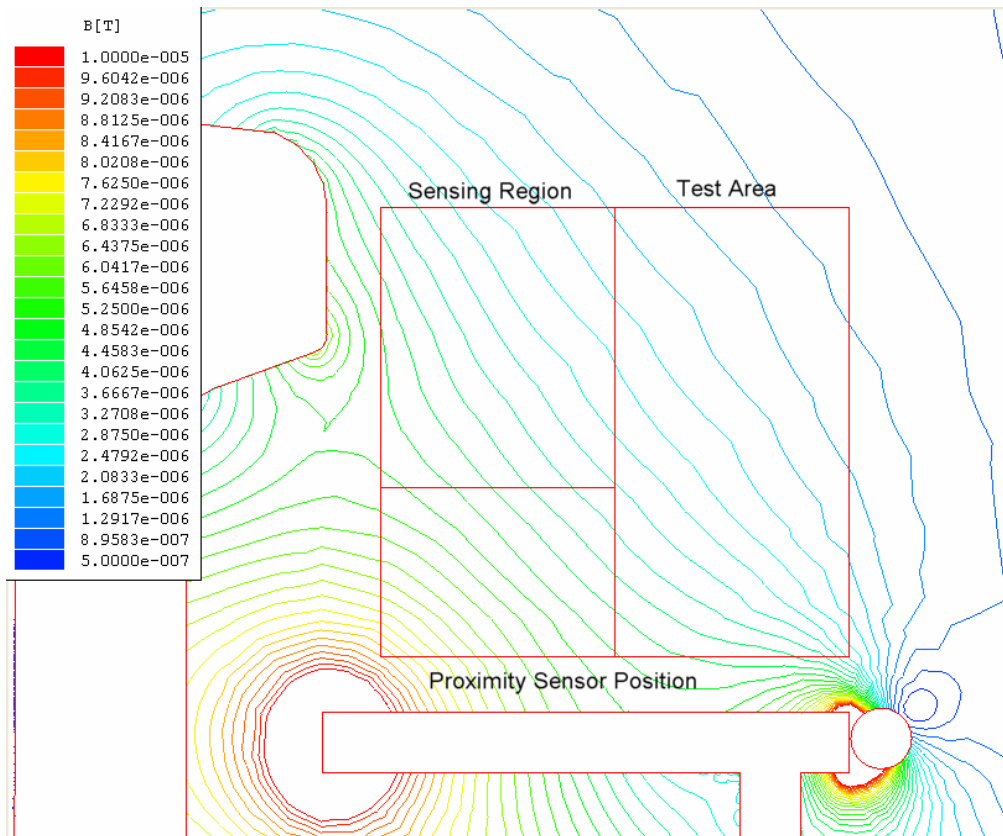


Figure 6-7: Simulated Results showing the Flux Density within the Test Area for the sub-base Simulation involving the Second parallel Cable carrying a 0.2 A current, with no shield.

Comparing the patterns of the flux density in Figure 6-7 to the previous cable test in Figure 6-5, it was noted that the visible patterns are very similar barring some minor variations. From this comparison it would appear that the flux density is higher than for the previous cable, this plausibly being due to the slightly lower current flowing in the cable.

6.4.6 Second Cable Simulation including a shield

The shielded case for the second parallel cable was simulated and once more it is reinforced that the introduction of the shield has a positive effect in reducing the flux density within the sensing region except for the region closest to the top of the introduced shield where the flux density again increases.

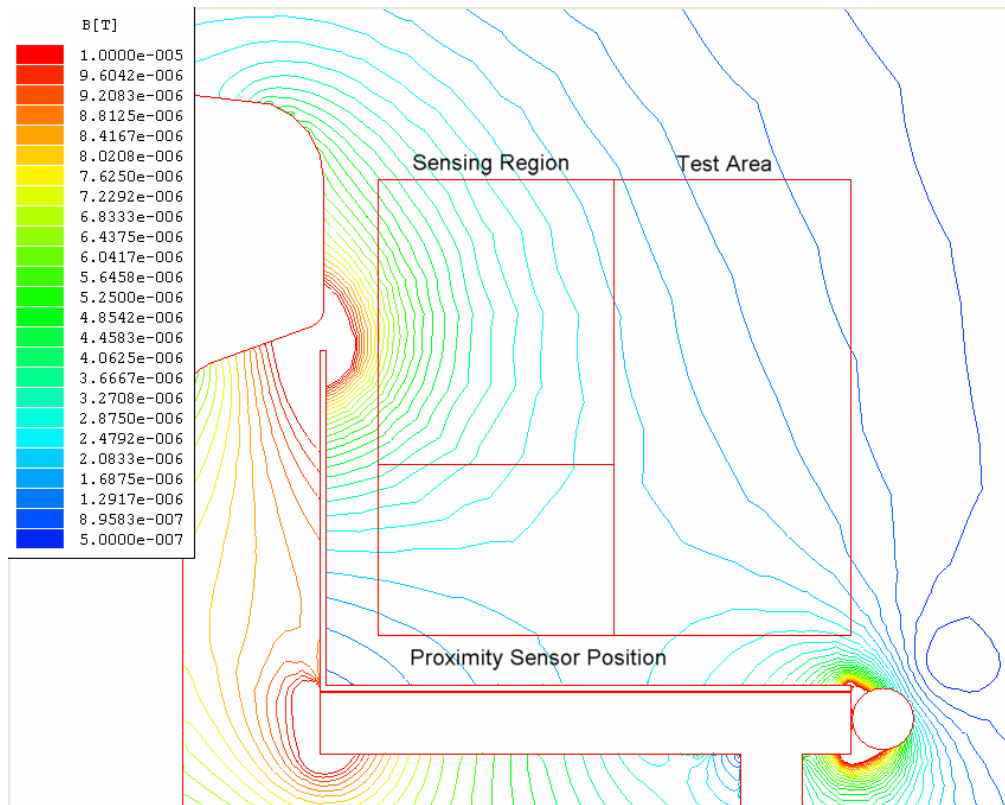


Figure 6-8: Simulated Results showing the Flux Density within the Test Area for the sub-base Simulation involving the Second parallel Cable carrying a 0.2 A current, with the inclusion of the shield.

An overall comparison again yielded that the total flux density has decreased compared to the simulation of the unaltered base measurement.

6.4.7 Sub-Base Simulation including the Third Parallel Cable

The final parallel cable tested in the experimental measurements was simulated by setting the cable current to 0.16 A and the railway track current to 1.84 A. Once more the introduction of the cable has a visible effect on the flux density within the test area, although it would seem that this cable has the lesser effect on the system as compared to the previous two cables.

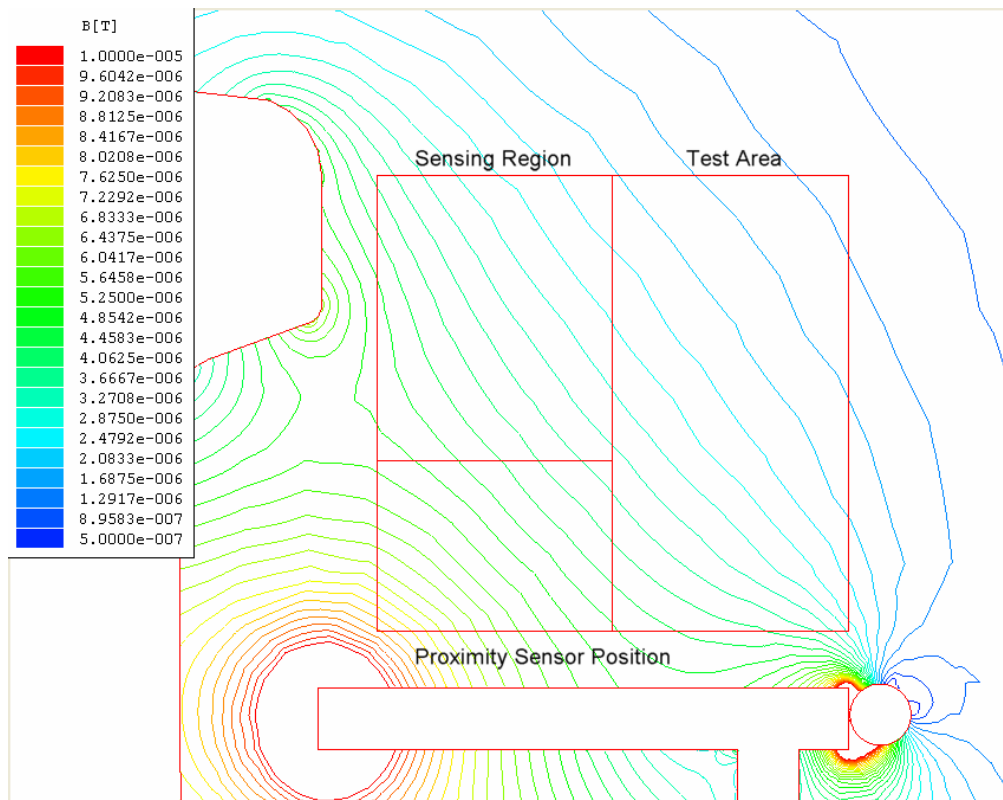


Figure 6-9: Simulated Results showing the Flux Density within the Test Area for the sub-base Simulation involving the Third parallel Cable carrying a 0.16 A current, with no shield.

The introduction of the third cable offers a much weakened effect compared to the previous two cables but nonetheless has a positive effect compared to the simulated base measurement.

6.4.8 Third Cable Simulation including a shield

Finally the inclusion of the shield with the third cable again yields a further improvement over the un-shielded case compared to the simulated base measurement but not as pronounced an improvement as compared to the previous two cables with the inclusion of the shield.

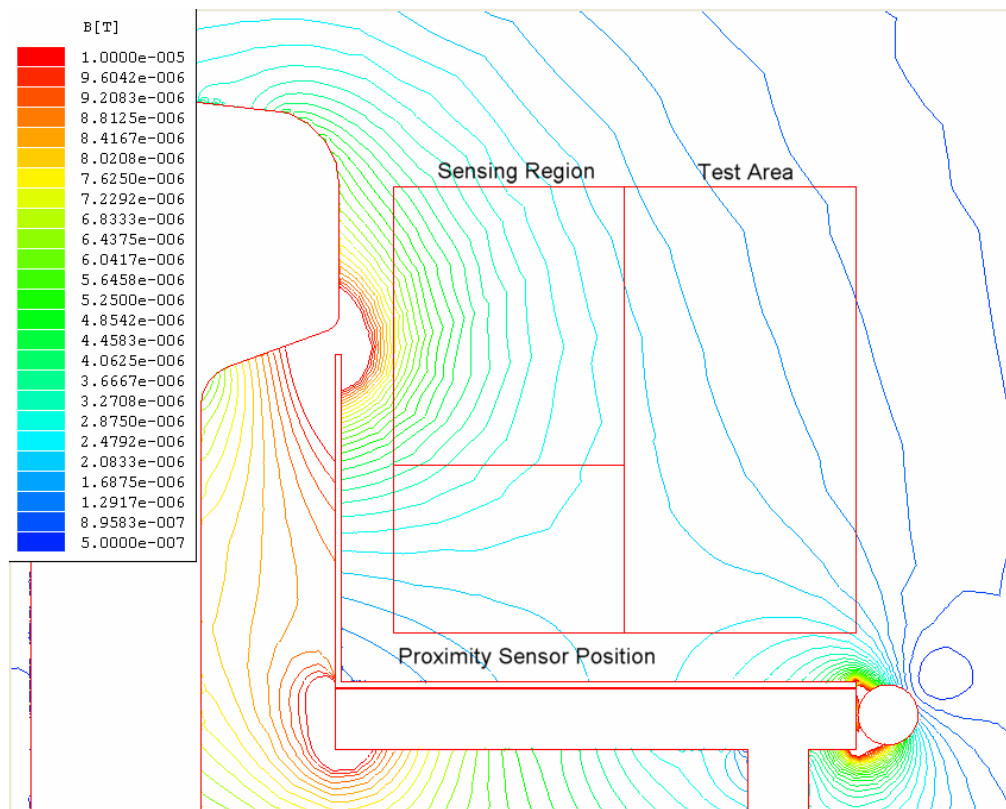


Figure 6-10: Simulated Results showing the Flux Density within the Test Area for the sub-base Simulation involving the Third parallel Cable carrying a 0.16 A current, with the inclusion of the shield.

Again an increase in the flux density within the sensing region occurs due to the introduction of the shield.

6.5 Direct Comparison of Simulation Results

The same method was employed to perform a direct comparison between the various simulation results obtained as that employed for the comparison between the various measured results in section 5.4, including the description given in section 1.5.4.

The comparison for each of the different case involving the shielded and un-shielded cases for each on the different simulation sets, which includes the Base set, the inclusion of the first cable, the second cable and finally the third cable, are given in Appendix 5.2, with the Matlab program used given in Appendix 6.6.

The major observations made from the comparison between the shielded and un-shielded cases, for each on the different sets, were that the inclusion of the shield has a positive effect below the top of the shield, at positions 4 and 5 on the Y axis, but a negative effect on reducing the flux density at the first two point on the X axis for all positions above 6 on the Y axis. However positions on the X axis that lay further away from the shield show a positive effect due to the introduction of the shield.

The total reduction in the simulated flux density within the sensing region can be seen in Table 6-1 below, making use of the Matlab program shown in Appendix 6.7.

Table 6-1: Total reduction in the Flux Density within the Sensing Region for each of the simulated cases compared to the Base Simulation.

Simulated Case	Percentage Reduction
Base with the Inclusion of a Shield	5.94%
First Parallel Cable with no shield (0.22A)	12.7%
First Parallel Cable with Shield (0.22A)	16.31%
Second Parallel Cable with no shield (0.2A)	11.62%
Second Parallel Cable with Shield (0.2A)	15.39%
Third Parallel Cable with no shield (0.16A)	9.51%
Third Parallel Cable with Shield (0.16A)	13.96%

Table 6-1 above shows that the first cable with the inclusion of the shield gives the best total reduction in the flux density present within the sensing region due to the high frequency, 300 kHz, traction current present within the railway track.

Although the inclusion of the shield causes an increase in the flux density in the area around the top of the shield, a reduction is experienced in totality when the changes at each point within the sensing region are assimilated.

Two further comparisons were performed to obtain an understanding in what effect the addition of the cables have on the flux density within the sensing region, and the effect on the inclusion of the shield with the different cable.

The two comparisons described in this section, firstly involve all the un-shielded simulations to find the effect on the flux density within the sensing region due solely to the introductions of the three different cables and hence the different current magnitudes flowing in each. The second comparison describes the effect of including the shield with the three different cables in place..

6.5.1 Direct comparison for all the unshielded Simulation

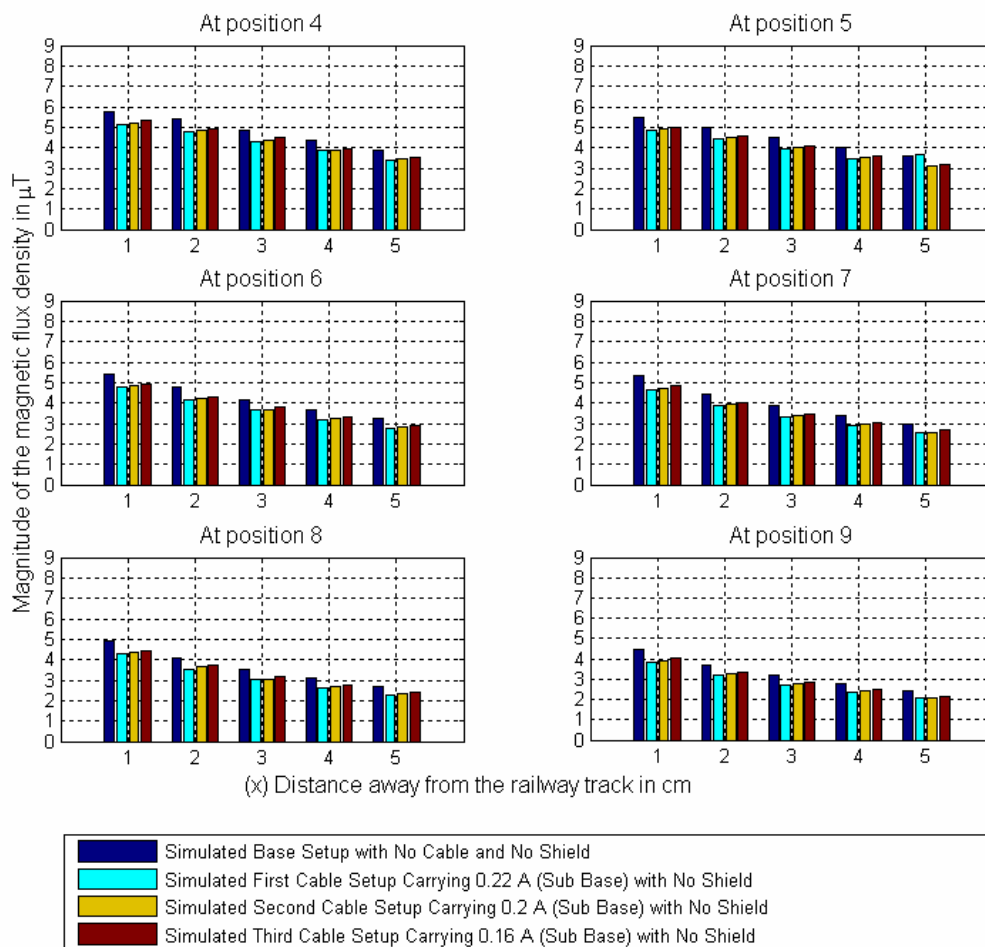


Figure 6-11: Direct comparison for all the un-shielded simulations.

From Figure 6-11 it was observed that the higher the current flowing through the parallel cables the greater the reduction in the flux density within the sensing region. This was due to the fact that the more current which flows through the cable, the less will flow through the railway track, resulting in a lower magnetic field being generated by the railway track. Secondly the greater the current flowing in the parallel cable the greater the opposing magnetic field, which causes a further reduction within the sensing region.

6.5.2 Direct comparison for all the shielded Simulation

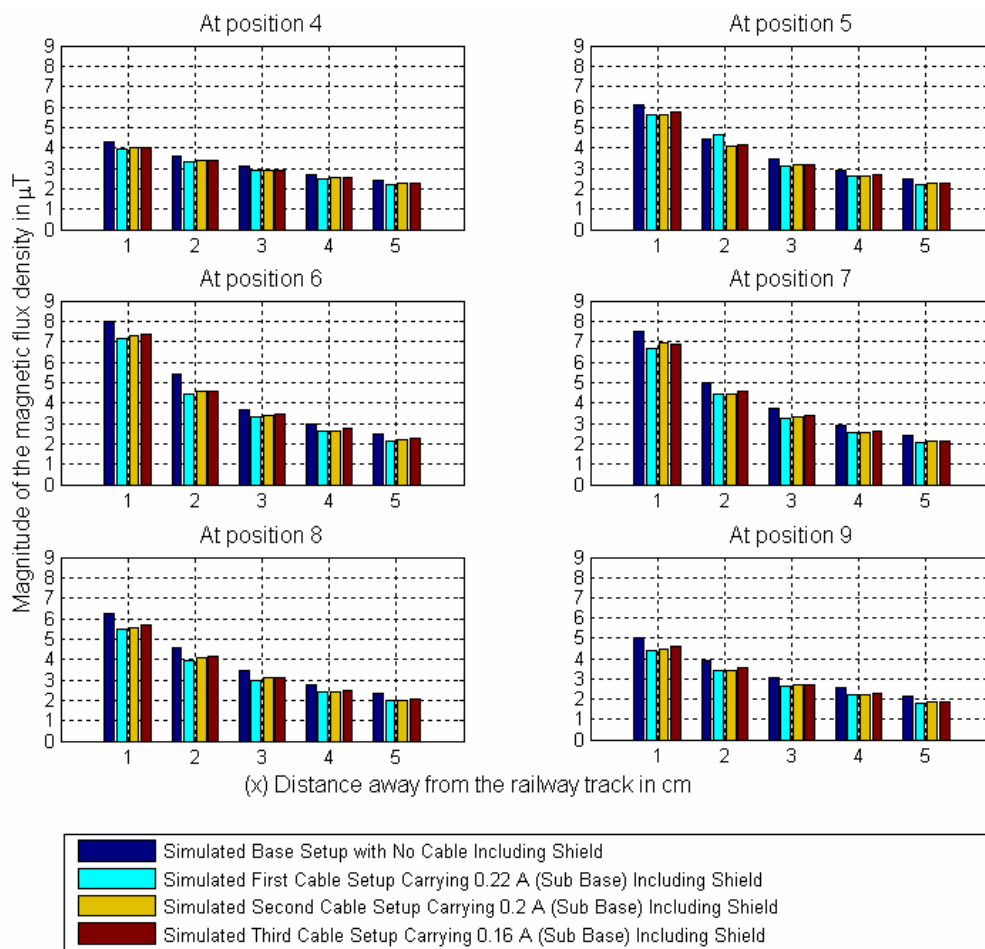


Figure 6-12: Direct comparison for all the shielded simulations.

Figure 6-12 shows that the combination of a shield with the parallel cable causes a further reduction in the total flux density within the sensing region. However a spike in the flux density was experienced in the area around the top of the shield due to the flux lines condensing between the top of the shield and the railway track. Again the cable carrying the highest current results in the greatest reduction in the flux density.

6.6 Other Simulations Performed

Additional simulations were performed to isolate the principles responsible for the change in the flux density within the sensing region for both the measured and simulation results obtained.

These principles include the deflection of the magnetic field due to induced eddy current flowing in the shield, with this effect increasing as the conductivity of the material used is increased. Secondly the absorption principle where the magnetic fields present are absorbed by the material and flow through it instead of flowing in the free space around it, where the field finally exits the material at its opposite end. The absorption of the magnetic field increases as the relative permeability of the material used for the shield increases since an increase in the relative permeability causes a decrease in the resistance experienced by the magnetic field flowing within the material. Details of each principle are presented in section 1.3.3.

To find the effects of each principle, two separate simulations were performed in concert with the first simulation, including a very conductive material with a lower relative permeability assigned to the shield, such as Aluminium, to minimize the absorption effect allowing the determination of the effects due to the deflection principle. To determine the effects of the absorption principle a second simulation was performed by assigning a material to the shield with a high relative permeability and low conductivity, such as a ferrite material, to prevent any influence of eddy currents.

6.6.1 Simulation Illustrating the Deflection Principle

To determine the effects of the deflection principle, aluminium was assigned as the constituent material of the shield. The flux density distribution above the proximity sensor platform and within the test area can be seen in Figure 6-13 below.

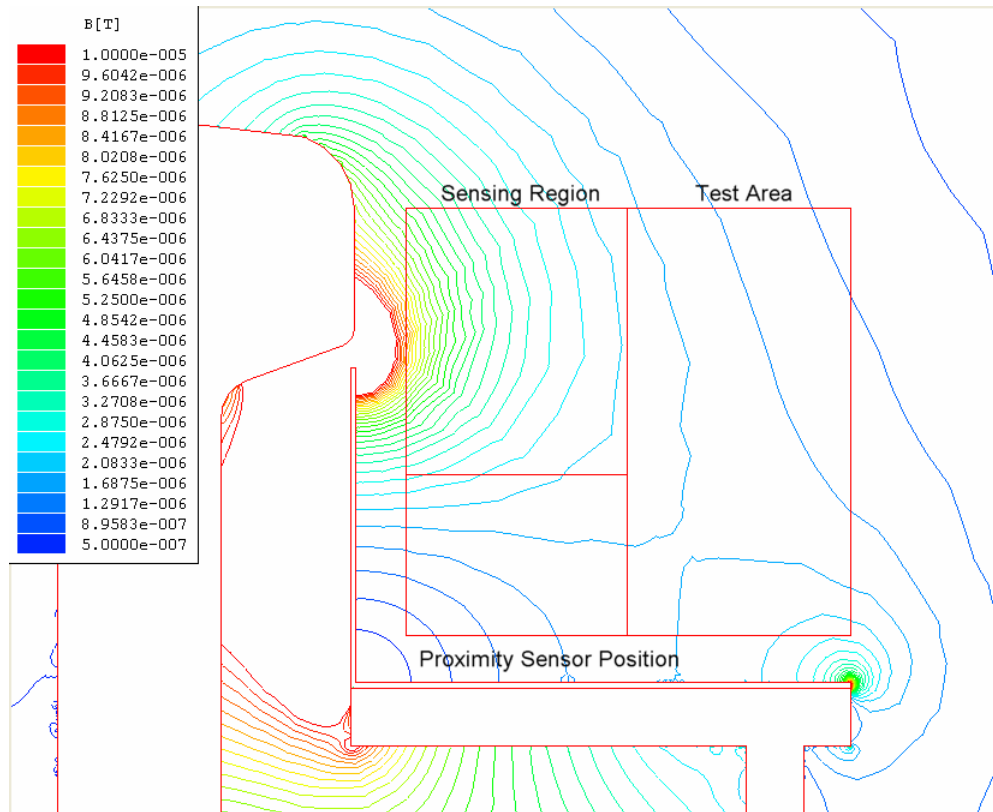


Figure 6-13: Simulated Results showing the Flux Density within the Test Area for the Base Simulation, with the inclusion of an Aluminium shield but no cable, showing the deflection principle.

From this contour plot it was observed that an increase in the flux density, when compared to the base simulation, occurs within the sensing region similar to those observed in all the simulations performed that included a shield. The flux line distribution for this simulation can be seen in Appendix 5.3, which shows how they have been deflected by the shield and forced to condense between the top of the shield and the railway track, resulting in the increase in the flux density within this region.

6.6.2 Simulation Illustrating the Absorption Principle

For the absorption principle, ferrite was assigned as the material for the shield in the simulation performed. The results of this simulation showing the flux density above the proximity sensor platform and within the test area is shown in Figure 6-14 below.

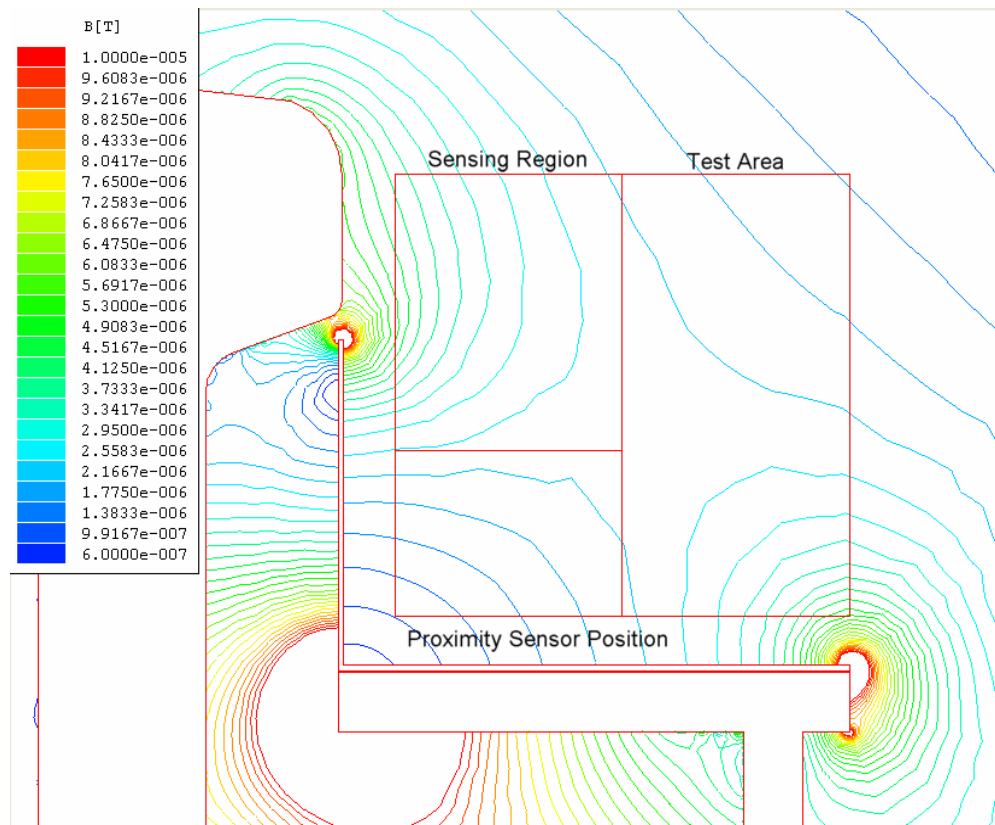


Figure 6-14: Simulated Results showing the Flux Density within the Test Area for the Base Simulation, with the inclusion of a Ferrite shield but no cable, showing the absorption principle.

Through observation of Figure 6-14 it was noted that the flux density spike noticed previously in the deflection simulation is noticeably reduced due to the material properties of the shield. Also, the region to the lower right of the test area has experienced an increase in flux density as the magnetic field that was absorbed exits the shield at this area. Looking at the contour plots for the flux lines, shown in Appendix 5.3, it can be seen how they flow into the top of the shield close to the railway track and out of the opposite end of the shield to the right of the proximity sensor platform.

The flux density within the test area and the sensing region appears lower when compared to the base simulation. With a definite reduction in the flux density within

the sensing region when compared to the simulation depicting the deflection principle, shown in Figure 6-13.

6.6.3 Direct comparison of the flux densities for the simulations of the deflection and absorption principles

A direct comparison between the base simulation, deflection principle involving the aluminium shield and the absorption principle involving the ferrite shield was performed to elucidate the effects of each with respect to the base simulation.

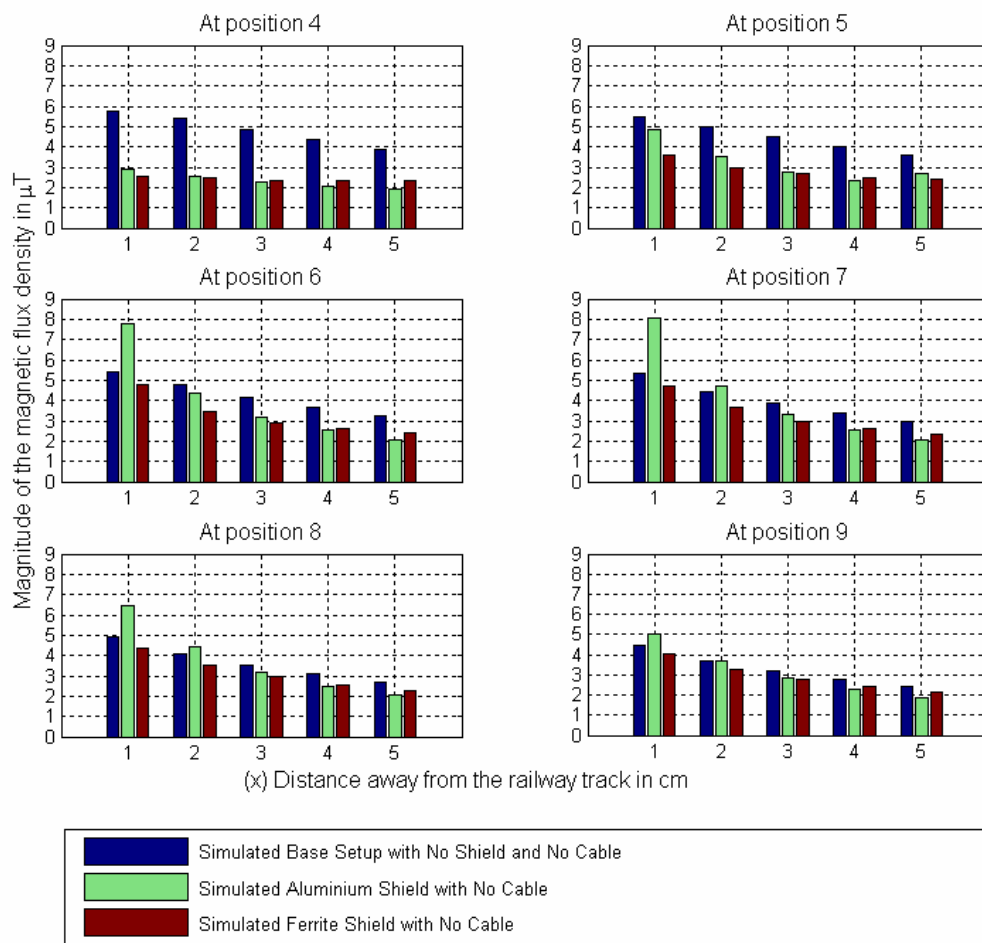


Figure 6-15: Direct Comparison between the Base simulation, deflection simulation and the absorption simulation.

As can be seen in Figure 6-15 the deflection simulation involving the aluminium shield results in an increase in the flux density for the first two points on the X axis at Y axis positions 6 and above. The results obtained from the absorption simulation involving the use of a ferrite shield shows a reduction in the flux density everywhere

within the sensing region with no spikes as those common to the deflection simulation.

The total reduction attained from the deflection simulation compared to the base simulation was 16.38%, where the total reduction within the sensing region for the absorption simulation was 27.6%, which is about an eleven percent improvement with the addition that no spikes occurred anywhere within the sensing region but generated a reduction at all positions within it.

For Figure 6-15 it can also be seen that the aluminium shield provides greater decrease in the flux density further away from the shield compared to the ferrite shield. A reason for this can be seen when comparing the two flux density contour plots shown in Figure 6-13 and Figure 6-14, where an increase in the flux density can be noted to the lower right of the proximity sensor platform at the end of the ferrite shield compared to the same position for the aluminium shield, due to the fact that the magnetic field flows through the shield and exits at this position.

A comparison was performed between the two flux density contour plots shown in Figure 6-13 and Figure 6-14, which represents the deflection and absorption principles respectively, and the contour plots for the measured and simulated results. This comparison showed that the flux density contour plots for the measured results resembled the contour plot for the absorption principle, and that those for the simulation results resembled the contour plot for the deflection principle. This means that the material utilized for the shield used to obtain the measured results had a low conductivity and a high relative permeability resulting in the absorption principle dominating. For the simulation results the conductivity of the material used was high enough with a low enough relative permeability to allow eddy currents to flow and hence the deflection principle to dominate.

In addition by comparing the direct comparison performed for the deflection and absorption principles, shown in Figure 6-15, to the direct comparisons performed for the measured and simulated results, the same observation was made. An additional observation of these indicated that the absorption principle yields a greater reduction in the flux density within the sensing region compared to the results where the deflection principle dominates.

And finally when comparing the patterns visibly in the flux density contour plots for the deflection and absorption principles to the contour plots produced from the low frequency test in section 2.3 in Figure 2-7 and Appendix 1 it can be seen that the deflection principle dominated in these tests since a shield constructed from a different material was employed compared to the shield used for the high frequency measurements. For the low frequency tests a stainless steel shield with a very low relative permeability was employed where a mild steel shield, which had a high relative permeability, was used for the high frequency tests.

6.7 Differences between the simulated and measured results

The principle differences between the physical measurements performed and the simulations are as follows:

- *The materials used for the shields in each case differed resulting in different principles dominating the measured and simulated results respectively.*
- *The proximity sensor platform drawn for the simulations differed compared to the setup in the laboratory, as the real platform contained slits along its length parallel to the railway track and holes drilled in to it.*
- *The parallel cable for the measured results was held in place by hollow square tube with the same length as the proximity sensor platform, which would effect the magnetic field produced around the cable, where in the simulations the parallel cable was placed free next to the proximity sensor platform and not within an enclosure as this would shield the magnetic field and keep it within the enclosure.*
- *The simulation presumes that the structure of the model used is infinitely long, this includes the railway track, the proximity sensor platform, the parallel cable and the shield, which was not true for the setup used in the laboratory to obtain the experimental results, where the proximity sensor platform and the shield used had a much shorted length compared to the railway track and thus the possibility that fringing effects would influence the measurements..*
- *And finally the presence of the shielded Flux Density Sensor within the test area when measurements are taken will have an effect on the measurements taken, where for the simulation results there was no shielded coil placed within the test area to obtain the results.*

7 Conclusion

The principle foci of this investigation were to develop means by which the train wheel detection system's susceptibility to magnetic interference could be reduced. This would result in a reduction in the occurrence of errors in the counting of the train wheels, which ensures the generation of more accurate information, thereby making the system itself more robust.

To achieve these objectives it is crucial to reduce the magnetic interference present within the region occupied by the sensing field of the proximity sensor, dubbed the sensing region, and is situated in the area above the device. Two paths are available to achieve this reduction in the interfering magnetic field. One path involves the installation of a metal shield between the proximity sensor and the railway track to either deflect or absorb the flux lines away from this sensing region.

The second path entails the installation of a cable running parallel to the railway track, with the proximity sensor platform intervening between the two, connected some distance before and after the proximity sensor platform. This path results in a reduction in the current flowing within the railway track thereby reducing the magnetic field it generates. A further reduction in the magnetic field present within the sensing region occurs due to the opposing magnetic field setup by the current that flows in the same direction within both the railway track and the parallel cable.

Experimental measurements were performed at 300 kHz, incorporating the paths available, both independently and together. The results of these experimental measurements yielded a reduction in the flux density present within the sensing region on integration of the shield and again for each of the three parallel cables tested. The greatest reduction was achieved when the two paths were applied in conjunction. Of these, the maximum reduction in the magnetic flux density within the sensing region was accomplished with the installation of the second cable, carrying a 0.2A peak current in combination with the mild steel shield placed between the proximity sensor and the railway track on top of the proximity sensor platform with the inclusion of isolation placed between the it proximity sensor platform..

Simulations were performed at 300 kHz, again incorporating the afore mentioned paths available, both separately and in combination. The results of these simulations served to vindicate the measured results in addition to reinforcing the notion that the introduction of the shield had a positive effect in reducing the magnetic flux density within the sensing region. Also the inclusion of the parallel cable, which carried the three independent currents used to emulate the placement of the three distinct cables tested for the experimental measurements, yielded a reduction in the flux density within the sensing region.

For the simulation episodes, however, the cable carrying the highest peak current of 0.22A produced the greatest reduction in the flux density and the cable carrying the lowest current of 0.16A produced the smallest reduction. The reduction was further enhanced by the inclusion of the shield with the parallel cable producing the maximum reduction for the simulations performed.

On collating the results for the experimental measurements to those derived from the simulations it was discovered that the absorption principle dominated for the measured results whereas the deflection principle dominated for the simulation results. This discrepancy in dominance is due to the material properties of the shield and it can be concluded that the metal assigned to the shield for the simulations had a higher conductivity and lower relative permeability than that used for the shield in the experimental results.

Through comparison between the results obtained from both the simulations and experimental measurements it was determined that the absorption principle provided the greatest improvement in reducing the magnetic flux density within the sensing region. Also the absorption principle resulted in no increase in the flux density within the sensing region compared to the base measurement thus resulting in a reduction in the flux density throughout the region. Conversely, the deflection principle produced increases in the flux density in the area of the sensing region closest to the gap between the shield and railway track.

However, further away from the shield, it was the deflection principle which produced a greater decrease in the flux density than compared to the absorption principle. This occurrence is explained in terms of the absorption principle yielding an increase in the

flux density to the lower right of the test area, due to the flux lines exiting the shield at its opposite end. Despite this apparent collapse in efficacy, cognition must reflect where the focus of this study resides. It is the sensing region of the proximity sensor which is the driving currency of the investigation and therefore it is the setup which yields the greatest reduction within this specific area that reigns as the ideal option.

In totality from both the experimental and simulated results the greatest reduction in the flux density within the sensing region was obtained through the used of a mild steel shield, where the absorption principle dominated, with the inclusion of the second parallel cable that carried a 0.2A peak current through it, and the introduction of an isolation layer between the shield and the proximity sensor platform. By implementing this solution a reduction of 22.8% was obtained in the experimental results.

To conclude, this study through its ingenuity and scientific vigour has managed to reconcile the pertinent problem in the field with a plausible solution developed via experimentation and simulation, these being the cornerstone sections of this current investigation. To this end it was established that in order to reduce the susceptibility of the wheel detection system to magnetic interference an appropriate setup of complementary interventions would need to be implemented. The results indicate that the most ideal setup would be installing a parallel current carrying cable, in the manner described, with the inclusion of a shield, where the absorption principle dominates, along with the inclusion of an isolation layer. It is through this union that an enhanced robustness of the proximity sensor and hence the wheel detection system is envisioned.

8 Recommendations

To continue with this work some recommendations are listed below:

- *The lower frequency test that served the purpose of establishing whether the introduction of a shield would have any effect of the magnetic field present within the test area should be repeated with the use of the improved measurement system and the mild steel shield. This would be important as it would allow a better comparison between the shielded and unshielded cases allowing the reduction in the flux density to be determined.*
- *Shields constructed from different materials should also be incorporated into the experimental design so as to determine their effects on the flux density within the sensing region. These materials include aluminium, copper, different mild steels with different relative permeability's and conductivities.*
- *Perform tests with the inclusion of different cables which have more known properties, for example the number of strands of wire it contains with the thickness of each.*
- *Construction of the improved resonant converter, which includes the higher frequency driving circuit and resonator, to produce higher frequency traction currents. These higher frequency traction currents would allow experimental measurements to be performed at the higher frequencies of 600 kHz, 800 kHz and 1 MHz not covered in this study.*
- *Finally to verify the findings obtained through the experimental measurements repetition of some of the tests performed is encouraged.*

9 References

- [1] J.D. Kraus, D.A. Fleisch, *Electromagnetics with Applications*, 5th Edition. New York: McGraw-Hill, 1999.
- [2] K. R. Demarest, *Engineering Electromagnetics*, Upper Saddle River, New Jersey: Prentice Hall, 1998.
- [3] T. Wildi, *Electrical Machines, Drives, and Power Systems*, 4th Edition. Upper Saddle River, New Jersey: Prentice Hall.
- [4] J. C. De Beer, “Analysis of the environment around a current carrying railway track”, South Africa, Rau 2003, unpublished.
- [5] *Using Matlab Graphics*, Version 6, Math Works Inc., 2003.
- [6] T. Williams, *EMC FOR PRODUCT DESIGNERS*, 2nd Edition, Great Britain: Newnes, Reed Educational and Professional Publishing Ltd 1992, 1996.
- [7] Timothy L. Skvarenina, *The Power Electronics Hand Book Industrial Electronics series*, London, CRC Press LLC 2002.
- [8] Dr IW Hofsajer, *Study Guide, Power Electronics*, January 2003 Department of Electrical and Electronic Engineering, RAU, Johannesburg, Gauteng, South Africa.
- [9] Ansoft Corporation. Maxwell 2D Version 11 – Online Help, 2006.

10 Appendices

10.1 Appendix 1: Results for the Low Frequency Test

The contour plots for the combined results of the low frequency tests are now shown below in Figure 10-1 and Figure 10-2.

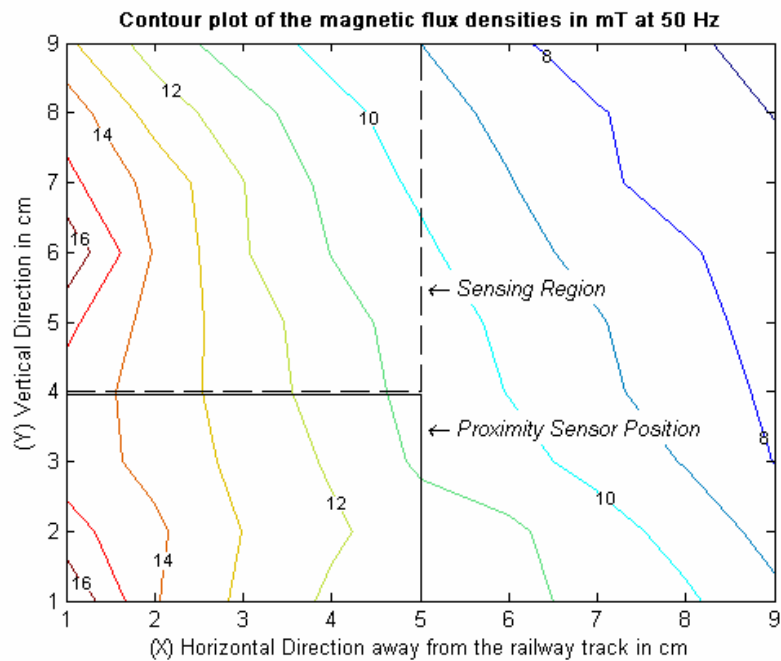


Figure 10-1: Contour plot of the combined magnitude magnetic flux density for the unshielded base measurement at 50 Hz.

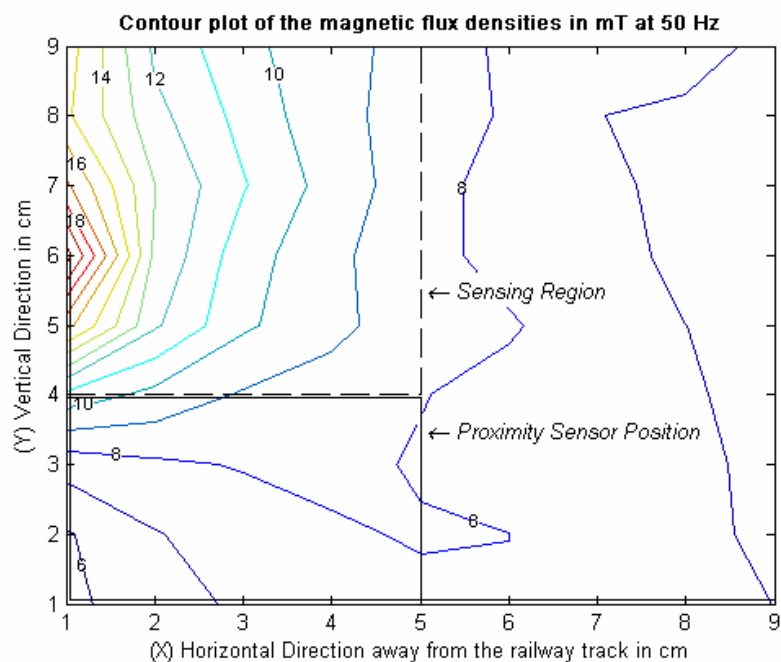


Figure 10-2: Contour plot of the combined magnitude magnetic flux density for the shielded measurement at 50 Hz.

The contour plots for the X component of the magnetic flux densities are now shown.

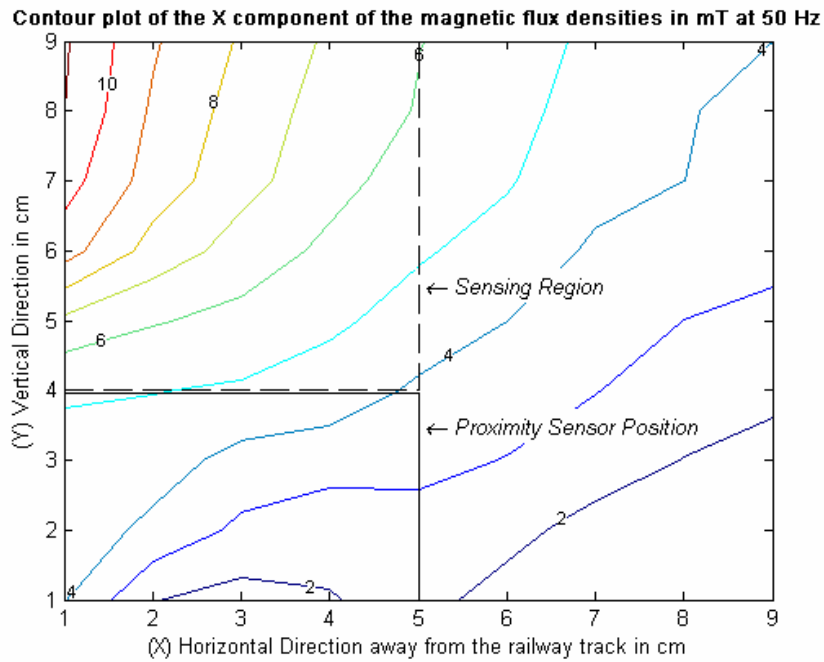


Figure 10-3: Contour plot of the X component of the magnitude magnetic flux density for the unshielded base measurement at 50 Hz.

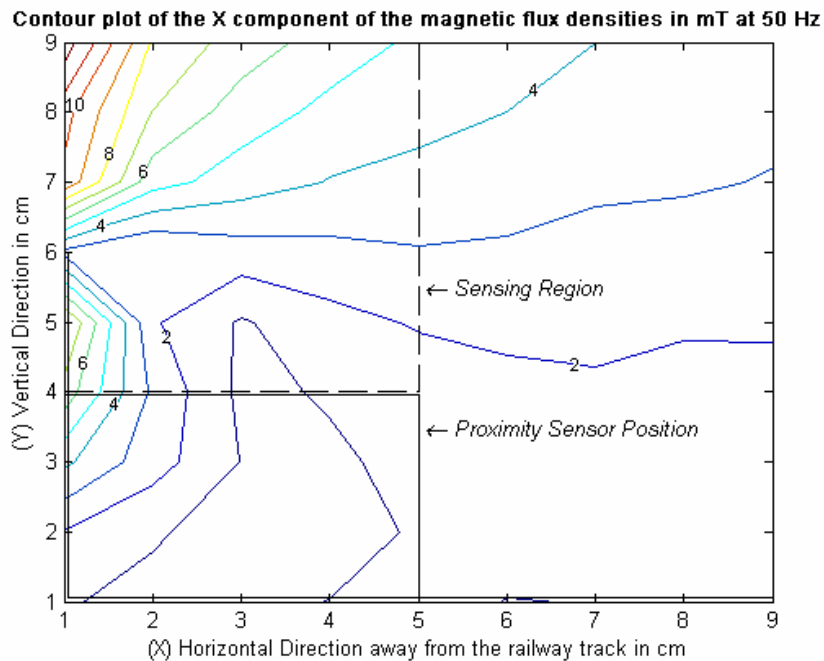


Figure 10-4: Contour plot of the X component of the magnitude magnetic flux density for the shielded measurement at 50 Hz.

By comparing Figure 10-1 and Figure 10-2 it can be seen that the combined magnetic flux density in the test area has been affected and in total reduced by the introduction of the shield. Also by comparing Figure 10-3 and Figure 10-4 the same can be seen.

10.2 Appendix 2: High Frequency Current Source, Resonator

10.2.1 Appendix 2.1: Determination of the laboratory railway track inductance by use of a buck converter

10.2.1.1 Measurement Technique for determining Inductance with the use of a Buck Converter

A buck converter was used for this purpose as it induces a positive and then a negative voltage pulse wave across its inductor with out the introduction of dead time between the pulses. This allows a steady increase in the current through out the positive pulse from a minimum to a maximum value, and then a steady decrease in current during the negative pulse. These voltage and current wave forms are described in Figure 10-5 below.

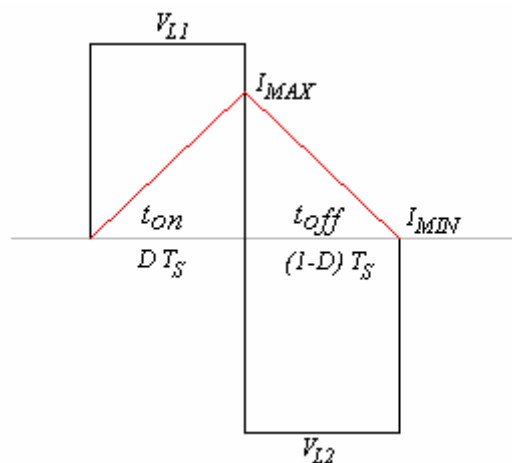


Figure 10-5: Voltage and current wave forms across the inductor of the buck converter.

In Figure 10-5 the following variables were used:

V_{L1}	-	<i>Voltage across the inductor for the positive pulse</i>
V_{L2}	-	<i>Voltage across the inductor for the negative pulse</i>
D	-	<i>Duty Cycle</i>
T_S	-	<i>Period</i>
I_{MAX}	-	<i>Maximum current through the inductor</i>
I_{MIN}	-	<i>Minimum current through the inductor</i>
t_{on}	-	<i>Time when the switch of the converter is conducting</i>
t_{off}	-	<i>Time when the switch is not conducting (open)</i>

To determine the inductance of the railway track, it was connected in series with the main inductor (or safety inductor) of the buck converter, and the voltage wave form

shown in Figure 10-5 was displayed on an oscilloscope and the main values marked in the figure were recorded.

These values consists of the maximum and minimum current through the inductor, the voltages across it for both the positive and negative pulses (V_{L1} and V_{L2}), and finally the period and the duty cycle used.

As a starting point for determining the inductance of the buck converter the equation that describes the voltage across an inductor was used and is below.

$$V_L = L \frac{di_L}{dt} \quad (10-1)$$

Solving for the inductance the subsequent equation was derived.

$$L = \frac{V_L \cdot dt}{di_L} \quad (10-2)$$

For the positive pulse portion of the voltage wave (V_{L1}), the change in time (dt) can be represented by the duty cycle multiplied by the frequency ($D \times T_S$), and the change in inductor current (di_L) was $I_{MAX} - I_{MIN}$.

For the negative pulse portion of the voltage wave (V_{L2}), the change in time is equal to $(1-D) \times T_S$, and the change in current is equal to $I_{MIN} - I_{MAX}$.

The following equations for both the positive and negative pulses were derived from previous two paragraphs.

$$L^+ = \frac{V_{L1} \cdot (D \cdot T_S)}{I_{MAX} - I_{MIN}} \quad (10-3)$$

$$L^- = \frac{V_{L2} \cdot (1 - D) \cdot T_S}{I_{MIN} - I_{MAX}} \quad (10-4)$$

From equations 10-3 and 10-4 it must be noted that V_{L2} is negative and $I_{MIN} - I_{MAX}$ is also negative, thus ensuring a positive answer. Also in theory L^+ and L^- are equal, small variations might be observed due to the resolution of the measurements taken.

If the duty cycle is set to exactly 50% (0.5) the pulse voltages V_{L1} and V_{L2} will be equal in magnitude.

And so by using equation 10-3 and or 10-4 the inductance of the railway track can be determined by subtracting the safety inductor from the result obtained.

10.2.1.2 Design procedure for a Buck converter

The buck is a step down converter taking a higher input voltage and outputting a lower voltage relative to the duty cycle used, the circuit diagram of this converter is shown in Figure 10-6 below.

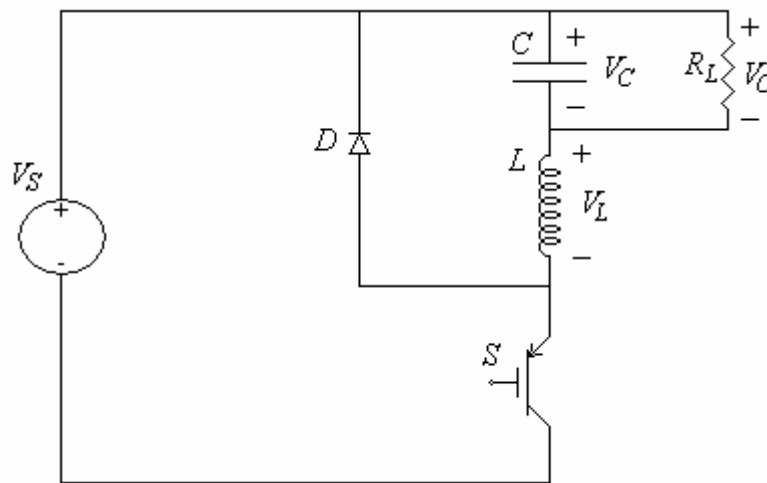


Figure 10-6: Circuit diagram of the buck converter used.

Where:

- V_S - DC Supply Voltage
- D - Diode
- C - Capacitor
- L - Inductor, consisting of the railway track and the safety inductor
- R_L - Resistive Load
- S - Switch (Mosfet)
- V_C - Voltage across the Capacitor
- V_O - Output voltage, which is equal to V_C
- V_L - Voltage across the Inductor

The first design choice was to operate the buck converter at the boarder between continuous and discontinuous mode thus ensuring that I_{MIN} would be zero. Secondly for convenience sake it was chosen to use a duty cycle of 50%.

Using Kirchhoff's voltage law on the circuit given in Figure 10-6 for the cases when the switch S was closed (on), and when it was open (off), equations for the maximum and minimum currents for the two cases were derived.

$$I_{MAX} - I_{MIN} = \frac{1}{L}(V_S - V_O) \cdot D \cdot T_S \quad (10-5)$$

$$I_{MAX} - I_{MIN} = \frac{1}{L} \cdot V_O \cdot (1 - D) \cdot T_S \quad (10-6)$$

By combining equations 10-5 and 10-6 the relationship between the supply voltage and the output voltage relative to the duty cycle was obtained.

$$\frac{V_O}{V_S} = D \quad (10-7)$$

By choosing the duty cycle to be 50% ensures that the output voltage will be half the supply voltage.

The purpose of this buck converter was to produce the wave forms shown in Figure 10-5 to allow the measurement of the railway track inductance, and not provide power to a load. So the purpose of the safety inductor was to limit the maximum current able to flow through the converter, as what ever inductance the railway track may have will have the effect of reducing this maximum current. The maximum current then set by the safety inductor allows the switch to be chosen which can handle the maximum current set.

The safety inductance needed can be derived by rearranging equation 10-5 or 10-6, and choosing a maximum current, frequency of operation and supply voltage.

Once the size of the safety inductor has been determined it can be designed and constructed by using the design procedure given in the next appendix, Appendix 2.2.

And finally ripple capacitance for the buck converter was determined by rearranging equation 10-8 below, (valid for the buck converter). [8]

$$\frac{\Delta V_O}{V_O} = \frac{1}{8} \cdot \frac{1}{L \cdot C} \cdot (1 - D) \cdot T_S^2 \quad (10-8)$$

10.2.2 Appendix 2.2: Design of an Inductor using a Ferrite E-Core

10.2.2.1 Introduction

Ferrite cores provide the following advantages for use in power converter designs.

- *Low flux density*
- *Low conductivity, resulting in no eddy current losses*
- *High frequency capabilities*

The following assumptions were utilized to carry out the design procedure describes in the subsequent section (10.2.2.2 Design Procedure).

- *The magnetic material is linear up to a maximum flux density.*
- *There is no leakage flux.*
- *The fringing in the air gap is neglected (use of a small air gap is imperative).*
- *The core has a constant cross sectional area.*
- *The air gap is uniform and constant.*

A ferrite E-Core has the following structure and is described by the variables given in Figure 10-7 below.

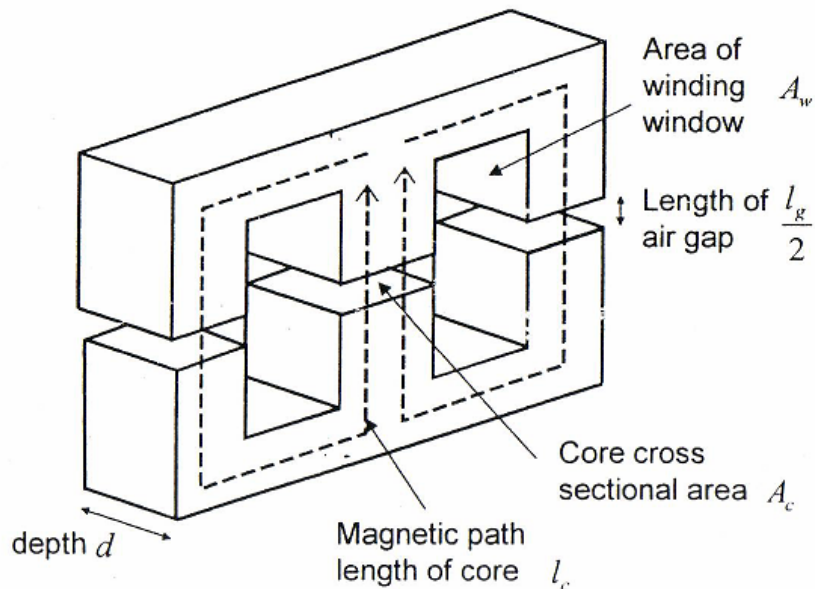


Figure 10-7: E Type magnetic cores, showing some variable definitions. [8]

10.2.2.2 Design Procedure

The procedure required to design an inductor using a Ferrite E-Core consists of eight iterative steps

1. Energy Requirements of the system and capacity of the chosen E-core

Once an E type core has been chosen, the measurements of the magnetic path length (l_C) and core cross sectional area (A_C) are required as well as determining the core properties such as its potential flux density (B) due to the magnetic field intensity (H) at the operating frequency from the core's data sheet.

By using equation for maximum energy in the inductor, equation (10-9), the energy needed to be transferred per cycle was determined.

$$W_L = \frac{1}{2} LI^2 \quad (10-9)$$

The next step involved determining the potential storage capacity of the E-core and equation (10-10) show here below was used.

$$W_m = \frac{1}{2} \hat{B} \cdot \hat{H} \cdot A_C \cdot l_C \quad (10-10)$$

For use in later steps the permeability of the core was required, and found using the relationship given below in equation (10-11).

$$\mu_C = \frac{\hat{B}}{\hat{H}} \quad (10-11)$$

Where

L	-	<i>Inductance of the inductor coil</i>
I	-	<i>Peak current through the inductor at a given time</i>
W_L	-	<i>Maximum energy in the inductor</i>
W_m	-	<i>Energy that can be stored in the core</i>
μ_C	-	<i>Permeability of the core</i>
μ_0	-	<i>Permeability of free space (Air)</i>

l_c - Magnetic path length of core
 A_c - Core cross sectional area
 A_w - Area of the window of the E-core
 l_g - Air gap length
 As defined in Figure 10-7 on pg 147.

2. Establishing the requirement or non requirement of an air gap.

From equations (10-9) and (10-10) a comparison between the total energy (W_L) and the potential energy storage of the inductor core (W_m) was achieved.

If $W_L < W_m$ then no air gap is required, resulting in an air gap length of zero $l_g=0$ resulting in step 3 being disregarded. But if $W_L > W_m$ then an air gap is required to store the excess energy in the system and step 3 must be taken in to account.

3. Required length of the air gap.

The energy needs to be stored in the air gap (W_g) is calculated by subtracting the energy that the core can store from the energy that must be transferred, as described in equation (10-12) below.

$$W_g = W_L - W_m \quad (10-12)$$

From the result of equation (10-12) the required length of the air gap could be obtained by the use of equation (10-13) given below.

$$l_g = \frac{2\mu_0 W_g}{A_c B^2} \quad (10-13)$$

4. Number of Turns required for the inductor.

To determine the number of turns required to obtain the desired inductance of the core the following equation can be used whether an air gap is needed or not.

$$N = \sqrt{\frac{L}{A_c} \left(\frac{l_c}{\mu_c} + \frac{l_g}{\mu_0} \right)} \quad (10-14)$$

Equation (10-14) is only valid if the air gap is small compared to the width of the core.

5. Cross sectional area of wire needed.

To find the cross sectional area of the wire needed for the inductor the peak current density (J) in the wire is chosen to be 3 to 5 A/mm² (which is a good initial guess).

$$A_{Wire} = \frac{I}{J} \quad (10-15)$$

Once the minimum required wire cross sectional area (A_{Wire}) has been determined from equation (10-15), a standard wire with diameter just larger than the calculated minimum is selected.

6. Determination of the maximum number of windings able to be wound around the chosen E-core.

To determine how many windings of the selected wire could fit on the chosen core, the window area (Figure 10-7) of the core was measured, and the previously calculated area divided by this windows area and multiplied by the packing factor to obtain the maximum number of turns that could fit around this core.

$$N_{MAX} = k_p \frac{A_C}{A_{Wire}} \quad (10-16)$$

The packing factor k_p generally lies between the region of 0.5 to 0.7, for this case k_p will be taken as 0.5 as the inductors will be manually wound.

7. Comparison between numbers of turns needed for the inductor required and the maximum number of turn that can fit on the chosen E-Core.

If $N > N_{MAX}$ then a larger core must be chosen, and all steps are repeated.

If $N < N_{MAX}$ then a smaller core can be chosen, and all steps are repeated.

8. Construction and verification of the designed inductor.

10.2.3 Appendix 2.3: PCB Design of Driving Circuit and 300 kHz Resonator Board

10.2.3.1 Driving Circuit of the Resonator (PWM Half Bridge Mosfet Driver)

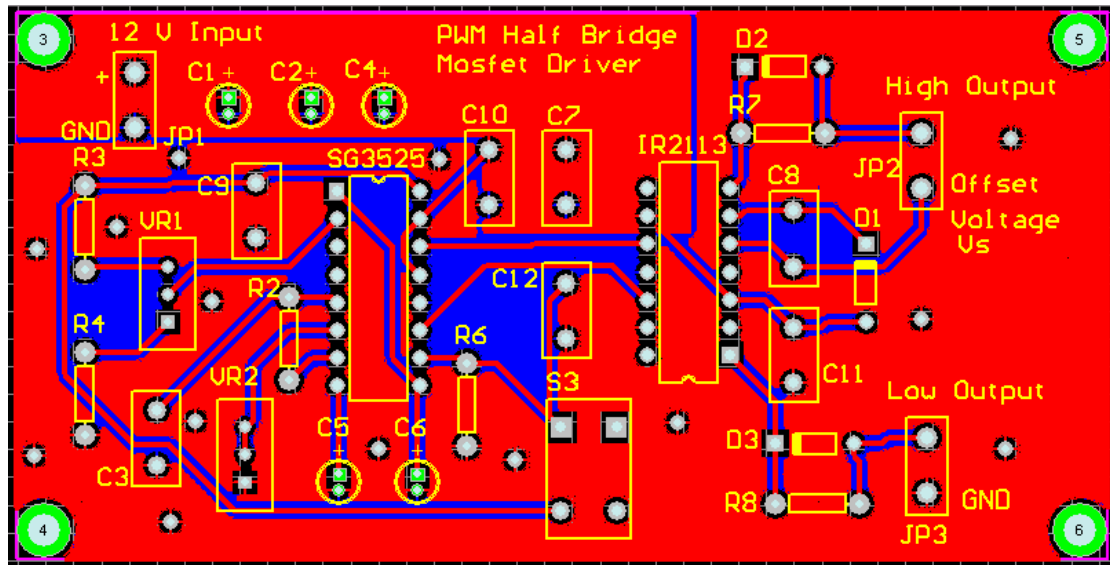


Figure 10-8: PCB of the Driving Circuit or PWM Half Bridge Mosfet Driver.

The PCB for the Driving Circuit was designed to be two sided with a ground plane on its underside (The Blue Layer visible from under the top red layer in Figure 10-9). This allowed the returning current to follow the path of least inductance, hence least impedance, which means that the return path used will lie as close to the supply path as possible and so reducing the inductance in the circuit. The ground plane also provides shielding on the bottom layer. The PCB was designed with dimensions of 100 by 50 mm.

The supply portion of the PCB (top left), which includes the supply connector (labelled 12 V Input) and the regulation capacitors, (C1, C2 and C4), was placed on top of a large layer with connections to the high voltage input (12V) from the supply. This was done to increase the capacitance of the supply portion to provide better voltage regulation for the driving circuit.

Most of the spaces on the top layer, not occupied by the tracks needed for the driving circuit to operate, were filled by a ground plane with connections, via through hole plating, to the grounded bottom layer. Many connections were used for this purpose to

reduce the resistance between the two layers by providing multiple paths and subsequently ensuring that all the ground layers are at the same level.

10.2.3.2 300 kHz Resonator Board

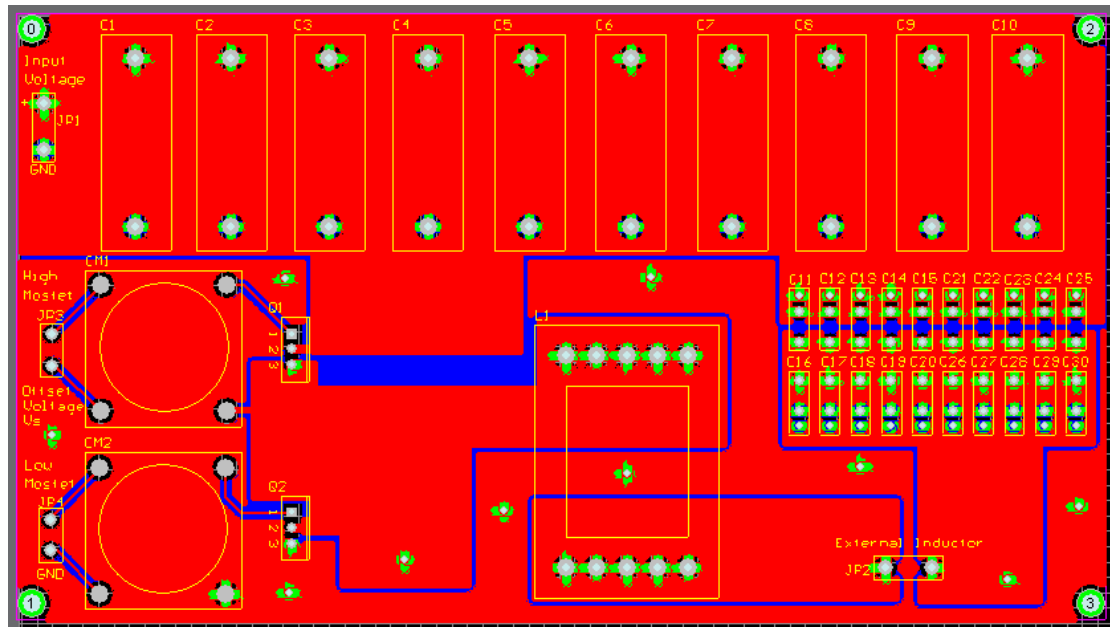


Figure 10-9: The PCB layout of the 300 kHz Resonator Board

The PCB design for the resonator board incorporated thicker copper layers (35 μ m) than for the driving circuit because of higher current requirements, and is also larger with dimensions of 100 by 150 mm.

All tracks on the high current side of the resonator PCB were designed wider to allow the transportation of more current through them with a lower resistance.

The larger input capacitor bank at the top of the PCB shown in Figure 10-9 provided regulation for the supply voltage entering the resonator. This capacitor bank was placed on top of a large layer of copper as to increase the capacitance of this region to assist with the supply regulation.

It must be noted that if the internal inductor used is constructed on anything other than an E42-Core, it cannot be connected on the PCB directly but can be connected in series with the railway track across the External Inductor connector shown at the bottom of Figure 10-9 above.

10.2.4 Appendix 2.4: P-Spice Simulations of the Resonant Converter (Resonator)

Simulations of the resonator board were performed using P-Spice by setting up a model that represented most of the components as real and not ideal. This circuit can be seen in Figure 10-10 below.

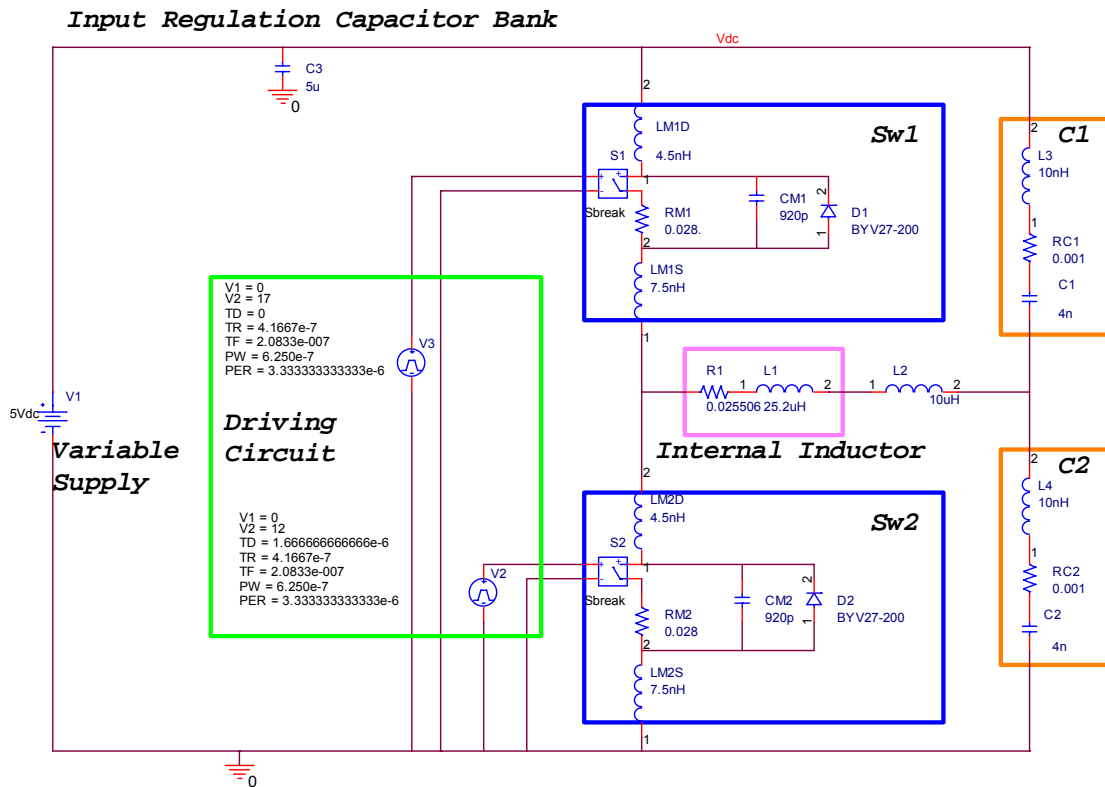


Figure 10-10: Circuit diagram simulated using P-Spice to predict the operation of the real resonator.

In Figure 10-10 *Sw1* and *Sw2* are the high and low side Mosfets respectively with their internal inductance, capacitance and resistance included. These values were obtained from the data sheet for the IRFZ44N Mosfets used (See Appendix 7.3).

For the resonant capacitor banks (*C1* and *C2*) the approximate series inductance and resistance were included, typical values were used that represented the range in which they would be expected to lie.

The Driving Circuit was modelled as two pulse generators each delivering the driving signals to both the high and low side Mosfets.

The expected wire resistance for the internal inductor (LI) was calculated using the expected skin depth at the resonant frequency of 300 kHz and was included in the model as RI .

The capacitance of the tracks on the PCB was omitted since they would usually fall in the range of a few pico-Farads (pF), which is well below the resonant capacitance of 4nF.

The capacitance between the windings of the internal inductor was also considered small enough to neglect since they were very sparsely spaced as only 8.5 turns were put on its E42-Core.

The internal inductance of the capacitor banks and the Mosfets were about 1000 times smaller than the combination of the internal inductor and the railway track, with the result that they contribute little to no effect on the resonant current, and voltage in the system.

The internal resistance of the capacitor bank is typically very small and has very little to no effect on the resonant current and voltage in the system.

Noisier switching of the Mosfet occurs due to its internal inductance and capacitance.

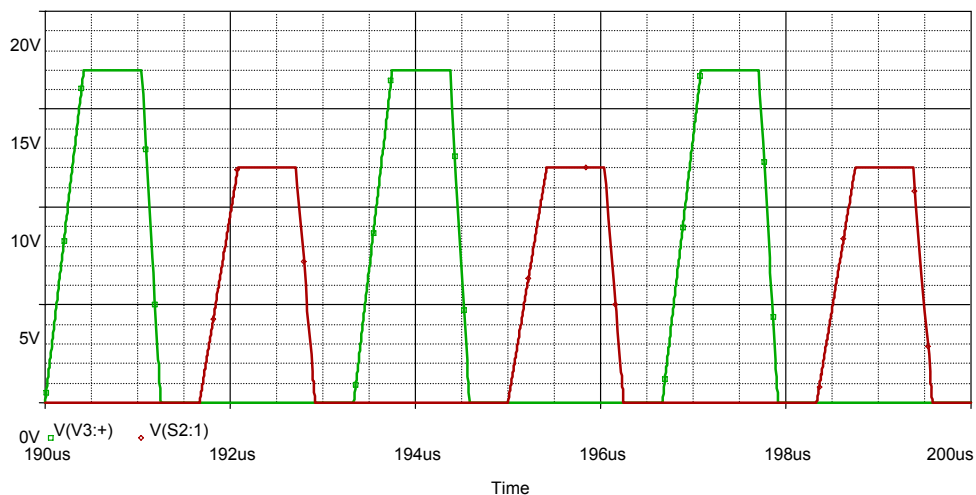


Figure 10-11: Driving signal being supplied to the high and low side Mosfets by the driving circuit.

Figure 10-11 displays the output signal from the driving circuit, which turns the Mosfets on and off. The shape of the wave forms are an approximation of the wave

forms observed from the output of the constructed driving circuit shown in Section 3.2.4.3.

To achieve this, the rise time was set to $0.41667 \mu\text{s}$ and a fall time of $0.20833 \mu\text{s}$, which has a similar shape to the observed output of the Driving Circuit.

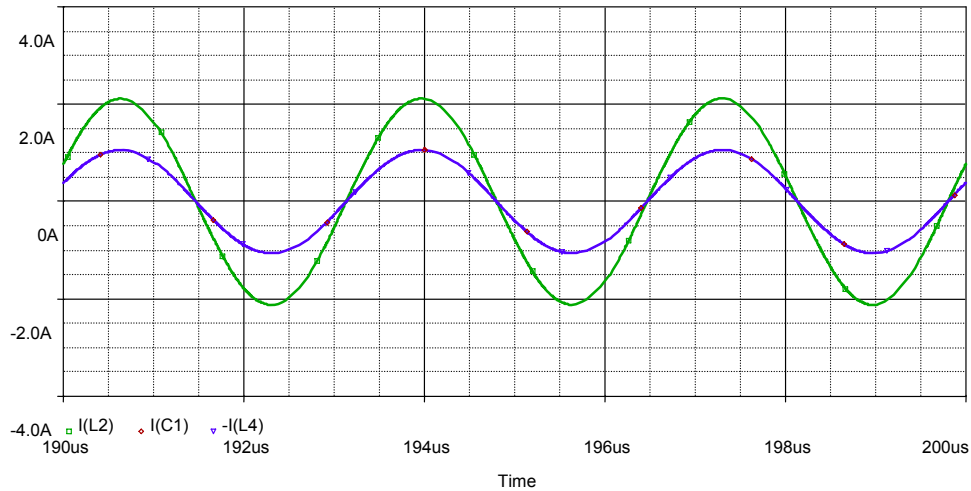


Figure 10-12: Current through the internal inductor and the railway track, and the currents flowing through the two capacitor banks $C1$ and $C2$.

From the simulation model the predicted resonant current that should flow through the railway track is just over 2A at 300 kHz, which meets the requirements needed for the resonator to perform well in generating the traction current needed for the high frequency tests.

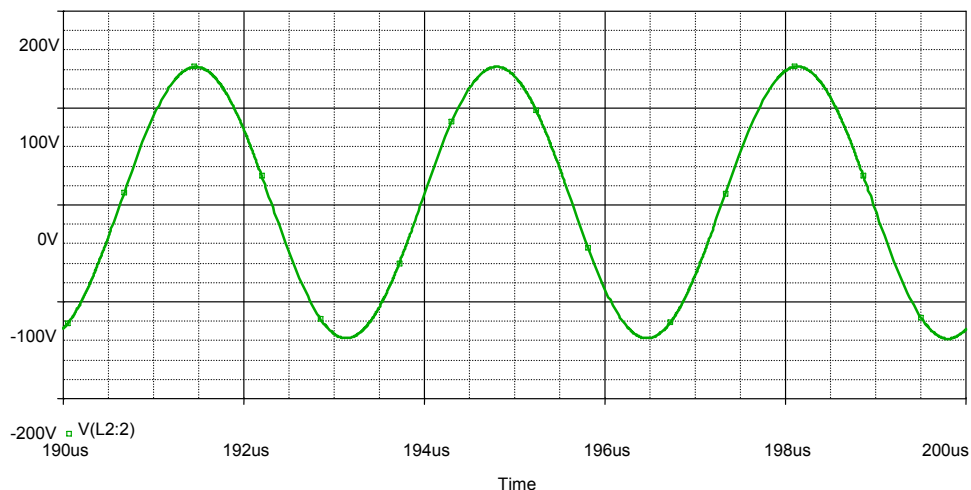


Figure 10-13: Resonant voltage between the two capacitor banks ($C1$ and $C1$) and the Railway Track.

The peak of the predicted resonant voltage lies just above 140V.

10.2.5 Appendix 2.5: Testing of the 300 kHz Resonator

The constructed 300 kHz Resonator was tested in its final operational setup with the railway track connected across its output terminals. The PWM of the Driving Circuit was set to the operational frequency of 300 kHz providing the desired switching frequency, and its pulse width was set to a maximum thus ensuring the maximum current flow through the railway track.



Figure 10-14: Test setup used along with the railway track.

The driving signal for the high and low side Mosfets was measured and is shown in Figure 10-15 below.

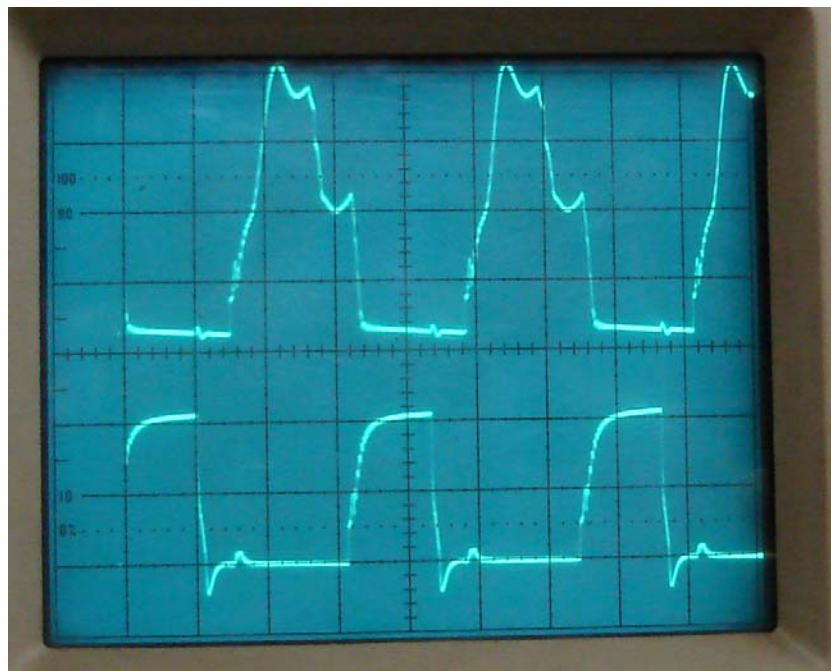


Figure 10-15: Driving signal sent to the high and low side Mosfets of the 300 kHz resonator board

The waveform at the top of Figure 10-15 shows the driving signal for the high side Mosfet, which has a magnitude of 10V (to activate the Mosfet) plus 9V (supply voltage) giving a total magnitude of 19V. This rise time of the driving signal was found to be 0.832 μ S.

The driving signal for the low side Mosfet, the bottom wave form shown in Figure 10-15, has a magnitude of 10V. The rise time of the driving signal was found to be approximately 0.4167 μ S with a fall time of 0.208 μ S which was applied to the simulation in Appendix 5, to try and predict the behaviour of the resonator.

The current through the resonator and therefore the railway track was measured using a current probe and is displayed in Figure 10-16 below.

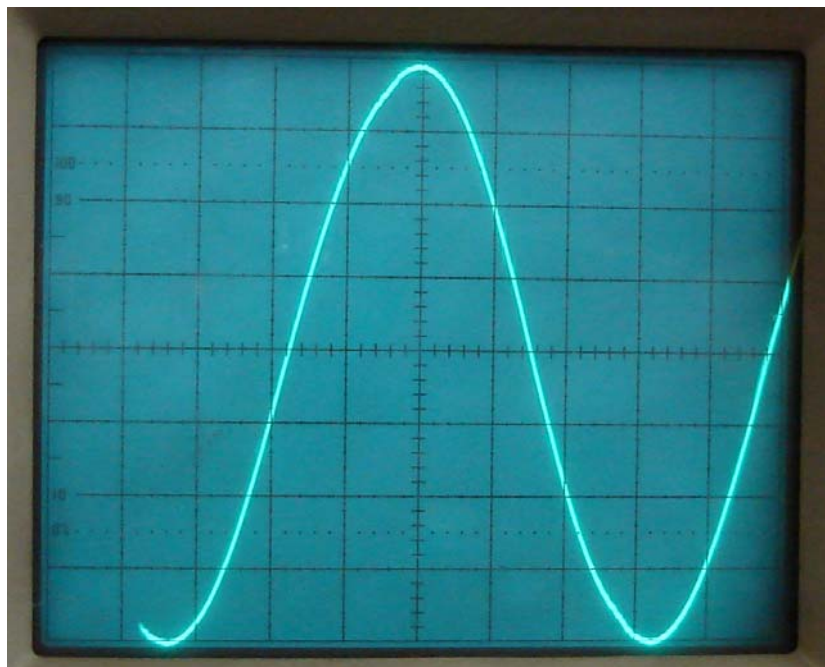


Figure 10-16: Measurement of Current Flowing Trough the Railway Track.

From Figure 10-16 the railway track current can be seen with a magnitude of 2A, to achieve this, a supply voltage of 9V was required which is higher than the predicted supply voltage.

The resonant voltage between the capacitor banks was also measured and has the following wave form.

It was found that the resonant voltage between the capacitor banks and the railway track had a magnitude of 135V (larger wave form in Figure 10-17 on pg 158), with a resonant voltage of 100V (smaller wave form in Figure 10-17 on pg 158) between the

internal inductor and the railway track, resulting in a 35V peak voltage wave form across the railway track.

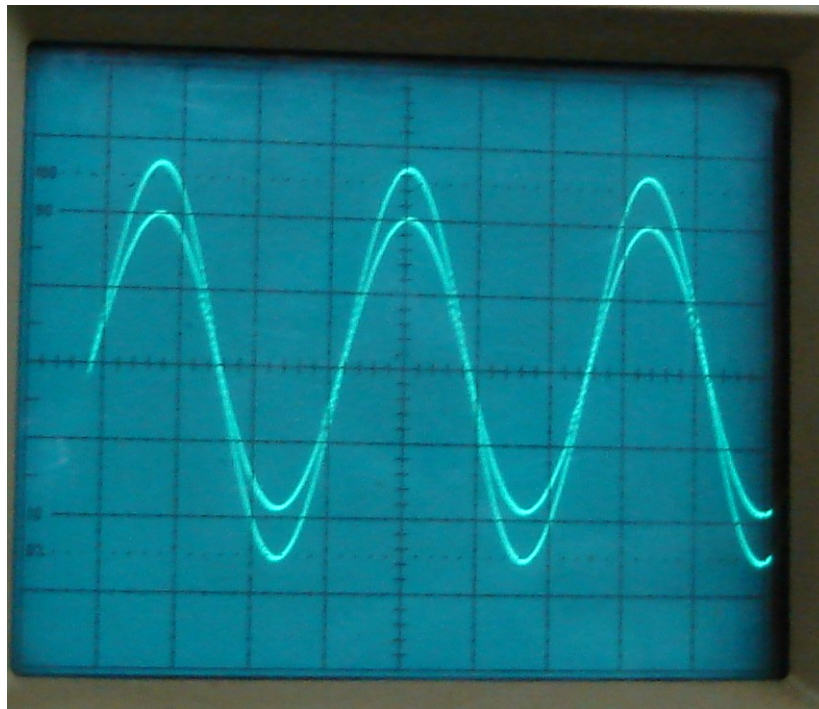


Figure 10-17: Resonant voltage between the capacitor banks and the railway track, with the resonant voltage between the internal inductor and the railway track

10.2.5.1 Differences between the simulated and constructed resonator

The main differences between the simulated and constructed resonators were, that the supply voltage needed to attain a peak current of 2A through the railway track was higher, and the driving signal in the constructed resonator was not as neat as the one predicted in the simulation.

The distorted driving signal was in part responsible for the higher supply requirements since the on time of the high side Mosfet was lower in the constructed resonator compared to the simulated version.

Mainly the need for an increased power supply was due to unaccounted resistance in the circuit, and deviation from the approximate measured inductance of the railway track.

For the constructed resonator the resistance of the tracks on the PCB, as well as the resistance of the railway track loop connected to it were not taken into account. An

increased resistance in the resonant circuit of the resonator would have the result of increasing the dampening (hence the dampening ratio) present in it. The side effect of an increase in the dampening is a reduced maximum current flowing through the resonator.

Any error in the measurement of the inductance of the railway track would result in a change in the inductance of the resonant circuit shifting its resonant point away from the desired 300 kHz resulting in a drop in the resonant current allowed to flow through the circuit. Even a small difference between the operating and resonant frequency of the resonator can result in a dramatic change in its operation.

An error of as little as $1\mu\text{H}$ in the measured railway track inductance can cause a drop substantial drop in current, as found using the simulation described in Appendix 2.4 and manipulating the railway track inductance.

10.2.6 Appendix 2.6: New PCB Layouts for the New Higher Frequency Driving Circuit and Resonator Board

10.2.6.1 PCB Layout of the New 300 kHz to 1 MHz Driving Circuit

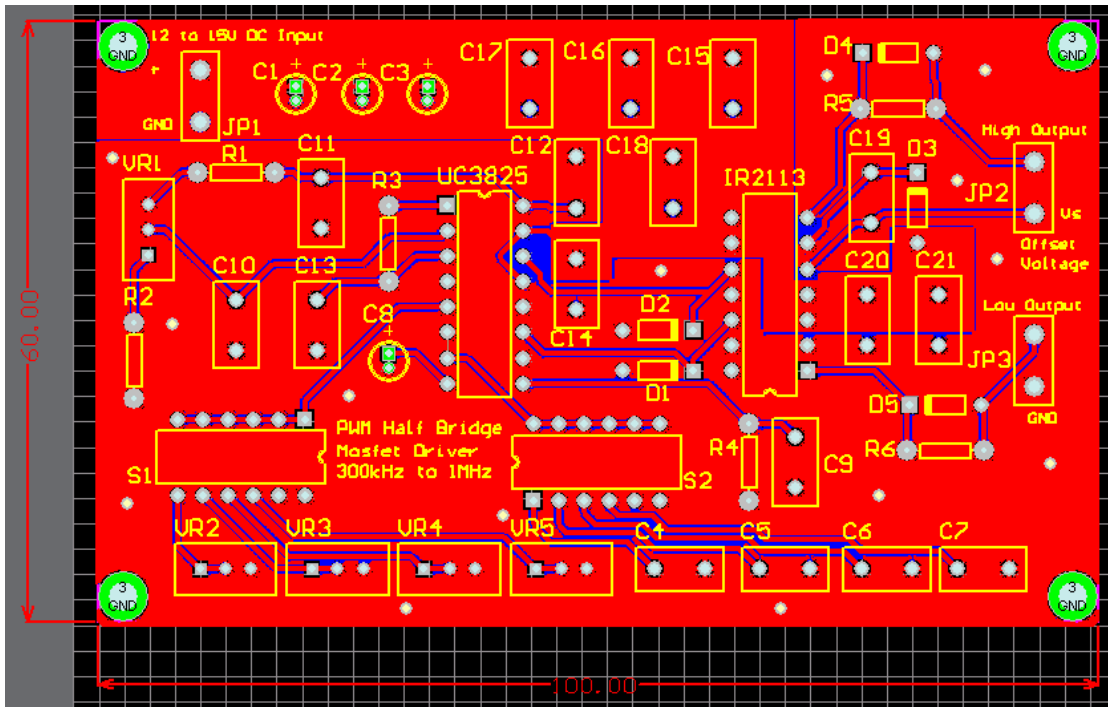


Figure 10-18: PCB for 300 kHz to 1 MHz Driving Circuit, with preset frequency controls.

The PCB layout uses all the same aspects mentioned in Appendix 2.3, except that more filter and regulation capacitors have been added to make it more robust for the higher frequency operation it has been designed for.

The Dip switches S1 and S2 in Figure 10-18 allow the variable resistors VR2 to VR5 and the capacitors C4 to C7, to be switched in to the circuit to attain one of the preset frequencies that were tuned for each variable resistor and capacitor set.

Each Dip switch has 6 on/off (1/0) pins that allow one path to be turned on at any given time. Only the first four of these switches are connected to the circuit the last two are left unconnected, this was done as only 4 connections were needed and this set up facilitates the use of both a 4 switch a 6 switch Dip switch, depending what is available.

Therefore to achieve a frequency of 300 kHz the first switch of both S1 and S2 would be set to on, with all the other switches set to off, thus connecting VR2 and C4 to the PWM IC and setting its operational frequency. For the next preset frequency the second switch on both S1 and S2 would be set to on, with all the other switches set to off, providing the PWM with its next operational frequency.

10.2.6.2 PCB of the New Modified Resonator Board for higher frequency operation

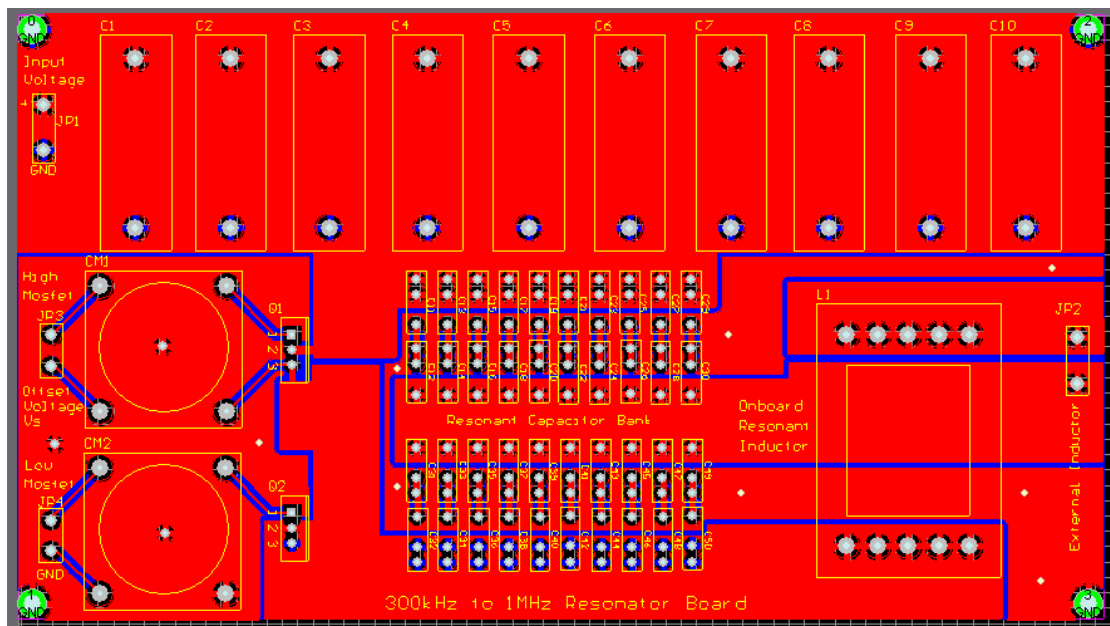


Figure 10-19: PCB of the New Modified Resonator Board for operation from 300 kHz to 1 MHz.

The modified PCB for the higher frequency resonator board used the same dimensions as the previous version, all components and component layouts are the same except for the internal inductor placement, the resonant capacitor banks and the connector for the external inductor.

The internal inductor was moved to the opposite side of the resonator board increasing its distance from the two Mosfets, as it produces magnetic interference that could have a detrimental effect on the operation of the Mosfet by disrupting its driving signal.

Also due to the increase in the operating frequency range of the resonator the relocation of the internal inductor was an advantage since, as the operating frequency

of the resonator increases the distance affected by the magnetic interference produced by it increases.

For the resonant capacitor bank (bottom middle in Figure 10-19) the number on capacitor has been increased from ten parallel capacitors to twenty, with ten parallel combinations consisting of two capacitors connected in series.

This was done to make allowance for a high resonant voltage between the two capacitor banks, which will occur as the resonant frequency increases. This increase in resonant voltage is due to the fact that as the desired resonant frequency increases the ratio between the resonant capacitance and inductance will decrease, which results in an increase in the difference between the magnitudes of the inductance and capacitance needed to obtain resonance.

Due to an increase in the inductance or a decrease in the capacitance the resultant resonant voltage will be higher than before to obtain the same current magnitude to flow through the railway track.

10.3 Appendix 3: Initial Improvement to the Measurement System to reduce its Susceptibility to Electro-Magnetic Interference

For the First iteration steps were taken to reduce the effects of Electro magnetic interference generated by the railway track system on the measurement system. The use of shielding, in the form of screened cable and conductive tape, was employed along with reducing the magnetic loop area between the conductors used in the measurement system.

The four main steps used to improve the measurement system are listed here below.

1. The first was to consider the winding layout of the sensor and where the ground terminal of the oscilloscope should be connected (Covered in chapter 4.3.2.1).
2. Wrapping a grounded copper shield around the sides of the sensor and so reducing the coupling on it (Covered in Chapter 4.3.2.2).
3. The use of shielded cabling to connect the sensor to the oscilloscope to prevent coupling on this path (Chapter 10.3.1).
4. And finally to add shielding to any exposed wire connections in the measurement system (Chapter 10.3.2).

These four steps lead to a much improved measurement system compared to a system comprising no shielding or conductor layout techniques.

10.3.1 Shielded Cable

Now that most of the capacitive coupling on the Flux Density Sensor has been taken care of, but the capacitive coupling as well as the magnetic coupling must also be reduced on the cable connecting the sensor to the oscilloscope.

To do this microphone cable was used since it contains two insulated signal wires within it, along with an exposed ground wire, all tightly wrapped in an aluminium foil shield (See Figure 10-20). The aluminium shield can then be grounded by connecting the exposed ground wire to the ground of the oscilloscope. This will intern reduce the capacitive and magnetic coupling effect on the connection cable.

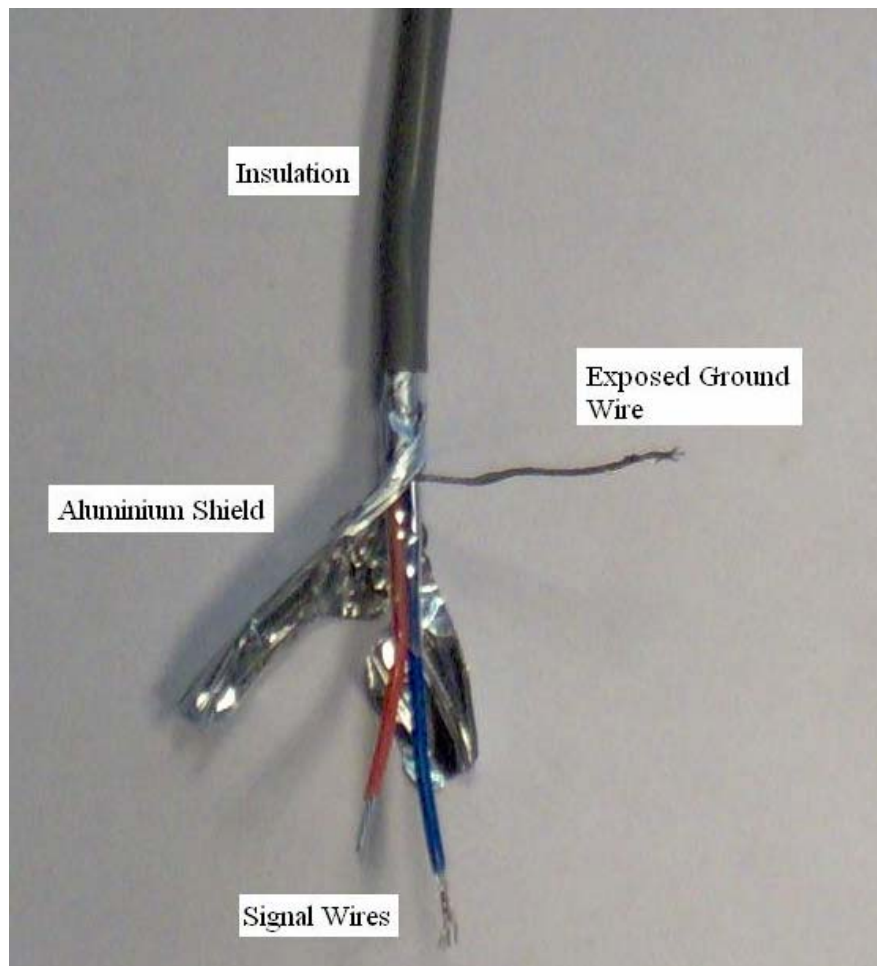


Figure 10-20: Microphone cable.

10.3.2 Connection Shielding

Figure 10-21 shows the Flux Density Sensor connected to the microphone cable, where the red wire is connected to the centre coil of the sensor and the blue wire is connected to the outer coil. At the oscilloscope the red wire is connected to the measurement terminal and the blue wire is connected to the ground terminal. The exposed ground wire is also connected to the ground connection on the oscilloscope, effectively grounding the shield on the microphone cable.

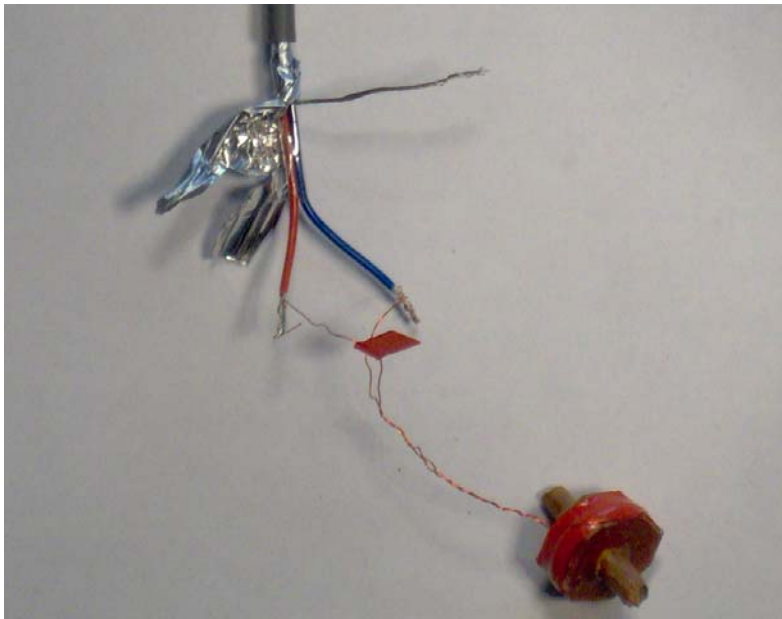


Figure 10-21: Flux Density Sensor connected to the microphone cable.

Once this is completed the only areas left being affected by the electric and magnetic field are the unshielded sections where the sensor is connected to the microphone cable and where the oscilloscope is connected to the microphone cable.

To reduce the effect of the magnetic field the wires were twisted together thus reducing the area that it can couple to, but all the areas can not be totally removed so shielding is needed.

To shield these areas aluminium foil is used. Firstly the exposed connections are insulated, by using insulation tape or heat shrink. Foil is then tightly wrapped around the unshielded areas to prevent any gaps which would allow capacitive and magnetic coupling to occur on the signal wires.

Insulation tape was used to tighten the aluminium foil around the connections to ensure that no gaps are present (see Figure 10-22).

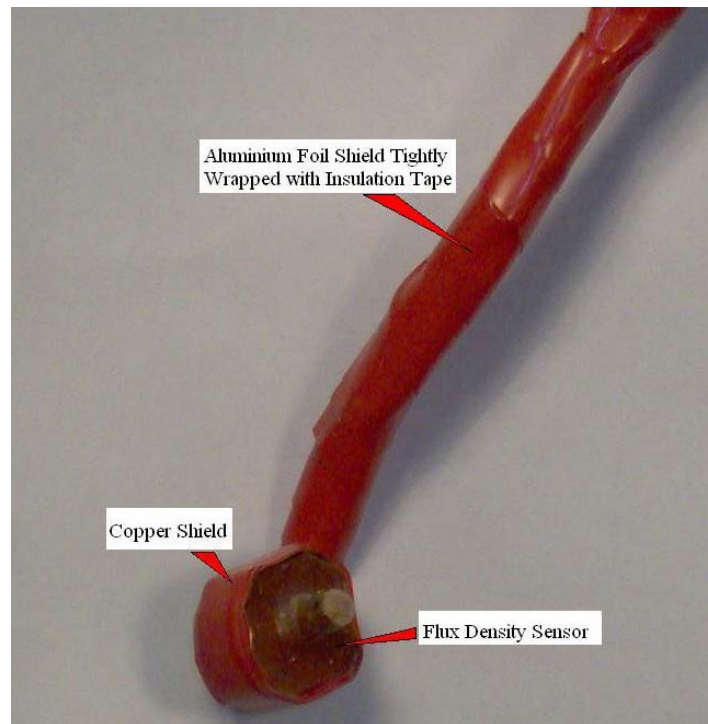


Figure 10-22: Flux Density Sensor connected to microphone cable with connection shielded.

At the oscilloscope end a male BNC connector is used to allow the sensor cable to be connected directly in to the oscilloscope, to avoid wire loops by using an oscilloscope probe (see Figure 10-23).

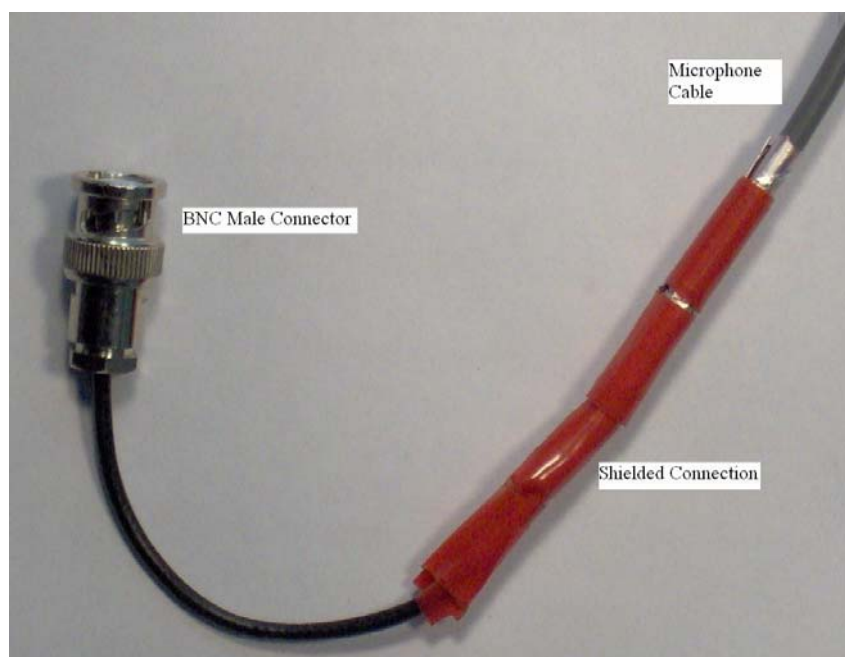


Figure 10-23: Connection to oscilloscope BNC Male Connector, with shielded connection.

10.4 Appendix 4: Experimental Results

10.4.1 Appendix 4.1: Y-Component Contour Plots for Experimental Results showing the measured magnetic flux densities

10.4.1.1 Seventh Test: Second Cable Test set (Sub-Base) with No shield or Isolation

The first cable was replaced by the second and the subsequent tests were performed to determine the effect of the different cable.

A comparison between this test (Figure 10-24) and the fourth test (Figure 5-7) yielded little difference in the pattern of the contour plots, but a difference in the magnitudes can be observed as the flux density to the top left of Figure 10-24 has increased and to the lower right has decreased. The occurrence of this is due to a lower magnitude current, compared to the first cable, flowing through the cable, resulting in a higher current remaining in the railway track.

Contour plot of the magnetic flux densities of the Y component in μT at 300 kHz

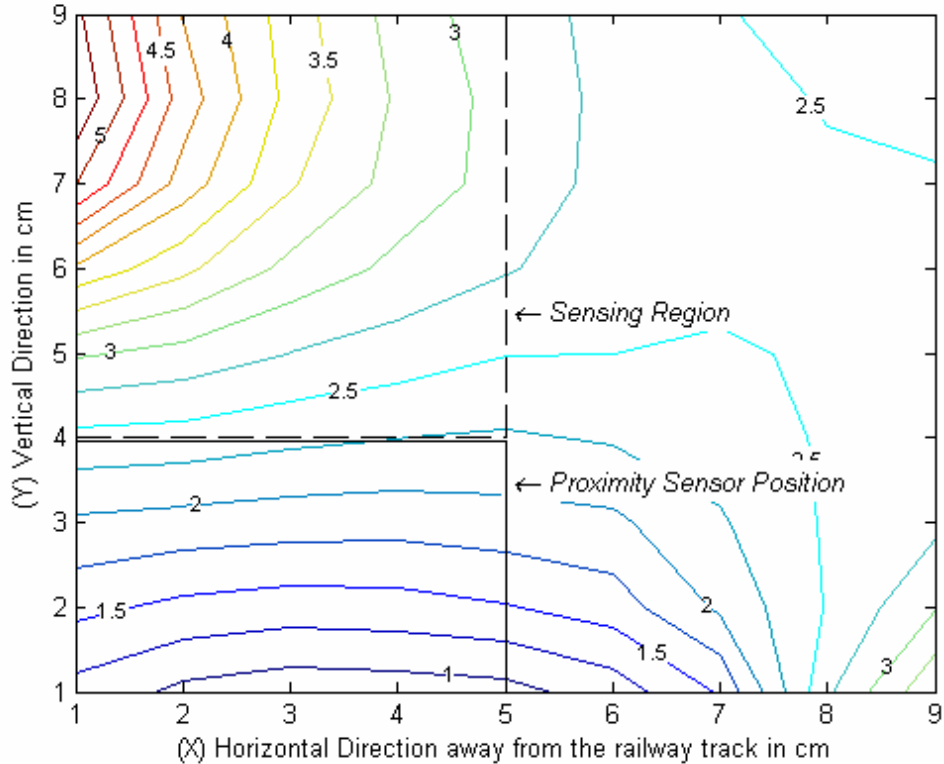


Figure 10-24: Contour Plot of the Y component of the magnetic flux density for the sub-base measurement with the second cable in place with no shield or isolation.

This test compared to the Base measurement yields a definite reduction in the flux density within the sensing region resulting in a lower interference being present.

10.4.1.2 Eighth Test: Second Cable Test set with the inclusion of a shield but no Isolation

The introduction of the shield has the effect of compacting the high magnitude flux density region therefore reducing the total flux density within the sensing region (see Figure 10-25). A more accurate comparison can be obtained by performing a direct comparison between the data sets to determine the difference in magnitudes at specific positions in the test area.

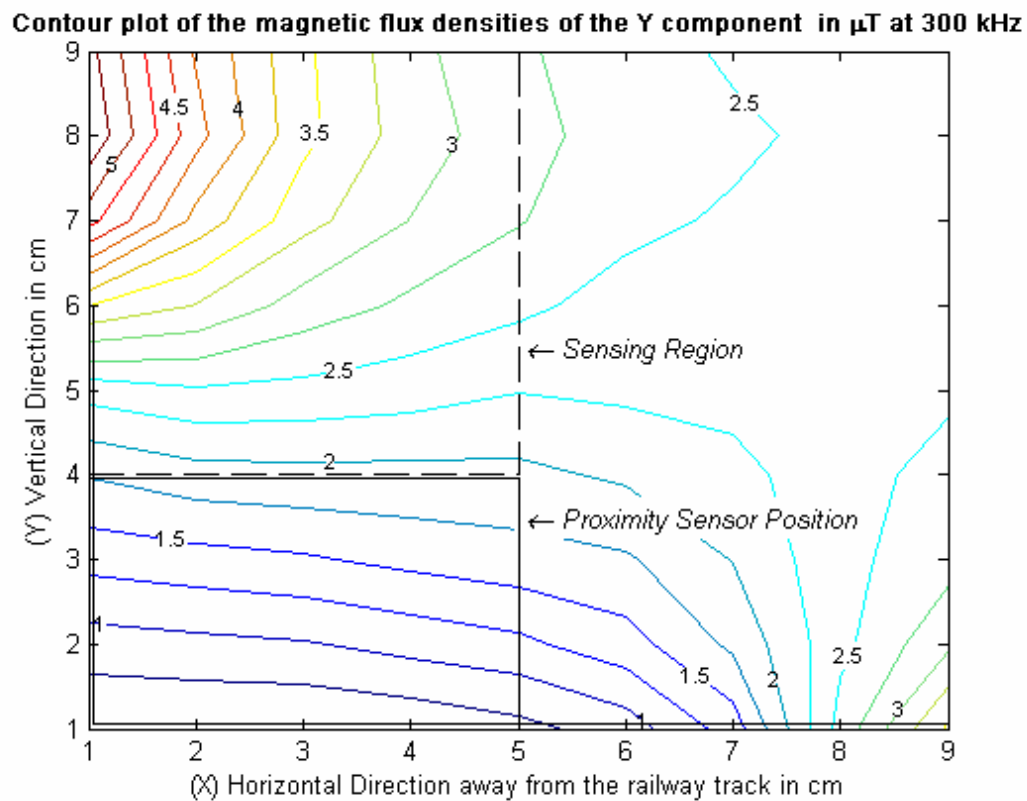


Figure 10-25: Contour Plot of the Y component of the magnetic flux density for the second cable in place with shield but no isolation.

10.4.1.3 Ninth Test: Second Cable Test set with the inclusion of a shield and Isolation

The introduction of the isolation layer has the effect of reducing the overall flux density within the sensing region, with little change in the observed pattern when Figure 10-26 is compared to Figure 10-25.

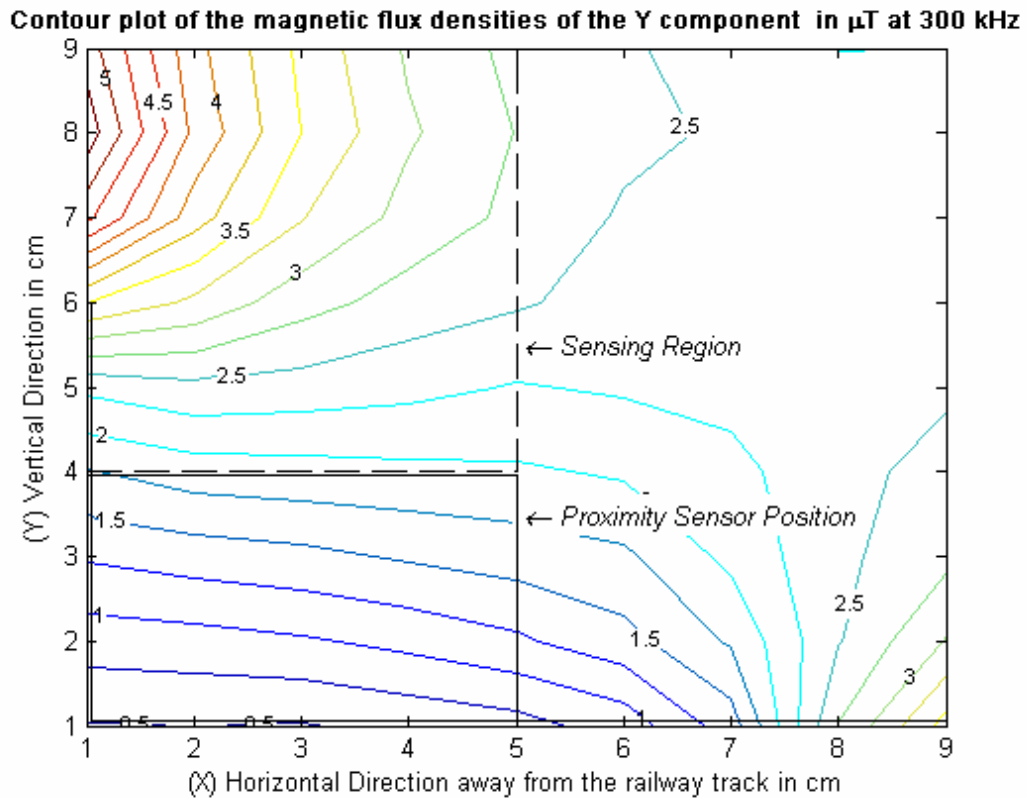


Figure 10-26: Contour Plot of the Y component of the magnetic flux density for the second cable in place with shield and isolation.

10.4.1.4 Tenth Test: Third Cable Test set (Sub-Base) with No shield or Isolation

The final third cable was installed, replacing the second cable, and the test were repeated to obtain comparative results for the cable tests.

A noticeable difference between this test and both the first and second cable test lies in the increased flux density to the top left of Figure 10-27, but similar flux densities at the lower right. This increase in the flux density was due to a higher current flowing through the railway track compared to the previous two cable tests. But when Figure 10-27 is compared to the Base measurement in Figure 5-4 it can be seen that a reduction in flux density within the sensing region is still observed, hence this cable still provides positive results in reducing the flux density, although it is not the better.

Contour plot of the magnetic flux densities of the Y component in μT at 300 kHz

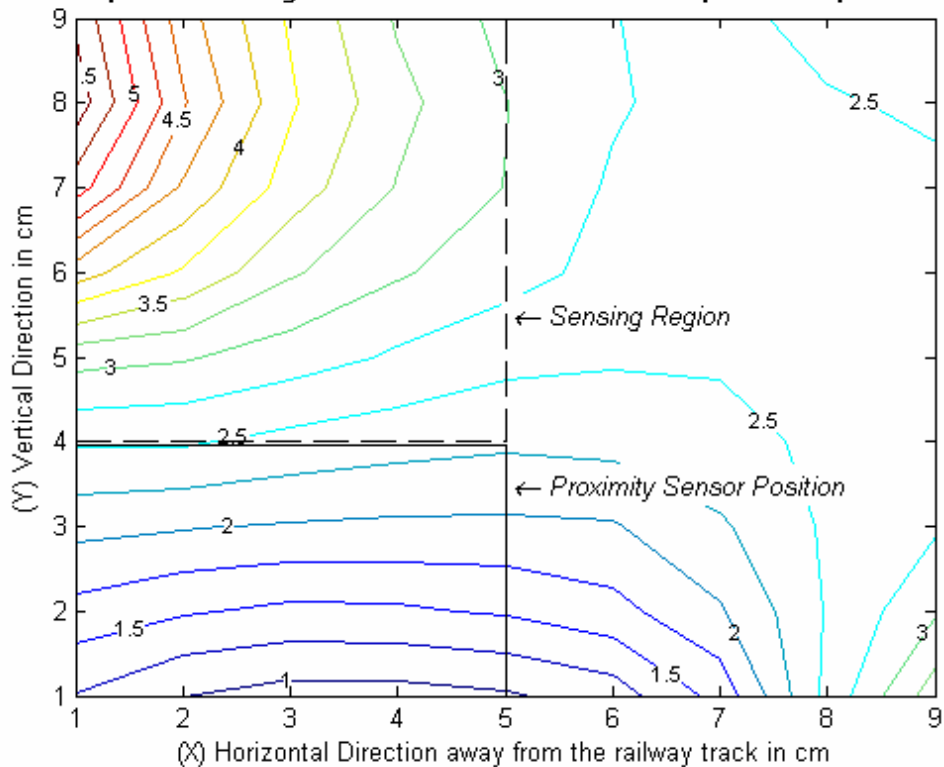


Figure 10-27: Contour Plot of the Y component of the magnetic flux density for the sub-base measurement with the third cable in place with no shield or isolation.

10.4.1.5 Eleventh Test: Third Cable Test set with the inclusion of a shield but no Isolation

The introduction of the shield again yields an improvement over the unshielded case and even the shielded case when no cables were involved, but a lesser improvement compared to the shielded cases for the first and second cables. There are no substantial differences in the patterns observed in Figure 10-28 compared to the previous cable and shielded cases (Figure 5-8 and Figure 10-25).

Contour plot of the magnetic flux densities of the Y component in μT at 300 kHz

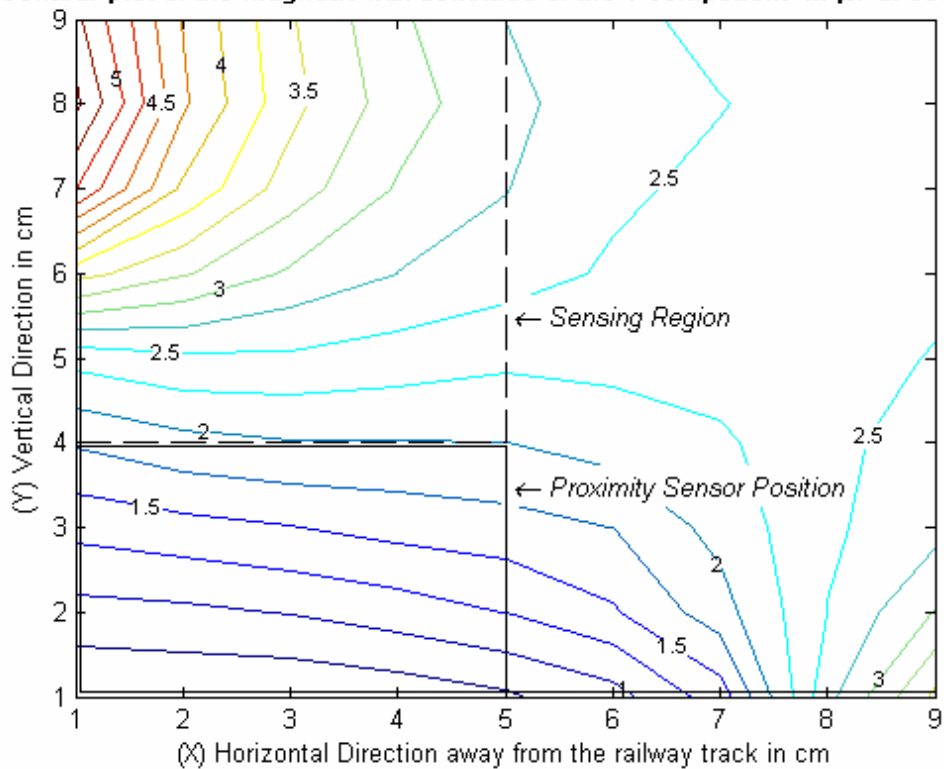


Figure 10-28: Contour Plot of the Y component of the magnetic flux density for the third cable in place with shield but no isolation.

10.4.1.6 Twelfth Test: Third Cable Test set with the inclusion of a shield and Isolation

Finally an isolation layer was placed between the shield and the proximity sensor platform, resulting in a reduction in flux density within the sensing region compared to the un-isolated test performed previously (Figure 10-28).

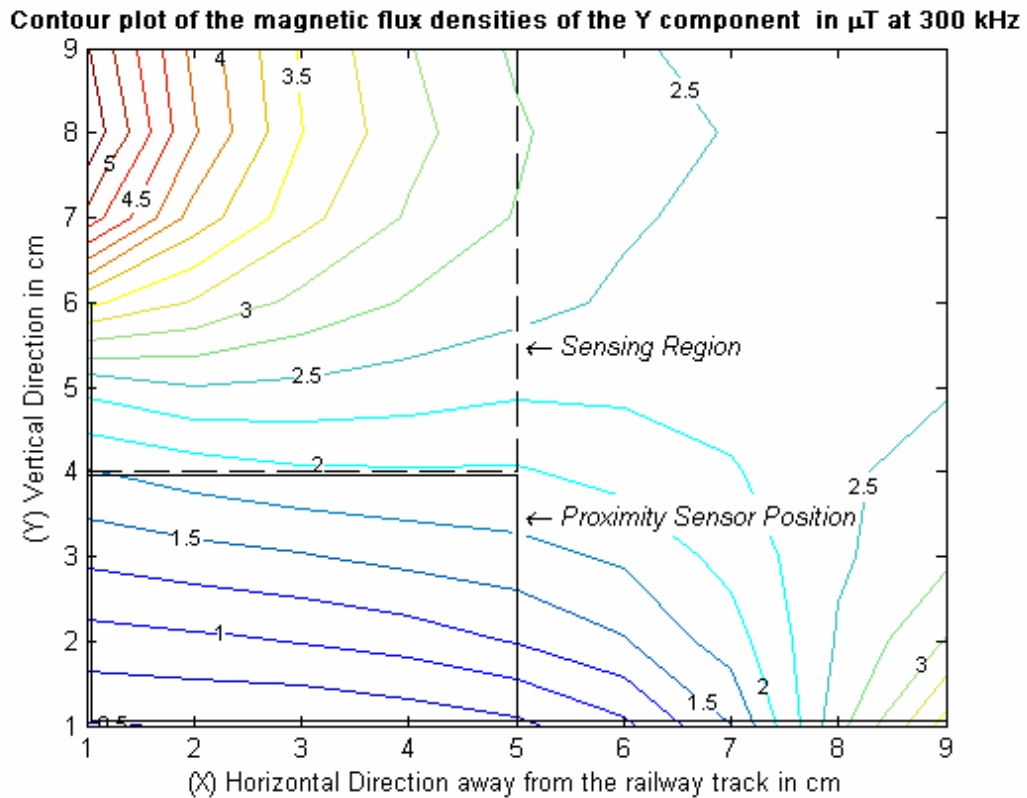


Figure 10-29: Contour Plot of the Y component of the magnetic flux density for the third cable in place with shield and isolation.

10.4.2 Appendix 4.2: X-Components and Combined contour plots showing the measured flux densities for the Experimental Results

10.4.2.1 First Test: Base Measurements of X-Component and Combined Results

The results for this test were obtained with no parallel cable, no shield and no isolation in place, as to obtain a base unaltered measurement for use as a reference for a comparison between all the difference tests. A comparison between the contour plots yielded the different effects that occur due to the different layouts of each on the performed test with the aim to reduce the Y-component of the magnetic flux density within the sensing region.

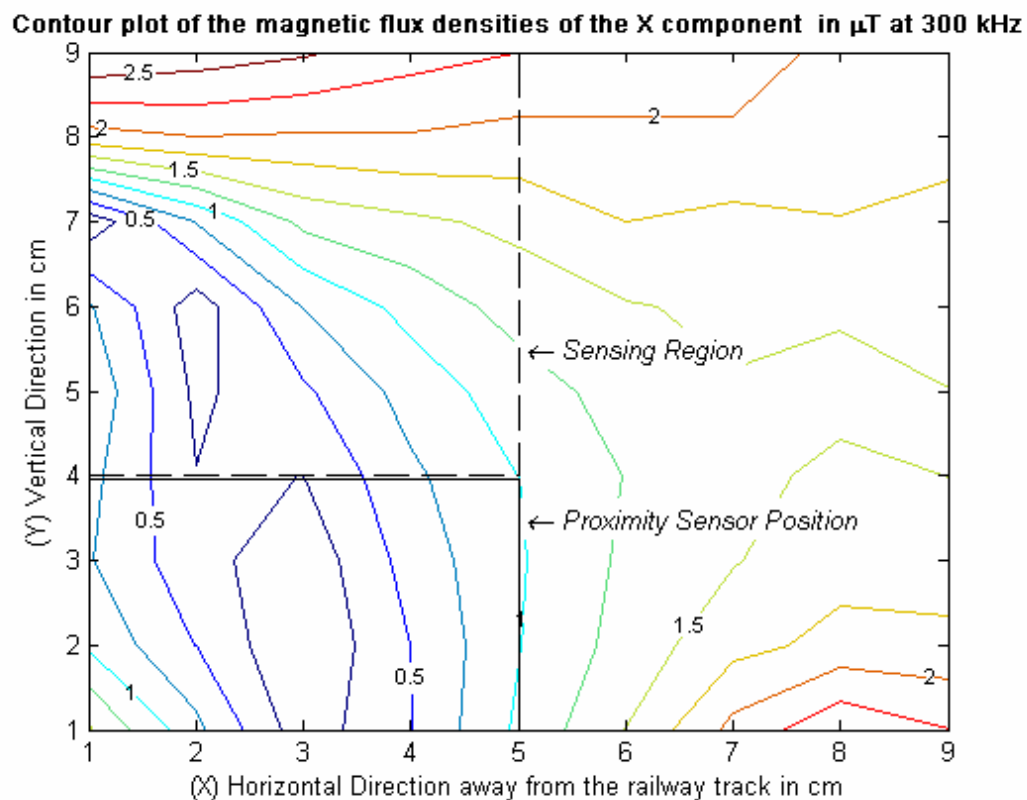


Figure 10-30: Contour Plot of the X component of the magnetic flux density for the base measurement with no shield, cable and isolation.

From the contour plot of the X-component of the flux density shown in Figure 10-30, it can be seen that the higher magnetic field intensities lie at the top left, due to the

magnetic field moving over the top of the railway track (see Figure 1-6 main report), and the bottom left corner as the proximity sensor platform comes to an end.

The region with low magnetic field intensity, between 1 to 5 on the X axis and 7 to 1 on the Y axis occurs as the magnetic field is mainly in the Y axis in this region.

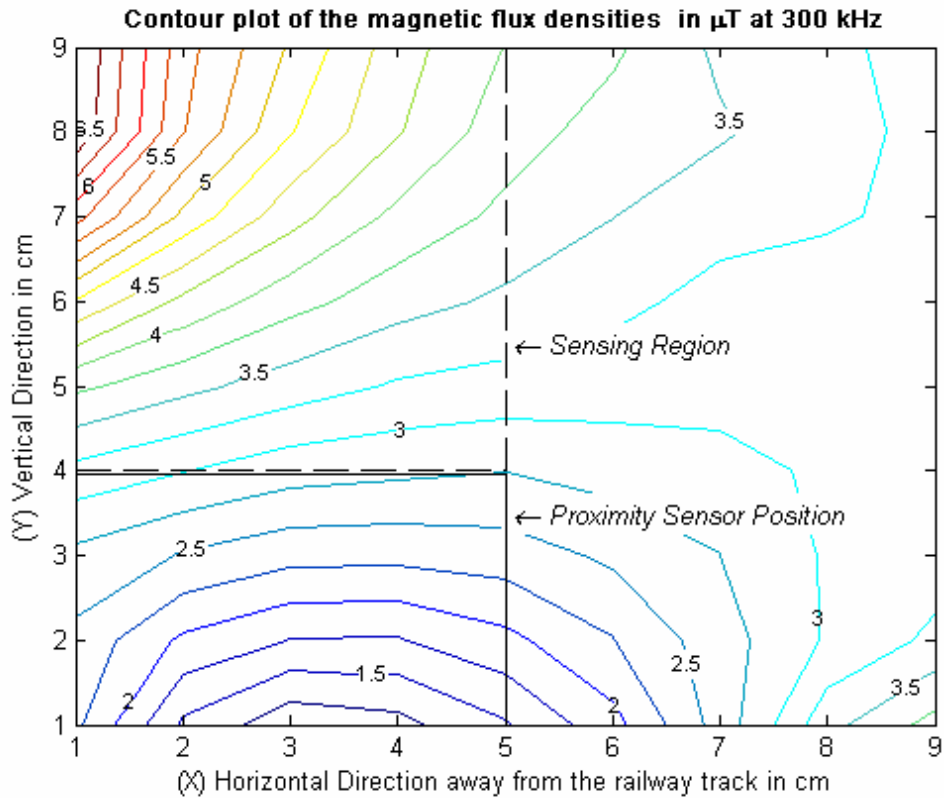


Figure 10-31: Contour Plot of the magnetic flux density for the base measurement with no shield, cable and isolation.

For the combined results shown in Figure 10-31 the maximum region occurs in the top left corner, which lies next to the top of the railway track, and the lower intensity region occurs to the bottom left that lies above the proximity sensor platform.

10.4.2.2 Second Test: Shield Measurement with No Cable or Isolation

For this test a shield was included above the proximity sensor platform, yielding the effects seen in Figure 10-32.

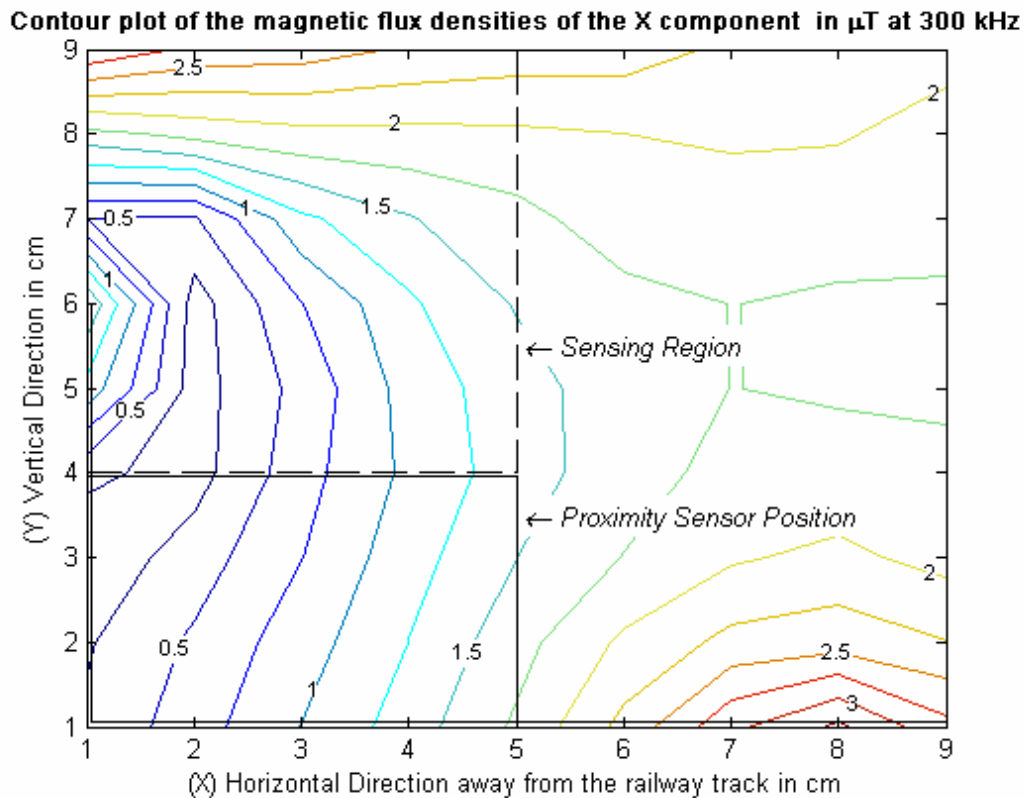


Figure 10-32: Contour Plot of the X component of the magnetic flux density for shielded case no cable or isolation.

The higher flux density regions have not been greatly effected by the introduction of the shield, but the lower intensity region has become larger with a slight higher intensity close to the top of the shield (position 6 on the Y axis), as the field moves over the shield.

For the combined results shown in Figure 10-33, it can again be seen that the lower flux density region at the lower left portion of the contour map has increased in size due to the introduction of the shield

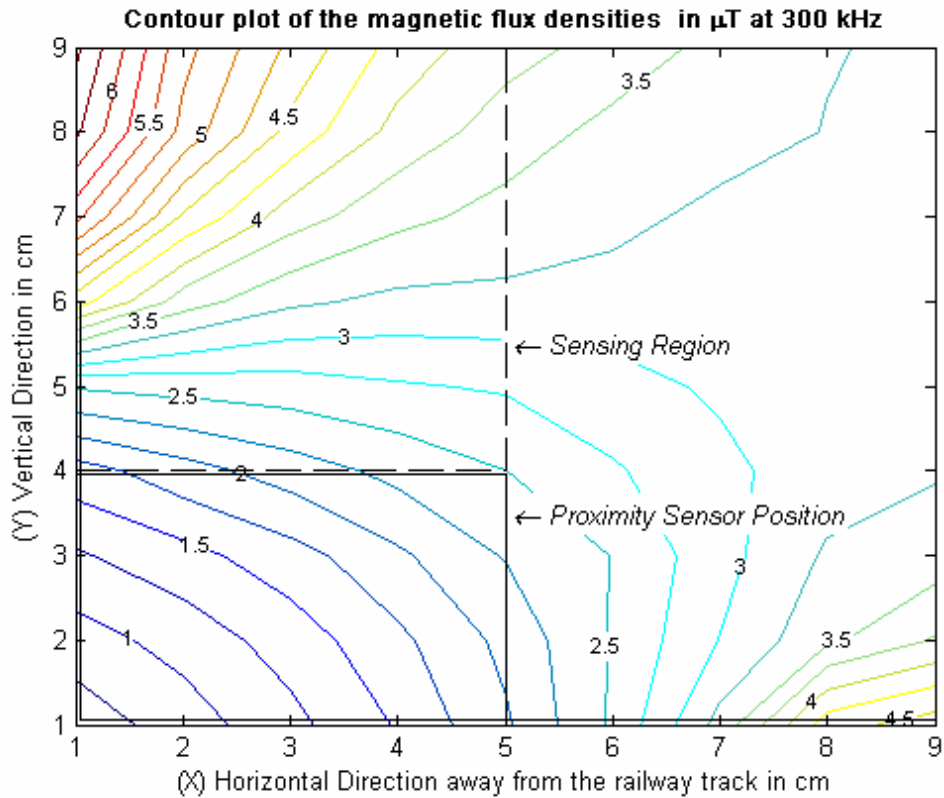


Figure 10-33: Contour Plot of the magnetic flux density for shielded case no cable or isolation.

10.4.2.3 Third Test: Inclusion of isolation between shield and proximity sensor platform

Figure 10-34 on the next page shows the X component of the flux density measured in the test area for the third test, which includes shielding and isolation. The visible effect of the introduction of the isolation layer between the shield and the proximity sensor platform, as compared to the purely shielded case (Figure 10-32) is minimal and little change can be seen.

Again for the combined result a comparison with the purely shielded case (Figure 10-33) yields minimal visual differences.

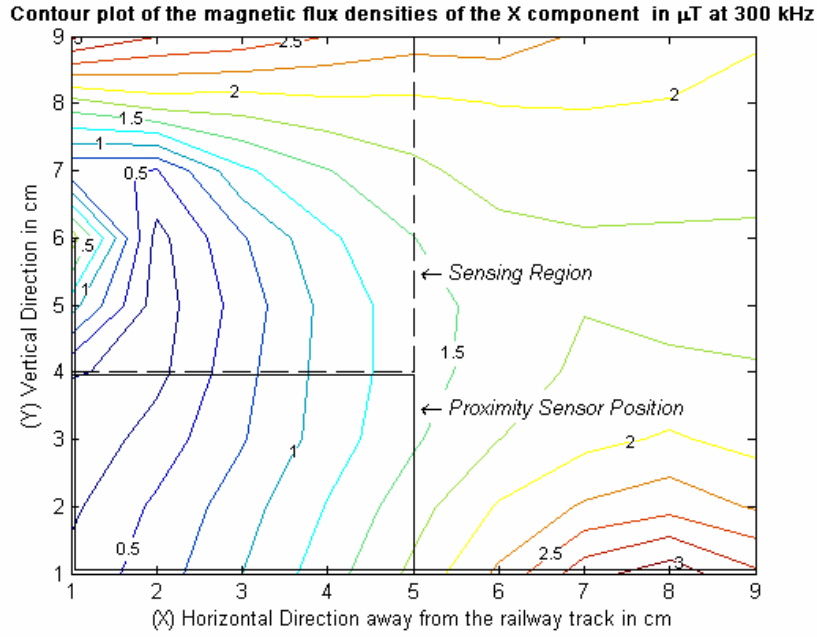


Figure 10-34: Contour Plot of the X component of the magnetic flux density for shielded case with isolation but no cable.

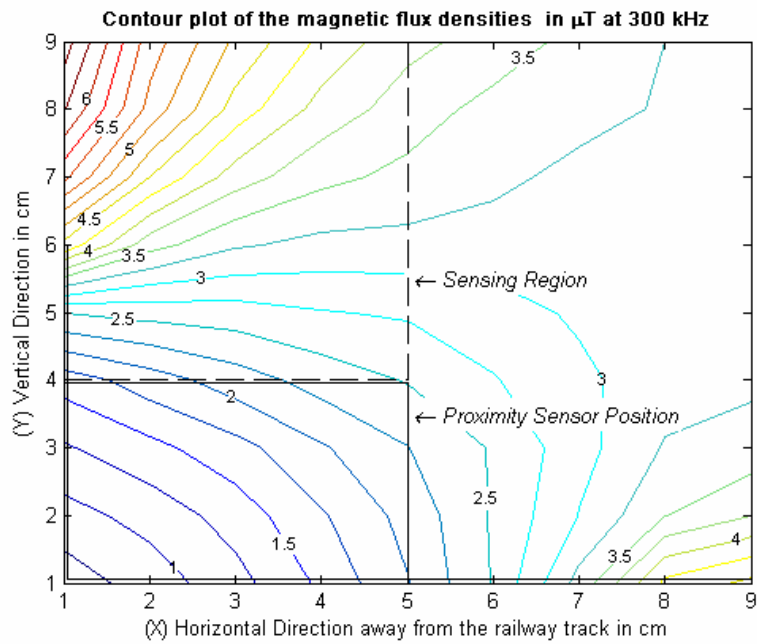


Figure 10-35: Contour Plot of the magnetic flux density for shielded case with isolation but no cable.

10.4.2.4 Fourth Test: First Cable Test (Sub-Base), with no shield or isolation

Due to the introduction of the cable for this test, a high flux density region has been formed to the lower right of the test area (Figure 10-36 and Figure 10-37), with an overall decrease within the sensing region.

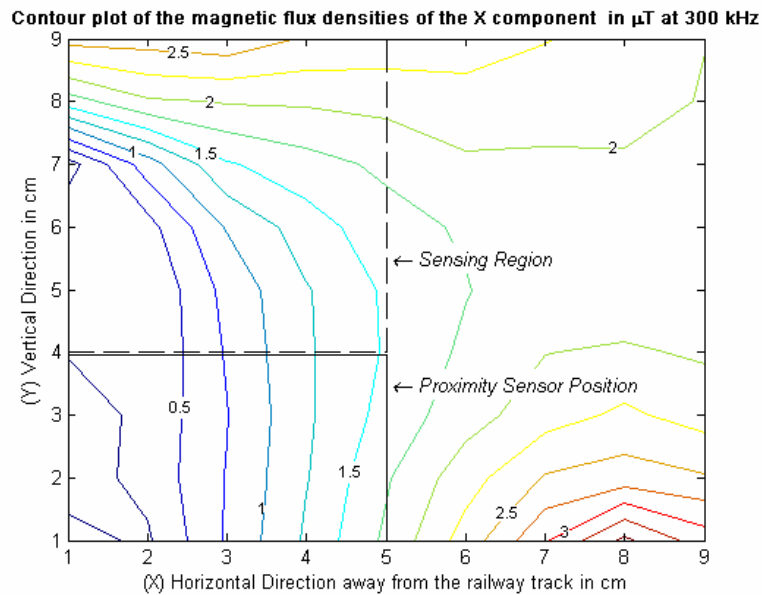


Figure 10-36: Contour Plot of the X component of the magnetic flux density for the sub-base measurement with the first cable in place with no shield or isolation.

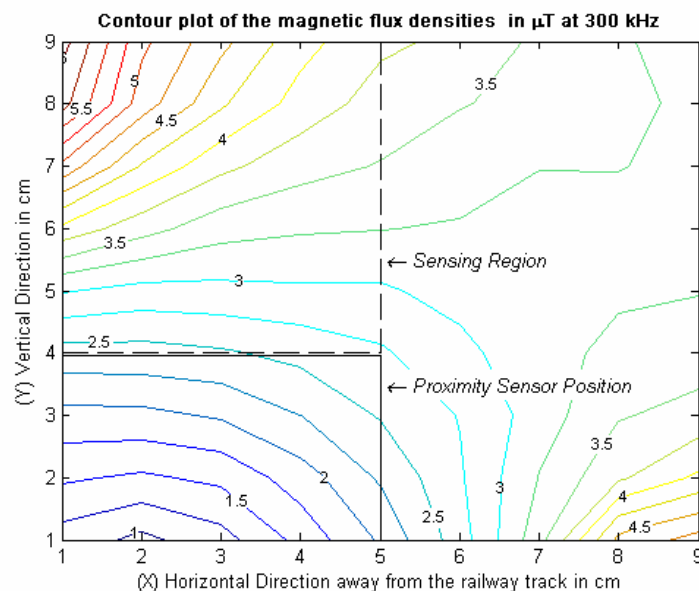


Figure 10-37: Contour Plot of the magnetic flux density for the sub-base measurement with the first cable in place with no shield or isolation.

10.4.2.5 Fifth Test: First Cable Test set with the inclusion of the shield but no isolation

The introduction of the shield results in an increase in the X-component (Figure 10-38) of the magnetic flux density at the top of the sensing region, and a decrease in the lower right portion of the test area.

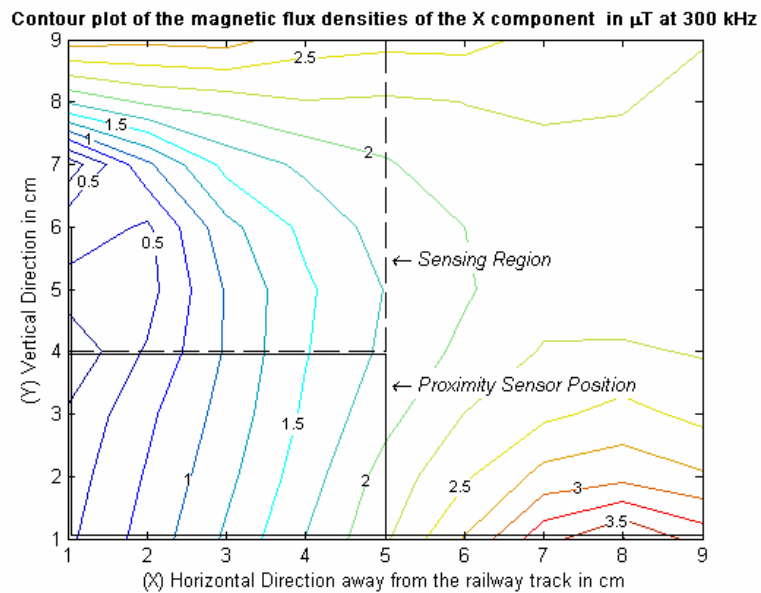


Figure 10-38: Contour Plot of the X component of the magnetic flux density for the first cable in place with shield but no isolation.

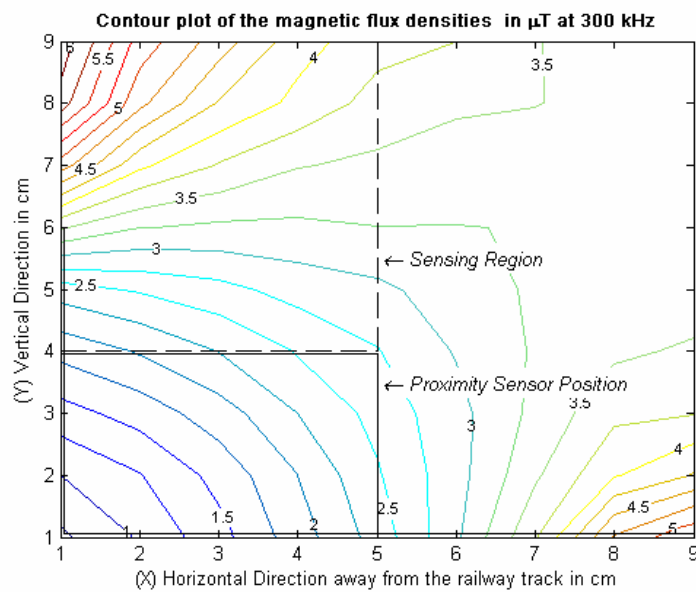


Figure 10-39: Contour Plot of the magnetic flux density for the first cable in place with shield but no isolation.

10.4.2.6 Sixth Test: First Cable Test set with the inclusion of the shield and isolation

The inclusion of the shield yields little visual difference in the contour plots for the X-component and Combined results for the magnetic flux density within the test area and therefore the sensing region.

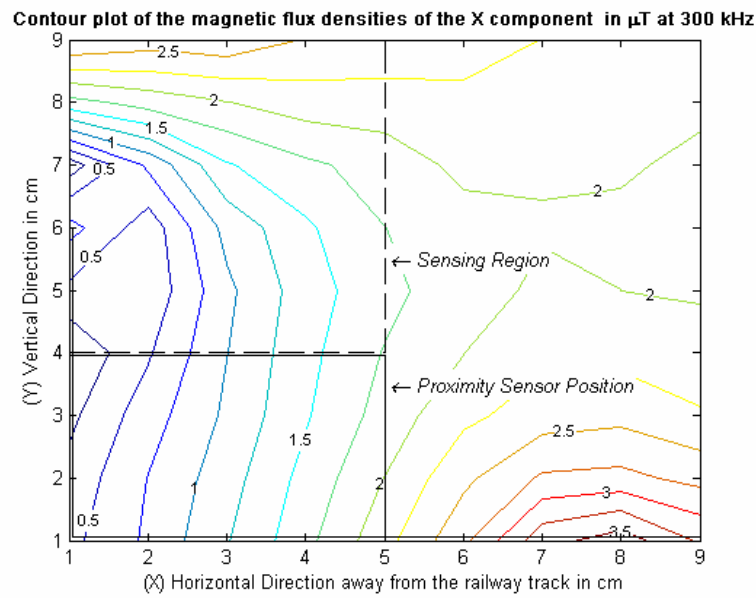


Figure 10-40: Contour Plot of the X component of the magnetic flux density for the first cable in place with shield and isolation.

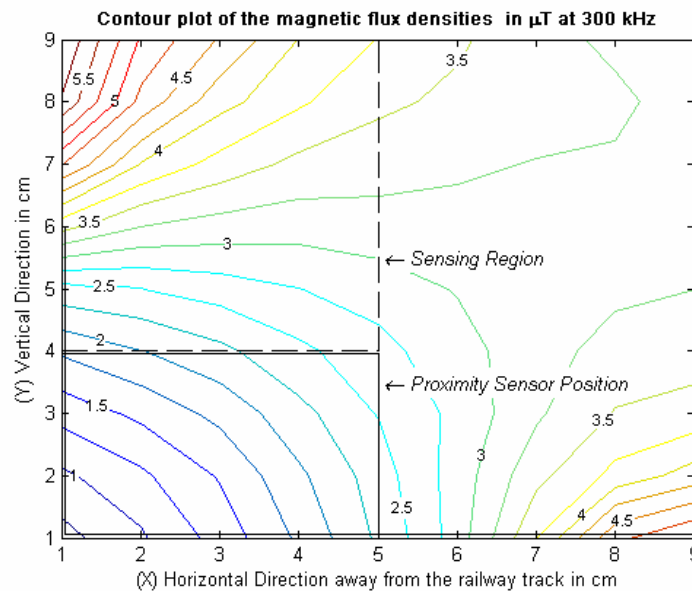


Figure 10-41: Contour Plot of the magnetic flux density for the first cable in place with shield and isolation.

The subsequent tests again yielded similar patterns to those seen in the pervious contour plots with only a difference in their magnitudes.

10.4.2.7 Seventh Test: Second Cable Test set (Sub-Base) with No shield or Isolation

Contour plot of the magnetic flux densities of the X component in μT at 300 kHz

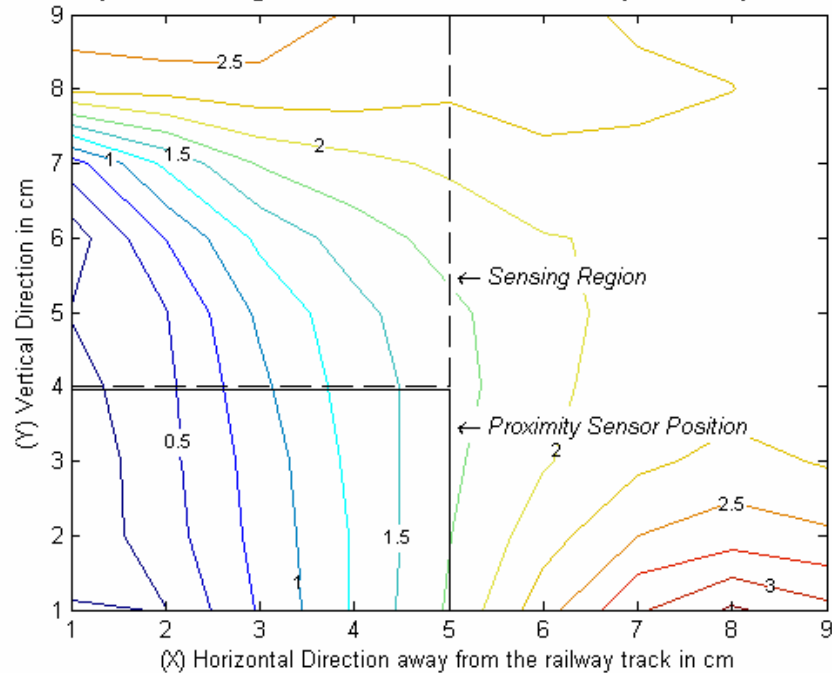


Figure 10-42: Contour Plot of the X component of the magnetic flux density for the sub-base measurement with the second cable in place with no shield or isolation.

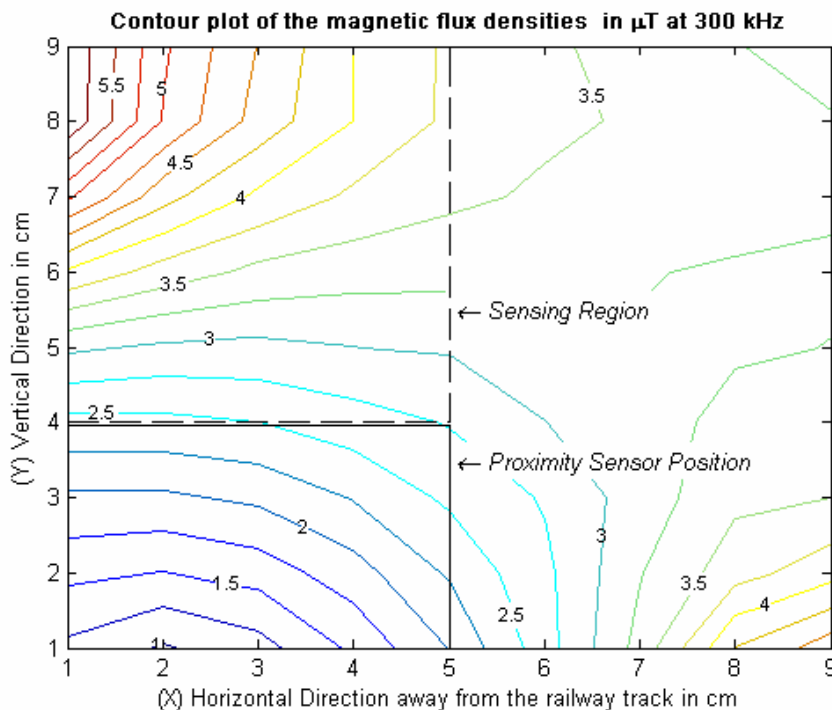


Figure 10-43: Contour Plot of the magnetic flux density for the sub-base measurement with the second cable in place with no shield or isolation.

10.4.2.8 Eighth Test: Second Cable Test set with the inclusion of a shield but no Isolation

Contour plot of the magnetic flux densities of the X component in μT at 300 kHz

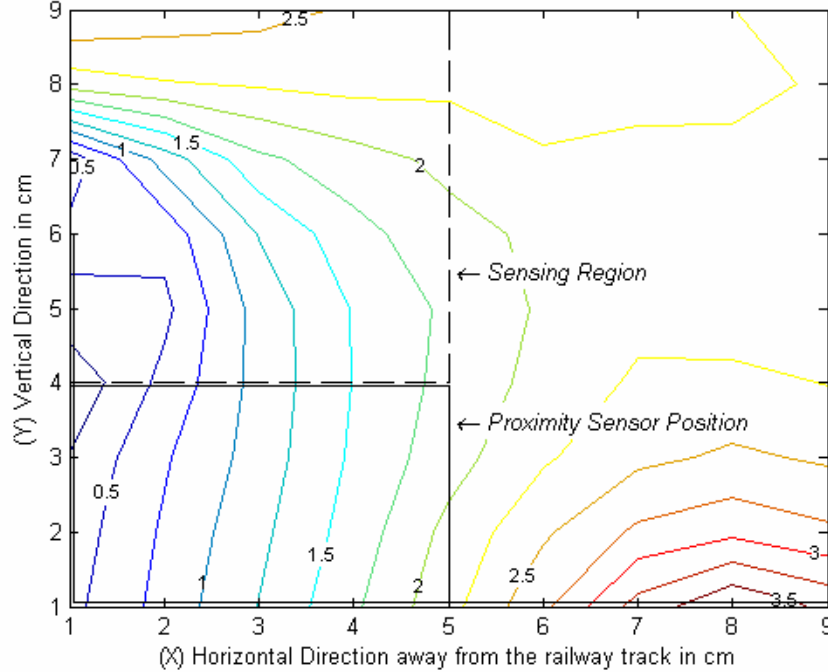


Figure 10-44: Contour Plot of the X component of the magnetic flux density for the second cable in place with shield but no isolation.

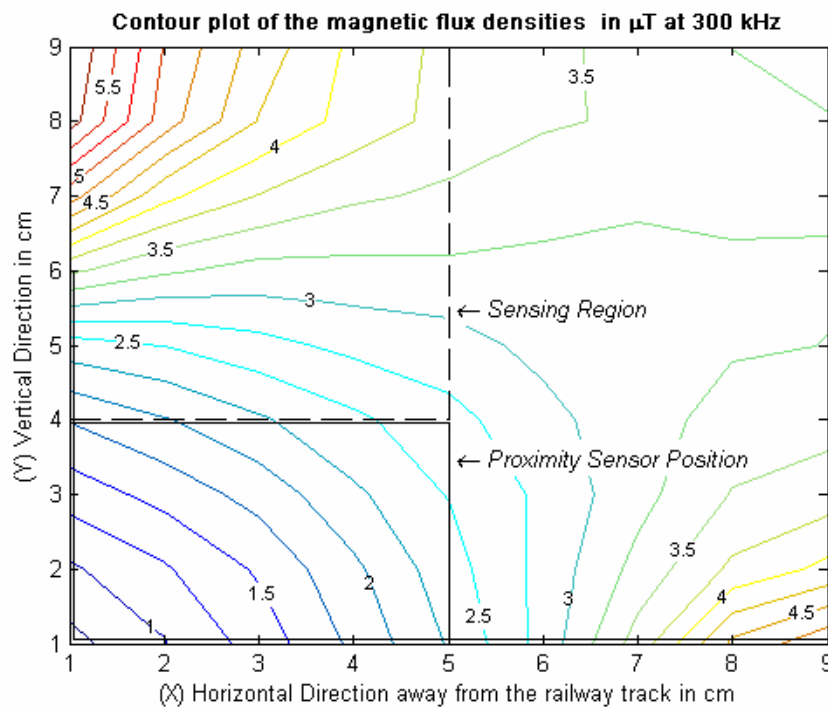


Figure 10-45: Contour Plot of the magnetic flux density for the second cable in place with shield but no isolation.

10.4.2.9 Ninth Test: Second Cable Test set with the inclusion of a shield and Isolation

Contour plot of the magnetic flux densities of the X component in μT at 300 kHz

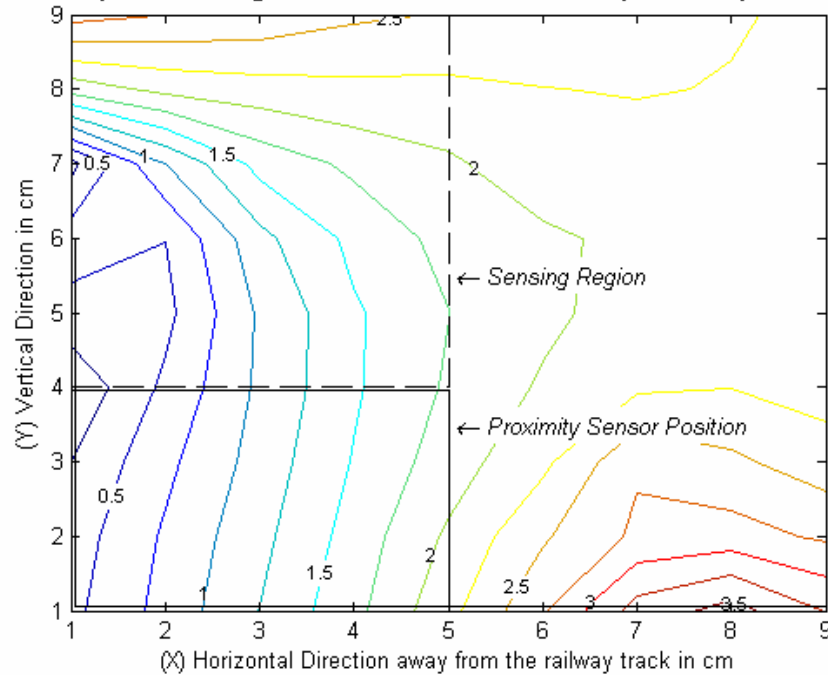


Figure 10-46: Contour Plot of the X component of the magnetic flux density for the second cable in place with shield and isolation.

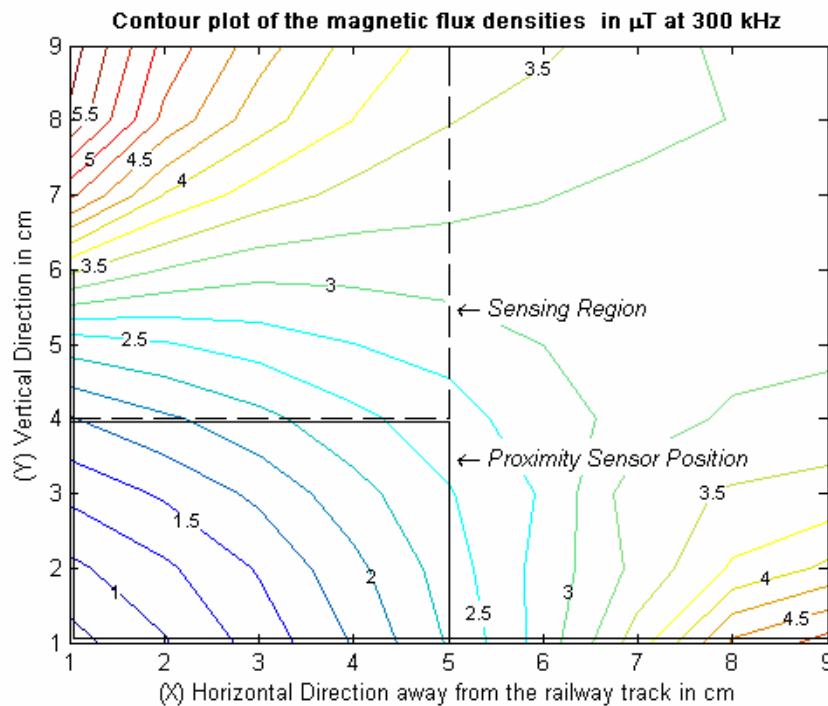


Figure 10-47: Contour Plot of the magnetic flux density for the second cable in place with shield and isolation.

10.4.2.10 Tenth Test: Third Cable Test set (Sub-Base) with No shield or Isolation

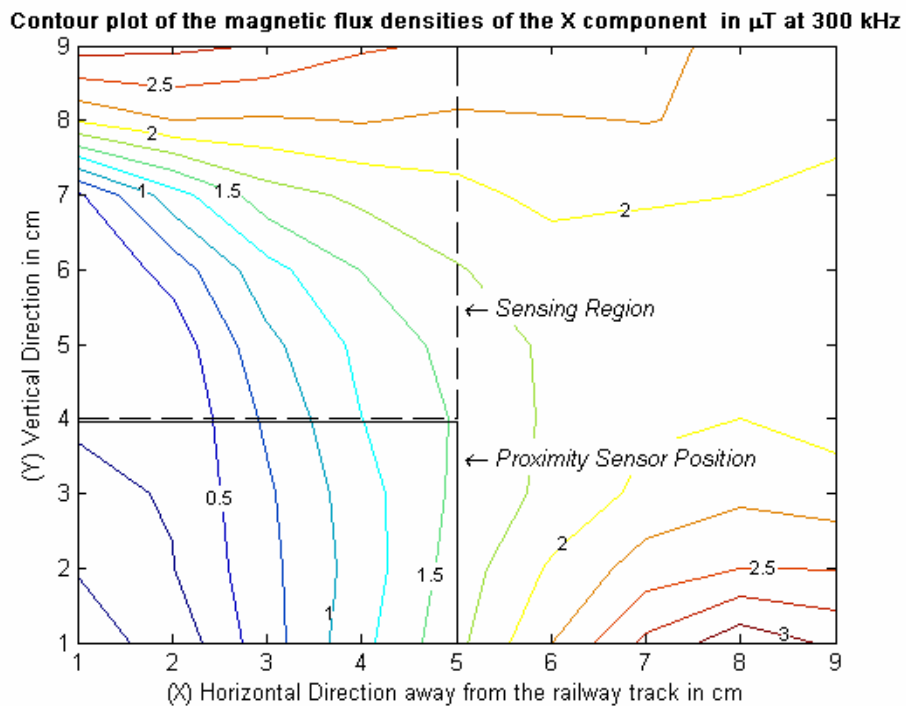


Figure 10-48: Contour Plot of the X component of the magnetic flux density for the sub-base measurement with the third cable in place with no shield or isolation.

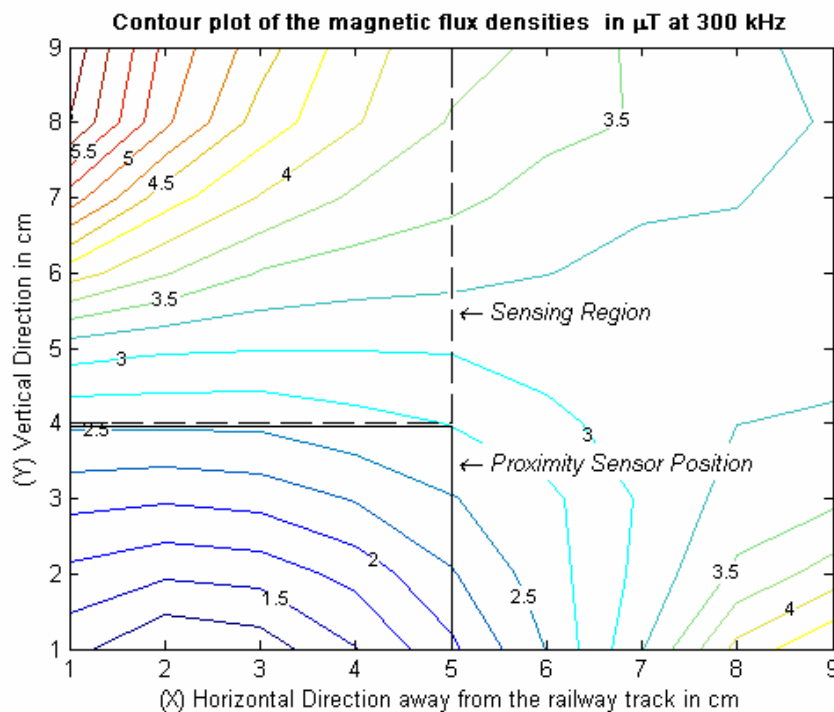


Figure 10-49: Contour Plot of the magnetic flux density for the sub-base measurement with the third cable in place with no shield or isolation.

10.4.2.11 Eleventh Test: Third Cable Test set with the inclusion of a shield but no Isolation

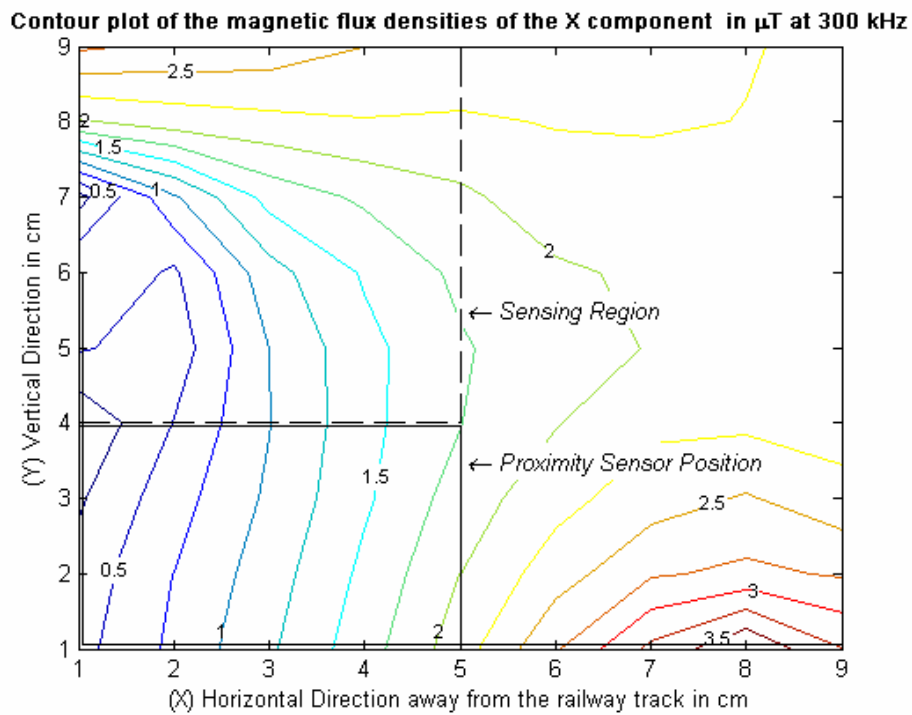


Figure 10-50: Contour Plot of the X component of the magnetic flux density for the third cable in place with shield but no isolation.

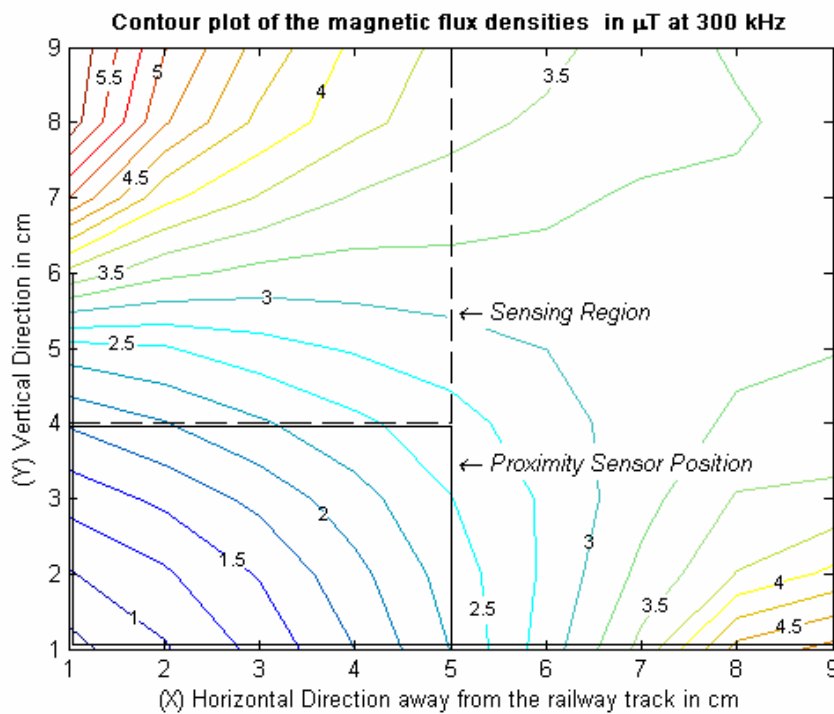


Figure 10-51: Contour Plot of the magnetic flux density for the third cable in place with shield but no isolation.

10.4.2.12 Twelfth Test: Third Cable Test set with the inclusion of a shield and Isolation

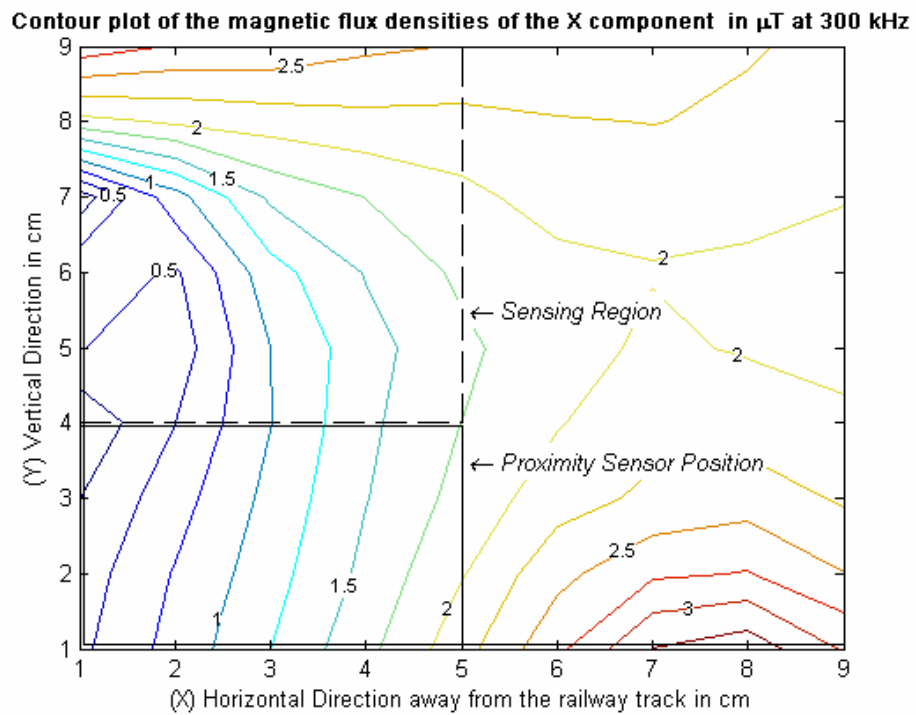


Figure 10-52: Contour Plot of the X component of the magnetic flux density for the third cable in place with shield and isolation.

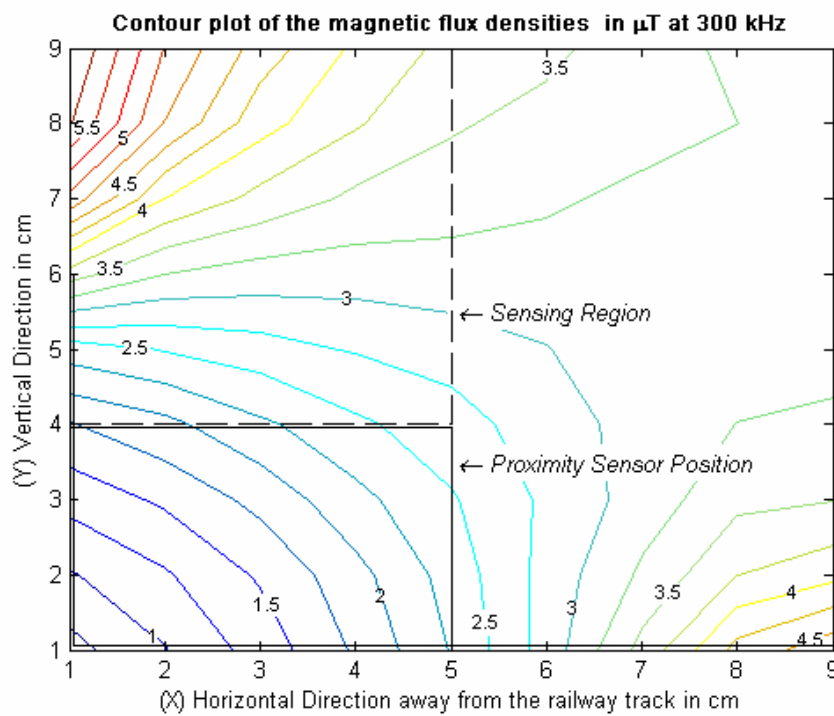


Figure 10-53: Contour Plot of the magnetic flux density for the third cable in place with shield and isolation.

10.4.3 Appendix 4.3: Direct Comparison, Results in Micro Tesla

10.4.3.1 Direct comparison, comparing the effect of the three different cables directly

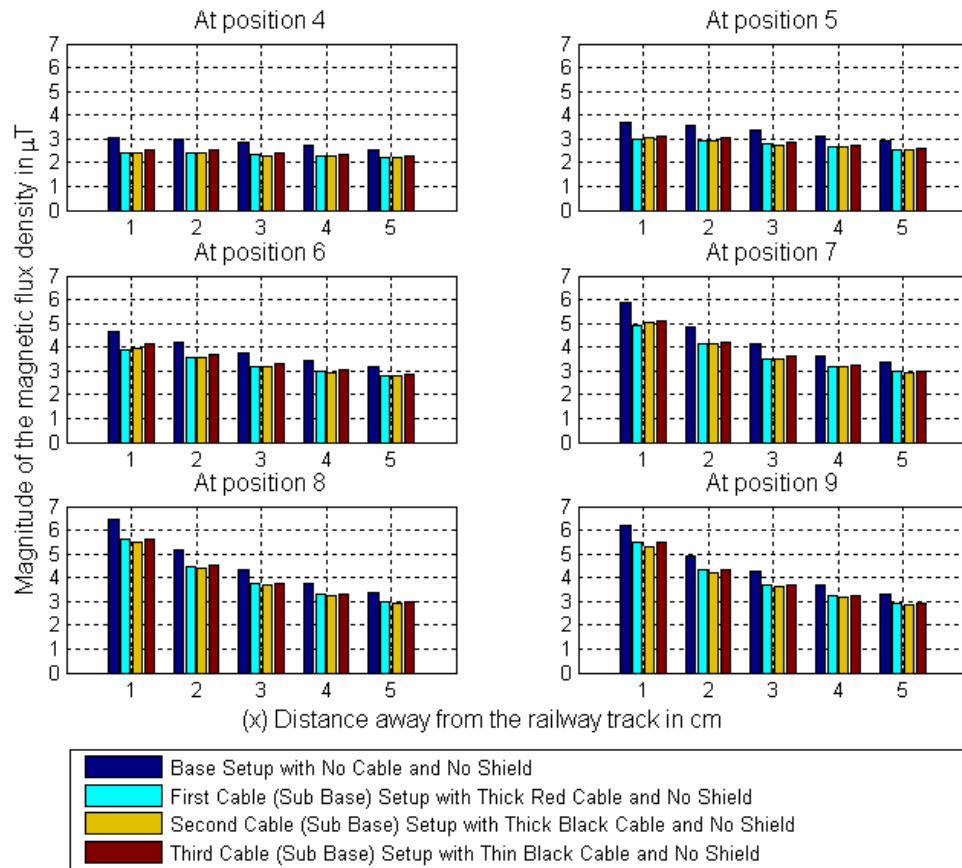


Figure 10-54: Direct comparison to determine the effect of the addition of the three separate cables to the railway track system.

10.4.3.2 Direct comparison Bar Graph, comparing the effect of the shielded cases for the three different parallel cables directly

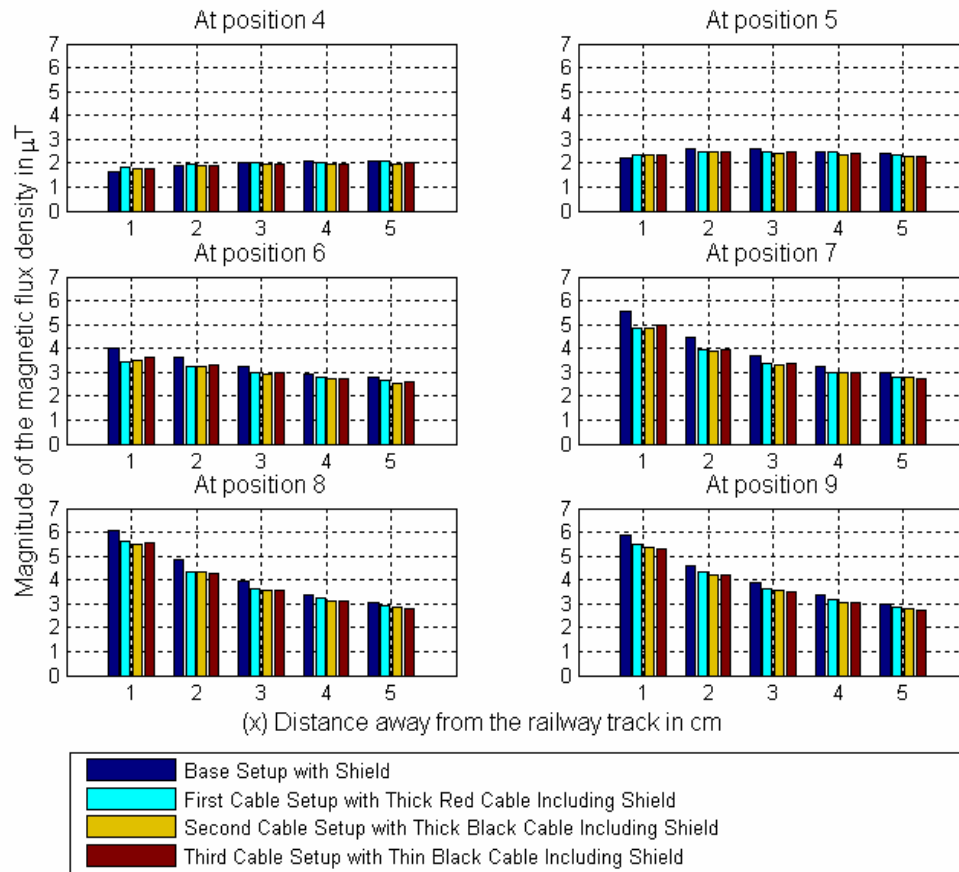


Figure 10-55: Direct comparison to determine the effect of the inclusion of the shield for the three separate cables.

10.4.3.3 Direct comparison, comparing the effect of the shielded and isolated cases for the three different cables directly

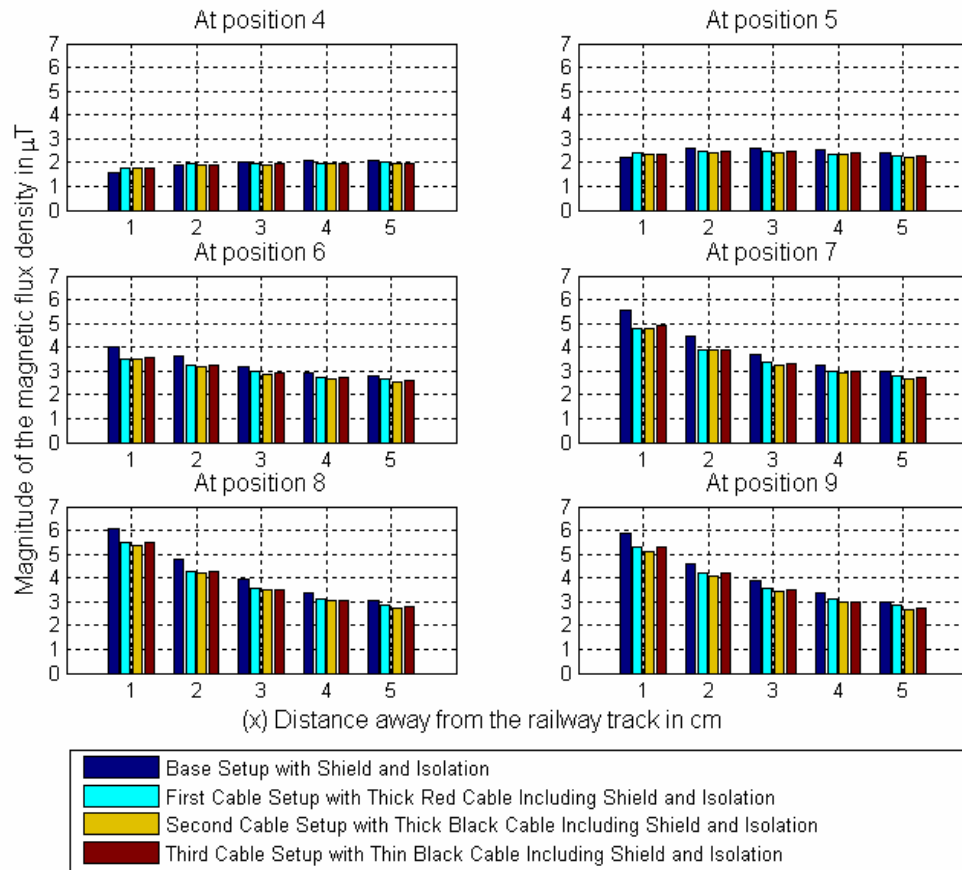


Figure 10-56: Direct comparison to determine the effect of the inclusion of the shield and isolation layer for the three separate cables.

10.5 Appendix 5: Simulation Results

10.5.1 Appendix 5.1: Simulation Results showing the Flux Lines Present in the Test Area next to the Railway Track

10.5.1.1 Base Simulation (Simulated Base Measurement)

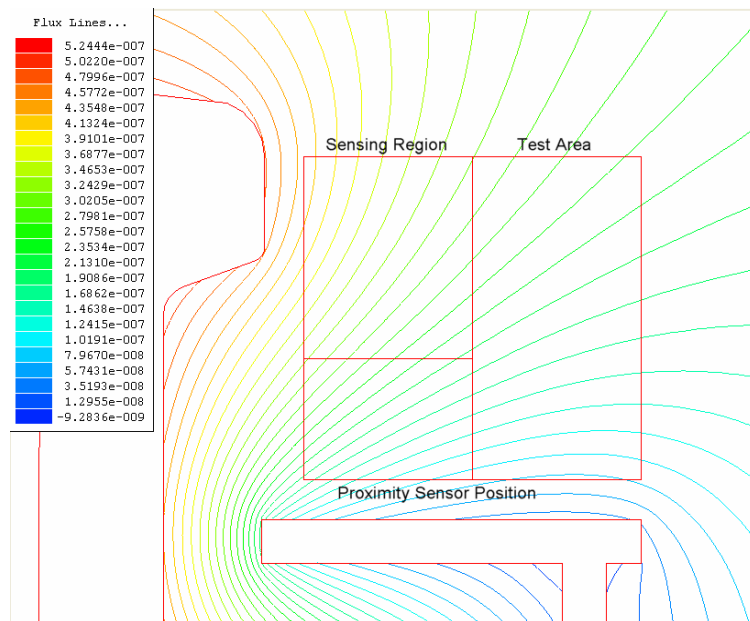


Figure 10-57: Simulated Results showing the Flux Lines within the Test Area for the Base Simulation, with no shield or cable.

10.5.1.2 Base Simulation with the addition of a shield

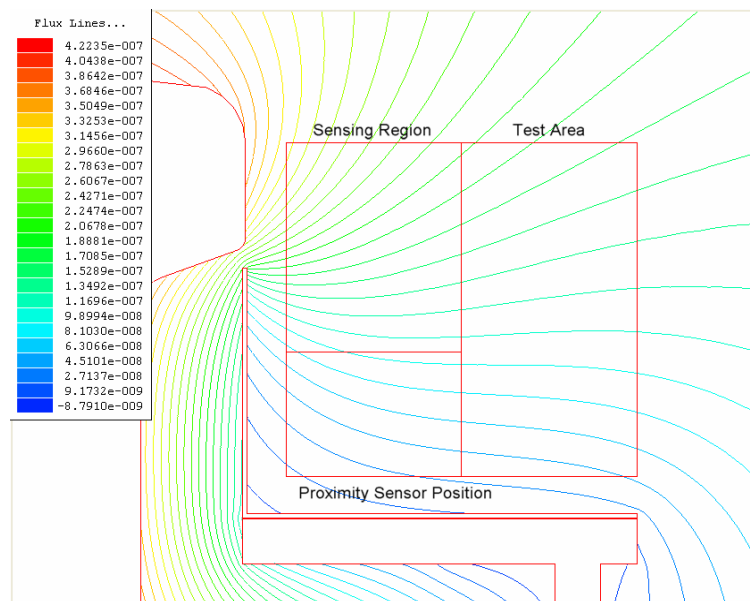


Figure 10-58: Simulated Results showing the Flux Lines within the Test Area for the Base Simulation, with the inclusion of a shield but no cable.

10.5.1.3 Sub Base Simulation including the First Parallel Cable

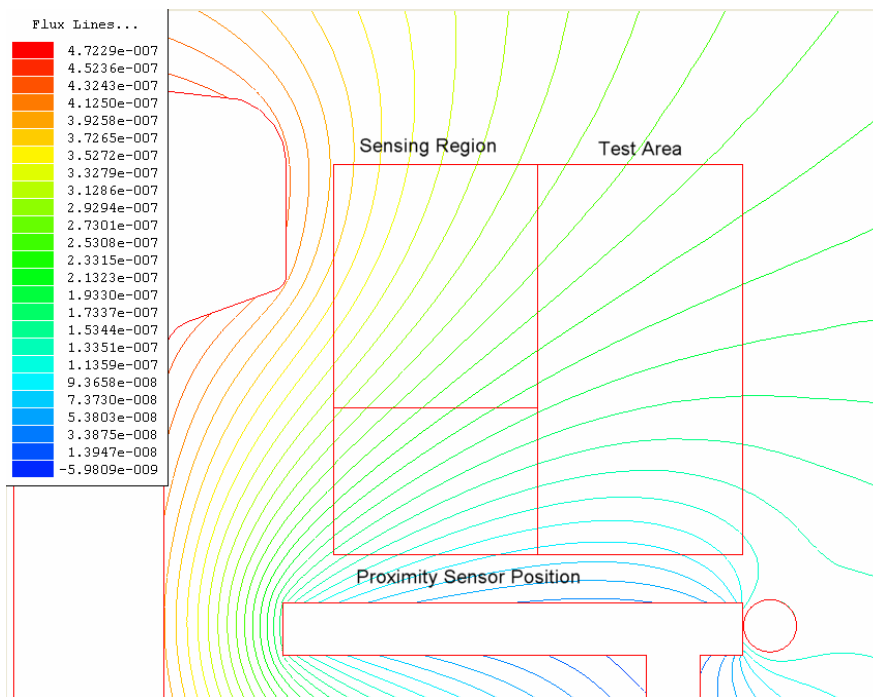


Figure 10-59: Simulated Results showing the Flux Lines within the Test Area for the Sub base Simulation involving the First parallel Cable, with no shield.

10.5.1.4 First Cable Simulation including a shield

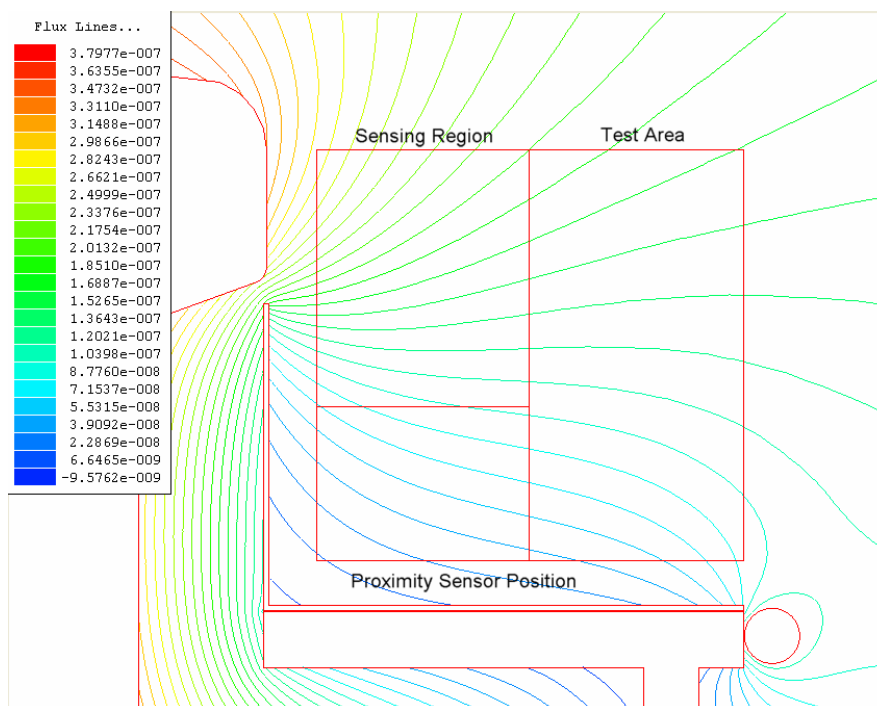


Figure 10-60: Simulated Results showing the Flux Lines within the Test Area for the Sub base Simulation involving the First parallel Cable, with the inclusion of the shield.

10.5.1.5 Sub Base Simulation including the Second Parallel Cable

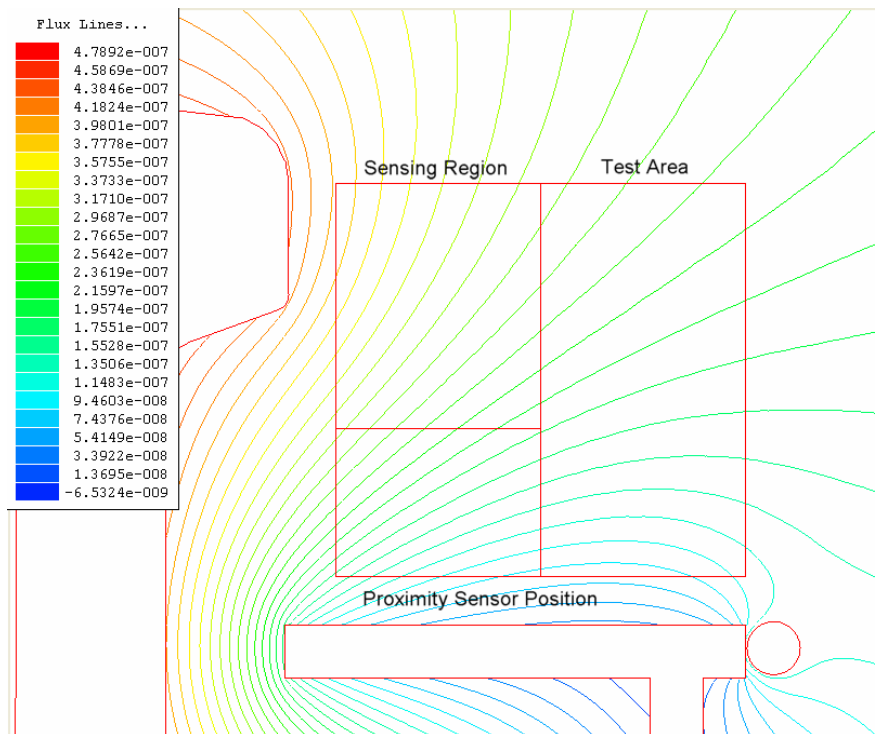


Figure 10-61: Simulated Results showing the Flux Lines within the Test Area for the Sub base Simulation involving the Second parallel Cable, with no shield.

10.5.1.6 Second Cable Simulation including a shield

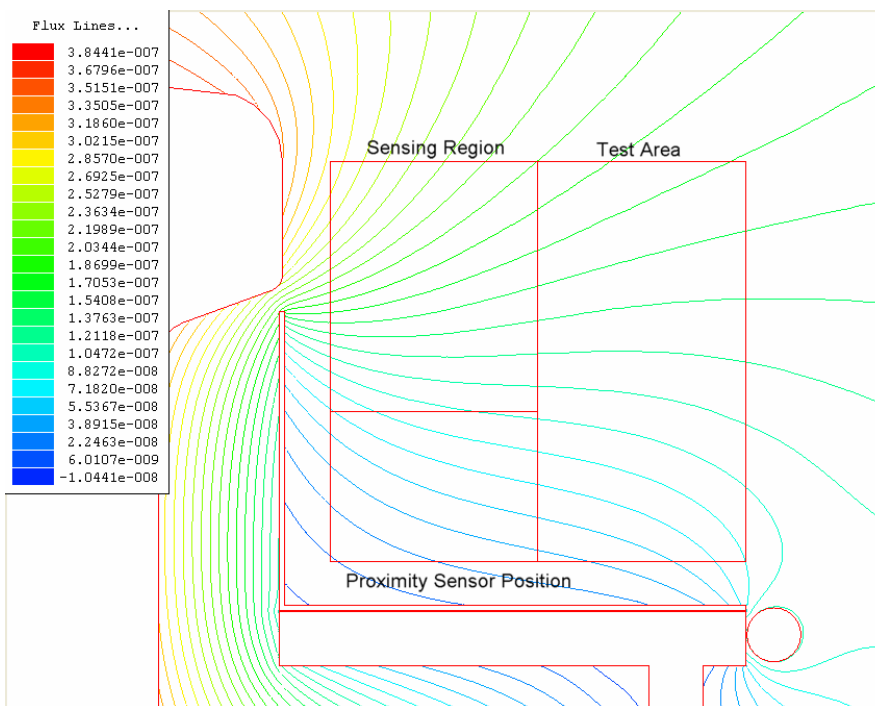


Figure 10-62: Simulated Results showing the Flux Lines within the Test Area for the Sub base Simulation involving the Second parallel Cable, with the inclusion of the shield.

10.5.1.7 Sub Base Simulation including the Third Parallel Cable

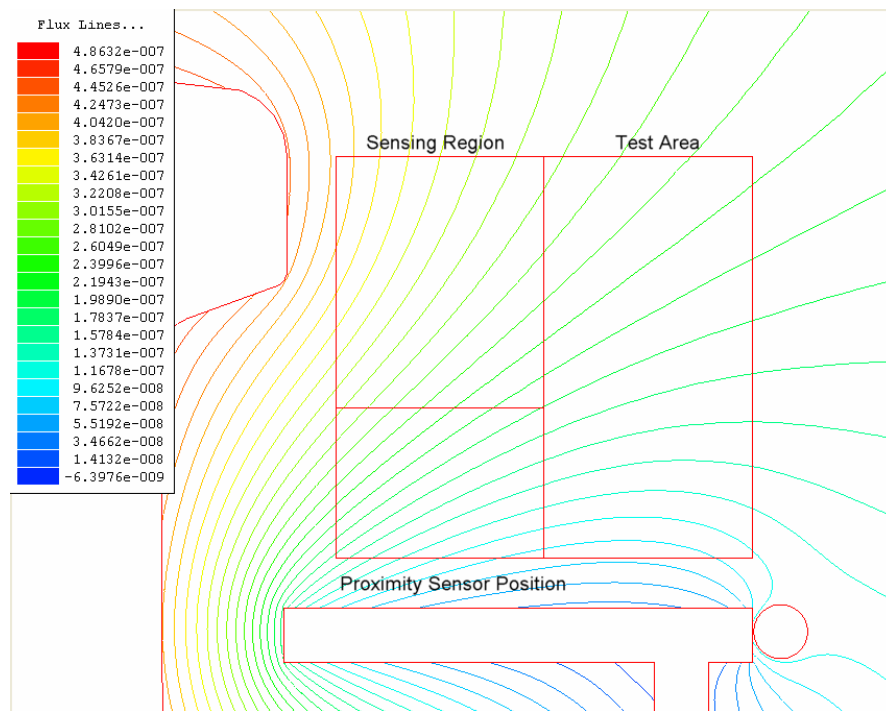


Figure 10-63: Simulated Results showing the Flux Lines within the Test Area for the Sub base Simulation involving the Third parallel Cable, with no shield.

10.5.1.8 Third Cable Simulation including a shield

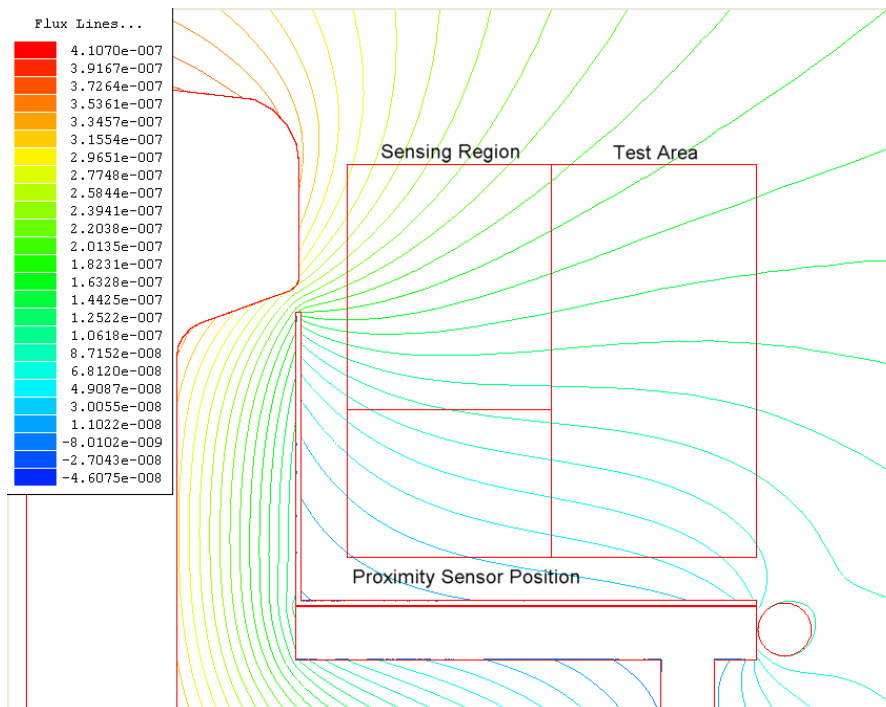


Figure 10-64: Simulated Results showing the Flux Lines within the Test Area for the Sub base Simulation involving the Third parallel Cable, with the inclusion of the shield.

10.5.2 Appendix 5.2: Comparison Bar graphs for each of the Simulated Results

10.5.2.1 Direct comparison for the shielded and un-shielded Base Simulations with no cable installed running parallel to the Railway Track

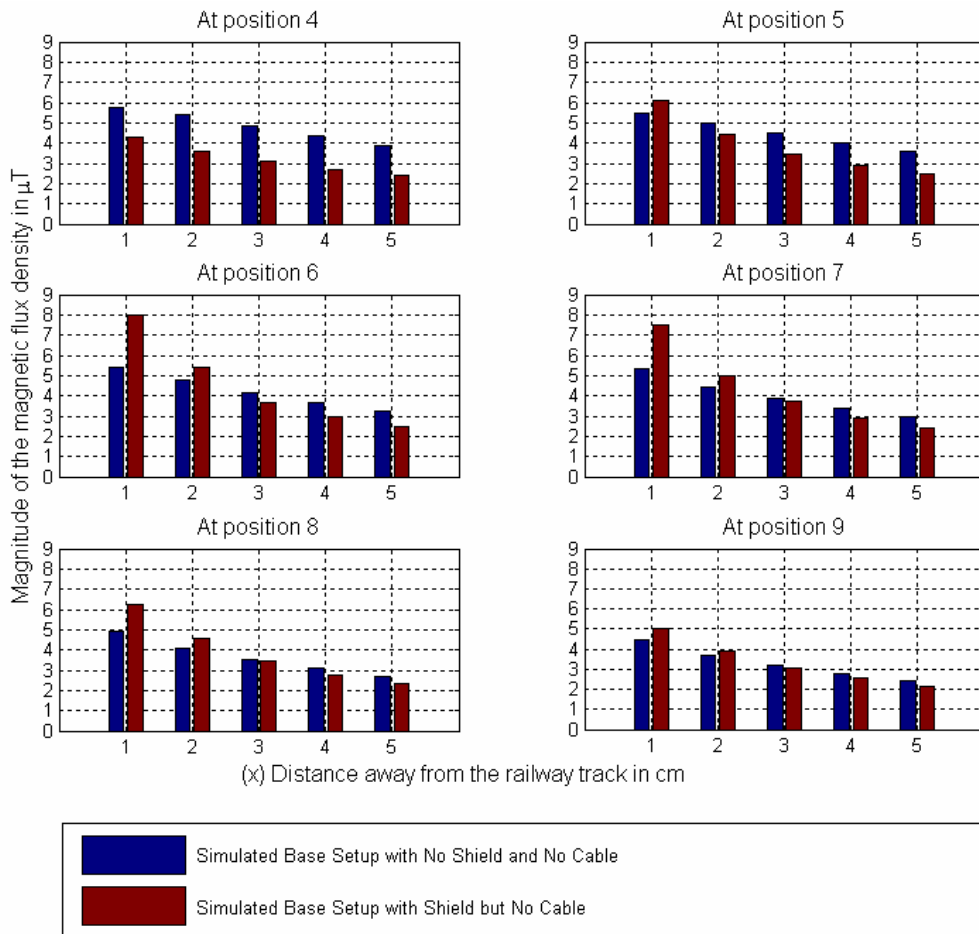


Figure 10-65: Direct Comparison between Shielded and Un-Shielded Base Simulation with no Cable.

From the comparison of these two simulations it can be seen that the introduction of the shield has a positive effect in reducing the flux density at positions 4 and 5 but a negative effect at positions 1 and 2 on the X axis from position 6 and upwards.

The introduction of the shield condenses the flux density in the area between the top of the shield and the railway track, as all the flux lines try to pass between the two, which can be seen in Figure 10-58.

10.5.2.2 Direct comparison with the first parallel cable connected between the shielded and un-shielded simulations

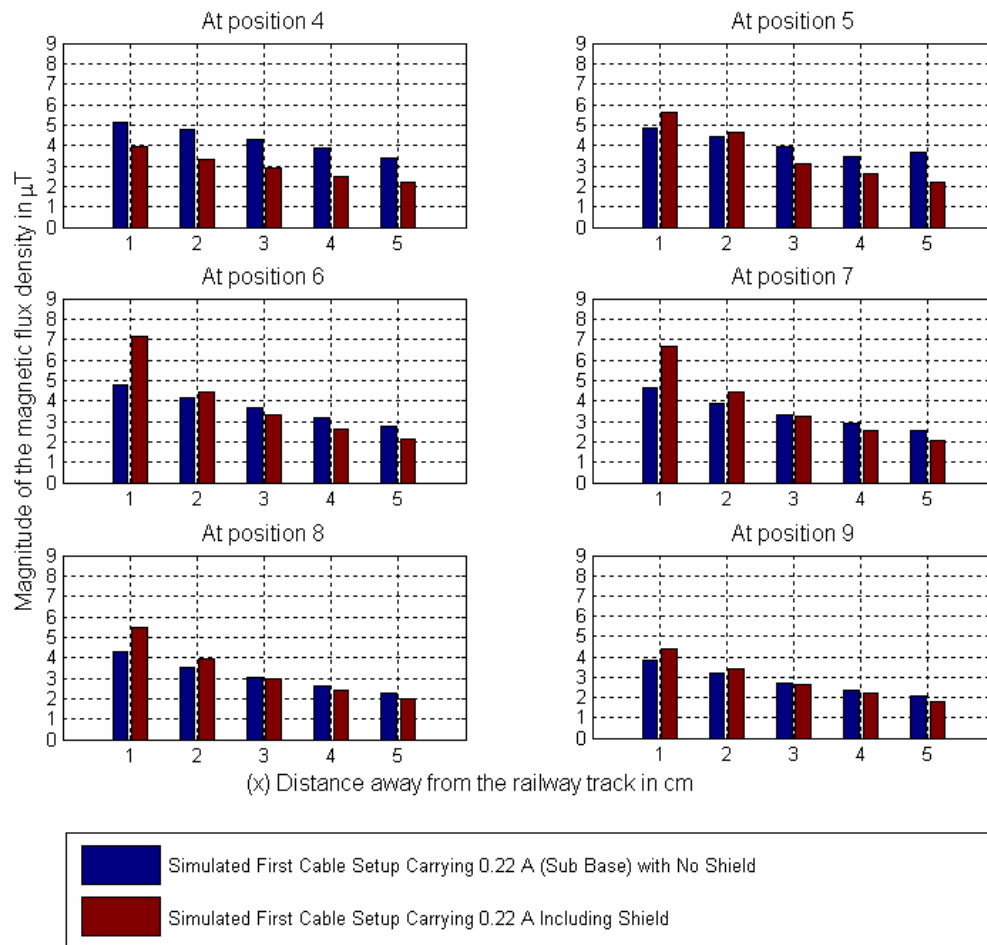


Figure 10-66: Direct Comparison between Shielded and Un-Shielded Simulation with the first parallel Cable in place carrying 0.22 A.

Again the introduction of the shield has a negative effect in reducing the flux density within the first two positions on the X axis from positions 6 and upwards on the Y axis. The effect of the shield was found to be positive further away from the shield. The change in the flux lines for the two cases being compared can be seen in Figure 10-59 and Figure 10-60.

10.5.2.3 Direct comparison with the Second parallel cable connected between the shielded and un-shielded simulations

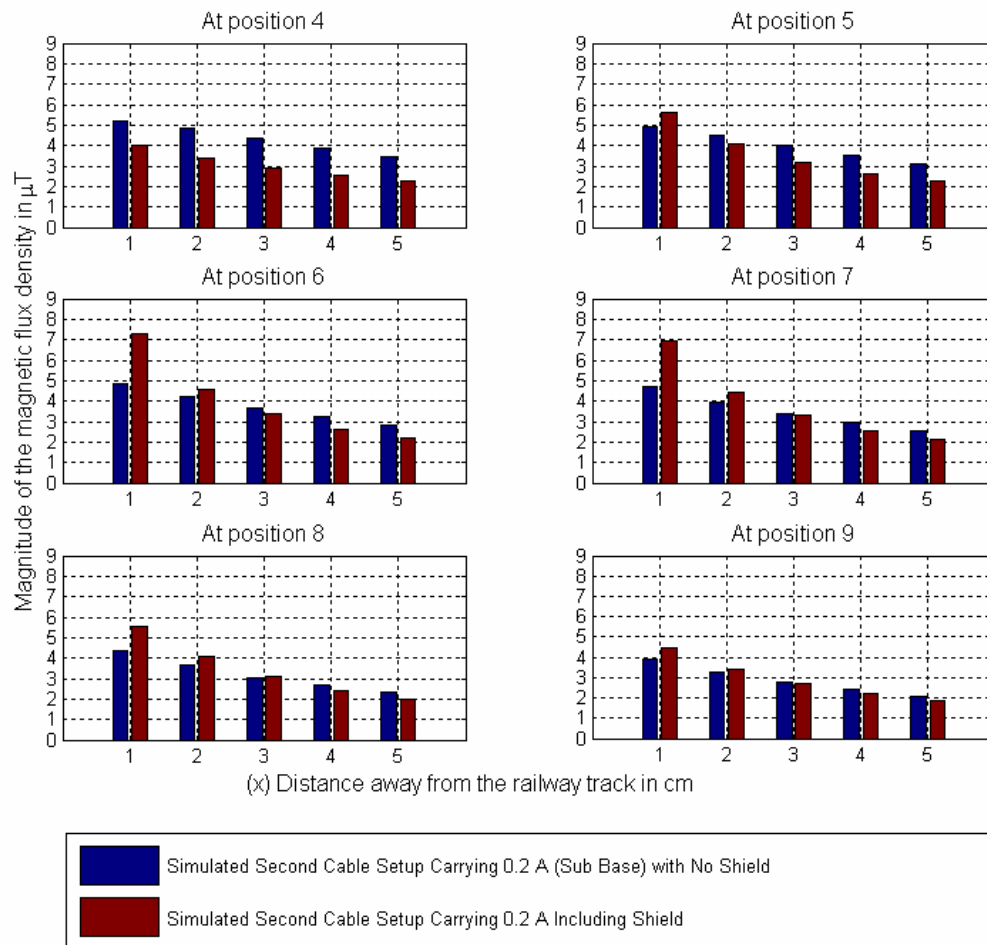


Figure 10-67: Direct Comparison between Shielded and Un-Shielded Simulation with the Second parallel Cable in place carrying 0.2 A.

The same observation can be made for this can which involves the shielded and un-shielded cases with the inclusion of the second parallel cable. The influence of the shield was found to be positive below position 6 on the Y axis but negative for the first two points on the X axis for positions above 6 on the Y axis. The flux lines for the two cases being compared can be seen in Figure 10-61 and Figure 10-62.

10.5.2.4 Direct comparison with the Third parallel cable connected between the shielded and un-shielded simulations

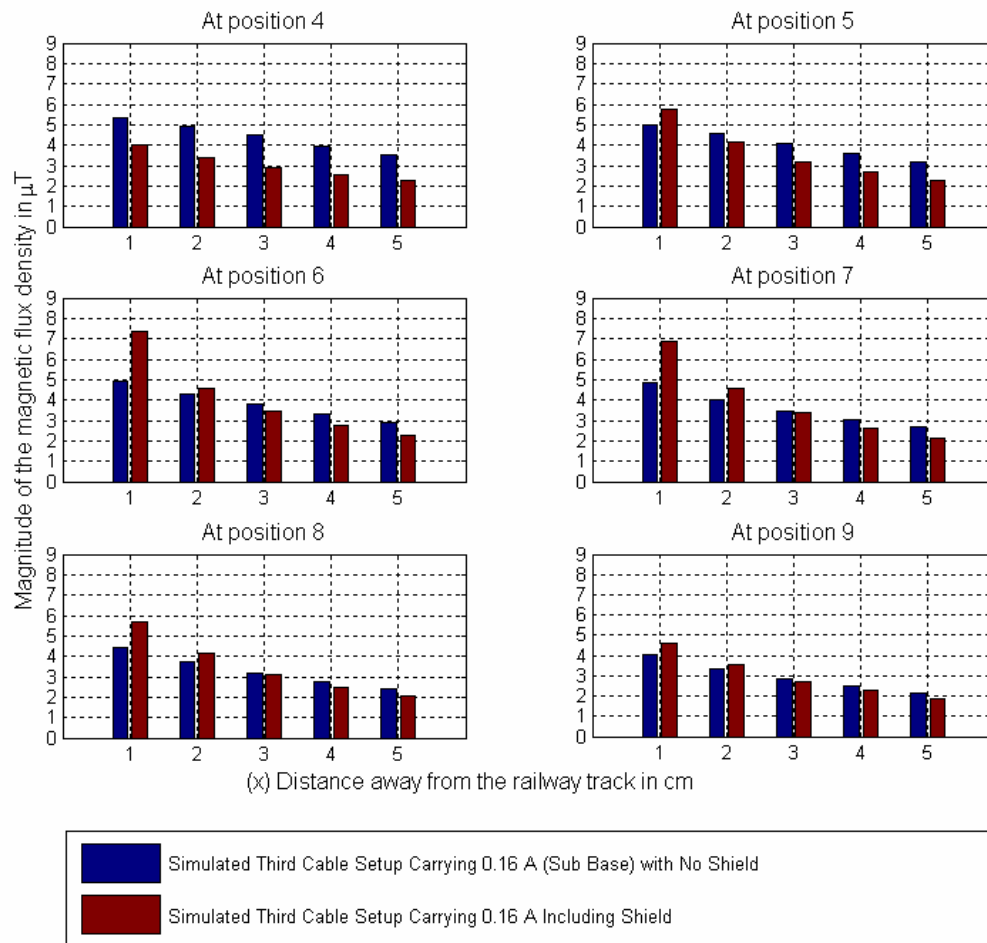


Figure 10-68: Direct Comparison between Shielded and Un-Shielded Simulation with the Third parallel Cable in place carrying 0.16 A.

Finally the comparison for the shielded and un-shielded cases for the third cable simulated yields the same observations as the previous comparisons performed. The introduction of the shield has a negative influence on the flux density within the first two points on the X axis from position 6 on the Y axis and above. The flux lines for the two cases compared can be seen in Figure 10-63 and Figure 10-64: Simulated Results showing the Flux Lines within the Test Area for the Sub base Simulation involving the Third parallel Cable, with the inclusion of the shield.

10.5.3 Appendix 5.3: Flux lines within the test area for the other simulations Performed

10.5.3.1 Inclusion of an Aluminium Shield

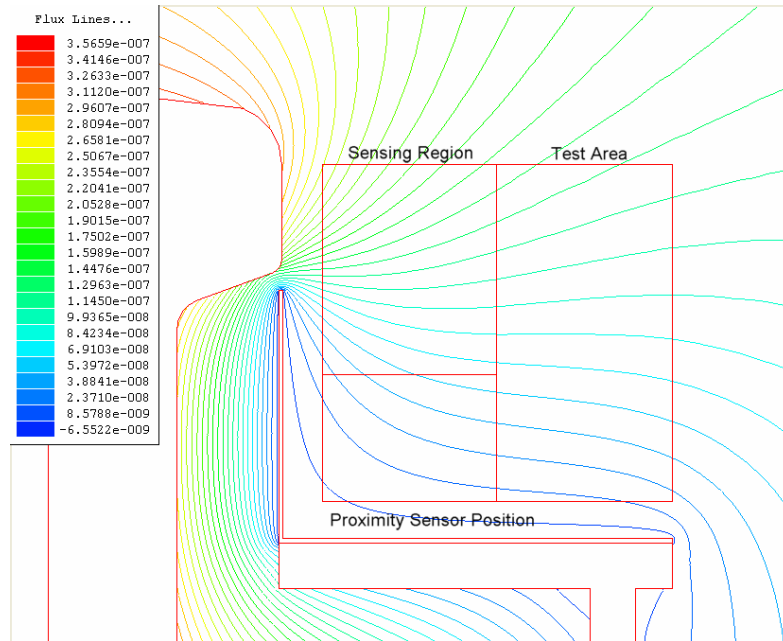


Figure 10-69: Simulated Results showing the Flux Lines within the Test Area for the inclusion of an aluminium shield.

10.5.3.2 Inclusion of a Ferrite Shield

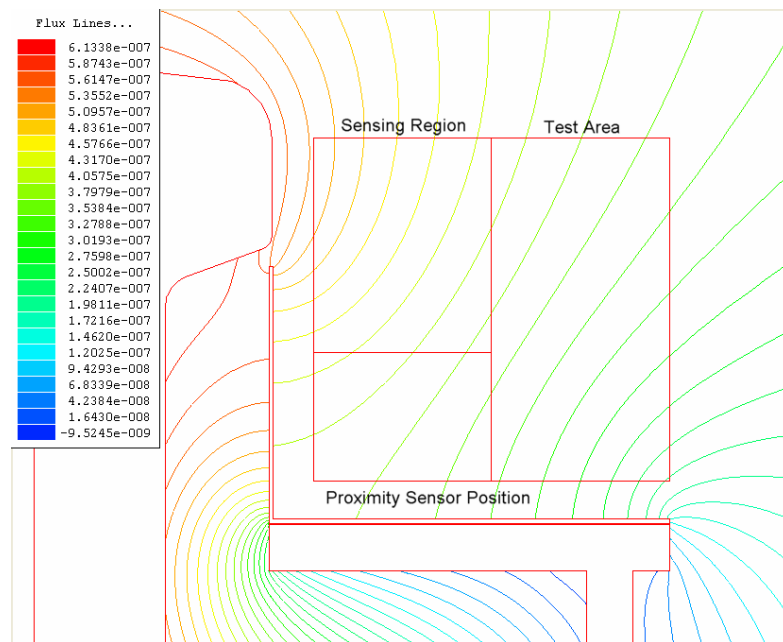


Figure 10-70: Simulated Results showing the Flux Lines within the Test Area for the inclusion of a Ferrite shield.

10.6 Appendix 6: Matlab Code

10.6.1 Appendix 6.1: Matlab Code for Finding the Calibration Coefficients for the Measurement System

File Name Calibration3.m

```
% Determining Calibration Constant Alpha from measured data
% Constant Variables that do not change with frequency
L = 0.722;           %m Length of the Solenoid
NS = 871;           %Turns of wire on the Solenoid
NFD = 200;          %Turns of wire around the Flux Density Sensor
d = 0.004;          %m Diameter of the Flux Density Sensor
Mu0 = 4*pi*1e-7;    %Permeability of Free Space
RLim = 10.04e3;     %Ohms Step-down Resistor at source measurement input R
RInt = 50;          %Ohms Internal impedance of the Network Analyser

% Components That Vary with Frequency
F = [300e3 600e3 800e3 1000e3]; %Operating/Measurement Frequency
ZL = [4.54e3 9.62e3 13.7e3 18.76e3]; %Ohms Impedance of the Solenoid (Magnitude ignoring Phase)
G = [3.79 3.63 3.53 3.43]; %Gain of the Amplification System Determined in Excel
Vout = [2.1493e-3 2.4479e-3 2.8244e-3 3.4414e-3]; %Measured Output Voltage at the input to the NW Analyser
input A
VInm = [686.91e-6 691e-6 693.44e-6 690.80e-6]; %Measured Stepped down Source Voltage measured at input
R of the NW Analyser
Bs = [0 0 0 0]; B0 = [0 0 0 0]; Alpha = [0 0 0 0];
% Solving for Alpha
n=1;
while n < 5
    % Equation 4-7 giving the Flux Density Bs through the Solenoid for the Voltage Vinm
    Bs(n) = (Mu0*NS*(1+RLim/RInt))/(L*ZL(n))*VInm(n);
    % Equation 4-11 giving the link between the Flux Density Measured (B0) by the
    % Flux Density Sensor to the Voltage (Vout) Measured at the Network Analyser.
    B0(n) = 2/(G(n)*NFD*pi^2*d^2*F(n))*Vout(n);
    Alpha(n) = Bs(n)/B0(n); % Calibration Coefficient Alpha
    n = n + 1;
end
display('Frequency') % Displaying the Solutions
F
Bs
B0
Alpha
```


10.6.2 Appendix 6.2: Matlab Program For converting the Measured Results to Tesla and displaying the flux density distribution within the test area in the form of contour plots.

File Name: AFieldPlot.m

```

clear;
clc;
% Importing Data
load 'd:\RAU\2004-2005\Masters\Final Measured Results With TC Amp\All Measurements - Base, 1st Red Cable,
2nd Black Cable and Thin Black Cable.mat';

% Global Physical variables
NFD = 200; % Number of turns
d = 4e-3; % Diameter of wooded rod
f = 300; % KHz Operating frequency
Alpha = 0.3867; % Calibration Constant
G = 6.9381; % Gain introduced due to the Transconductance Amplifier
%.....END Variable Definition.....

% Defining Shield, Sensor Area and Sensing Region
ShH = 6; % Shield Height
ShW = 9; % Shield Width
ShT = 0.05; % Shield Thickness

ShX = [ 1 ; 1+ShT ; 1+ShT ; ShW ; ShW ];
ShY = [ ShH ; ShH ; 1+ShT ; 1+ShT ; 1 ];

BkH = 3.95; %3.5; % Sensor Height
BkW = 5; %4.5; % Sensor Width

BkX = [ 1 ; BkW ; BkW ];
BkY = [ BkH ; BkH ; 1 ];

SRX = [1 ;5 ;5]; %Sensing Region Width X
SRY = [4 ;4 ;9]; %Sensing Region Hight Y
%.....END

%Defining Main Output Destination (Directory)
Destination = 'd:\RAU\2004-2005\Masters\Contour plots at 300kHz';

%Begining Sequence conversion
n = 1;
t = 1;

while n < 13
    if n == 1
        Xco = XcoB;
        Yco = YcoB;
        Shield = 'N';
        %Defining Sub Output Destination
        Sub = 'No Cable';
        %Defining End of File Name
        Name = 'No Shield, No Isolation and No Cable';
    end

    if n == 2
        Xco = XcoSB;
        Yco = YcoSB;
        Shield = 'Y';
        %Defining Sub Output Destination
        Sub = 'No Cable';
        %Defining End of File Name
        Name = 'Shield, No Isolation and No Cable';
    end

    if n == 3
        Xco = XcoISB;
        Yco = YcoISB;
    end
end

```

```

Shield = 'Y';
%Defining Sub Output Destination
Sub = 'No Cable';
%Defining End of File Name
Name = 'Shield, Isolation and No Cable';
end

if n == 4
Xco = XcoTRCB;
Yco = YcoTRCB;
Shield = 'N';
%Defining Sub Output Destination
Sub = '1st Thick Red Cable';
%Defining End of File Name
Name = '1st Thick Red Cable with No Shield and No Isolation';
end

if n == 5
Xco = XcoTRCS;
Yco = YcoTRCS;
Shield = 'Y';
%Defining Sub Output Destination
Sub = '1st Thick Red Cable';
%Defining End of File Name
Name = '1st Thick Red Cable with Shield and No Isolation';
end

if n == 6
Xco = XcoTRCIS;
Yco = YcoTRCIS;
Shield = 'Y';
%Defining Sub Output Destination
Sub = '1st Thick Red Cable';
%Defining End of File Name
Name = '1st Thick Red Cable with Shield and Isolation';
end

if n == 7
Xco = XcoTBCB;
Yco = YcoTBCB;
Shield = 'N';
%Defining Sub Output Destination
Sub = '2nd Thick Black Cable';
%Defining End of File Name
Name = '2nd Thick Black Cable with No Shield and No Isolation';
end

if n == 8
Xco = XcoTBCS;
Yco = YcoTBCS;
Shield = 'Y';
%Defining Sub Output Destination
Sub = '2nd Thick Black Cable';
%Defining End of File Name
Name = '2nd Thick Black Cable with Shield and No Isolation';
end

if n == 9
Xco = XcoTBCIS;
Yco = YcoTBCIS;
Shield = 'Y';
%Defining Sub Output Destination
Sub = '2nd Thick Black Cable';
%Defining End of File Name
Name = '2nd Thick Black Cable with Shield and Isolation';
end

if n == 10
Xco = XcoTnBCB;
Yco = YcoTnBCB;
Shield = 'N';
%Defining Sub Output Destination
Sub = '3rd Thin Black Cable';
%Defining End of File Name
Name = '3rd Thin Black Cable with No Shield and No Isolation';

```

```

end

if n == 11
    Xco = XcoTnBCS;
    Yco = YcoTnBCS;
    Shield = 'Y';
    %Defining Sub Output Destination
    Sub = '3rd Thin Black Cable!';
    %Defining End of File Name
    Name = '3rd Thin Black Cable with Shield and No Isolation!';
end

if n == 12
    Xco = XcoTnBCIS;
    Yco = YcoTnBCIS;
    Shield = 'Y';
    %Defining Sub Output Destination
    Sub = '3rd Thin Black Cable!';
    %Defining End of File Name
    Name = '3rd Thin Black Cable with Shield and Isolation!';
end

% Xco & Yco are in mV there fore A*mV /(kHz*B*C)gives MicroT

XcoM = Alpha *(2/(G*NFD*pi^2*d^2*f) * Xco); % Micro Tesla
YcoM = Alpha *(2/(G*NFD*pi^2*d^2*f) * Yco); % Micro Tesla

Comp = XcoM + i*YcoM;

Mag = abs(Comp);
Ang = angle(Comp);

pl = 1;
% Preparing to Plot the contour plots of the flux density
v = 20 : -0.25 : 0;
sp = 20 : -0.5 : 0;

while pl < 4

    if pl == 1
        Data = Mag;
        %Defining Figure Title
        Comp = " ";
    end

    if pl == 2
        Data = XcoM;
        %Defining Figure Title
        Comp = 'of the X component ';
    end

    if pl == 3
        Data = YcoM;
        %Defining Figure Title
        Comp = 'of the Y component ';
    end

    %Defining Output File Name
    FileName = ['Contour plot of the magnetic flux densities in MicroT at 300KHz ' Comp ' with ' Name];
    % Plotting The Contour Plots of the flux density
    figure(t);[C,h] = contour(Data,v); clabel(C,h,sp,'FontSize',8,'Color',[0 0 0],'Rotation',0,'LabelSpacing',288); %72
    points is one Inch
    title(['Contour plot of the magnetic flux densities ' Comp ' in \muT at 300 kHz'],'FontSize',10,'FontWeight','demi');
    xlabel('(X) Horizontal Direction away from the railway track in cm','FontSize',10);
    ylabel('(Y) Vertical Direction in cm','FontSize',10);
    text(5,5.5,' \leftarrow Sensing
    Region','FontSize',10,'FontWeight','normal','FontAngle','oblique','BackgroundColor',[1 1 1]);
    text(5,3.5,' \leftarrow Proximity Sensor
    Position','FontSize',10,'FontWeight','normal','FontAngle','oblique','BackgroundColor',[1 1 1]);
    % Drawing the Shield and Sensor Area
    hold on; plot(BkX,BkY,'k'); hold off;
    hold on; plot(SRX,SRY,'--k'); hold off;
    if Shield == 'Y'
        hold on; plot(ShX,ShY,'k'); hold off;
    end
end

```

```

% Saving the Contour Plot to File
saveas(gcf,[Destination Sub FileName], 'bmp')
pl = pl + 1;
t = t + 1;
end
% .....END Ploting and Saving File.

if n == 1
    XcoBM = XcoM;
    YcoBM = YcoM;
    BMag = Mag;
    BAng = Ang;
end

if n == 2
    XcoSBM = XcoM;
    YcoSBM = YcoM;
    SBMag = Mag;
    SBAng = Ang;
end

if n == 3
    XcoISBM = XcoM;
    YcoISBM = YcoM;
    ISBMag = Mag;
    ISBAng = Ang;
end

if n == 4
    XcoTRCBM = XcoM;
    YcoTRCBM = YcoM;
    TRCBMag = Mag;
    TRCBAng = Ang;
end

if n == 5
    XcoTRCSM = XcoM;
    YcoTRCSM = YcoM;
    TRCSMag = Mag;
    TRCSAng = Ang;
end

if n == 6
    XcoTRCISM = XcoM;
    YcoTRCISM = YcoM;
    TRCISMag = Mag;
    TRCISAng = Ang;
end

if n == 7
    XcoTBCBM = XcoM;
    YcoTBCBM = YcoM;
    TBCBMag = Mag;
    TBCBAng = Ang;
end

if n == 8
    XcoTBCSM = XcoM;
    YcoTBCSM = YcoM;
    TBCSMag = Mag;
    TBCSAng = Ang;
end

if n == 9
    XcoTBCISM = XcoM;
    YcoTBCISM = YcoM;
    TBCISMag = Mag;
    TBCISAng = Ang;
end

if n == 10
    XcoTnBCBM = XcoM;
    YcoTnBCBM = YcoM;
    TnBCBMag = Mag;

```

```
TnBCBAng = Ang;
end

if n == 11
    XcoTnBCSM = XcoM;
    YcoTnBCSM = YcoM;
    TnBCSMag = Mag;
    TnBCSAng = Ang;
end

if n == 12
    XcoTnBCISM = XcoM;
    YcoTnBCISM = YcoM;
    TnBCISMag = Mag;
    TnBCISAng = Ang;
end

n = n + 1;

end
```

10.6.3 Appendix 6.3: Matlab program for generating the bar graphs used for the direct comparison of the measured results

Filename: DirectAll.m

```
clc;
```

```
% Direct comparison section where the y component values from just above the  
% sensor to the top of the test area for the unshielded, shielded not  
% grounded and shielded grounded cases are compared.
```

```
Destination = 'd:\RAU\2004-2005\Masters\Contour plots at 300kHz!';  
Sub = 'Direct Comparison Bar!';
```

```
N = 5;
```

```
while N < 8
```

```
  if N == 1
```

```
    YcoM1 = YcoBM;  
    YcoM2 = YcoSBM;  
    YcoM3 = YcoISBM;  
    % Defining the File Name for the Plot of this Data Set  
    FileName = 'No Cable';  
    % Setting the Legend Titles  
    Legend1 = 'Base Setup with No Cable and No Shield';  
    Legend2 = 'Base Setup with Shield';  
    Legend3 = 'Base Setup with Shield and Isolation';
```

```
  end
```

```
  if N == 2
```

```
    YcoM1 = YcoTRCBM;  
    YcoM2 = YcoTRCSM;  
    YcoM3 = YcoTRCISM;  
    % Defining the File Name for the Plot of this Data Set  
    FileName = 'Thick Red Cable';  
    % Setting the Legend Titles  
    Legend1 = 'First Cable (Sub Base) Setup with Thick Red Cable and No Shield';  
    Legend2 = 'First Cable Setup with Thick Red Cable Including Shield';  
    Legend3 = 'First Cable Setup with Thick Red Cable Including Shield and Isolation';
```

```
  end
```

```
  if N == 3
```

```
    YcoM1 = YcoTBCBM;  
    YcoM2 = YcoTBCSM;  
    YcoM3 = YcoTBCISM;  
    % Defining the File Name for the Plot of this Data Set  
    FileName = 'Thick Black Cable';  
    % Setting the Legend Titles  
    Legend1 = 'Second Cable (Sub Base) Setup with Thick Black Cable and No Shield';  
    Legend2 = 'Second Cable Setup with Thick Black Cable Including Shield';  
    Legend3 = 'Second Cable Setup with Thick Black Cable Including Shield and Isolation';
```

```
  end
```

```
  if N == 4
```

```
    YcoM1 = YcoTnBCBM;  
    YcoM2 = YcoTnBCSM;  
    YcoM3 = YcoTnBCISM;  
    % Defining the File Name for the Plot of this Data Set  
    FileName = 'Thin Black Cable';  
    % Setting the Legend Titles  
    Legend1 = 'Third Cable (Sub Base) Setup with Thin Black Cable and No Shield';  
    Legend2 = 'Third Cable Setup with Thin Black Cable Including Shield';  
    Legend3 = 'Third Cable Setup with Thin Black Cable Including Shield and Isolation';
```

```
  end
```

```
  if N == 5
```

```
    YcoM1 = YcoBM;
```

```

YcoM2 = YcoTRCBM;
YcoM3 = YcoTBCBM;
YcoM4 = YcoTnBCBM;
% Defining the File Name for the Plot of this Data Set
FileName = 'Comparison Between Base and Sub Base Measurements';
% Setting the Legend Titles
Legend1 = 'Base Setup with No Cable and No Shield';
Legend2 = 'First Cable (Sub Base) Setup with Thick Red Cable and No Shield';
Legend3 = 'Second Cable (Sub Base) Setup with Thick Black Cable and No Shield';
Legend4 = 'Third Cable (Sub Base) Setup with Thin Black Cable and No Shield';
end

if N == 6
YcoM1 = YcoSBM;
YcoM2 = YcoTRCSM;
YcoM3 = YcoTBCSM;
YcoM4 = YcoTnBCSM;
% Defining the File Name for the Plot of this Data Set
FileName = 'Comparison Between All Shielded Cases';
% Setting the Legend Titles
Legend1 = 'Base Setup with Shield';
Legend2 = 'First Cable Setup with Thick Red Cable Including Shield';
Legend3 = 'Second Cable Setup with Thick Black Cable Including Shield';
Legend4 = 'Third Cable Setup with Thin Black Cable Including Shield';
end

if N == 7
YcoM1 = YcoISBM;
YcoM2 = YcoTRCISM;
YcoM3 = YcoTBCISM;
YcoM4 = YcoTnBCISM;
% Defining the File Name for the Plot of this Data Set
FileName = 'Comparison Between All Shielded and Isolated Cases';
% Setting the Legend Titles
Legend1 = 'Base Setup with Shield and Isolation';
Legend2 = 'First Cable Setup with Thick Red Cable Including Shield and Isolation';
Legend3 = 'Second Cable Setup with Thick Black Cable Including Shield and Isolation';
Legend4 = 'Third Cable Setup with Thin Black Cable Including Shield and Isolation';
end

% Defining Counters
r = 1;
l = 4;
x = 1:1:5;
s = [1:1:5];
a = 1;

% Setting Figure Size
set(0,'Units','pixels');
FigSize = get(0,'ScreenSize');
Pos = [0.16*FigSize(3),0.1*FigSize(4),0.66*FigSize(3),0.8*FigSize(4)];
figure('Position',Pos);

while l < 10

if N < 5
Y = [YcoM1(l,s) YcoM2(l,s) YcoM3(l,s)];
Bar_handles = [0 0 0];
end

if N > 4
Y = [YcoM1(l,s) YcoM2(l,s) YcoM3(l,s) YcoM4(l,s)];
Bar_handles = [0 0 0 0];
end

%figure(N);
subplot(4,2,a,'align');
Bar_handles(r,:) = Bar(Y);

test = ceil(max(YcoM1(l,s)/10)*7);
set(gca,'YTick',[0:1:test]);
axis([0 6 0 test]);

hold off; zoom on; grid on;

```

```

if l == 4
    strr1 = (cat(2,'Flux densities parallel to the top of the sensor at position ',num2str(l),' along the Y axis'));
end

if 4 < l < 10
    strr1 = (cat(2,'At position ',num2str(l)));
end

TITLE(strr1,'FontSize',12);

if l == 9
    legend_handles = [Bar_handles(r,:)];
    if N < 5
        legend(legend_handles,Legend1,Legend2,Legend3,'Location',[0.133 0.15 0.773 0.1]) % [left bottom width
height]
    end

    if N > 4
        legend(legend_handles,Legend1,Legend2,Legend3,Legend4,'Location',[0.133 0.15 0.773 0.1]) % [left
bottom width height]
    end
end

if l == 6
    YLABEL('Magnitude of the magnetic flux density in  $\mu\text{T}$ ','FontSize',12);
end

if l == 8
    XLABEL('
cm','FontSize',12);
end
l = l + 1;
a = a + 1;

end
r = r + 1;
% Saving the Contour Plot to File
saveas(gcf,[Destination Sub FileName], 'bmp')

N = N + 1;
end

```


10.6.4 Appendix 6.4: Matlab program for generating the Normalized bar graphs used for the direct comparison of the measured results

Filename: DirectAllNormal.m

```
clc;
```

```
% Direct comparison section where the y component values from just above the  
% sensor to the top of the test area for the unshielded, shielded not  
% grounded and shielded grounded cases are compared.
```

```
Destination = 'd:\RAU\2004-2005\Masters\Contour plots at 300kHz';  
Sub = 'Direct Comparison Bar Norml';
```

```
N = 1;
```

```
while N < 8
```

```
  if N == 1
```

```
    YcoM1 = YcoBM;  
    YcoM2 = YcoSBM;  
    YcoM3 = YcoISBM;  
    % Defining the File Name for the Plot of this Data Set  
    FileName = 'No Cable';  
    % Setting the Legend Titles  
    Legend1 = 'Base Setup with No Cable and No Shield';  
    Legend2 = 'Base Setup with Shield';  
    Legend3 = 'Base Setup with Shield and Isolation';
```

```
  end
```

```
  if N == 2
```

```
    YcoM1 = YcoTRCBM;  
    YcoM2 = YcoTRCSM;  
    YcoM3 = YcoTRCISM;  
    % Defining the File Name for the Plot of this Data Set  
    FileName = 'Thick Red Cable';  
    % Setting the Legend Titles  
    Legend1 = 'First Cable (Sub Base) Setup with Thick Red Cable and No Shield';  
    Legend2 = 'First Cable Setup with Thick Red Cable Including Shield';  
    Legend3 = 'First Cable Setup with Thick Red Cable Including Shield and Isolation';
```

```
  end
```

```
  if N == 3
```

```
    YcoM1 = YcoTBCBM;  
    YcoM2 = YcoTBCSM;  
    YcoM3 = YcoTBCISM;  
    % Defining the File Name for the Plot of this Data Set  
    FileName = 'Thick Black Cable';  
    % Setting the Legend Titles  
    Legend1 = 'Second Cable (Sub Base) Setup with Thick Black Cable and No Shield';  
    Legend2 = 'Second Cable Setup with Thick Black Cable Including Shield';  
    Legend3 = 'Second Cable Setup with Thick Black Cable Including Shield and Isolation';
```

```
  end
```

```
  if N == 4
```

```
    YcoM1 = YcoTnBCBM;  
    YcoM2 = YcoTnBCSM;  
    YcoM3 = YcoTnBCISM;  
    % Defining the File Name for the Plot of this Data Set  
    FileName = 'Thin Black Cable';  
    % Setting the Legend Titles  
    Legend1 = 'Third Cable (Sub Base) Setup with Thin Black Cable and No Shield';  
    Legend2 = 'Third Cable Setup with Thin Black Cable Including Shield';  
    Legend3 = 'Third Cable Setup with Thin Black Cable Including Shield and Isolation';
```

```
  end
```

```
  if N == 5
```

```
    YcoM1 = YcoBM;
```

```

YcoM2 = YcoTRCBM;
YcoM3 = YcoTBCBM;
YcoM4 = YcoTnBCBM;
% Defining the File Name for the Plot of this Data Set
FileName = 'Comparison Between Base and Sub Base Measurements';
% Setting the Legend Titles
Legend1 = 'Base Setup with No Cable and No Shield';
Legend2 = 'First Cable (Sub Base) Setup with Thick Red Cable and No Shield';
Legend3 = 'Second Cable (Sub Base) Setup with Thick Black Cable and No Shield';
Legend4 = 'Third Cable (Sub Base) Setup with Thin Black Cable and No Shield';
end

if N == 6
YcoM1 = YcoSBM;
YcoM2 = YcoTRCSM;
YcoM3 = YcoTBCSM;
YcoM4 = YcoTnBCSM;
% Defining the File Name for the Plot of this Data Set
FileName = 'Comparison Between All Shielded Cases';
% Setting the Legend Titles
Legend1 = 'Base Setup with Shield';
Legend2 = 'First Cable Setup with Thick Red Cable Including Shield';
Legend3 = 'Second Cable Setup with Thick Black Cable Including Shield';
Legend4 = 'Third Cable Setup with Thin Black Cable Including Shield';
end

if N == 7
YcoM1 = YcoISBM;
YcoM2 = YcoTRCISM;
YcoM3 = YcoTBCISM;
YcoM4 = YcoTnBCISM;
% Defining the File Name for the Plot of this Data Set
FileName = 'Comparison Between All Shielded and Isolated Cases';
% Setting the Legend Titles
Legend1 = 'Base Setup with Shield and Isolation';
Legend2 = 'First Cable Setup with Thick Red Cable Including Shield and Isolation';
Legend3 = 'Second Cable Setup with Thick Black Cable Including Shield and Isolation';
Legend4 = 'Third Cable Setup with Thin Black Cable Including Shield and Isolation';
end

r = 1;
l = 4;
x = 1:1:5;
s = [1:1:5];
a = 1;
set(0,'Units','pixels');
FigSize = get(0,'ScreenSize');
Pos = [0.16*FigSize(3),0.1*FigSize(4),0.66*FigSize(3),0.8*FigSize(4)];
figure('Position',Pos);

while l < 10

figure(N);
subplot(4,2,a,'align');

la = 1;
while la < 6
YcoM1Norm(l,la) = YcoM1(l,la)/YcoBM(l,la)*100;
YcoM2Norm(l,la) = YcoM2(l,la)/YcoBM(l,la)*100;
YcoM3Norm(l,la) = YcoM3(l,la)/YcoBM(l,la)*100;
if N > 4
YcoM4Norm(l,la) = YcoM4(l,la)/YcoBM(l,la)*100;
end
la = la + 1;
end

if N < 5
Bar_handles = [0 0 0];
Y = [YcoM1Norm(l,s)' YcoM2Norm(l,s)' YcoM3Norm(l,s)];
end

if N > 4
Bar_handles = [0 0 0 0];
Y = [YcoM1Norm(l,s)' YcoM2Norm(l,s)' YcoM3Norm(l,s)' YcoM4Norm(l,s)];
end

```

```

end

Bar_handles(r,:) = Bar(Y);

% test = ceil(max(YcoM1(l,s)/10))*10;
set(gca,'YTick',[50:10:100]);
axis([0 6 50 100]);

hold off; zoom on; grid on;

if l == 4
    str1 = (cat(2,'Flux densities parallel to the top of the sensor at position ',num2str(l),' along the Y axis'));
end

if 4 < l < 10
    str1 = (cat(2,'At position ',num2str(l)));
end

TITLE(str1,'FontSize',12);

if l == 9
    legend_handles = [Bar_handles(r,:);
    if N < 5
        legend(legend_handles,Legend1,Legend2,Legend3,'Location',[0.133 0.15 0.773 0.1]) % [left bottom width
height]
    end
    if N > 4
        legend(legend_handles,Legend1,Legend2,Legend3,Legend4,'Location',[0.133 0.15 0.773 0.1]) % [left
bottom width height]
    end
end

if l == 6
    YLABEL('Normalized Comparison between Flux Denisty Measurements in %','FontSize',12);
end

if l == 8
    XLABEL('
(x) Distance away from the railway track in
cm','FontSize',12);
end
l = l + 1;
a = a + 1;

end
r = r + 1;
% Saving the Contour Plot to File
saveas(gcf,[Destination Sub FileName], 'bmp')

N = N + 1;
end

```

10.6.5 Appendix 6.5: Matlab Program for determining the total percentage reduction of the flux density within the sensing region

Filename: TotalPerRed.m

```
clc;
% Determining the Total Percentage of magnetic Flux Density within the
% sensing region for each modification performed with respect to the total
% magnetic Flux Density present for the Base Condition

% Defining Variables
TYcoBM = 0; TYcoSBM = 0; TYcoISBM = 0;

TYcoTRCBM = 0; TYcoTRCSM = 0; TYcoTRCISM = 0;

TYcoTBCBM = 0; TYcoTBCSM = 0; TYcoTBCISM = 0;

TYcoTnBCBM = 0; TYcoTnBCSM = 0; TYcoTnBCISM = 0;

Row = 4; % Defining Counter

while Row < 10

    Col = 1; % Defining Counter

    while Col < 6

        TYcoBM = TYcoBM + YcoBM(Row,Col);
        TYcoSBM = TYcoSBM + YcoSBM(Row,Col);
        TYcoISBM = TYcoISBM + YcoISBM(Row,Col);

        TYcoTRCBM = TYcoTRCBM + YcoTRCBM(Row,Col);
        TYcoTRCSM = TYcoTRCSM + YcoTRCSM(Row,Col);
        TYcoTRCISM = TYcoTRCISM + YcoTRCISM(Row,Col);

        TYcoTBCBM = TYcoTBCBM + YcoTBCBM(Row,Col);
        TYcoTBCSM = TYcoTBCSM + YcoTBCSM(Row,Col);
        TYcoTBCISM = TYcoTBCISM + YcoTBCISM(Row,Col);

        TYcoTnBCBM = TYcoTnBCBM + YcoTnBCBM(Row,Col);
        TYcoTnBCSM = TYcoTnBCSM + YcoTnBCSM(Row,Col);
        TYcoTnBCISM = TYcoTnBCISM + YcoTnBCISM(Row,Col);

        Col = Col + 1;
    end

    Row = Row + 1;
end

% Determining the Total Percentage of the Magnetic Flux Density that is
% left for each of the modifications performed

PerTYcoSBM = (1-TYcoSBM/TYcoBM) * 100
PerTYcoISBM = (1-TYcoISBM/TYcoBM) * 100

PerTYcoTRCBM = (1-TYcoTRCBM/TYcoBM) * 100
PerTYcoTRCSM = (1-TYcoTRCSM/TYcoBM) * 100
PerTYcoTRCISM = (1-TYcoTRCISM/TYcoBM) * 100

PerTYcoTBCBM = (1-TYcoTBCBM/TYcoBM) * 100
PerTYcoTBCSM = (1-TYcoTBCSM/TYcoBM) * 100
PerTYcoTBCISM = (1-TYcoTBCISM/TYcoBM) * 100

PerTYcoTnBCBM = (1-TYcoTnBCBM/TYcoBM) * 100
PerTYcoTnBCSM = (1-TYcoTnBCSM/TYcoBM) * 100
PerTYcoTnBCISM = (1-TYcoTnBCISM/TYcoBM) * 100
```

10.6.6 Appendix 6.6: Matlab Program written to produce the direct comparison of the simulated results

Filename : DirectSimF.m

```
clc;
```

```
% Direct comparison section where the y component values from just above the  
% sensor to the top of the test area for the unshielded, shielded not  
% grounded and shielded grounded cases are compared.
```

```
% Importing Data
```

```
load 'd:\RAU\2004-2005\Masters\Masters Report\Simulations\Data\Simulation Data.mat';
```

```
% Setting Destination to Save all the Figures Generated
```

```
Destination = 'd:\RAU\2004-2005\Masters\Masters Report\Simulations';
```

```
Sub = 'Direct Comparison Bar of Simulations';
```

```
N = 1;
```

```
while N < 8
```

```
    if N == 1
```

```
        YcoM1 = SBnC;
```

```
        YcoM2 = SBSnC;
```

```
        % Defining the File Name for the Plot of this Data Set
```

```
        FileName = 'Base with No Cable';
```

```
        % Setting the Legend Titles
```

```
        Legend1 = 'Simulated Base Setup with No Shield and No Cable';
```

```
        Legend2 = 'Simulated Base Setup with Shield but No Cable';
```

```
    end
```

```
    if N == 2
```

```
        YcoM1 = SFC022;
```

```
        YcoM2 = SFC022S;
```

```
        % Defining the File Name for the Plot of this Data Set
```

```
        FileName = 'First Cable 022A - Thick Red Cable';
```

```
        % Setting the Legend Titles
```

```
        Legend1 = 'Simulated First Cable Setup Carrying 0.22 A (Sub Base) with No Shield';
```

```
        Legend2 = 'Simulated First Cable Setup Carrying 0.22 A Including Shield';
```

```
    end
```

```
    if N == 3
```

```
        YcoM1 = SSC02;
```

```
        YcoM2 = SSC02S;
```

```
        % Defining the File Name for the Plot of this Data Set
```

```
        FileName = 'Second Cable 02A - Thick Black Cable';
```

```
        % Setting the Legend Titles
```

```
        Legend1 = 'Simulated Second Cable Setup Carrying 0.2 A (Sub Base) with No Shield';
```

```
        Legend2 = 'Simulated Second Cable Setup Carrying 0.2 A Including Shield';
```

```
    end
```

```
    if N == 4
```

```
        YcoM1 = STC016;
```

```
        YcoM2 = STC016S;
```

```
        % Defining the File Name for the Plot of this Data Set
```

```
        FileName = 'Third Cable 016A - Thin Black Cable';
```

```
        % Setting the Legend Titles
```

```
        Legend1 = 'Simulated Third Cable Setup Carrying 0.16 A (Sub Base) with No Shield';
```

```
        Legend2 = 'Simulated Third Cable Setup Carrying 0.16 A Including Shield';
```

```
    end
```

```
    if N == 5
```

```
        YcoM1 = SBnC;
```

```
        YcoM2 = SASnC;
```

```
        YcoM3 = SFSnC;
```

```
        % Defining the File Name for the Plot of this Data Set
```

```
        FileName = 'Comparison of Different Shield Types';
```

```
        % Setting the Legend Titles
```

```

Legend1 = 'Simulated Base Setup with No Shield and No Cable';
Legend2 = 'Simulated Aluminium Shield with No Cable';
Legend3 = 'Simulated Ferrite Shield with No Cable';

end

if N == 6
    YcoM1 = SBnC;
    YcoM2 = SFC022;
    YcoM3 = SSC02;
    YcoM4 = STC016;
    % Defining the File Name for the Plot of this Data Set
    FileName = 'Comparison Between Base and Sub Base Measurements';
    % Setting the Legend Titles
    Legend1 = 'Simulated Base Setup with No Cable and No Shield';
    Legend2 = 'Simulated First Cable Setup Carrying 0.22 A (Sub Base) with No Shield';
    Legend3 = 'Simulated Second Cable Setup Carrying 0.2 A (Sub Base) with No Shield';
    Legend4 = 'Simulated Third Cable Setup Carrying 0.16 A (Sub Base) with No Shield';
end

if N == 7
    YcoM1 = SBSnC;
    YcoM2 = SFC022S;
    YcoM3 = SSC02S;
    YcoM4 = STC016S;
    % Defining the File Name for the Plot of this Data Set
    FileName = 'Comparison Between All Shielded Cases';
    % Setting the Legend Titles
    Legend1 = 'Simulated Base Setup with No Cable Including Shield';
    Legend2 = 'Simulated First Cable Setup Carrying 0.22 A (Sub Base) Including Shield';
    Legend3 = 'Simulated Second Cable Setup Carrying 0.2 A (Sub Base) Including Shield';
    Legend4 = 'Simulated Third Cable Setup Carrying 0.16 A (Sub Base) Including Shield';
end

% Defining Counters
r = 1;
l = 4;
x = 1:1:5;
s = [1:1:5];
a = 1;

% Setting Figure Size
set(0,'Units','pixels');
FigSize = get(0,'ScreenSize');
Pos = [0.16*FigSize(3),0.1*FigSize(4),0.66*FigSize(3),0.8*FigSize(4)];
figure('Position',Pos);

while l < 10

    if N < 5
        Y = [YcoM1(l-3,s) YcoM2(l-3,s)];
        Bar_handles = [0 0];
    end

    if N < 6
        if N > 4
            Y = [YcoM1(l-3,s) YcoM2(l-3,s) YcoM3(l-3,s)];
            Bar_handles = [0 0 0];
        end
    end

    if N > 5
        Y = [YcoM1(l-3,s) YcoM2(l-3,s) YcoM3(l-3,s) YcoM4(l-3,s)];
        Bar_handles = [0 0 0 0];
    end

    %figure(N);
    subplot(4,2,a,'align');
    Bar_handles(r,:) = Bar(Y);

    test = ceil(max(YcoM1(l-3,s)/10))*9;
    set(gca,'YTick',[0:1:test]);
    axis([0 6 0 test]);

```

```

hold off; zoom on; grid on;

if l == 4
    strr1 = (cat(2,'Flux densities parallel to the top of the sensor at position ',num2str(l),' along the Y axis'));
end

if 4 < l < 10
    strr1 = (cat(2,'At position ',num2str(l)));
end

TITLE(strr1,'FontSize',12);

if l == 9
    legend_handles = [Bar_handles(r,:)];
    if N < 5
        legend(legend_handles,Legend1,Legend2,'Location',[0.133 0.15 0.773 0.1]) % [left bottom width height]
    end

    if N < 6
        if N > 4
            legend(legend_handles,Legend1,Legend2,Legend3,'Location',[0.133 0.15 0.773 0.1]) % [left bottom
width height]
        end
    end

    if N > 5
        legend(legend_handles,Legend1,Legend2,Legend3,Legend4,'Location',[0.133 0.15 0.773 0.1]) % [left
bottom width height]
    end

    if l == 6
        YLABEL('Magnitude of the magnetic flux density in  $\mu\text{T}$ ','FontSize',12);
    end

    if l == 8
        XLABEL('
cm','FontSize',12);
    end
    l = l + 1;
    a = a + 1;

end
r = r + 1;
% Saving the Contour Plot to File
saveas(gcf,[Destination Sub FileName], 'bmp')

N = N + 1;
end

```

(x) Distance away from the railway track in

10.6.7 Appendix 6.7: Matlab Program used to determine the total percentage reduction of the flux density within the sensing region for each of the simulation cases.

Filename: TPerRedSim.m

```
clc;
% Determining the Total Percentage of magnetic Flux Density within the
% sensing region for each modification performed with respect to the total
% magnetic Flux Density present for the Base Condition

% Defining Variables
TSBnC = 0; TSBSnC = 0;
TSFC022 = 0; TSFC022S = 0;
TSSC02 = 0; TSSC02S = 0;
TSTC016 = 0; TSTC016S = 0;
TSASnC = 0; TSFSnC = 0;

Row = 1; % Defining Counter

while Row < 7

    Col = 1; % Defining Counter

    while Col < 6

        TSBnC = TSBnC + SBnC(Row,Col);
        TSBSnC = TSBSnC + SBSnC(Row,Col);

        TSFC022 = TSFC022 + SFC022(Row,Col);
        TSFC022S = TSFC022S + SFC022S(Row,Col);

        TSSC02 = TSSC02 + SSC02(Row,Col);
        TSSC02S = TSSC02S + SSC02S(Row,Col);

        TSTC016 = TSTC016 + STC016(Row,Col);
        TSTC016S = TSTC016S + STC016S(Row,Col);

        TSASnC = TSASnC + SASnC(Row,Col);
        TSFSnC = TSFSnC + SFSnC(Row,Col);

        Col = Col + 1;
    end

    Row = Row + 1;
end

% Determining the Total Percentage of the Magnetic Flux Density that is
% left for each of the modifications performed

PerTSBSnC = (1 - TSBSnC/TSBnC)*100

PerTSFC022 = (1 - TSFC022/TSBnC)*100
PerTSFC022S = (1 - TSFC022S/TSBnC)*100

PerTSSC02 = (1 - TSSC02/TSBnC)*100
PerTSSC02S = (1 - TSSC02S/TSBnC)*100

PerTSTC016 = (1 - TSTC016/TSBnC)*100
PerTSTC016S = (1 - TSTC016S/TSBnC)*100

PerTSASnC = (1 - TSASnC/TSBnC)*100
PerTSFSnC = (1 - TSFSnC/TSBnC)*100
```


10.7 Appendix 7: Data Sheets

10.7.1 Appendix 7.1: SG3525 – Pulse Width Modulator Control Circuit

P1

P2

10.7.2 Appendix 7.2: IR2113 – High and Low Side Driver

P1

P2

P3

P4

10.7.3 Appendix 7.3: IRFZ44 – 60V 50A Mosfet

P1

P2

10.7.4 Appendix 7.4: UC3825 – High Speed Pulse Width Modulator (PWM) Controller

P1

P2

10.7.5 Appendix 7.5: MAX436 – Wideband Transconductance Amplifier

P1

P2

P3

P4

11 List of Figures

FIGURE 1-1: INDUCTIVE PROXIMITY SENSOR ON PROXIMITY SENSOR PLATFORM NEXT TO A RAILWAY TRACK IN LABORATORY.....	3
FIGURE 1-2: A DIAGRAMMATIC REPRESENTATION OF THE SENSING HEAD OF THE INDUCTIVE PROXIMITY SENSOR AND ITS POSITION RELATIVE TO PROXIMITY SENSOR PLATFORM ADJACENT TO THE RAILWAY TRACK.....	3
FIGURE 1-3: EXAMPLE OF MAGNETIC FIELD DISTORTION WHEN TWO CONDUCTORS CARRYING CURRENT ARE PLACED IN PARALLEL.....	7
FIGURE 1-4: PROPOSED SHIELDING SOLUTION GEOMETRY, SHOWING THE INFLUENCE OF THE SHIELD ON THE MAGNETIC FLUX LINES.....	10
FIGURE 1-5: MEASUREMENT GRID USED FOR THE MAPPING PROCESS, FOR BOTH THE UNSHIELDED AND SHIELDED CASES.....	13
FIGURE 1-6: BREAK DOWN OF THE SENSING REGION FOR THE DIRECT COMPARISON BETWEEN ALL DIFFERENT TEST CASES.....	15
FIGURE 2-1: HIGH CURRENT TRANSFORMER (LEFT) AND ITS CONTROL BENCH (RIGHT).....	17
FIGURE 2-2: CONNECTION DIAGRAM SHOWING THE RAILWAY TRACK SYSTEM FOR THE LOW FREQUENCY TESTS.....	17
FIGURE 2-3: CONSTRUCTION OF MAGNETIC FLUX DENSITY SENSOR COIL.....	20
FIGURE 2-4: TEST RIG PLACED AROUND RAILWAY TRACK, SHOWING METAL SHIELD AND MAGNETIC FLUX DENSITY SENSOR AND MOUNTING.....	21
FIGURE 2-5: MAGNETIC FLUX DENSITY SENSOR MOUNTED ONTO THE TEST RIG IN THE XY GRID.....	22
FIGURE 2-6: CONTOUR PLOT OF THE MAGNITUDE OF THE Y COMPONENT OF THE MAGNETIC FLUX DENSITY FOR THE UNSHIELDED BASE MEASUREMENT AT 50 HZ.....	23
FIGURE 2-7: CONTOUR PLOT OF THE MAGNITUDE OF THE Y COMPONENT OF THE MAGNETIC FLUX DENSITY FOR THE SHIELDED MEASUREMENT AT 50 HZ.....	24
FIGURE 3-1: CIRCUIT DIAGRAM FOR A HALF BRIDGE PHASE ARM RESONATOR.....	27
FIGURE 3-2: SIMPLIFIED CIRCUIT DIAGRAM SHOWING A SERIES RESONANT CIRCUIT.....	28
FIGURE 3-3: OUTPUT VOLTAGE WAVE FORMS COMPARED TO INPUT VOLTAGE AT FREQUENCIES BELOW, EQUAL TO AND ABOVE RESONANCE, FOR A SERIES RESONANT CIRCUIT [7].....	31
FIGURE 3-4: OPERATION OF THE HALF BRIDGE RESONANT CONVERTER (RESONATOR) AT SWITCHING AT ITS RESONANT FREQUENCY.....	33
FIGURE 3-5: CIRCUIT DIAGRAM OF THE PULSE WIDTH MODULATOR (PWM) CONTROLLER.....	39
FIGURE 3-6: DRIVING SIGNALS FOR THE TWO SWITCHES $Sw1$ AND $Sw2$	40
FIGURE 3-7: CONSTRUCTED PULSE WIDTH MODULATOR (PWM) CONTROLLER.....	42
FIGURE 3-8: FREQUENCY CONTROL CIRCUIT (LABEL A FIGURE 3-7).....	42
FIGURE 3-9: FINAL CIRCUIT DIAGRAM OF THE 300 KHZ RESONATOR.....	44
FIGURE 3-10: CONSTRUCTED 300 KHZ RESONATOR, WHERE A INDICATES THE SWITCHES (MOSFETS), B THE COMMON MODE CHOKES, C THE INPUT POWER CAPACITOR BANK, D THE RESONANT CAPACITOR BANKS, E THE INTERNAL INDUCTOR AND F THE OUTPUT TERMINAL FOR THE RAILWAY TRACK.....	45

FIGURE 3-11: RAILWAY CONNECTED ACROSS OUTPUT TERMINAL (LABEL F) OF RESONATOR.....	46
FIGURE 3-12: CONNECTION BETWEEN THE DRIVING CIRCUIT (PWM) AND THE RESONATOR BOARD.....	47
FIGURE 3-13: THE FINALLY ASSEMBLED 300 KHZ RESONATOR, WITH ALL THE PORTS MARKED.....	48
FIGURE 3-14: CIRCUIT DIAGRAM FOR THE NEW 300 KHZ TO 1 MHZ DRIVING CIRCUIT INCORPORATING THE UC3825 IC.....	50
FIGURE 3-15: PRESET OPERATING FREQUENCY SWITCHER.....	51
FIGURE 4-1: DIAGRAMMATIC REPRESENTATION OF THE CAPACITIVE COUPLING BETWEEN THE RAILWAY TRACK AND THE FLUX DENSITY SENSOR.....	54
FIGURE 4-2: INDUCTANCE CAUSED BY THE PIGTAIL CONNECTION OF THE DRAIN WIRE LINKING THE CABLE SCREEN TO THE GROUND OF AN INSTRUMENT.....	57
FIGURE 4-3: WINDING LAYOUT FOR THE FLUX DENSITY SENSOR.....	62
FIGURE 4-4: PLACEMENT OF COPPER SHIELD AROUND THE FLUX DENSITY SENSOR.....	62
FIGURE 4-5: COPPER SHEET USED FOR THE SHIELD OF THE FLUX DENSITY SENSOR.....	63
FIGURE 4-6: COMPOSITE CABLE USED FOR IMPROVED MEASUREMENT SYSTEM.....	63
FIGURE 4-7: 360° TERMINATION AT COPPER SHIELD OF FLUX DENSITY SENSOR.....	64
FIGURE 4-8: FLUX DENSITY SENSOR WITH DOUBLE BRAIDING SCREEN CONNECTED TO COPPER SHIELD WITH A 360° TERMINATION.....	65
FIGURE 4-9: BRAIDED LINK BETWEEN THE PREPARED FLUX DENSITY SENSOR AND THE CABLING.....	65
FIGURE 4-10: SILVER TAPE FOR IMPROVED ELECTRIC FIELD SCREENING OVER THE CONSTRUCTED BRAIDED SECTIONS.....	66
FIGURE 4-11: GREEN AND RED WIRE PAIR CONNECTED TO TIP OF THE IN-LINE 2 PORT MICROPHONE CONNECTOR.....	66
FIGURE 4-12: SCREEN OF CABLE TERMINATING WITH 360° OF CONTACT ON THE MICROPHONE CONNECTOR (LEFT), AND WITH THE CONTACT POINT CLOSED (RIGHT).....	66
FIGURE 4-13: 2 PORT MICROPHONE PLUG CONNECTOR MOUNTED TO THE CHASSIS OF ONE OF THE SHIELDED ENCLOSURES, TOP VIEW ON THE LEFT WITH A FRONT VIEW ON THE RIGHT.....	67
FIGURE 4-14: SCREENED CABLE CONNECTED TO SHIELDED ENCLOSURE VIA SHIELDED MICROPHONE CONNECTORS.....	67
FIGURE 4-15: SCREENED CABLE CONNECTED TO BNC CONNECTOR FOR THE OSCILLOSCOPE (LEFT), AND CONNECTIONS FROM THE SIGNAL CONDUCTORS FOR THE BCN CONNECTOR (RIGHT).....	68
FIGURE 4-16 : CIRCUIT DIAGRAM OF +/- 9V TO +/- 5V VOLTAGE REGULATOR.....	70
FIGURE 4-17: CIRCUIT DIAGRAM OF THE WIDEBAND TRANSCONDUCTANCE AMPLIFIER.....	70
FIGURE 4-18: WIDEBAND TRANSCONDUCTANCE AMPLIFIER WITH IN A SHIELDED ENCLOSURE, WITH THE FLUX DENSITY SENSOR CONNECTED TO THE INPUT AND THE OUTPUT CONNECTED TO THE REMAINDER OF THE MEASUREMENT SYSTEM.....	72
FIGURE 4-19: COMMON MODE CHOKE BEFORE THE OSCILLOSCOPE WITH IN A SHIELDED ENCLOSURE AND SECURED WITH CONDUCTIVE CONTACT TO THE GROUND PLANE.....	73
FIGURE 4-20: COMMON MODE CHOKE AT INPUT TO WIDEBAND TRANSCONDUCTANCE AMPLIFIER.....	73
FIGURE 4-21: GROUNDING CONNECTION BETWEEN THE SHIELDING SYSTEM OF THE MEASUREMENT SYSTEM TO THE GROUND PLANE.....	74

FIGURE 4-22: DC AND LOW FREQUENCY GROUND CONNECTION	75
FIGURE 4-23: BRAIDED CONNECTION ON GROUND PLANE TO LINK TO THE OSCILLOSCOPE'S GROUND....	75
FIGURE 4-24: DISPLAY ON THE NETWORK ANALYSER FOR THE TESTS ON THE 200 TURN FLUX DENSITY SENSOR COIL.....	76
FIGURE 4-25: THE CALIBRATION SETUP USED TO DETERMINE THE CALIBRATION COEFFICIENTS FOR THE MEASUREMENT SYSTEM.....	78
FIGURE 4-26: PORTS ON THE NETWORK ANALYSER FOR USE WITH THE CALIBRATION SYSTEM.	79
FIGURE 4-27: CIRCUIT DIAGRAM FOR THE ELECTRICAL MODEL OF THE CALIBRATION SYSTEM.....	80
FIGURE 5-1: RAILWAY TRACK SYSTEM'S PROBE CONNECTIONS TO MONITOR RESONANT VOLTAGES AND CURRENTS.	87
FIGURE 5-2: CIRCUIT DIAGRAM FOR THE ELECTRICAL MODEL OF THE FINAL MEASUREMENT SYSTEM... 88	
FIGURE 5-3: FINAL TEST SETUP USED FOR THE 2A 300 KHZ HIGH FREQUENCY TESTS, SHOWING THE SHIELD POSITION, ISOLATION, PARALLEL CABLE MOUNTING AND POSITIONING ALL RELATIVE TO THE RAILWAY TRACK AND THE PROXIMITY SENSOR PLATFORM.	91
FIGURE 5-4: CONTOUR PLOT OF THE Y COMPONENT OF THE MAGNETIC FLUX DENSITY FOR THE BASE MEASUREMENT WITH NO SHIELD, CABLE AND ISOLATION.	93
FIGURE 5-5: CONTOUR PLOT OF THE Y COMPONENT OF THE MAGNETIC FLUX DENSITY FOR SHIELDED CASE NO CABLE OR ISOLATION.....	95
FIGURE 5-6: CONTOUR PLOT OF THE Y COMPONENT OF THE MAGNETIC FLUX DENSITY FOR SHIELDED CASE WITH ISOLATION BUT NO CABLE.....	96
FIGURE 5-7: CONTOUR PLOT OF THE Y COMPONENT OF THE MAGNETIC FLUX DENSITY FOR THE SUB-BASE MEASUREMENT WITH THE FIRST CABLE IN PLACE WITH NO SHIELD OR ISOLATION.	97
FIGURE 5-8: CONTOUR PLOT OF THE Y COMPONENT OF THE MAGNETIC FLUX DENSITY FOR THE FIRST CABLE IN PLACE WITH SHIELD BUT NO ISOLATION.....	98
FIGURE 5-9: CONTOUR PLOT OF THE Y COMPONENT OF THE MAGNETIC FLUX DENSITY FOR THE FIRST CABLE IN PLACE WITH SHIELD AND ISOLATION.	99
FIGURE 5-10: DIRECT COMPARISON FOR THE FIRST TEST SET WITH NO PARALLEL CABLE INSTALLED COMPRISING OF THE BASE MEASUREMENT, THE INCLUSION OF A SHIELD AND THE INCLUSION OF BOTH THE SHIELD AND ISOLATION LAYER.....	102
FIGURE 5-11: NORMALIZED DATA FOR THE DIRECT COMPARISON OF THE FIRST TEST SET WITH THE INCLUSION OF NO PARALLEL CABLE.....	103
FIGURE 5-12: DIRECT COMPARISON FOR THE SECOND TEST SET WITH THE ADDITION OF THE FIRST PARALLEL CABLE, COMPRISING OF THE SUB-BASE MEASUREMENT, THE INCLUSION OF A SHIELD AND THE INCLUSION OF BOTH THE SHIELD AND ISOLATION LAYER.....	104
FIGURE 5-13: NORMALIZED DATA FOR THE DIRECT COMPARISON OF THE SECOND TEST SET THAT INCLUDES THE ADDITION OF THE FIRST PARALLEL CABLE.....	105
FIGURE 5-14: DIRECT COMPARISON FOR THE THIRD TEST SET WITH THE ADDITION OF THE SECOND PARALLEL CABLE, COMPRISING OF THE SUB-BASE MEASUREMENT, THE INCLUSION OF A SHIELD AND THE INCLUSION OF BOTH THE SHIELD AND ISOLATION LAYER.....	106

FIGURE 5-15: NORMALIZED DATA FOR THE DIRECT COMPARISON OF THE THIRD TEST SET THAT INCLUDES THE ADDITION OF THE SECOND PARALLEL CABLE.	107
FIGURE 5-16: DIRECT COMPARISON FOR THE FOURTH TEST SET WITH THE ADDITION OF THE THIRD PARALLEL CABLE, COMPRISING OF THE SUB-BASE MEASUREMENT, THE INCLUSION OF A SHIELD AND THE INCLUSION OF BOTH THE SHIELD AND ISOLATION LAYER.....	108
FIGURE 5-17: NORMALIZED DATA FOR THE DIRECT COMPARISON OF THE FOURTH TEST SET THAT INCLUDES THE ADDITION OF THE THIRD PARALLEL CABLE.	109
FIGURE 5-18: NORMALISED DIRECT COMPARISON TO DETERMINE THE EFFECT OF THE ADDITION OF THE THREE SEPARATE CABLES TO THE RAILWAY TRACK SYSTEM.....	110
FIGURE 5-19: NORMALISED DIRECT COMPARISON TO DETERMINE THE EFFECT OF THE INCLUSION OF THE SHIELD FOR THE THREE SEPARATE CABLES.	111
FIGURE 5-20: NORMALISED DIRECT COMPARISON TO DETERMINE THE EFFECT OF THE INCLUSION OF THE SHIELD AND ISOLATION LAYER FOR THE THREE SEPARATE CABLES.....	112
FIGURE 6-1: SIMULATION MODEL USED, SHOWING THE CONSTANT RAILWAY TRACK AND PROXIMITY SENSOR PLATFORM AND THE SOME TIMES PRESENT SHIELD AND OR PARALLEL CABLE.	114
FIGURE 6-2: NEW AND FINAL SIMULATION MODEL USED, SHOWING THE CONSTANT RAILWAY TRACK AND PROXIMITY SENSOR PLATFORM AND THE SOME TIMES PRESENT SHIELD AND OR PARALLEL CABLE.	115
FIGURE 6-3: SIMULATED RESULTS SHOWING THE FLUX DENSITY WITHIN THE TEST AREA FOR THE BASE SIMULATION, WITH NO SHIELD OR CABLE.	119
FIGURE 6-4: SIMULATED RESULTS SHOWING THE FLUX DENSITY WITHIN THE TEST AREA FOR THE BASE SIMULATION, WITH THE INCLUSION OF A SHIELD BUT NO CABLE.	120
FIGURE 6-5: SIMULATED RESULTS SHOWING THE FLUX DENSITY WITHIN THE TEST AREA FOR THE SUB-BASE SIMULATION INVOLVING THE FIRST PARALLEL CABLE CARRYING A 0.22 A CURRENT , WITH NO SHIELD.....	121
FIGURE 6-6: SIMULATED RESULTS SHOWING THE FLUX DENSITY WITHIN THE TEST AREA FOR THE SUB-BASE SIMULATION INVOLVING THE FIRST PARALLEL CABLE CARRYING A 0.22 A CURRENT, WITH THE INCLUSION OF THE SHIELD.	122
FIGURE 6-7: SIMULATED RESULTS SHOWING THE FLUX DENSITY WITHIN THE TEST AREA FOR THE SUB-BASE SIMULATION INVOLVING THE SECOND PARALLEL CABLE CARRYING A 0.2 A CURRENT, WITH NO SHIELD.....	123
FIGURE 6-8: SIMULATED RESULTS SHOWING THE FLUX DENSITY WITHIN THE TEST AREA FOR THE SUB-BASE SIMULATION INVOLVING THE SECOND PARALLEL CABLE CARRYING A 0.2 A CURRENT, WITH THE INCLUSION OF THE SHIELD.	124
FIGURE 6-9: SIMULATED RESULTS SHOWING THE FLUX DENSITY WITHIN THE TEST AREA FOR THE SUB-BASE SIMULATION INVOLVING THE THIRD PARALLEL CABLE CARRYING A 0.16 A CURRENT, WITH NO SHIELD.....	125
FIGURE 6-10: SIMULATED RESULTS SHOWING THE FLUX DENSITY WITHIN THE TEST AREA FOR THE SUB-BASE SIMULATION INVOLVING THE THIRD PARALLEL CABLE CARRYING A 0.16 A CURRENT, WITH THE INCLUSION OF THE SHIELD.	126

FIGURE 6-11: DIRECT COMPARISON FOR ALL THE UN-SHIELDED SIMULATIONS.	128
FIGURE 6-12: DIRECT COMPARISON FOR ALL THE SHIELDED SIMULATIONS.	129
FIGURE 6-13: SIMULATED RESULTS SHOWING THE FLUX DENSITY WITHIN THE TEST AREA FOR THE BASE SIMULATION, WITH THE INCLUSION OF AN ALUMINIUM SHIELD BUT NO CABLE, SHOWING THE DEFLECTION PRINCIPLE.	131
FIGURE 6-14: SIMULATED RESULTS SHOWING THE FLUX DENSITY WITHIN THE TEST AREA FOR THE BASE SIMULATION, WITH THE INCLUSION OF A FERRITE SHIELD BUT NO CABLE, SHOWING THE ABSORPTION PRINCIPLE.	132
FIGURE 6-15: DIRECT COMPARISON BETWEEN THE BASE SIMULATION, DEFLECTION SIMULATION AND THE ABSORPTION SIMULATION.	133
FIGURE 10-1: CONTOUR PLOT OF THE COMBINED MAGNITUDE MAGNETIC FLUX DENSITY FOR THE UNSHIELDED BASE MEASUREMENT AT 50 HZ.	141
FIGURE 10-2: CONTOUR PLOT OF THE COMBINED MAGNITUDE MAGNETIC FLUX DENSITY FOR THE SHIELDED MEASUREMENT AT 50 HZ.	142
FIGURE 10-3: CONTOUR PLOT OF THE X COMPONENT OF THE MAGNITUDE MAGNETIC FLUX DENSITY FOR THE UNSHIELDED BASE MEASUREMENT AT 50 HZ.	142
FIGURE 10-4: CONTOUR PLOT OF THE X COMPONENT OF THE MAGNITUDE MAGNETIC FLUX DENSITY FOR THE SHIELDED MEASUREMENT AT 50 HZ.	142
FIGURE 10-5: VOLTAGE AND CURRENT WAVE FORMS ACROSS THE INDUCTOR OF THE BUCK CONVERTER.	143
FIGURE 10-6: CIRCUIT DIAGRAM OF THE BUCK CONVERTER USED.	145
FIGURE 10-7: E TYPE MAGNETIC CORES, SHOWING SOME VARIABLE DEFINITIONS. [8].....	147
FIGURE 10-8: PCB OF THE DRIVING CIRCUIT OR PWM HALF BRIDGE MOSFET DRIVER.	151
FIGURE 10-9: THE PCB LAYOUT OF THE 300 KHZ RESONATOR BOARD.....	152
FIGURE 10-10: CIRCUIT DIAGRAM SIMULATED USING P-SPICE TO PREDICT THE OPERATION OF THE REAL RESONATOR.	153
FIGURE 10-11: DRIVING SIGNAL BEING SUPPLIED TO THE HIGH AND LOW SIDE MOSFETS BY THE DRIVING CIRCUIT.....	154
FIGURE 10-12: CURRENT THROUGH THE INTERNAL INDUCTOR AND THE RAILWAY TRACK, AND THE CURRENTS FLOWING THROUGH THE TWO CAPACITOR BANKS $C1$ AND $C2$	155
FIGURE 10-13: RESONANT VOLTAGE BETWEEN THE TWO CAPACITOR BANKS ($C1$ AND $C1$) AND THE RAILWAY TRACK.....	155
FIGURE 10-14: TEST SETUP USED ALONG WITH THE RAILWAY TRACK.	156
FIGURE 10-15: DRIVING SIGNAL SENT TO THE HIGH AND LOW SIDE MOSFETS OF THE 300 KHZ RESONATOR BOARD	156
FIGURE 10-16: MEASUREMENT OF CURRENT FLOWING THROUGH THE RAILWAY TRACK.	157
FIGURE 10-17: RESONANT VOLTAGE BETWEEN THE CAPACITOR BANKS AND THE RAILWAY TRACK, WITH THE RESONANT VOLTAGE BETWEEN THE INTERNAL INDUCTOR AND THE RAILWAY TRACK.....	158
FIGURE 10-18: PCB FOR 300 KHZ TO 1 MHZ DRIVING CIRCUIT, WITH PRESET FREQUENCY CONTROLS.	160

FIGURE 10-19: PCB OF THE NEW MODIFIED RESONATOR BOARD FOR OPERATION FROM 300 kHz TO 1 MHz.	161
FIGURE 10-20: MICROPHONE CABLE.	164
FIGURE 10-21: FLUX DENSITY SENSOR CONNECTED TO THE MICROPHONE CABLE.	165
FIGURE 10-22: FLUX DENSITY SENSOR CONNECTED TO MICROPHONE CABLE WITH CONNECTION SHIELDED.	166
FIGURE 10-23: CONNECTION TO OSCILLOSCOPE BNC MALE CONNECTOR, WITH SHIELDED CONNECTION.	166
FIGURE 10-24: CONTOUR PLOT OF THE Y COMPONENT OF THE MAGNETIC FLUX DENSITY FOR THE SUB-BASE MEASUREMENT WITH THE SECOND CABLE IN PLACE WITH NO SHIELD OR ISOLATION.	167
FIGURE 10-25: CONTOUR PLOT OF THE Y COMPONENT OF THE MAGNETIC FLUX DENSITY FOR THE SECOND CABLE IN PLACE WITH SHIELD BUT NO ISOLATION.	168
FIGURE 10-26: CONTOUR PLOT OF THE Y COMPONENT OF THE MAGNETIC FLUX DENSITY FOR THE SECOND CABLE IN PLACE WITH SHIELD AND ISOLATION.	169
FIGURE 10-27: CONTOUR PLOT OF THE Y COMPONENT OF THE MAGNETIC FLUX DENSITY FOR THE SUB-BASE MEASUREMENT WITH THE THIRD CABLE IN PLACE WITH NO SHIELD OR ISOLATION.	170
FIGURE 10-28: CONTOUR PLOT OF THE Y COMPONENT OF THE MAGNETIC FLUX DENSITY FOR THE THIRD CABLE IN PLACE WITH SHIELD BUT NO ISOLATION.	171
FIGURE 10-29: CONTOUR PLOT OF THE Y COMPONENT OF THE MAGNETIC FLUX DENSITY FOR THE THIRD CABLE IN PLACE WITH SHIELD AND ISOLATION.	172
FIGURE 10-30: CONTOUR PLOT OF THE X COMPONENT OF THE MAGNETIC FLUX DENSITY FOR THE BASE MEASUREMENT WITH NO SHIELD, CABLE AND ISOLATION.	173
FIGURE 10-31: CONTOUR PLOT OF THE MAGNETIC FLUX DENSITY FOR THE BASE MEASUREMENT WITH NO SHIELD, CABLE AND ISOLATION.	174
FIGURE 10-32: CONTOUR PLOT OF THE X COMPONENT OF THE MAGNETIC FLUX DENSITY FOR SHIELDED CASE NO CABLE OR ISOLATION.	175
FIGURE 10-33: CONTOUR PLOT OF THE MAGNETIC FLUX DENSITY FOR SHIELDED CASE NO CABLE OR ISOLATION.	176
FIGURE 10-34: CONTOUR PLOT OF THE X COMPONENT OF THE MAGNETIC FLUX DENSITY FOR SHIELDED CASE WITH ISOLATION BUT NO CABLE.	177
FIGURE 10-35: CONTOUR PLOT OF THE MAGNETIC FLUX DENSITY FOR SHIELDED CASE WITH ISOLATION BUT NO CABLE.	177
FIGURE 10-36: CONTOUR PLOT OF THE X COMPONENT OF THE MAGNETIC FLUX DENSITY FOR THE SUB-BASE MEASUREMENT WITH THE FIRST CABLE IN PLACE WITH NO SHIELD OR ISOLATION.	178
FIGURE 10-37: CONTOUR PLOT OF THE MAGNETIC FLUX DENSITY FOR THE SUB-BASE MEASUREMENT WITH THE FIRST CABLE IN PLACE WITH NO SHIELD OR ISOLATION.	178
FIGURE 10-38: CONTOUR PLOT OF THE X COMPONENT OF THE MAGNETIC FLUX DENSITY FOR THE FIRST CABLE IN PLACE WITH SHIELD BUT NO ISOLATION.	179
FIGURE 10-39: CONTOUR PLOT OF THE MAGNETIC FLUX DENSITY FOR THE FIRST CABLE IN PLACE WITH SHIELD BUT NO ISOLATION.	179

FIGURE 10-40: CONTOUR PLOT OF THE X COMPONENT OF THE MAGNETIC FLUX DENSITY FOR THE FIRST CABLE IN PLACE WITH SHIELD AND ISOLATION.	180
FIGURE 10-41: CONTOUR PLOT OF THE MAGNETIC FLUX DENSITY FOR THE FIRST CABLE IN PLACE WITH SHIELD AND ISOLATION.	180
FIGURE 10-42: CONTOUR PLOT OF THE X COMPONENT OF THE MAGNETIC FLUX DENSITY FOR THE SUB-BASE MEASUREMENT WITH THE SECOND CABLE IN PLACE WITH NO SHIELD OR ISOLATION.	181
FIGURE 10-43: CONTOUR PLOT OF THE MAGNETIC FLUX DENSITY FOR THE SUB-BASE MEASUREMENT WITH THE SECOND CABLE IN PLACE WITH NO SHIELD OR ISOLATION.	181
FIGURE 10-44: CONTOUR PLOT OF THE X COMPONENT OF THE MAGNETIC FLUX DENSITY FOR THE SECOND CABLE IN PLACE WITH SHIELD BUT NO ISOLATION.	182
FIGURE 10-45: CONTOUR PLOT OF THE MAGNETIC FLUX DENSITY FOR THE SECOND CABLE IN PLACE WITH SHIELD BUT NO ISOLATION.	182
FIGURE 10-46: CONTOUR PLOT OF THE X COMPONENT OF THE MAGNETIC FLUX DENSITY FOR THE SECOND CABLE IN PLACE WITH SHIELD AND ISOLATION.	183
FIGURE 10-47: CONTOUR PLOT OF THE MAGNETIC FLUX DENSITY FOR THE SECOND CABLE IN PLACE WITH SHIELD AND ISOLATION.	183
FIGURE 10-48: CONTOUR PLOT OF THE X COMPONENT OF THE MAGNETIC FLUX DENSITY FOR THE SUB-BASE MEASUREMENT WITH THE THIRD CABLE IN PLACE WITH NO SHIELD OR ISOLATION.	184
FIGURE 10-49: CONTOUR PLOT OF THE MAGNETIC FLUX DENSITY FOR THE SUB-BASE MEASUREMENT WITH THE THIRD CABLE IN PLACE WITH NO SHIELD OR ISOLATION.	184
FIGURE 10-50: CONTOUR PLOT OF THE X COMPONENT OF THE MAGNETIC FLUX DENSITY FOR THE THIRD CABLE IN PLACE WITH SHIELD BUT NO ISOLATION.	185
FIGURE 10-51: CONTOUR PLOT OF THE MAGNETIC FLUX DENSITY FOR THE THIRD CABLE IN PLACE WITH SHIELD BUT NO ISOLATION.	185
FIGURE 10-52: CONTOUR PLOT OF THE X COMPONENT OF THE MAGNETIC FLUX DENSITY FOR THE THIRD CABLE IN PLACE WITH SHIELD AND ISOLATION.	186
FIGURE 10-53: CONTOUR PLOT OF THE MAGNETIC FLUX DENSITY FOR THE THIRD CABLE IN PLACE WITH SHIELD AND ISOLATION.	186
FIGURE 10-54: DIRECT COMPARISON TO DETERMINE THE EFFECT OF THE ADDITION OF THE THREE SEPARATE CABLES TO THE RAILWAY TRACK SYSTEM.	187
FIGURE 10-55: DIRECT COMPARISON TO DETERMINE THE EFFECT OF THE INCLUSION OF THE SHIELD FOR THE THREE SEPARATE CABLES.	188
FIGURE 10-56: DIRECT COMPARISON TO DETERMINE THE EFFECT OF THE INCLUSION OF THE SHIELD AND ISOLATION LAYER FOR THE THREE SEPARATE CABLES.	189
FIGURE 10-57: SIMULATED RESULTS SHOWING THE FLUX LINES WITHIN THE TEST AREA FOR THE BASE SIMULATION, WITH NO SHIELD OR CABLE.	190
FIGURE 10-58: SIMULATED RESULTS SHOWING THE FLUX LINES WITHIN THE TEST AREA FOR THE BASE SIMULATION, WITH THE INCLUSION OF A SHIELD BUT NO CABLE.	190
FIGURE 10-59: SIMULATED RESULTS SHOWING THE FLUX LINES WITHIN THE TEST AREA FOR THE SUB-BASE SIMULATION INVOLVING THE FIRST PARALLEL CABLE, WITH NO SHIELD.	191

FIGURE 10-60: SIMULATED RESULTS SHOWING THE FLUX LINES WITHIN THE TEST AREA FOR THE SUB BASE SIMULATION INVOLVING THE FIRST PARALLEL CABLE, WITH THE INCLUSION OF THE SHIELD.	191
FIGURE 10-61: SIMULATED RESULTS SHOWING THE FLUX LINES WITHIN THE TEST AREA FOR THE SUB BASE SIMULATION INVOLVING THE SECOND PARALLEL CABLE, WITH NO SHIELD.	192
FIGURE 10-62: SIMULATED RESULTS SHOWING THE FLUX LINES WITHIN THE TEST AREA FOR THE SUB BASE SIMULATION INVOLVING THE SECOND PARALLEL CABLE, WITH THE INCLUSION OF THE SHIELD.	192
FIGURE 10-63: SIMULATED RESULTS SHOWING THE FLUX LINES WITHIN THE TEST AREA FOR THE SUB BASE SIMULATION INVOLVING THE THIRD PARALLEL CABLE, WITH NO SHIELD.	193
FIGURE 10-64: SIMULATED RESULTS SHOWING THE FLUX LINES WITHIN THE TEST AREA FOR THE SUB BASE SIMULATION INVOLVING THE THIRD PARALLEL CABLE, WITH THE INCLUSION OF THE SHIELD.	193
FIGURE 10-65: DIRECT COMPARISON BETWEEN SHIELDED AND UN-SHIELDED BASE SIMULATION WITH NO CABLE.	194
FIGURE 10-66: DIRECT COMPARISON BETWEEN SHIELDED AND UN-SHIELDED SIMULATION WITH THE FIRST PARALLEL CABLE IN PLACE CARRYING 0.22 A.	195
FIGURE 10-67: DIRECT COMPARISON BETWEEN SHIELDED AND UN-SHIELDED SIMULATION WITH THE SECOND PARALLEL CABLE IN PLACE CARRYING 0.2 A.	196
FIGURE 10-68: DIRECT COMPARISON BETWEEN SHIELDED AND UN-SHIELDED SIMULATION WITH THE THIRD PARALLEL CABLE IN PLACE CARRYING 0.16 A.	197
FIGURE 10-69: SIMULATED RESULTS SHOWING THE FLUX LINES WITHIN THE TEST AREA FOR THE INCLUSION OF AN ALUMINIUM SHIELD.	198
FIGURE 10-70: SIMULATED RESULTS SHOWING THE FLUX LINES WITHIN THE TEST AREA FOR THE INCLUSION OF A FERRITE SHIELD.	198

12 List of Tables

TABLE 4-1: LOAD IMPEDANCE AND GAIN FOR THE AMPLIFICATION SYSTEM FOR THE CALIBRATION SETUP.	84
TABLE 4-2: IMPEDANCE OF THE SOLENOID AT THE DIFFERENT PRINCIPLE FREQUENCIES.	85
TABLE 4-3: MEASURED VOLTAGES FROM THE CALIBRATION SYSTEM.	85
TABLE 4-4: CALIBRATION COEFFICIENTS FOR THE PRINCIPLE FREQUENCIES.	85
TABLE 5-1: TOTAL OUTPUT IMPEDANCE OF THE AMPLIFICATION SYSTEM AND ITS ACCOMPANYING GAIN.	90
TABLE 6-1: TOTAL REDUCTION IN THE FLUX DENSITY WITHIN THE SENSING REGION FOR EACH OF THE SIMULATED CASES COMPARED TO THE BASE SIMULATION.	127